Characterization of Mixing and Combustion Processes of Diesel Spray in High Ambient Gas Density

(高密度雰囲気中におけるデイーゼル噴霧の混合と燃焼過程の特性)

by

Zhu, Jingyu

Dissertation

Submitted to the Graduate School of Engineering

Hiroshima University

in Partial Fulfillment of the Requirements

For the Degree of

Doctor of Engineering

Hiroshima University

September, 2012

Acknowledgements

I would like to express my greatest gratitude to my supervisor, Prof. Keiya Nishida, who grants me the opportunity to study in his laboratory and provides me with kind guidance and tutorship not only in the scientific research but also in the everyday life. It is impossible for me to achieve this accomplishment within the three years without his patient and thoughtful instruction. I also would like to thank the associate Prof. Yoichi Ogata in our laboratory, his kind instruction especially his experience in numerical simulation facilitates our research.

I express my special compliment to China Scholarship Council (CSC), a non-profit institution affiliated with the Ministry of Education of China, who sponsors me the living expense in Japan. The China General Consulate in Osaka gives us the immediate response and suggestion as soon as we have need.

I am indebted to my predecessors and colleagues in our laboratory who are committed to the research in the spray and combustion field. Dr. Seoksu Moon, Dr. Wu Zhang, Dr. Jiangping Tian and Dr. Olawole Abiola Kuti give me their precious experience and kind assistance any time. Mr. Ogawa, Mr. Egashira, Mr. Uemura and many other master students join in my group and we cooperate all the time. Meanwhile, I never forget the kind help and instruction from the staff of students supporting office of faculty of engineering and service room of department of mechanical engineering.

At last, my deepest gratitude is sent to my family. My wife and I married during my doctor course study period, her firm support, encouragement and love is the most important source for my career. I also never forget the great love from my parents in all my life. My best wishes and love will be given to my baby, who will be born in October. The fetal movement brought us the happiness when I composed this dissertation, my Ph.D diploma will be his/her first present.

ABSTRACT

It is worth understanding the fundamental mechanism of the mixture formation process and combustion characteristics of the D.I. Diesel spray, which is believed to be one of the key factors to determine the subsequent combustion and pollutant formation process in the Diesel engines.

This study is aimed at clarifying the mixing process and the combustion characteristics of the high pressure D.I. Diesel spray in the quiescent condition. A wide range of injection pressure from the ordinary values in the current Diesel engines (100MPa, 200MPa) to the ultra-high (300MPa) value was selected. Three representative ambient gas density conditions (11, 15, 20 kg/m^3) were selected. A micro-hole nozzle (0.08mm) and a conventional nozzle (0.12mm) were applied as the test nozzles in this study.

The direct photography was used to characterize the spray development. The ambient gas motion characteristics such as the velocity distribution and the ambient gas mass flow rate around the entire periphery of the transient Diesel spray were analyzed quantitatively using LIF-PIV technique. The spray internal flow characteristics such as the velocity distribution and the vorticity distribution were measured using PIV technique. The effects of the fuel injection pressure, ambient gas density, nozzle-hole size, on the ambient gas/internal flow of the spray were taken into account. The non-evaporating/evaporating condition, and the free spray/ flat-wall impinging spray were considered respectively.

The characteristics of the combustion process of the Diesel spray were investigated using the direct imaging of natural flame luminosity, OH* chemiluminescence imaging and two color pyrometry techniques. The combustion behaviors were related to the previously measured spray evolution and ambient gas motion features.

Finally, the CFD Numerical simulation on the Diesel spray evolution was carried out to provide insightful understanding of the microscopic spray characteristics. The primary findings in the experimental results also provide useful information for the design of new Diesel fuel injection systems and for the calibration of predicative spray models.

TABLE OF CONTENTS

NOMENCLATURES

AMD	Arithmetic mean diameter (um)
$A(x,\alpha)$	Surface area of spray side from x to x+dx
$A(\theta)$	Axial projected surface area of spray tip from θ to $\theta+\mathrm{d}\theta$
C_a	Area contraction coefficient
C_v	Velocity coefficient
C_d	Discharge coefficient
C_P	Heat capacity (J/(g·K)
CCD	Charge-coupled device
CFD	Computational fluids dynamics
CO	Monoxides of carbon
d	Droplet diameter
D	Nozzle hole diameter(mm)
$E_{b,\lambda}$	Monochromatic emissive power of a blackbody
EGR	Exhaust Gas Recirculation
EOI	End of injection
fps	Frame per second
HC	Hydrocarbon
HCCI	Homogeneous Charge Compression Ignition
HWA	Hot Wire Anemometry
I	Light intensity
i, j	Coordinate index of region of interest
K	Cavitation number
KL	A coefficient proportional to line-of-sight integrated soot concentration
L_0	Lift-off length
LAS	Laser Absorption/Scattering
LDA	Laser Doppler Anemometer
LDSA	Laser Diffraction Size Analyzer
LEA	Laser Extinction/Absorption
LIF-PIV	Laser induced fluorescence-particle image velocimetry

LIEF	Laser Induced Exciplex Fluorescence
LII	Laser Induced Incandescence
LIS	Laser Induced Scattering
L_{th}	stoichiometric air/fuel ratio
LRS	Laser Rayleigh Scattering
L/D	Orifice length to diameter ratio
M_a	Ambient gas mass in spray(mg)
$\dot{M}_a$	Total ambient gas mass flow rate (mg/s)
$\dot{M}a_{ent}$	Ambient gas mass flow rate at entrainment section (mg/s)
$\dot{M}a_{cap}$	Ambient gas mass flow rate at capturing section (mg/s)
$\dot{M}a_{rec}$	Ambient gas mass flow rate at recirculation section of impinging spray (mg/s)
$\dot{M}at_{penetrating}$	Ideal ambient gas mass flow rate at tip periphery due to spray penetration (mg/s)
$\dot{M}at_{pushing}$	Ambient gas mass flow rate pushed out of the tip periphery (mg/s)
M_f	Injected fuel mass (mg)
$\dot{M}_f$	Fuel injection mass flow rate (mg/s)
MK	Modulated kinetics
NOx	Oxides of nitrogen
OH	Hydroxyl
PAH	Polycyclic aromatic hydrocarbon
PIV	Particle Image Velocimetry
P_{amb}	Ambient gas pressure (MPa)
P_{inj}	Fuel injection pressure measured in common rail (MPa)
P_{vap}	Fuel vapor pressure (MPa)
P_l	Liquid fuel pressure (MPa)
PCI	Premixed Compression Ignition
PDPA	Phase Doppler Particle Anemometry
PM	Particulate matters
R	Radius of ideal spray tip half sphere (mm)
R/D	Orifice inlet radius to diameter ratio

$RoHR$	Rate of heat release (J/.deg CA)
Re	Reynold number
$R_{II}(S, \Gamma, D)$	Cross-correlation function
$R_{II}(x, y)$	Integrated form of cross-correlation function
S	Spray tip penetration (mm)
SMD	Sauter mean diameter (μm)
SOI	Start of injection
SRS	Spontaneous Raman Scattering
t	Time after start of injection (ms)
T	Actual temperature (K)
T_a	Ambient gas temperature (K)
t_{break}	Break-up time defined by Hiroyasu and Arai [1991]
TDC	Top dead center
UV	Ultra-violet
$V(x, \alpha)$	Gas velocity at side periphery (m/s)
$V_n(x, \alpha)$	Normal velocity at side periphery (m/s)
$V(\theta)$	Gas flow velocity at tip periphery (m/s)
$V_x(\theta)$	Radial component of gas velocity at tip periphery (m/s)
$V_y(\theta)$	Axial component of gas velocity at tip periphery (m/s)
V_{upward}	Time rate of displacement of spray height of impinging spray (m/s)
V_{sp}	Spray tip penetrating velocity (m/s)
V_0	Fuel injection velocity (m/s)
V_p	Tracer particle velocity (m/s)
V_{rel}	Relative velocity of liquid/gas phase (m/s)
We_a	Gas phase weber number
x	Axial distance from nozzle tip (mm)
x^+	Characteristic length scale defined in Eq. (1.17)
x_1	Coordinate of downstream of entrainment section (mm)
Z	Impingement distance (mm)
α	Spray angle

θ	Arc angle relative to the horizontal direction in spray tip region
θ_1	Arc angle between horizontal direction and spray axis (90 deg.)
ρ_a	Ambient gas density (kg/m^3)
ρ_l	Liquid fuel density (kg/m^3)
U	Radial component of the flow velocity (m/s)
V	Axial component of the flow velocity (m/s)
σ	Surface tension
σ	Deviation of velocity distribution
M	Dynamic Viscosity (N s/m^2)
φ	Crank angle
ϕ_{mean}	Mean equivalence ratio
ϕ_{inst}	Instantaneous equivalence ratio
Z	Stoichiometric air to burn the injected fuel
λ	Wavelength length (μm)
λ	Heat transfer coefficient (w/(m Ƙ))
ω	Vorticity intensity (1/m^2)
ε_λ	Emissivity
τ	Stress tensor (N)
ΔP	Difference of fuel injection pressure and ambient gas pressure
Δt_{shot}	Time interval of two frames
Δt_{inj}	Time interval from tracer injection to fuel injection
Δz	Laser sheet thickness

CHAPTER 1 INTRODUCTION

1.1 BACKGROUND AND MOTIVATION

Diesel Engines have been widely used as the power source of commercial vehicles for a long period, which benefits from there high power output and high thermal efficiency compared with the conventional gasoline engines. In recent years, thanks to the introduction of new techniques such as the downsizing engine body, sophisticated injection strategy, common-rail injection system, VGT (Variable Geometry Turbo), and inter-cooled EGR system et al., the Diesel engines are capable to meet more stringent exhaust emission regulation. However, DI Diesel engines are confronted by the enhancing requirement for the reduction of NOx and particulate emission, which is one of the main disadvantages compared with the gasoline engines. Moreover, the global warming problem caused by the so-called green-house gas has gotten a great deal of international attention recently, thus the reduction of carbon dioxides emission as well as the improvement of fuel economy will become the most important concern for the automobile industry in the next several decades [Scorari, 1997]. Figure 1.1 exhibits the gradually tightened exhaust emission regulation for on-road Diesels in the global main markets from past to the future [Endo, 2011].

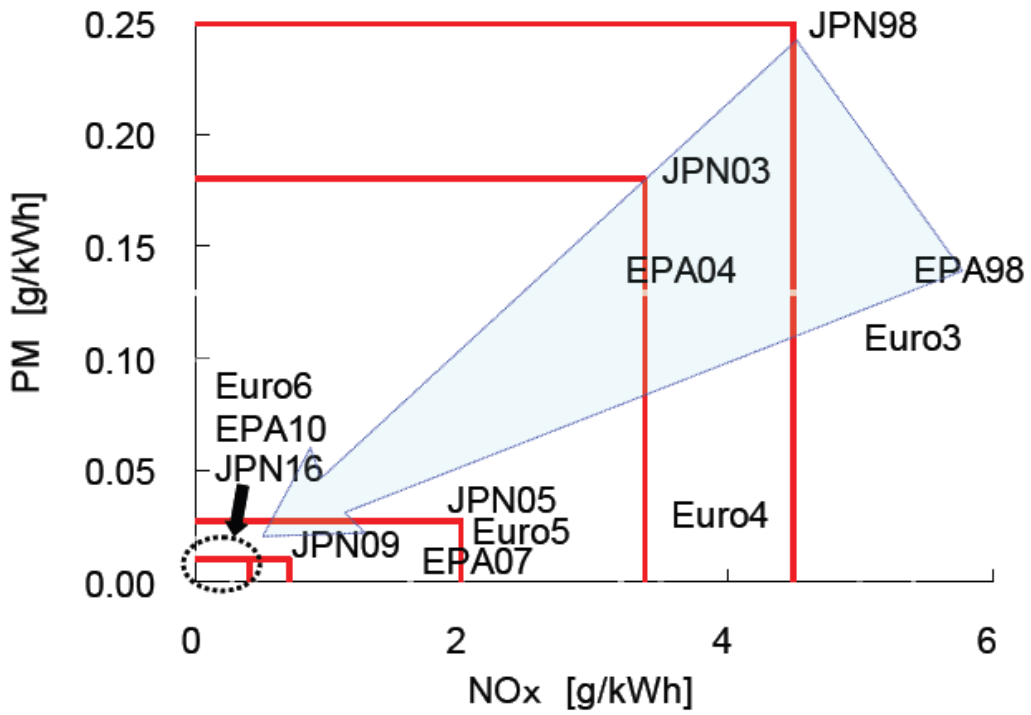

Figure 1.1 Regulation of NOx and PM Emissions for Diesel Engines

Because of the high cost of after treatment facility such as the NOx trapper, the main approach is still to maintain and improve the current techniques, in addition, the advanced combustion concepts such as HCCI (Homogeneous Charge Compression Ignition), PCI (Premixed Compression Ignition), MK(Modulated Kinetics) et al. have been proposed and studied worldwide because of their potential to achieve the ultra-low emission even without the help of after-treatment systems. In order to realize such low temperature and quasi-homogeneous combustion, it is necessary to improve the understanding of the fundamental mechanism of the combustible mixture formation process, which has been proved to be one of the key factors to determine the subsequent combustion and pollutant formation process in the Diesel engines [Higgins et al., 2000].

There have been numerous studies that investigated the fuel/air mixing process, mixture formation behavior and the combustion characteristics by using the optical diagnostic methods. It had quite a long history to use the visualization method to study the macroscopic spray characteristics. For example, Wakuri [1957] studied the spray tip penetration and excessive air ratio of a Diesel spray by using high speed photography technique and established relevant theory. In recent years, the laser diagnostics techniques such as PIV(Particle Image Velocimetry), PDPA(Phase Doppler Particle Anemometry), LIF(Laser Induced Fluorescence) and LAS(Laser Absorption/Scattering) have made great progress, which make it possible to study the microscopic characters of the spray evolution and combustion process. The optical diagnostics for in-cylinder mixture formation measurement was summarized by Zhao et al. [1998]. Soid et al. [2011] also systematically reviewed the main optical measurement methods regarding the in-cylinder mixture formation and combustion process. Yao et al. [2009] particularly focused on the development of optical diagnostics in the research of HCCI engines.

The application of higher injection pressure and smaller nozzle-hole size is believed to be the effective way to improve the spray atomization and mixture preparation process especially in the advanced combustion mode [Siebers et al., 2000; Minato et al., 2005; Tao et al., 2008; Zhang et al., 2008]. However, so far most of optical diagnostics researches were conducted with conventional injection pressure and relatively larger nozzle-hole size. The mixture formation and combustion process under the usage of ultra-high injection pressure and micro-hole nozzle, especially in relatively higher ambient density condition, needs more profound understanding, which will facilitate the engine design and modeling in the future.

1.2 OBJECTIVES AND APPROACHES

This study was aimed at clarifying the mixture formation process and the combustion characteristics of the high pressure D.I. Diesel spray, which was carried out in a constant volume chamber. Several main objectives which were paid special attention are shown as follows:

1) The ambient gas motion characteristics such as the velocity distribution and the ambient gas mass flow rate around the entire periphery of the transient Diesel spray were analyzed quantitatively.

2) The spray internal flow characteristics such as the velocity distribution and the vorticity distribution were measured.

3) The effects of the fuel injection pressure, ambient gas density, nozzle-hole size, on the ambient gas/internal flow of the spray were taken into account.

4) The non-evaporating/evaporating condition, and the free spray/ flat-wall impinging spray were considered respectively.

5) The combustion characteristics were measured at the same condition, the correlation of the mixing process and the combustion feature was analyzed.

6) CFD Numerical simulation results provide insightful understanding of the microscopic spray characteristics.

The LIF-PIV(Laser Induced Fluorescence- Particle Image Velocimetry) and PIV (Particle Image Velocimetry) techniques were applied to measure the spray internal flow and ambient gas flow. Different tracer supplying methods were selected according to the different experimental conditions. The combustion features such as the natural luminosity of the reacting Diesel spray was visualized by using a high speed video camera. The OH chemiluminescence measurement and the soot concentration/temperature distribution measurement by two-color pyrometry provide the quantitative information of the Diesel flame. Numerical Simulation was conducted by AVL® FIRE commercial software.

1.3 OUTLINES

The organization of this dissertation is shown as follows: Firstly, a review of the previous work such as the Diesel combustion concept, the optical diagnostic techniques on spray and combustion process and the numerical simulation foundation is introduced in Chapter 1. Chapter 2 introduces the set-up of experimental apparatus and the measuring methods. In Chapter 3, the ambient gas motion characteristics of the free Diesel spray was measured by using LIF-PIV and

PIV technique in non-evaporating and evaporating condition, respectively. The ambient gas motion characteristics of the flat-wall impinging Diesel spray was described in Chapter4. Correspondingly, Chapter5 and 6 deal with the internal flow field of the free spray and the impinging spray, respectively. The combustion characteristics of the reacting spray measured by several visualization methods were introduced in Chapter 7. The correlation of the combustion features and the ambient gas mass flow were discussed comprehensively. In Chapter 8, the numerical simulation results of the spray evolution conducted at the same conditions were expressed. At last, the general knowledge of the mechanism of the fuel/air mixing process and their correlation to the combustion features and the prospect to the future work were concluded in Chapter 9.

1.4 LITERATURE REVIEW

1.4.1 Diesel Spray Evolution and Spray/Gas Interaction Process

1.4.1.1 Free Spray

The spraying concept has been widely applied in almost every field in the human lives which usually involves the multiphase flow phenomenon such as the liquid permeates into the gaseous atmosphere. In internal combustion engines, the characterization of the direct injection Diesel spray and gasoline spray plays a key role in improving the thermal efficiency.

A schematic description of the full-cone Diesel spray injected from a sac-hole nozzle was presented by Baumgarten [2006] as shown in Fig 1.2.

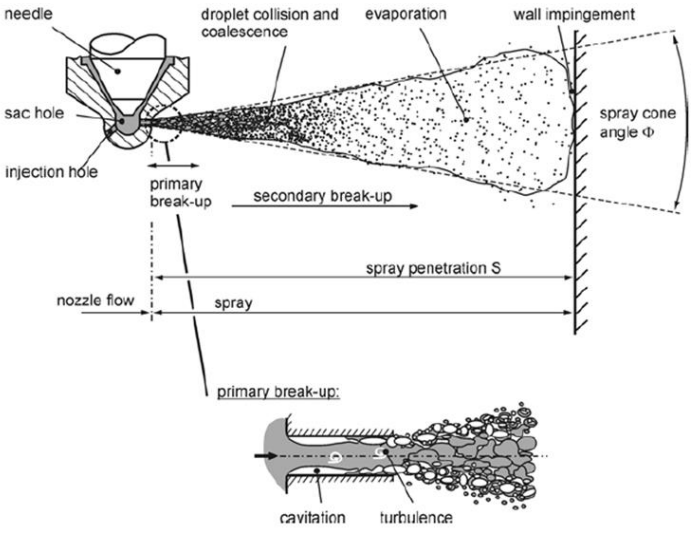

Figure 1.2 Schematic of Development of Full-Cone Diesel Spray

It is believed that the disintegration process of the liquid core region appears even before the spray comes out of the nozzle hole because of the turbulence and cavitation phenomenon. This process happening at the early stage of the spray development is called primary break-up. The turbulence-induced disintegration is one of the most dominant primary break-up mechanisms. Wu et al. [1995] discussed that the increasing turbulent eddy inside the nozzle is possible to overcome the surface tension and form the initial droplets. The cavitation occurs because the abrupt acceleration of the liquid flow inside the nozzle hole results in a significant reduction of the local static pressure, the liquid phase probably vaporizes instantaneously if the static pressure is lower than the vapor pressure. The nozzle hole geometry such as the curvature of the orifice inlet and the needle open/close are related to the increase of the cavitation. Several studies [Arai et al., 1991; Hiroyasu et al., 1991; Soteriou et al., 1995] showed that the cavitation flow increases the spray cone angle and decreases the spray tip penetration, the implosion of the gas bubble after emerging from the orifice exit improves the turbulent energy and the spray integration. However, the cavitation also impacts the fuel flow rate because of the decrease of cross section area especially in the high injection pressure condition, and the subsequent spray evolution becomes instable. Thus the extent of cavitation flow should be reduced in the engine design. The cavitation number K is used to analyze the cavitation phenomenon quantitatively, one of the typical form is shown as follows [Nurick., 1976]:

$$K = \frac{P_{inj} - P_{vap}}{P_{inj} - P_{amb}} \tag{1.1}$$

In which P_{inj} is the fuel injection pressure, P_{amb} is the ambient gas pressure, and P_{vap} is the fuel vapor pressure. The cavitation does not occur unless the K is lower than the critical cavitation number K_{cri}, which is a function of the pressure drop and the orifice geometry.

The break-up process downstream of the liquid core region is called secondary break-up, which is dominated by the counteraction of the aerodynamic force and the liquid surface tension. The surface tension keeps the external force from deforming the liquid shape. On the other hand, the aerodynamic force induced by the velocity difference of the liquid/gas phase causes the growth of instable surface wave, as a result, the liquid ligaments generated in the primary break-up process is further disintegrated into droplets. The gas phase Weber number $We_a$is used to describe the secondary break-up mechanism, which is defined as the ratio of the aerodynamic force to the surface tension:

$$We_a = \frac{\rho_a \cdot v_{rel}^2 \cdot d}{\sigma} \tag{1.2}$$

ρ_a is the ambient gas density, v_{rel} is the relative velocity of liquid/gas phase, d is the liquid droplet's diameter, σ is surface tension. Generally, the increase of jet velocity improves the break-up extent and decreases the break-up length. Reitz et al. [1986] summarized that with the increase of the jet velocity, the liquid break-up experiences the drip flow, Rayleigh break-up regime, first wind-induced break-up, second wind-induced break-up and atomization regime.

The liquid droplets at the spray head moves downwards and lose the momentum gradually, the following droplets behind with larger momentum pursue the precedent ones and push them aside, as a result, the spray tip penetrates downwards, and the large vortex motion forms at both sides of spray plume. During this process, the spray droplets collide with each other, which would enhance the atomization process. On the other hand, the coalescence of spray droplets makes it possible to form the new droplets with larger size. The downstream of the spray is subject to the influence of the ambient condition more than the spray body itself, such as the ambient gas temperature, pressure and viscosity. The liquid droplets vaporize if the gas temperature is higher than the room temperature. In most of the commercial Diesel engines with small bore size, it is inevitable that a fraction of fuel impinges on the piston wall and probably the liquid film forms, which impacts the subsequent fuel/air mixing and pollutant formation results. Thus the regime of the spray/wall interaction needs to be investigated.

In recent decades, thanks to the development of optical diagnostics techniques, the fundamental experiments especially the visualization of the spray evolution have made great progress. The macroscopic characteristics such as the spray morphology, droplets' size distribution and equivalence ratio distribution have been studied comprehensively, numerous semi-empirical equations and theories have been summarized.

Several empirical equations with respect to the spray tip penetration are introduced as follows. Hiroyasu et al. [1990] divided the spray development into two steps. Firstly, the liquid core region moves downwards without break-up, the penetration length is proportional to the time. Secondly, With the development of the spray, the momentum of the droplets is gradually transmitted to the surrounding gas, the longer the spray penetrates downwards, the slower the velocity of the spray droplets at the tip region is. As a result, the spray tip penetration follows a square root function over time. The equations are listed as follows:

$$S = 0.39 \cdot \left(\frac{2\Delta P}{\rho_l}\right)^{0.5} \cdot t \qquad (t < t_{break}) \tag{1.3}$$

$$S = 2.95 \cdot \left(\frac{\Delta P}{\rho_a}\right)^{0.25} \cdot (D \cdot t)^{0.5} \qquad (t > t_{break}) \tag{1.4}$$

$$t_{break} = \frac{28.65 \cdot \rho_l \cdot D}{(\rho_a \cdot \Delta P)^{0.5}} \tag{1.5}$$

ΔP is the pressure drop at the nozzle exit in [Pa], ρ_l is the liquid density in [kg/m^3], D is the nozzle hole diameter in [m]. Dent [1971] furtherly took into account of the influence of the ambient gas temperature T_a(K), the increase of ambient gas temperature tends to shorten the penetration length.

$$S = 3.07 \cdot (\frac{\Delta P}{\rho_a})^{0.25} \cdot (t \cdot D)^{0.5} \cdot (\frac{294}{T_a})^{0.25} \tag{1.6}$$

Based on the assumptions of a model spray such as the radially uniform velocity and fuel concentration profile, no velocity slip between the liquid and gas phase at any cross section and the same total mass and momentum fluxes at any cross sections, Wakuri et al. [1957] presented the equation (1.7). *Ca* is the area contraction coefficient which accounts for the limit of cross section of the nozzle flow due to cavitation, in addition, the spray cone angle α was taken into account.

$$S = (\frac{2c_a \cdot \Delta P}{\rho_a})^{0.25} \cdot (\frac{t \cdot D}{\tan(\alpha/2)})^{0.5} \tag{1.7}$$

Siebers et al. [2009] developed the scaling law of non-evaporating spray based on the idealized, isothermal, incompressible "model" jet proposed by Wakuri et al. [1957] as shown in Fig. 1.3. The dimensional forms of the spray tip penetration are shown as follows:

$$In\ near\ field: \qquad S = C_v \cdot \sqrt{\frac{2(P_f - P_a)}{\rho_l}} \cdot t \tag{1.8}$$

$$In\ far\ field: \qquad S = \sqrt{\frac{C_v \cdot \sqrt{2C_a}}{\tan(\alpha/2)}} \cdot \sqrt{\sqrt{\frac{(P_f - P_a)}{\rho_a}} \cdot D \cdot t} \tag{1.9}$$

The transition position *Sr* from the near field to the far field corresponds to the position where the dominant factor transfers from the injected fuel to the ambient gas [Naber et al., 1996]. The definition of *Sr* is shown as follows:

$$S_r = \frac{\sqrt{C_a} \cdot D}{\tan(\alpha/2)} \sqrt{\frac{\rho_l}{\rho_a}} \tag{1.10}$$

It can be found that the equation forms are similar to the equations (1.3-1.5) proposed by Hiroyasu et al., however, the coefficient pays more attention on the internal nozzle flow, in which C_v is the velocity coefficient. The discharge coefficient *Cd* which is the ratio of the mass flow rate injected in the cylinder to the theoretical mass flow rate computed from the Bernoulli equation can be calculated with the following equation:

$$C_d = C_a \cdot C_v \tag{1.11}$$

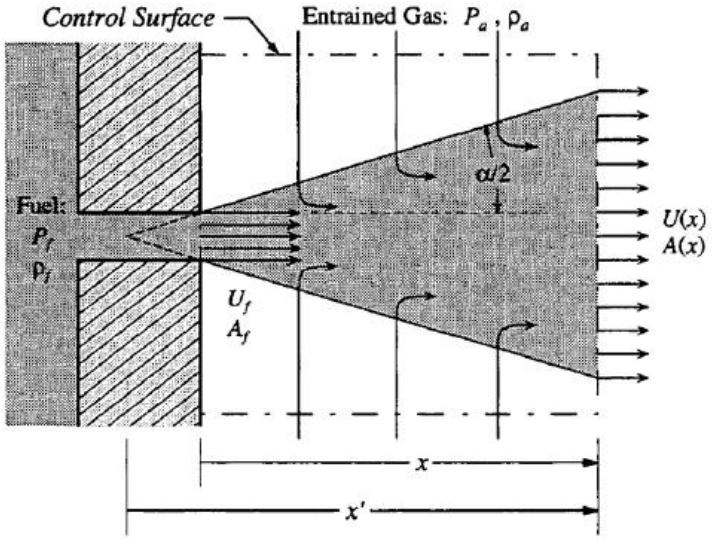

Figure 1.3 Schematic of the Idealized Model Fuel Jet

SMD is usually used to quantitatively analyze the averaged droplets' size, which is the diameter of a "modeled" droplet whose volume-surface area ratio equals the ratio of the volume of all the droplets in the spray to the surface area of all the droplets. The definition of SMD is shown as follows:

$$SMD = \frac{\sum_{i=1}^{n} d_i^3}{\sum_{i=1}^{n} d_i^2} \tag{1.12}$$

Hiroyasu et al. [1990] proposed a predictive equation for calculating the SMD:

$$\frac{SMD}{D} = 0.38 \cdot Re^{0.25} \cdot We_l^{-0.32} \cdot \left(\frac{\mu_l}{\mu_a}\right)^{0.37} \cdot \left(\frac{\rho_l}{\rho_a}\right)^{-0.47} \tag{1.13}$$

SMD is in [m] and μ is dynamic viscosity in [N·s/m^2]. Reynold number *Re* is a dimensionless value that compares the inertial force with the viscous force.

$$Re = \frac{\rho_l \cdot v_{rel} \cdot d}{\mu_l} \tag{1.14}$$

Increase of ambient gas density results in the increase of the SMD, because the possibility of the droplets' collision is higher. The higher injection pressure and smaller nozzle-hole size tend to reduce the SMD significantly. It is worth noticing that the SMD result is a statistical concept to give an overall image of the droplets distribution and may defer from the certain droplets' size.

For the real application, it is more meaningful to investigate the fuel/air mixture result. Wakuri et al. [1957] presented an equation for calculating the equivalence ratio at a certain cross section of a "modeled" steady Diesel spray with infinite long injection duration based on the ratio of mass flow rate of fuel and gas. L_{th} is the stoichiometric air/fuel ratio. The local equivalence ratio decreases with the increase of distance from the nozzle tip linearly.

$$\emptyset_{inst} = \frac{L_{th}\sqrt{C_a}}{2\tan(\alpha/2)}\sqrt{\frac{\rho_l}{\rho_a}}\frac{D}{x} \tag{1.15}$$

One of the main focuses of this research is to study the spray induced ambient gas flow and spray droplets flow. The ambient gas mass flow rate around the spray periphery was widely investigated because of its significant influence on the mixture concentration and combustion behavior. In the early time, Ricou et al. [1961] and Hill [1972] studied the air entrainment law of a steady gas jet by using the "porous-wall technique" and concluded that the air entrainment rate increases linearly with the axial distance after reaching the fully developed region. Kuniyoshi et al. [1980] investigated the ambient gas flow field around a Diesel spray by using the smoke wire method. Cho et al. [1990] also investigated the surrounding gas flow field of the Diesel spray with the injection pressure of 40MPa by means of the smoke wire method. Figure 1.4 exhibits the model of fully developed Diesel spray. It was shown that the "penetration part" of the jet or the spray entrains their surroundings, while the "stagnation part" of the jet or the spray pushes aside their surroundings. The ratio of the entrainment volume at the "penetration part" to the total volume of the unsteady jet or the Diesel spray is almost 50%.

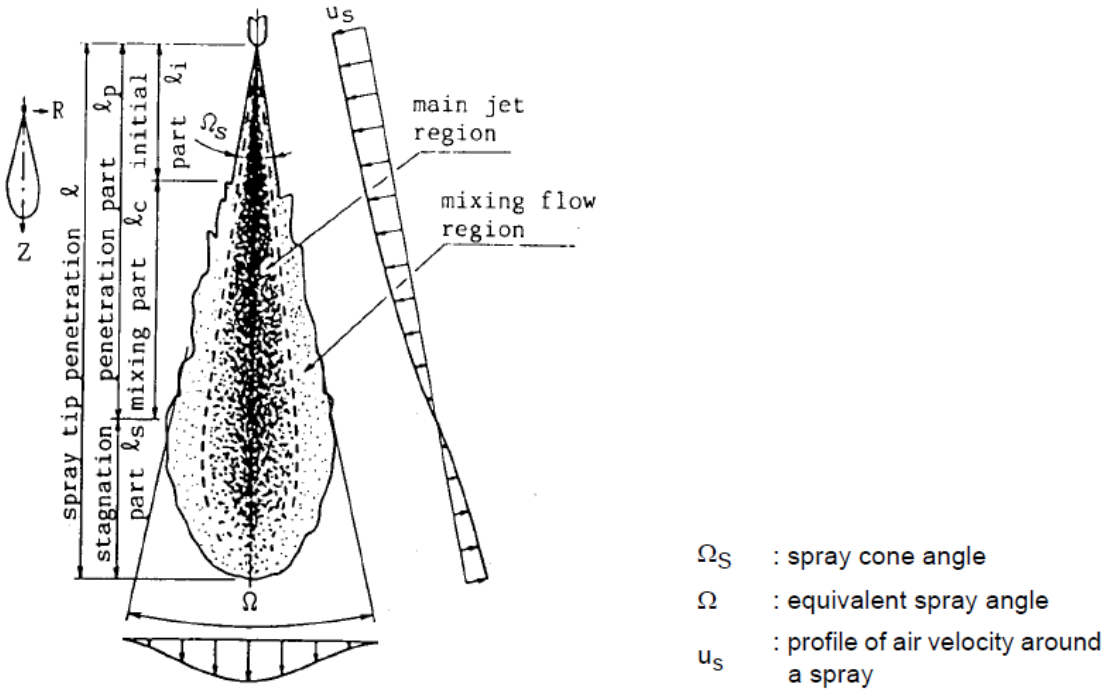

Figure 1.4 Model of Fully Developed Diesel Spray and Movement of Its Surroundings

More recently, Sepret et al. [2010] investigated the result of the local variation of fuel and air mixing rate on the side periphery of full cone fuel spray by using the LIF-PIV technique. According to the mean gas velocity field as shown in Fig. 1.5, the periphery of the spray is categorized to three parts. The section in which the gas normal velocity is positive is defined as the gas aspiration zone.

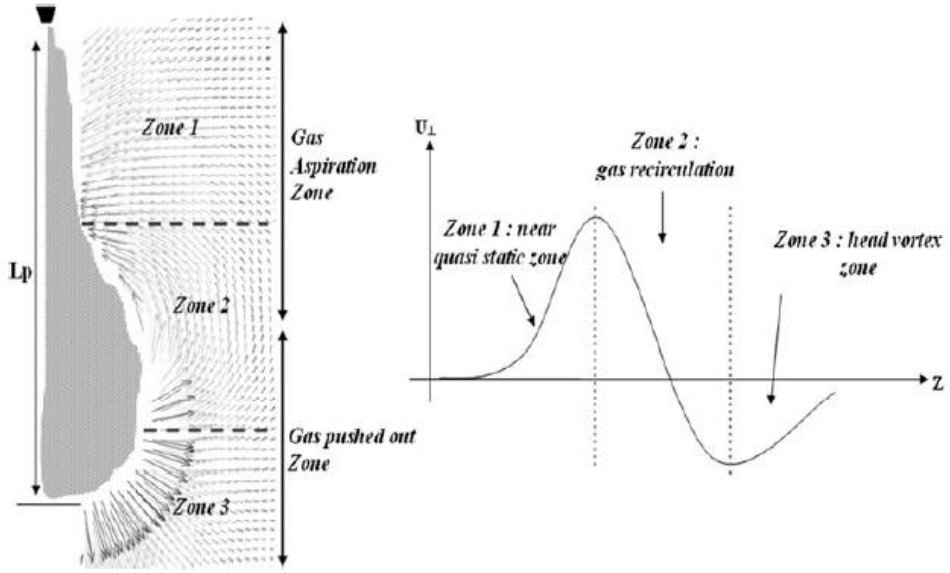

Figure 1.5 Mean Gas Velocity Field and Evolution of Normal Component of Gas Velocity

The ambient gas velocity distribution on the side periphery of the transient Diesel spray with the injection pressure of 146MPa was also measured by using PIV technique by Rhim et al. [2001]. The ambient gas flow was categorized as three regimes: (1) entrainment through side-periphery, (2) air pushed-out by head-vortex and (3) entrainment by spray-capturing at the spray tip. By comparing the volume of the non-evaporating spray and the measured mass of entrained gas along the side periphery, the author assumed that almost 60% of the total ambient gas mass in the spray is captured by the spray tip periphery. Figure 1.6 shows the schematic of relative gas flow surrounding the spray boundary.

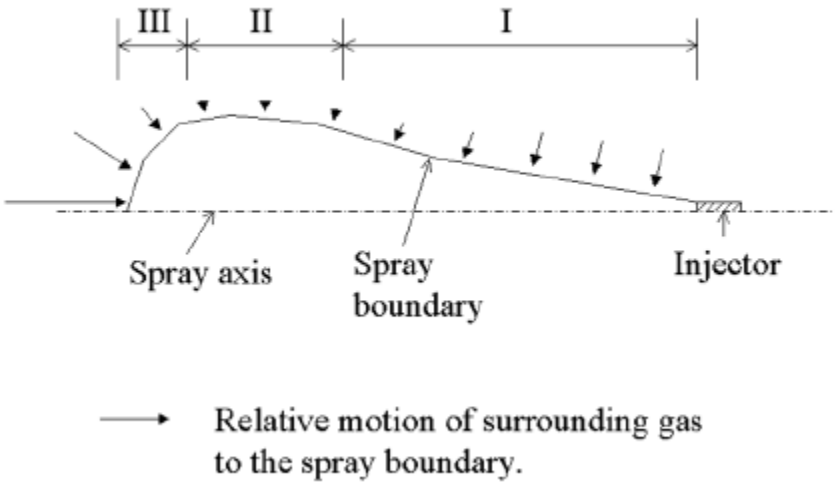

Figure 1.6 General Image of Gas Motion Relative to the Spray Boundary for Non-evaporating Transient Sprays

1.4.1.2 Wall-impinging Spray

Spray-wall Impingement characteristics attract wide attention among the automobile engineers since it occurs commonly in internal combustion engines. Figure 1.7 shows a typical model of a flat wall-impinging spray proposed by Katura et al. [1990]. It is observed that after impinging on the wall, the droplets with large momentum move radially along the wall, due to the resistance from the ambient gas, a vortex structure forms near the spray tip, and the spray height at the stagnation region enhances with time. The dense fuel concentration can be found near the wall due to the liquid film and in the tip region due to the centrifugal force.

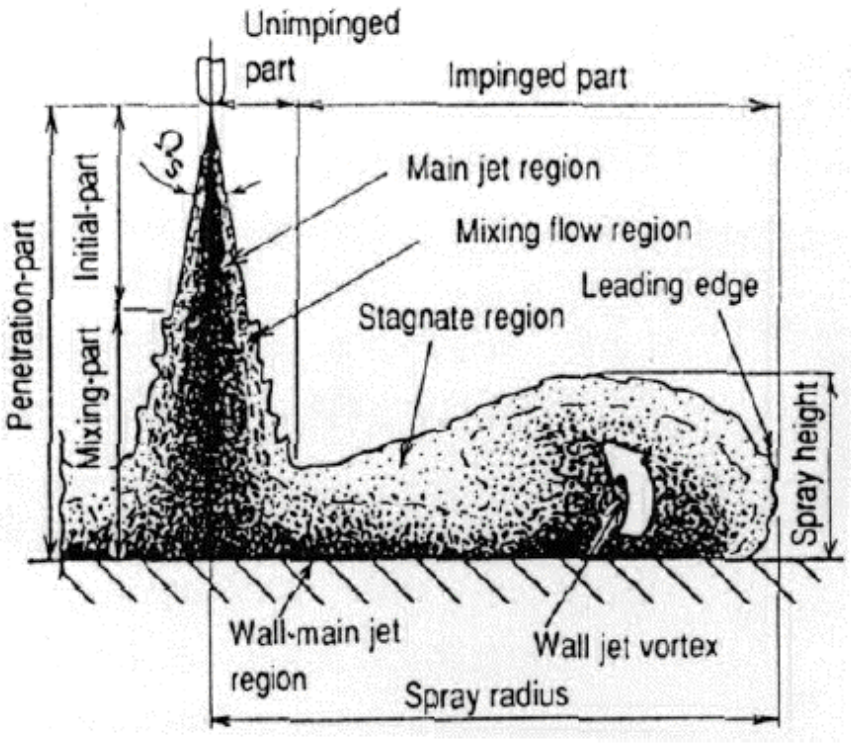

Figure 1.7 Model of A Flat Wall-impinging Spray

Numerous works have reported the investigation of wall-jet interaction by means of optical diagnostics method and numerical simulation, which usually involve into two aspects: (1). Single droplet-wall impact process. Shen et al. [2009] studied the effect of wall temperature and different wall structures on the droplet's evolution by using high speed video camera. Arifin et al. [2010] investigated the effect of the hot surface temperature on the deposit formation for diesel fuel by using the hot surface deposition test. Numerical modeling for classifying the transition criteria of different impingement regimes has made great progress in recent years. For example, Bai and Gosman [1995] proposed seven regimes to analyze the impinging droplet's behavior as a function of incident droplet's weber number and temperature. Especially if the wall temperature is less than TB (Temperature of boiling) or TPA (Pure Adhesion Temperature), four regimes are taken into account: stick, rebound, spread and splash. Figure 1.8 suggests a schematic of the transition criteria when a single droplet impinges on a dry wall. Lee et al. [2006] systematically summarized the recent progress of numerical models on the droplet-wall interaction characteristics and post-impingement spray development.

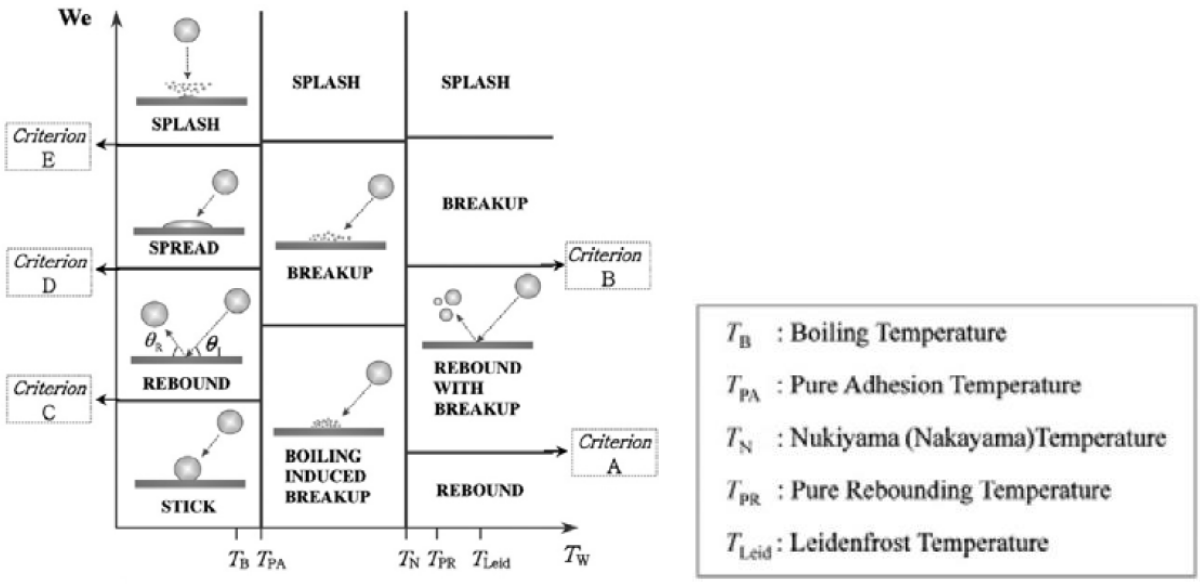

Figure 1.8 Overview of Transition Criteria of Single Droplet Impinging on Dry Wall

(2). Spray-wall interaction process and its post development. Due to the difficulty of the optical observation of the spray-wall impact in the real combustion chamber of engines, most of the works were carried out in the quiescent condition by simulating the impingement condition [Allocca et al., 2007; Stanton et al., 1998; Andreassi et al., 2007]. The effects of injection pressure, wall temperature on the impinged spray profile, gas flow field, droplets' size distribution and fuel mass distribution were investigated. The experimental result was compared with the simulation result in order to improve the validation of the modified models. However, there are still plenty of unclear subjects regarding the spray-wall impingement characteristics. In cold start or the operation condition with the medium wall temperature, the direct interaction of liquid phase and wall results in the poor fuel/air mixing and higher soot emission level [Zhang et al., 2009; Wang et al., 2011; Song et al., 2003]. However, the relatively high wall temperature and the interaction of gas phase and wall may also improve the turbulent mixing and air entrainment, which is beneficial to the low soot combustion [Katsura et al., 1989; Jafarmadar et al., 2009; Pickett et al., 2005]. It implies that the effect of injection parameters, combustion chamber configuration and engine load on the spray/wall interaction and subsequent combustion characteristics still deserves more careful investigation.

1.4.2 Diesel Combustion Analysis

1.4.2.1 Conventional Diesel Combustion

In conventional Diesel combustion mode, the combustion process is usually governed by the fuel property, spray/gas mixing process, auto-ignition and mixing-controlled combustion process. The compression ratio of the conventional Diesel engine is much higher than that of gasoline engine, resulting in a high in-cylinder gas temperature and pressure at top dead center TDC in the range of 1000~2000 K and 4~12 MPa respectively [Kamimoto et al., 1991].

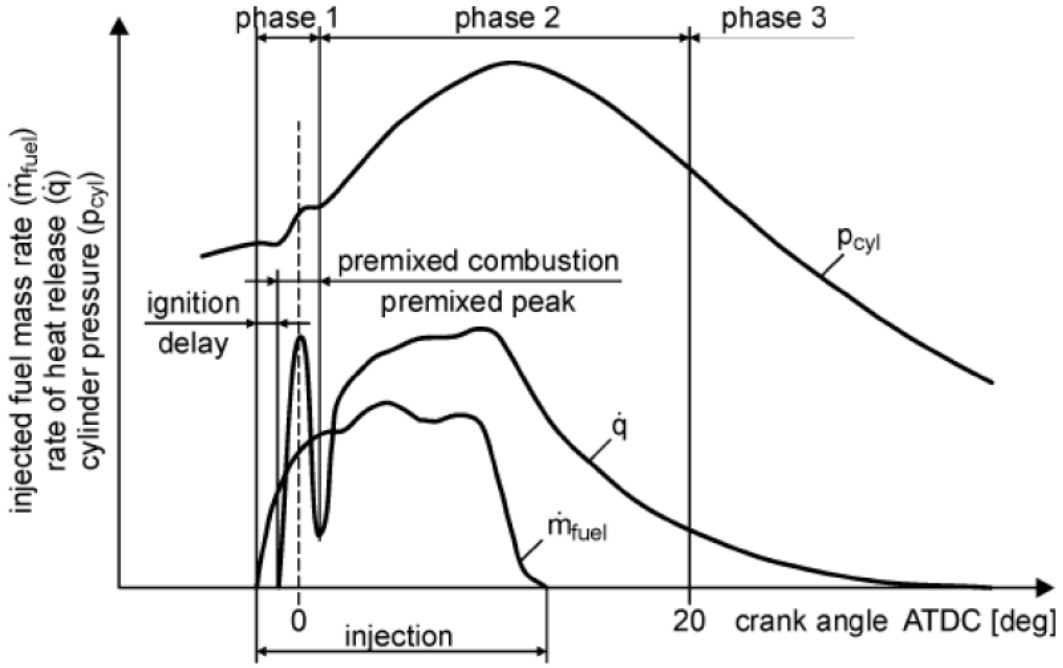

Figure 1.9 Phases of the conventional diesel combustion process

Figure 1.9 indicates a typical conventional Diesel combustion process, in which three phases can be divided. The high pressure liquid fuel is injected from a multi-hole nozzle to the combustion chamber several crank angles before TDC. The entrainment of hot ambient gas into a fraction of the fuel mass results in the vaporization and the formation of fuel/gas mixture. As long as the temperature of the mixture exceeds the auto ignition point of some certain fractions in the fuel with low cetane number, and the equivalence ratio of the mixture is within the ignition limit, the sudden chemical reaction occurs throughout the region with well-prepared fuel/air mixture. Thus phase 1 is called premixed combustion phase, which is characterized by the peak heat release rate. The strong pressure gradients ($dP/d\varphi$) cause considerable noise, and the high

temperatures in the premixed zone may exceed 2000K, which are responsible for a first production of nitric oxides (NOx). The time interval from the start of fuel injection to the onset of the rise of heat release rate is marked as the ignition delay. Ikegami et al. [2009] argued that the ignition delay is a period during which the spray is likely a gaseous jet containing a lot of unburned hydrocarbons due to gasification and thermal decomposition with assistance of partial oxidation of the spray mantle. Both the physical process governing the mixture formation and the chemical process leading to exothermic reactions occur during the ignition delay.

The second phase is called diffusive combustion phase. According to the evolution of the conventional Diesel spray combustion as shown in Fig. 1.10, the temperatures of the inner spray region downstream of the premixed combustion region increases to about 1600–1700K, and all available oxygen in this region is consumed by the premixed combustion and the partial oxidation of the fuel fragments. As the unburned fuel and decomposed molecule continue entering this region, it is appropriate to form a large amount of soot here. Subsequently, the partial burnt products are diffused from inside the spray to the outer regions, and are completely burnt in a very thin reaction zone at the periphery of the spray due to the sufficient supply of air. The significant increase of temperature (2700K) in diffusive flame region is ideal for the oxidation of soot, one the other hand, the significant NOx formation can also be observed. It is reported that only 10–15% of the fuel energy is released in the inner partial burning zone, the diffusion flame releases the rest of the energy [Flynn et al. 1999].

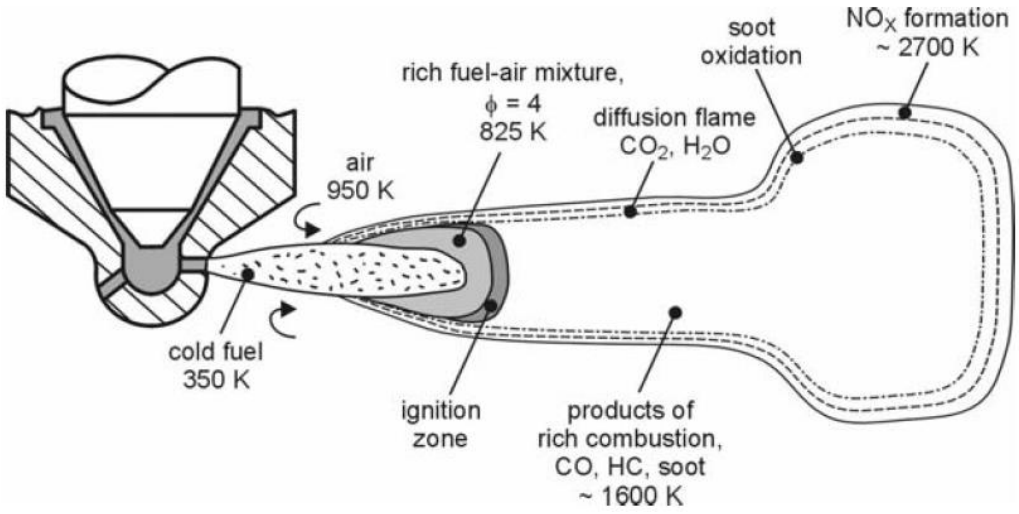

Figure 1.10 Conventional Diesel Spray Combustion and Production of NOx and Soot

Kosaka et al. [2005] presented a detailed model of the soot formation and oxidation process as shown in Fig. 1.11. It is found that formaldehyde and some other intermediate species form downstream of the rich fuel/air mixture as a mark of low temperature oxidation. After the premixed combustion, the young soot has formed in the inner cloud near the spray tip. During the diffusive combustion phase, a large amount of soot mass form in the inner partial oxidation region, and most of them will be consumed when conveyed to the outer region. Particularly, the head vortex motion is responsible for promoting the soot oxidation.

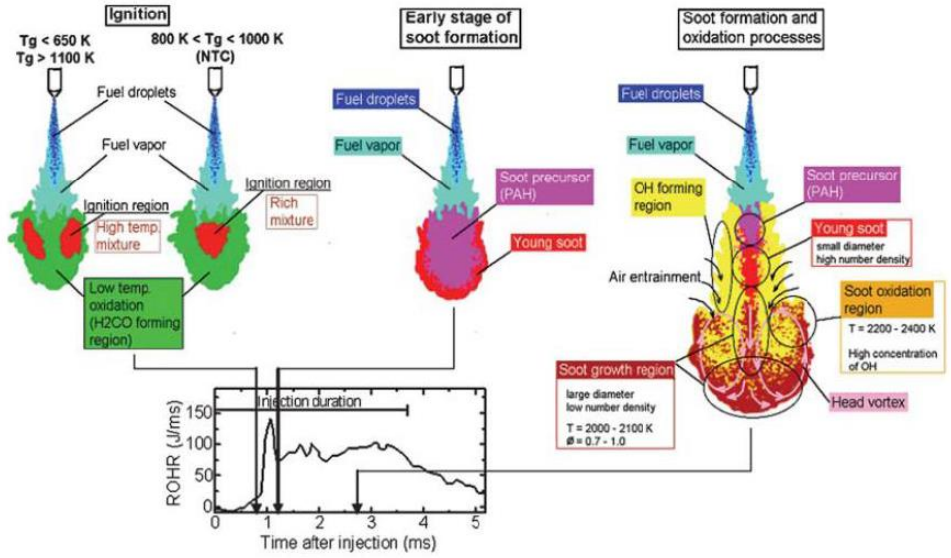

Figure 1.11 Conceptual model of ignition, soot formation, and oxidation processes in a diesel spray flame

The “lift-off length” is defined as the distance from the nozzle tip to the most upstream of the stable flame location. The location of the initial flame is determined by the interaction of several factors such as the turbulent mixing mechanism and the chemical kinetics reaction process. The optical measurement by Dec [1997] indicated that premixed fuel and air reacts in a rich, distributed reaction zone located in the central region of the spray, just downstream of the lift-off length. Thus the air entrainment upstream of the lift-off length is considered to have significant influence on the subsequent initial combustion phase and emission process. Base on the cross-sectional averaged equivalence ratio shown in Eq. 1.15, Siebers et al. [2000] developed the equation of the air entrained up to the lift-off location as a percentage of the total air required to burn the fuel being injected (Stoichiometric air ζ):

$$\zeta_{st}(\%) = \frac{100}{\emptyset_{\text{inst}}} = \frac{10}{3} \cdot \left(\sqrt{1 + 16 \cdot \left(\frac{L_0}{x^+} \right)^2} - 1 \right) \tag{1.16}$$

L_0 is the lift-off length and x^+ is the characteristic length scale for the spray, defined as:

$$x^+ = \sqrt{\frac{\rho_l}{\rho_a}} \frac{\sqrt{C_a} \cdot D}{0.66 \cdot \tan(\alpha/2)} \tag{1.17}$$

Base on the above mentioned equations, the authors provided a schematic which shows the relationship of the liquid length and the lift-off length with different injection pressure and orifice diameter as shown in Fig. 1.12. Generally, the increase in the fuel injection and the decrease in the orifice diameter tend to lessen the direct interaction of the cold liquid phase and the premixed combustion zone, and improve the percentage of air entrainment up to the lift-off length. As a result, the soot formation can be effectively limited.

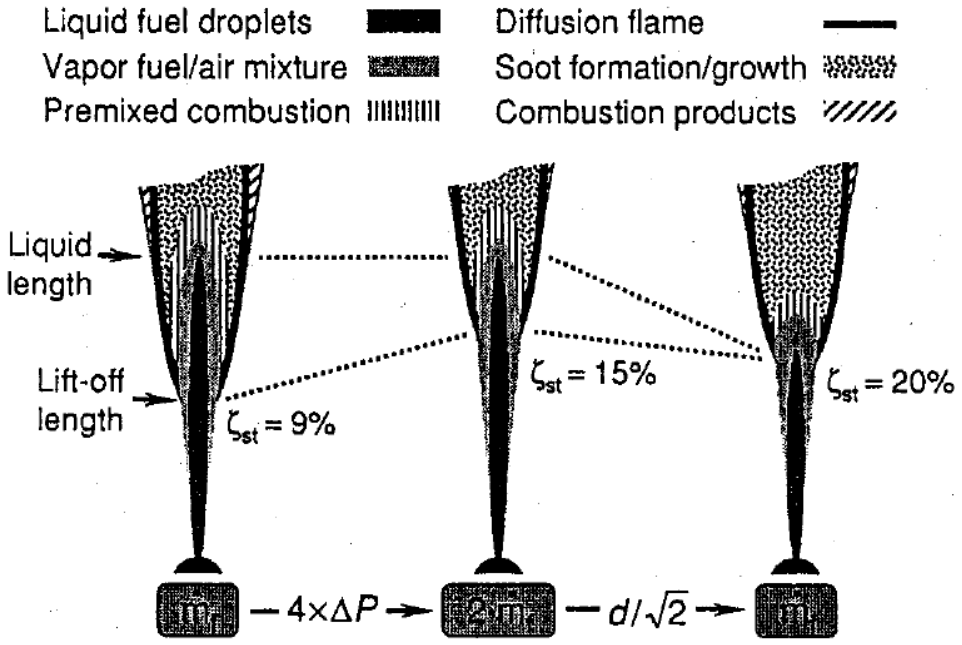

Figure 1.12 Schematic of Relationship of Liquid Length, Lift-off Length and Combustion Characteristics of a Diesel Flame

The third phase is called post combustion phase. No more low temperate fuel mass is supplied to the downstream region, thus the remaining fuel vapor mass and partial oxidized products are consumed in this phase with relatively slow reactive rate. Most of the soot can be

oxidized during this phase, however, some would be left and exhausted when the in-cylinder temperature decreases to a certain level during the expansion stroke.

1.4.2.2 Advanced Diesel Combustion

It is really challenging to reduce the NOx and Soot emission of the Diesel engines simultaneously. There have been numerous effective approaches to try to achieve this objective, such as the multi injection and more complicated injection rate shape, the inter-cooler EGR to reduce the NOx, low swirl ratio and the early intake port close to get a lower compression temperature(Miller Cycle). A combination of an increase of intake charge pressure (reduction of soot due to increased amount of oxygen) and reduced compression ratio (prevention of increased peak temperatures and NOx-formation) is also advantageous.

The spontaneous ignition of the over lean homogeneous fuel/air mixture occurring throughout the whole combustion chamber results in low combustion temperature, which would offer a significant reduction in both NOx and soot emission. This is the concept of advance Diesel combustion.

Noguchi et al. [1979] and Onishi et al. [1979] firstly reported the operating homogeneous charge in a two-stroke cycle gasoline engine with compression ignition mode. Oppenheim [1984] firstly proposed the concept of homogeneous charge compression ignition (HCCI). Unlike the conventional Diesel combustion mode in which the diffusive combustion phase is inevitable and a large amount of soot forms in the inner cloud with insufficient oxygen and NOx forms in the flame frontier, the HCCI mode has the potential to form the homogeneous or partial homogeneous fuel/air mixture before auto-ignition, thus the rich mixture zone and high temperature can be avoided, which contributes to a low Soot and NOx emission. The peak cylinder temperature for HCCI combustion ranges from 1400K to 1600K and is significantly lower than 1700-2200K in conventional Diesel combustion.

Figure 1.13 shows a typical heat release rate curve of HCCI Combustion with n-heptane fuel [Yao et al., 2009]. In the first stage called low-temperature regime, very weak peak value of the heat release rate can be detected which results from the thermal decomposition of the fuel fractions with lower octane number. Between the low-temperature regime and the main heat release stage, there is a period called “negative temperature coefficient” regime, in which the heat release becomes moderate and in-cylinder temperature increases gradually. It is crucial for the preparation of the combustible mixture in this period. In the subsequent high-temperature

regime, the bulk burn and rapid energy release can be detected, the optical diagnostics results [Iida, 1994; Aoyama et al., 1996] found the HCCI combustion initiates at multiple sites in the combustion chamber almost simultaneously without apparent flame propagation. HCCI combustion is mainly a chemical kinetic combustion process controlled by temperature, pressure, and composition of the in-cylinder charge.

The real application of Diesel fueled HCCI combustion mode is still limited due to the several challenges.

(1). The early fuel injection in Diesel HCCI combustion causes the spray interaction with the intake pipe or the piston wall, which results in the wall quenching and high HC and CO emission.

(2). The onset of the combustion of the homogeneous mixture is controlled by the fuel property, charge property, thermal condition inside the combustion chamber and so on [Stanglmaier et al., 1999]. Thus the accurate control of the combustion phase becomes difficult.

(3). The Diesel HCCI combustion can be achieved within a very narrow region, the upper limit is bounded by knock, and misfire occurs at the low operating condition range [Peng et al., 2003].

(4). The HCCI combustion mode may encounter the difficult in the cold-start operating condition, which requires a smooth switch strategy from the conventional combustion to the HCCI combustion during the warming-up period.

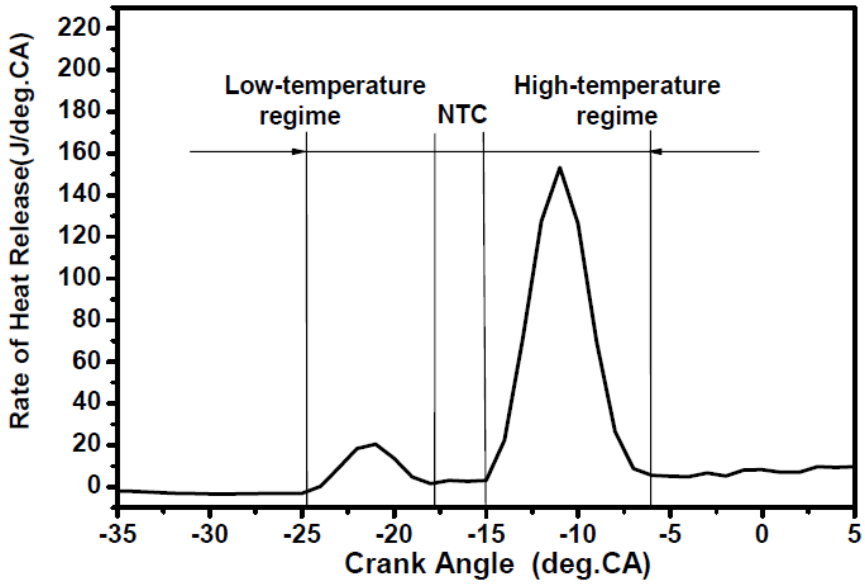

Figure 1.13 A typical heat release rate curve of HCCI Combustion of n-heptane fuel

In order to resolve these difficulties, several approaches have been developed according to the different combustion concepts.

(1). Early direct-injection HCCI combustion. Many combustion systems of early direct-injection HCCI have been developed such as PREDIC (premixed lean diesel combustion) [Takeda et al., 1996; Nakagomi et al., 1997], UNIBUS (uniform bulky combustion system) [Yanagihara, 2001]. Both of them employed the early fuel direct injection during the compression stroke. They were still suffered by the wall-wetting and the difficult combustion phase control.

(2). Late direct-injection HCCI combustion. Some of the most famous concepts are the MK (Modulated Kinetics) combustion [Kawashima et al., 1998; Kimura et al., 1999], LTRC (Low temperature fuel rich combustion) [Sasaki, 2000] and PCCI (Premixed charge compression ignition). They employed near TDC fuel injection timing like the conventional combustion mode. As a result, HC and CO can be effectively reduced compared with the early direct-injection HCCI and the combustion phase can be accurately control according to the fuel injection timing. The main subject of this concept is how to prolong the ignition delay to form the partial premixed mixture.

(3). Premixed/direct-injected HCCI combustion. Most of the fuel was injected in the early time to form the homogeneous mixture, and a fraction of fuel was injected near TDC to change the concentration and triggered the onset of combustion [Odaka et al., 1999]. It was found that the NOx and soot emission was improved compared with the conventional Diesel combustion.

The relationship of the fuel injection timing and combustion event in advanced and conventional Diesel combustion is summarized in Fig. 1. 14[Shimazaki et al., 2003].

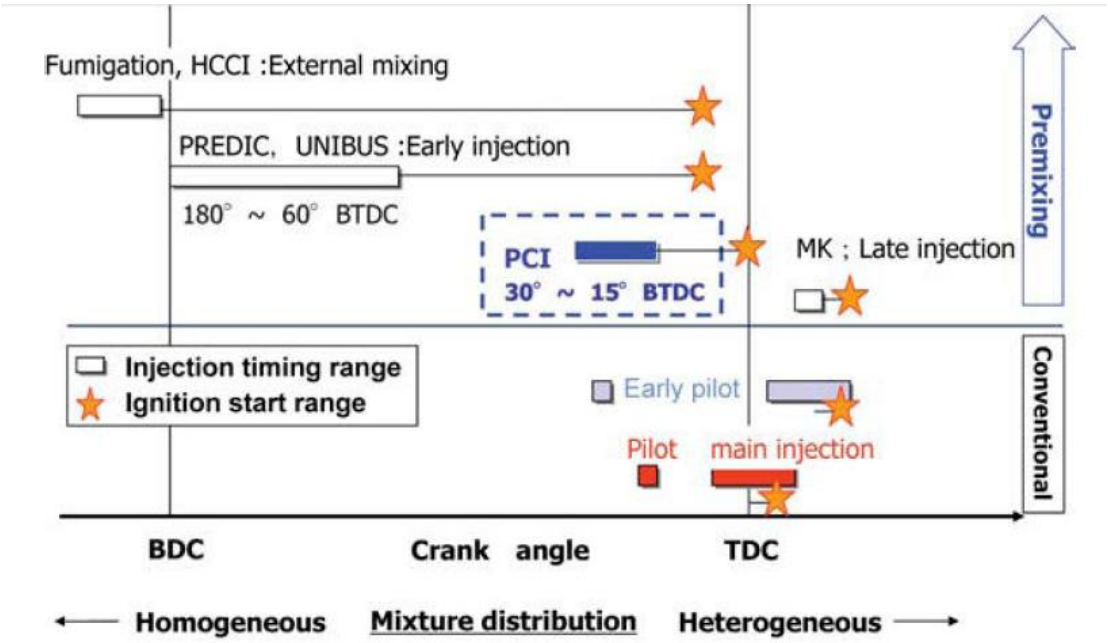

Figure 1.14 Classification of advanced and conventional combustion concepts according to injection timing

Generally, the management of the mixture formation is still the key factor for the advanced combustion concept, the advanced control strategy of fuel/air mixture is more important than simple "homogeneous charge" in the control of HCCI combustion processes. The mixing control methods include the high injection pressure, smaller nozzle size, high swirl ratio, cooled high pressure charge and stratification control. While the temperature control methods include the high inter-cooled EGR and the fuel modification.

1.4.3 Optical Diagnostic Techniques for Diesel Spray and Combustion

1.4.3.1 Spray Evolution Diagnostic Techniques

The optical techniques have been widely used to identify the macroscopic and microscopic characteristics of the spray evolution. Mie scattering, Schlieren and Shadowgrapy techniques are capable of providing the qualitative information such as the liquid/vapor phase development and droplets distribution. Settles. [2001] and Kook et al. [2011] summarized the application of these techniques.

For the investigation of the vapor phase concentration, Laser Rayleigh Scattering (LRS) measures the gas density according to the elastic interaction of between incident laser light and gas density, because the intensity of the Rayleigh scattering light is proportional to the number

density of the gas molecules [Arcoumanis et al., 1991; Espey et al., 1994]. Spontaneous Raman Scattering (SRS) is capable of measuring most of the stable species in the spray or combustion according to the inelastic interaction between incident light and the electronic-mediated vibrational-rotational modes of molecules [Johnston., 1980]. However, this technique suffers from the influence of the noise due to the very weak Raman scattering light. Laser Induced Fluorescence (LIF) makes use of the principle of the electronic absorption and emission process of the certain species exited by the incident laser source, the intensity of emitted fluorescent light is proportional to the mole fraction of the certain species of interest [Andresen et al., 1990; Meyer et al., 1995]. This technique has the advantage for the higher fluorescent light intensity, but is sensitive to the ambient temperature and pressure.

The techniques for the simultaneous measurement of liquid and vapor concentration have made great progress recently, especially the Laser Induced Exciplex Fluorescence (LIEF) and Laser Extinction/Absorption (LEA) technique. Laser Absorption/Scattering (LAS) technique shares the same principle with LEA. In the case of LIEF, the fluorescent molecular at the exited state called monomer reacts with another molecular at ground state, the second fluorescent molecular called exciplex is formed. The concentration of monomer is dominant in the gas phase while the exciplex is dominant in the liquid phase. As a result, the fluorescent intensity is directly proportional to the fuel concentration. This technique was originally developed by originally developed by Melton et al. [1985], and has been applied in numerous studies [Düwel et al., 2009; Styron et al., 2000]. LEA or LAS carries out a transmission measurement at a non-absorbing wavelength to determine the droplet optical thickness due to the scattering and a transmission measurement at an absorbing wavelength to determine the joint vapor and droplet optical thickness due to the spectral absorption and scattering, respectively. The simultaneous measurements of fuel vapor concentration and liquid droplets can be achieved according to this principle. Chraplyvy. [1981] firstly proposed and applied the dual wavelength LEA technique to measure the vapor concentration inside an evaporating n-heptane fuel spray using two He-Ne lasers at 3.39μm and 0.6328 μm. Suzuki et al. [1993] developed this technique, they used 280 nm and 560 nm beams from a dye laser to probe an J-methylnaphthalene spray. More recently, Zhang et al., [2001] and Gao et al. [2007] improved the accuracy of this technique and studied the effect of split injection and group-hole nozzle on the mixture formation of the Diesel spray,

Dimethylnaphthalene (DMN) was used as the surrogate fuel. Zhao et al. [1998] systematically reviewed the optical measuring methods of the In-cylinder mixture formation.

Several techniques are available for the measurement of the flow field and fuel/ambient gas mixing process. The traditional Hot Wire Anemometry (HWA) is capable of measuring the gas flow field continuously, however the disadvantage of this system is that it is intrusive to the flow field, and the information of the velocity direction is not obtained [Witze., 1980]. Phase Doppler Particle Anemometer (PDPA) or Laser Doppler Anemometer (LDA) has been widely used to measure the spray droplets velocity and size simultaneously. Figure 1.15 shows a typical PDPA experimental set-up by Suh et al., [2007], which mainly comprises of a laser light source, a transmitter, a receiver, an analyzer and a digital delay generator. When the transient spray droplets passes through a measurement volume in the path of the laser beam, the dispersed beam signal can be obtained by the receiver. The velocity of the droplets will be related to the temporal modulation, while the droplet size will be related to the spatial frequency. Since a large amount of the droplets can be detected in the measurement volume, the representative SMD will be obtained by averaging the captured droplets over the all measuring area. This method is limited by the number density of the droplets, and it is difficult to get the space resolved information of the whole spray each time. The PDA system was applied to measure the spray and surrounding gas flow velocity and droplet size in numerous studies [Larsson, 1999; Lacoste et al., 2003; Rottenkolber et al., 2001]. Koo et al. [1990] studied the Diesel spray by using PDPA technique and concluded that the droplets' size and velocity decreases rapidly as the distance from the nozzle tip increases, and both drop velocity and diameter distributions show very strong dependence on the radial position in the spray. Spray droplet velocity characterization for convergent nozzles was also studied by Payri et al. [2008] in order to obtain the local speed of fuel droplets at various points of diesel DI sprays using PDPA techniques.

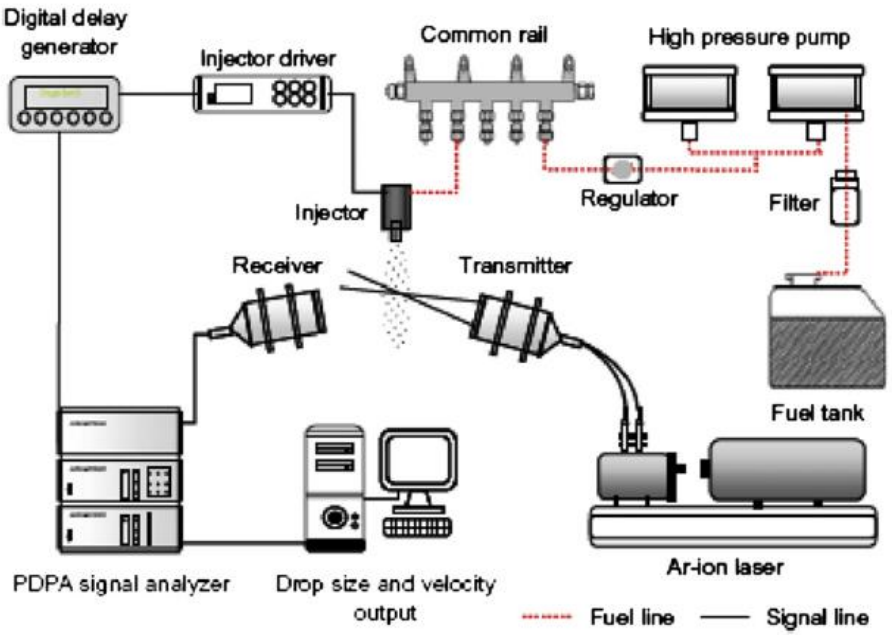

Figure 1.15 A typical PDPA System for Analyzing Droplets Size and Velocity

Particle Image Velocimetry (PIV) is an advanced measuring method which is able to capture the 2-dimensional or 3-dimensional flow field with high spatial resolution. Adrian [1991] and Raffel et al. [2000] systematically introduced the application of Particle Image Velocimetry (PIV) technique in the experimental fluid mechanics. The appropriate seeding particles are introduced into the flow field in advance, at a desired timing, a short duration high energy thin laser sheet traverses and illuminates the particles. The CCD camera placed perpendicular to the laser sheet plane records two continuous frames of the locations of the seeding particles with very short interval. The images are divided into rectangular regions, known as interrogation areas. A pair of interrogation areas from each frame is correlated to produce an average particle displacement vector. The displacement vectors of the whole field of interest are converted into a map of so-called raw velocity vectors. The post-processing of the PIV results is carried out to remove the spurious velocity vectors usually by a threshold filter or smoothing process. A number of experimental parameters need to be carefully adjusted to obtain the reliable results such the laser sheet thickness, interrogation size, seeding particles and frame rate, which will be discussed in the next chapter.

Rhim et al. [2000, 2001] measured the air flow induced by non-evaporating and evaporating diesel spray. The Al_2O_3 powder with the average diameter of 1μm was selected as the seeding particles, which was blown into the spray chamber from a fluidized bed type seed

particle generator before pressurizing the chamber. They also proposed an effective way to test the PIV interrogation scheme by making the fabricated holes with the certain distances in emulsion plates. The measured velocity was compared with the estimated velocity according to the particles distance. Figure 1.16 shows a typical FPIV (Fluorescent-PIV) experimental set-up by Sepret et al. [2010] for measuring the effect of ambient gas pressure on the spray induced gas flow field. The propylene carbonate solution doped with saturated dichloromethane (DCM) which has the fluorescence property was used as the source of the seeding particles. The seeding particles were produced by a medical atomizer inside a gas pressurized cylinder.

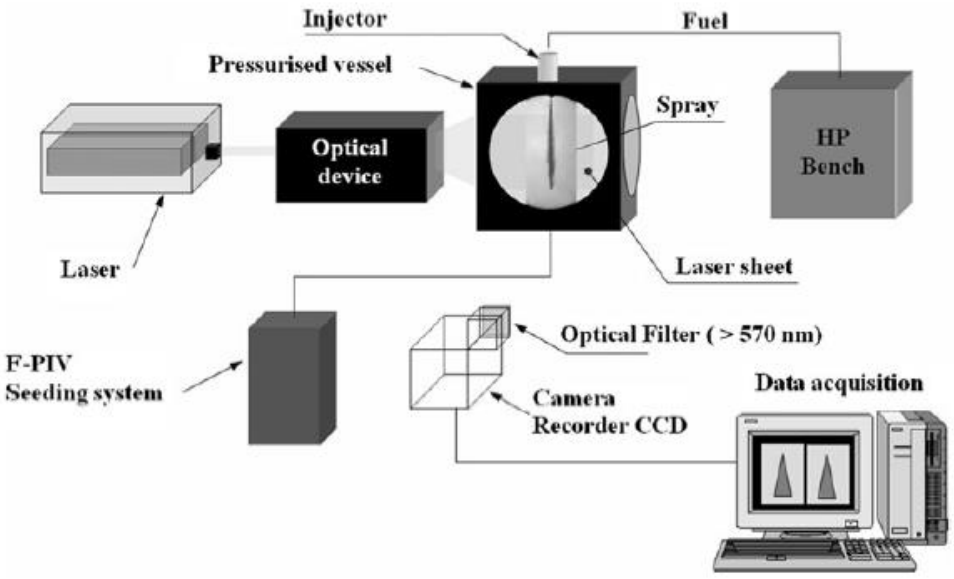

Figure 1.16 Schematic of FPIV System for Measuring the Spray Flow Field

In order to detect the in-cylinder gas flow while eliminating the luminosity of the combustion products, a high speed ultra-violet PIV technique was developed by Fajardo et al. [2009]. Figure 1.17 shows the dual-laser single camera UV-PIV set-up. The silicon oil droplets were mixed with the intake gas prior to the intake process. A high-speed CMOS camera (Phantom 7.3) was positioned parallel to the cylinder axis and fitted with a 105 mm f/4.5 UV lens. This method is capable of detecting the flow fluctuation in the real engine combustion conditions such as in the case of miss fire.

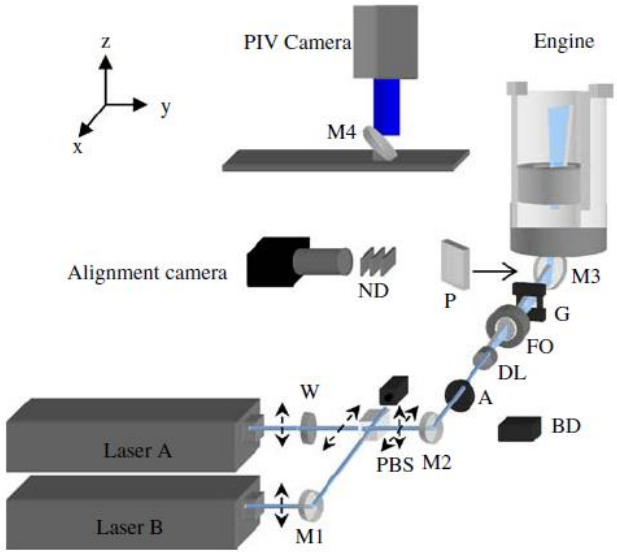

Figure 1.17 Experimental Setup for Dual-laser Single-camera High Speed UV–PIV System

Bo ödec et al. [2001] proposed a way for simultaneous measurements of velocity of droplets and ambient gas in the case of two-phase flow mixing as shown in Fig.1.18. The liquid phase was tagged with rhodamine 6G dye (with a concentration of 200ppm), and the ambient gas was seeded with incense particles of 0.1 to 3μm diameter. Two types of CCD camera captured the Mie scattering light and fluorescent light respectively, the sensitivity of the cameras were adjusted manually.

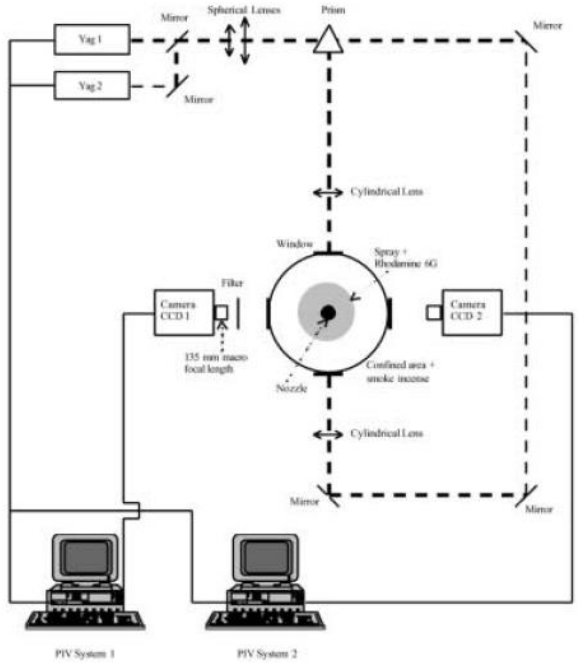

Figure 1.18 Experimental Setup for Simultaneous Measurements of Droplets Flow and Gas Flow

Recently, the stereoscope PIV system is being developed to obtain the three-component velocity vectors. Figure 1.19 shows a typical schematic proposed by Stella et al. [2001] by using the angular displacement method (ADM). Two recording cameras were used to observe the motion of seeding particles from different directions. From the third component, these two cameras recorded different apparent particle displacements. Soid et al. [2011] systematically reviewed the main optical measurement methods regarding the in-cylinder mixture formation process.

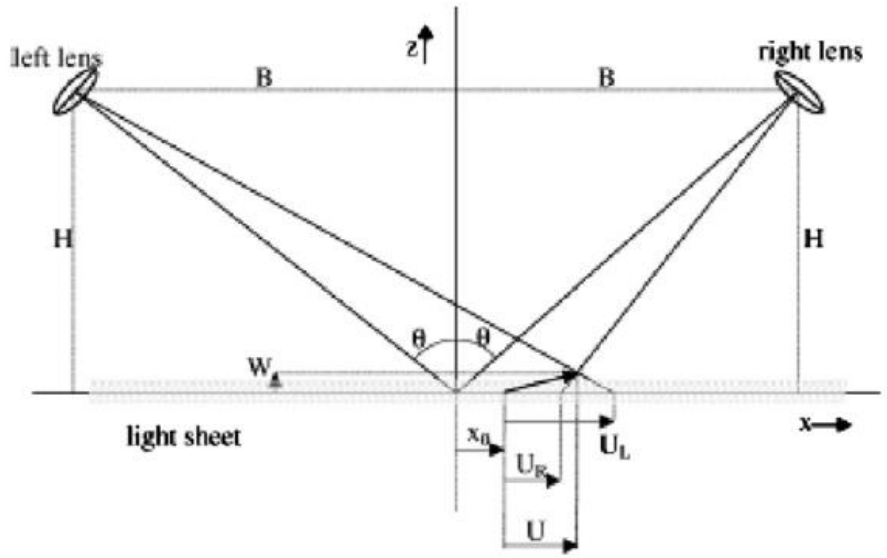

Figure 1.19 Schematic of Principle of Stereoscopic PIV System

As for the planar measurement of spray induced gas motion, LIF-PIV (Laser Induced Fluorescence-Particle Image Velocimetry) technique has proved to be one of the most promising measuring methods [Yeom et al., 2008; Lee et al., 2002; Driscoll et al., 2003; Moon et al., 2010]. Since only the fluorescent signal from the tracer itself can be derived without the influence of the scattered light from the spray droplets, this measuring method is feasible at the field approaching the spray periphery, even at the spray tip region where the diluted spray droplets may superpose with the tracer droplets. For measuring the spray internal flow, some studies [Cao et al., 2000; Hillamo et al., 2008] successfully measured the spray droplets' velocity distribution by capturing the image of diluted spray droplets or the fluorescent tracers dissolved in the fuel. However, it is still challenging to measure spray droplets' velocity and internal gas flow velocity simultaneously with high resolution especially in the dense non-evaporating Diesel spray.

1.4.3.2 Diesel Combustion Diagnostic Techniques

The optical investigation of the Diesel combustion process is particularly necessary for the engine researchers to optimize the combustion efficiency, power output and reduce the emission level. Natural luminosity from a sooting flame such as those in the Diesel engines is mainly taken by the gray body thermal radiation of the soot particles, thus the observation of the natural luminosity by high speed video camera provides the qualitative information of the line-of –sight soot formation. Gao et al. [2009] studied the natural luminous flame structure of a wall-impinging spray injected by a group-hole nozzle. This study pays concentration on the chemiluminescence of the flame and the quantitative measuring techniques of the soot concentration.

At the early time of combustion, the relatively very week flame luminosity is attributed to the chemiluminescence [Dec et al., 1995]. Because chemiluminescence is produced directly by exothermic chemical reactions [Gaydon., 1974], it marks the location of the initial combustion reactions both temporally and spatially. This emission arises from specific molecules that are raised to an excited state by exothermic chemical reactions and then subsequently decay back to equilibrium energy levels by emitting a photon. Chemiluminescence emission occurs in specific wavelength bands that are characteristic of the emitting molecules. In hydrocarbon-air flames, the strongest chemiluminescent intensity peaks are produced by the excited hydroxyl radical (OH*) at 280 to 310 nm and methylidyne radical (CH*) at 431 nm. The primary path for forming CH* is the reaction $C_2+OH \rightarrow CH^*+CO$. Succeeding this process, OH* is produced by the reaction $CH+O_2 \rightarrow CO+OH^*$ [Gaydon, 1974]. The chemiluminescence has been widely applied as a marker for the autoignition diagnostics. OH* maximum peak value was found to be well-correlated with the rate of heat release (RoHR) [Tinaut et al., 2010]. Several works [Higgins et al., 2001; Dandy et al., 1992] also found the connection of the chemiluminescence intensity and the equivalent ratio. Tinaut et al. [2011] concluded that the ratio of CH* to OH* is linearly proportional to the equivalence ratio with the fixed temperature by using the n-heptane fuel, the chemiluminescence intensity tends to show the peak value if the equivalent ratio is approaching the stoichiometric condition. Dec et al. [1998] studied the natural emission spectra of the Diesel flame and concluded that: (1). In early stage, the CH* emission (430nm) and CH_2O (368nm-470nm) play the dominant role in the chemiluminescence, the OH* is hardly observed which is probably due to the rich mixture (equivalence ratio 2-4); (2). In the later sooting combustion

stage, a distinct OH peak appears at 310 nm, and a strong gray-body emission totally dominates the spectrum at wavelengths longer than about 340 nm, which covers the light emission from CH* and C2 at the similar wavelength range. Siebers et al. [2001] studied the lift-off length and the corresponding air entrainment characteristics of a Diesel spray by investigating the OH* chemiluminescence, which is considered to occur under high temperature, stoichiometric combustion conditions. In recent years, the PLIF (Planar Laser Induced Fluorescence) -OH and PLIF-CH_2O techniques have also been widely used to obtain the space-resolved rather than the line-of-sight information of the chemical kinetic analysis [Singh et al., 2009; Collins et al., 2003]. The radical intermediate species generated in the flame are excited by the incident laser and form the relatively strong fluorescence, which acts a marker for analyzing the auto ignition feature.

Optical diagnostics for the soot measurement of Diesel Flame have made great progress recently. The two-color method utilizes the thermal radiation from soot particles to obtain the line-of-sight information of the soot concentration (KL factor, which is proportional to the soot concentration) and temperature. This technique has often been used in the past to measure flame temperature in diesel engines [Uyehara et al., 1946; Lyn., 1957]. Matsui et al. [1979] extended the technique to simultaneous temperature and soot concentration measurements in a direct-injection diesel engine. Shakal et al. [1994] studied the effect of multiple injection on the soot formation in a two stroke Diesel engine by two-color meter, they concluded that the pilot injection results in a high temperature region (> 2300 K) around the injection nozzle at the start of main injection. Miyamoto et al. [1996] found that significant smoke and particulate suppression could be achieved without increases in NOx by adding the oxygenated additive to the Diesel fuel according to the two-color method result. Kobayashi et al. [1992] found that KL factor persists through the combustion process and possibly contributes to exhaust emissions. The flame temperature increases with injection pressure, and the soot is reduced in the case of high-pressure injection. Since only the integrated line-of-sight soot concentration can be observed by two-color meter, which lacks the spatial resolution. Laser Induced Incandescence (LII) is capable of obtaining the planar soot distribution by inducing a laser sheet across the flame. The soot particles are heated to a temperature well above the surrounding gas temperature due to the absorption of laser energy. The heated soot particles subsequently emit black body radiation corresponding to the elevated soot particle temperature. Dec et al. [1995] modified an optical engine by replacing a part of cylinder liner with the glass which allow the laser access,

the LII and LIS (Laser Induced Scattering) signal were obtained from the cylinder head by two intensified CCD camera, respectively. The optical set-up is shown in Fig. 1.20. Zhao et al. [1998] systematically presented the optical diagnostics of soot and temperature measurement.

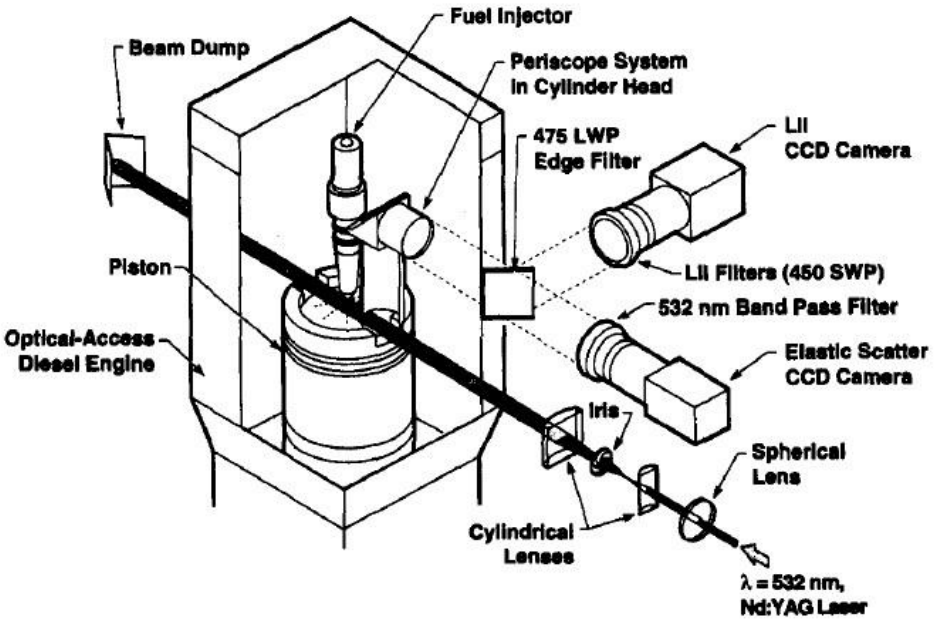

Figure 1.20 Schematic of Optical Set-up for Simultaneous Measurement of LII and LIS Signals

1.5 SUMMARY

In order to realize such low temperature and quasi-homogeneous combustion, it is necessary to improve the understanding of the fundamental mechanism of the combustible mixture formation process. This study was aimed at clarifying the mixture formation process and the combustion characteristics of the high pressure D.I. Diesel spray, which was carried out under the quiescent condition.

Firstly, the approaches and outlines for this research are introduced. The main fruits of the previous researches on the free spray and impinging spray are presented, including the main predictive models and empirical equations. Subsequently, the conventional combustion concept and advanced combustion concept and the main technique paths for improving the combustion efficiency are summarized. Finally, the latest optical diagnostics methods on the spray development especially the mixing process and the combustion characteristics are introduced.

CHAPTER 2 EXPERIMENTAL APPARATUS AND MEASUREMENT METHODS

2.1 FUEL INJECTION SYSTEM

Figure 2.1 shows the schematic diagram of fuel injection system. The air driven high pressure liquid pump (5L-ST-900) is manufactured by HYDRAULICS INTERNATIONAL, INC. (USA), which mainly consists of the drive section, pump section and cycling section. With the air supply from the air compressor, the liquid pump is able to build the pressure as high as 5000PSI. All the high pressure components such as the tubes, valves and elbows are manufactured by High Pressure Equipment Co., USA. The preset liquid pressure can be controlled by the air regulator. Due to the usage of the common rail, the fuel pressure at the inlet of the injector can be maintained constant during the injection period. The pressure gauge and pressure transducer provide the real-time pressure value simultaneously. The digital delay generator (Stanford Inc., DG 535) supplies the pulse for triggering the injection at the desirable timing.

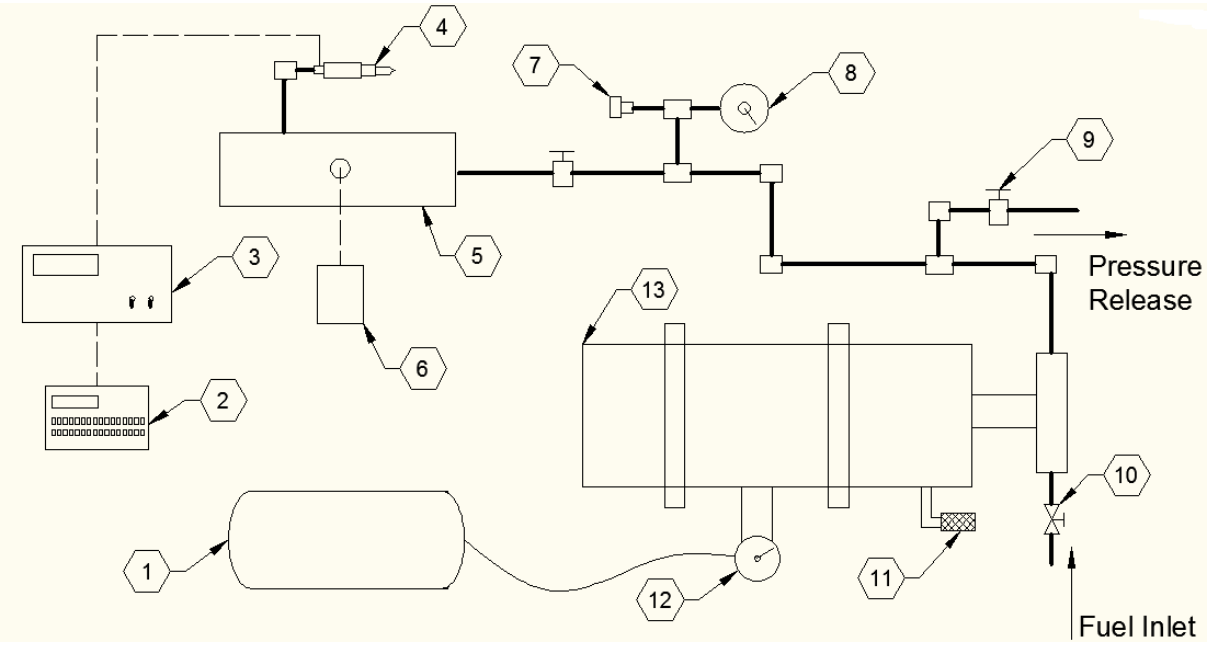

1. Air Compressor; 2. Digital Delay Generator; 3. Injector Controller; 4. Injector;
5. Common Rail; 6. Pressure transducer; 7. Safety Head; 8. Pressure Gauge;
9. High Pressure Valve; 10. Ball valve; 11. Air Exhaust; 12. Air Regulator;
13. Air Driven High Pressure Liquid Pump.

Figure 2.1 Schematic Diagram of Fuel Injection System

The electrical controlled solenoid Diesel injector was used in this study, with which the single orifice sac-hole nozzles with different nozzle hole size can be connected alternatively. Two nozzle hole sizes, 0.08mm and 0.12mm were selected. Figure 2.2 shows the schematic diagram of the nozzle tip of 0.08mm, in which the L/D=15. The sac volume was 0.488 mm^3.

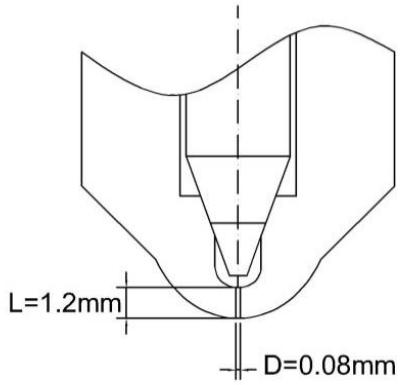

Figure 2.2 Schematic of Nozzle Tip

In this work, the fuel injection duration was determined as 2.2ms for all the cases. The fuel injection rate measurement was carried out by using the Zeuch type injection rate meter (Onno Sokki Co. Ltd, FJ-7000). Figure 2.3 shows injection rate profile of the two nozzles measured under the condition of 100MPa, 200MPa and 300MPa, respectively. This solenoid injector produces a square-like injecting rate shape. The duration from the start of injection to quasi-steady state is approximately 0.2ms and ramp-down duration is 0.3ms.

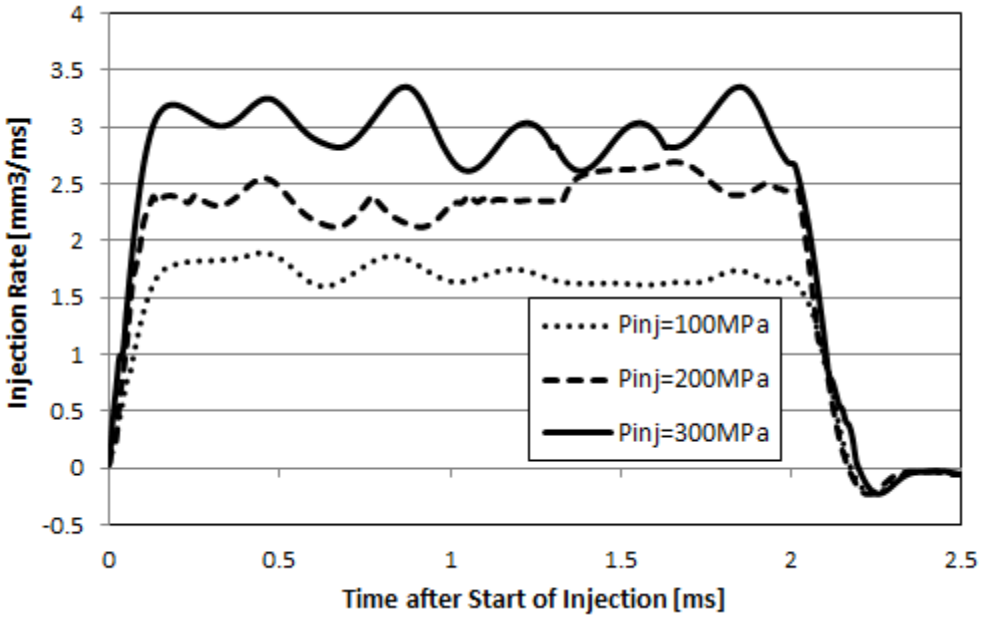

(a) D=0.08mm

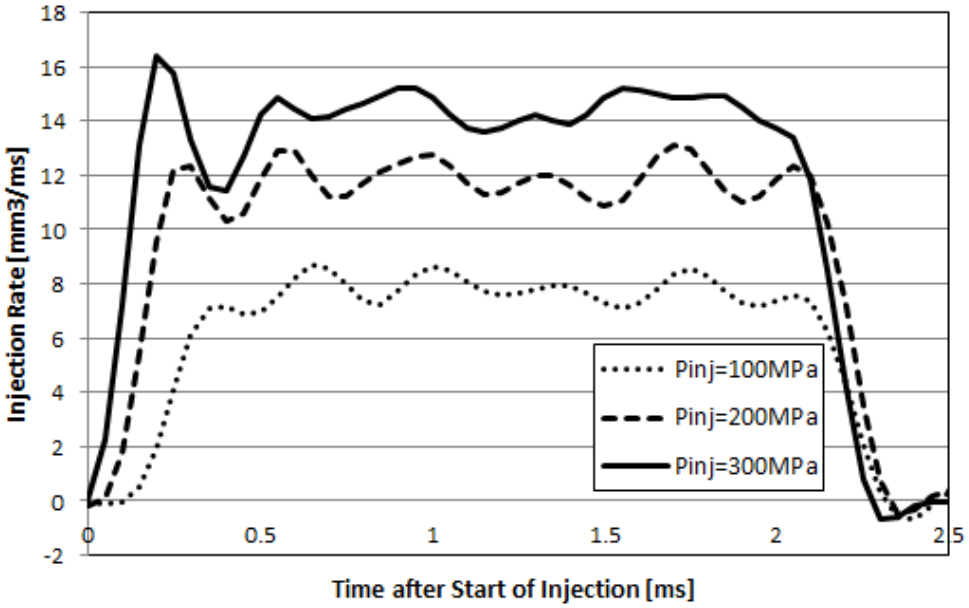

(b) D=0.12mm

Figure 2.3 Fuel Injection Rate

2.2 CONSTANT VOLUME VESSEL

The investigation of the spray and combustion evolution was conducted under the quiescent condition in a constant volume vessel. Figure 2.4 shows the schematic diagram of the structure of the constant volume vessel. The internal space of the chamber has the height of 300mm and the radius of 100mm. The sufficient chamber's volume ($9.4\times10^{6}mm^{3}$) ensures that the free spray develops in the nearly quiescent condition. A kanthal alloy heating unit is placed inside the chamber to produce the engine like high temperature condition as high as 1000K. The compressed N_2 or air can be introduced from the intake port to produce the in-cylinder pressure as high as 6MPa. Three thermal couple antennas were inserted to detect the heater temperature and the ambient temperature at different positions without the intrusion to the spray. The inner surface of the chamber was covered by the thermal insulator to avoid direct heat conduction and the fuel injection was carried out after the ambient temperature reached a stable value, thus the spatial distribution of temperature inside the chamber could be regarded as homogeneous condition. Both the injector adapter and the quartz window adapter were equipped with the

cooling water jacket, which prevents the over-heating. The optical access is available from all of the four sides of chamber.

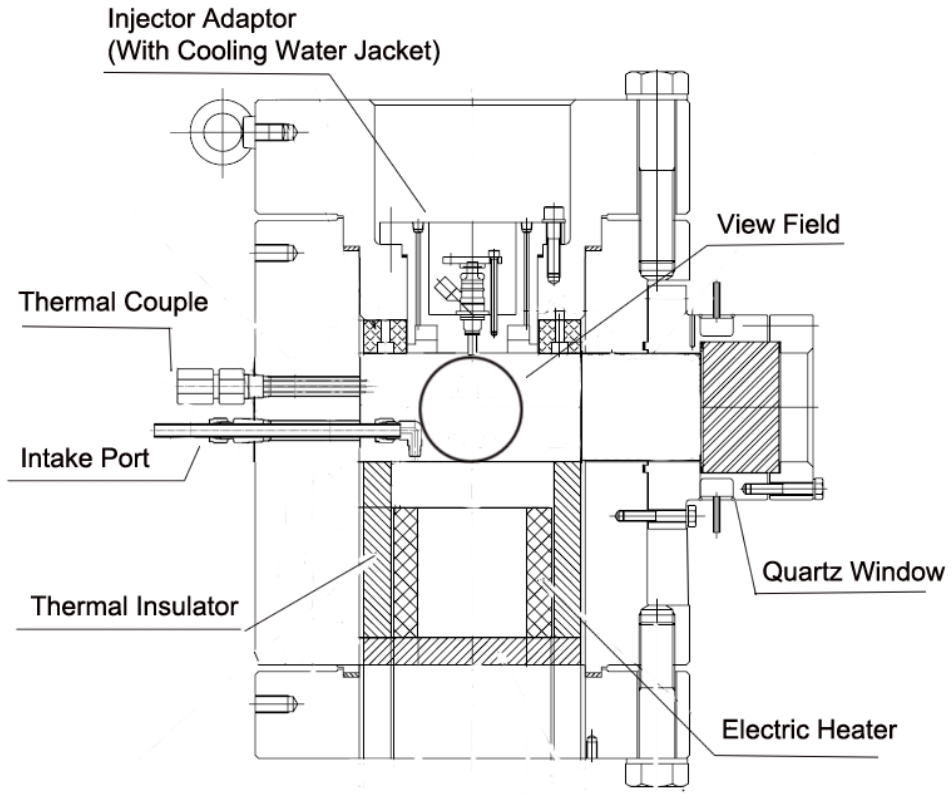

Figure 2.4 Schematic Diagram of Structure of Constant Volume Vessel

2.3 OBSERVATION TECHNIQUES

2.3.1 LIF-PIV (Laser Induced Fluorescence-Particle Image Velocimetry) Technique

2.3.1.1 Principle of PIV Technique

The principle of the PIV technique is simple, the flow velocity can be measured according to the displacement of the elements which trace the flow in a known shot time interval. For single-frame/ double-exposure PIV images, the particle image displacement vector is determined by calculating the digital auto-correlation of the double-exposed particle image field. For double-frame/single exposure PIV images, cross-correlation of the two separate images is used to work out the displacement vector. The cross-correlation algorithm is advantageous to reduce the in-plain loss of correlation and increase the correlation peak strength. Figure 2.5 shows the

comparison of the flow chart of the auto-correlation and cross-correlation by FFT analysis [Raffel et al., 2000].

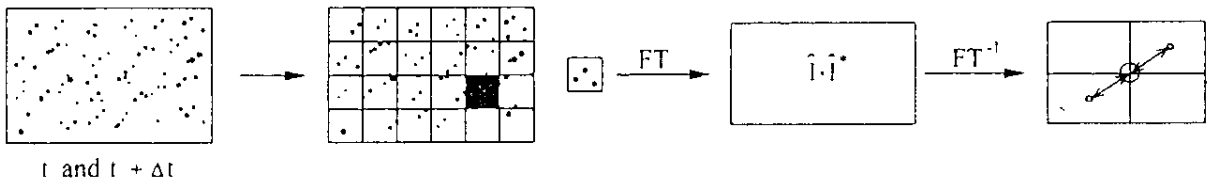

(a) Analysis of Single Frame/ Double Exposure Recordings: Fully Digital Auto-Correlation Method

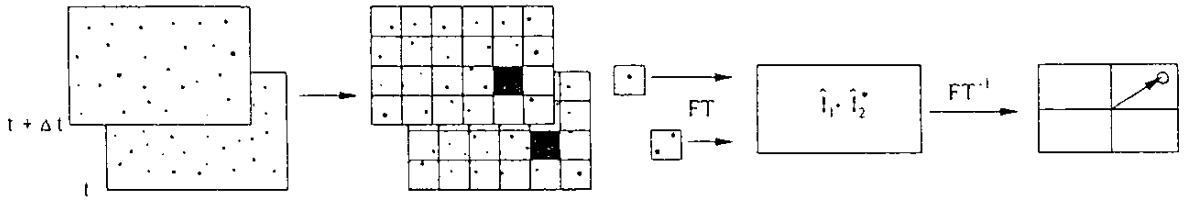

(b) Analysis of Double Frame/ Single Exposure Recordings: Fully Digital Cross-Correlation Method

Figure 2.5 Comparison of Flow Chart of Auto-Correlation and Cross-Correlation

The two frames are sub-divided into groups of interrogation windows, in each interrogation window, the cross-correlation function $R_{II}(S,\Gamma,D)$ is calculated, and the position of the displacement peak is determined, which corresponds to the particle image displacement vector.
The cross-correlation function can be subdivided into three terms:

$$R_{II}(S,\Gamma,D) = R_C(S,\Gamma,D) + R_F(S,\Gamma,D) + R_D(S,\Gamma,D) \quad (2.1)$$

Where the first two terms R_C and R_F contribute to the background noise in the correlation plane. R_D represents the component of the cross-correlation function that corresponds to the correlation of images of particles obtained from the first exposure with images of identical particles obtained from the second exposure:

$$R_D(S,\Gamma,D) = R_T(s-d)\sum_{i=1}^{N} V_0(X_i)V_0(X_i+D) \quad (2.2)$$

Where d is the particle image displacement, s is the separation vector in the correlation plane. Hence, for a given distribution of particles inside the flow, the displacement correlation

peak reaches a maximum for $s=d$. Figure 2.6 shows the composition of peaks in the cross-correlation function [Zhao et al., 2001].

Equation (2.3) presents the integral formulation of the cross-correlation function:

$$R_{II}(x,y) = \sum_{i=-K}^{K} \sum_{j=-L}^{L} I(i,j)I'(i+x, j+y) \tag{2.3}$$

The plain of the image is subdivided into slight interrogation windows with i rows and j columns. The variable of I and I' are the intensity value corresponding to the samples from two images. For each choice of the sample shift (x, y), the product of all overlapping pixel intensities generates one cross-correlation value. By applying this operation in a range of shifts, a composition of correlation plain is formed. There would be a peak in the correlation plain in which shift value makes the samples' particle images align with each other. Thus the particle image displacement will be calculated statistically in the sample window based on the peak correlation value.

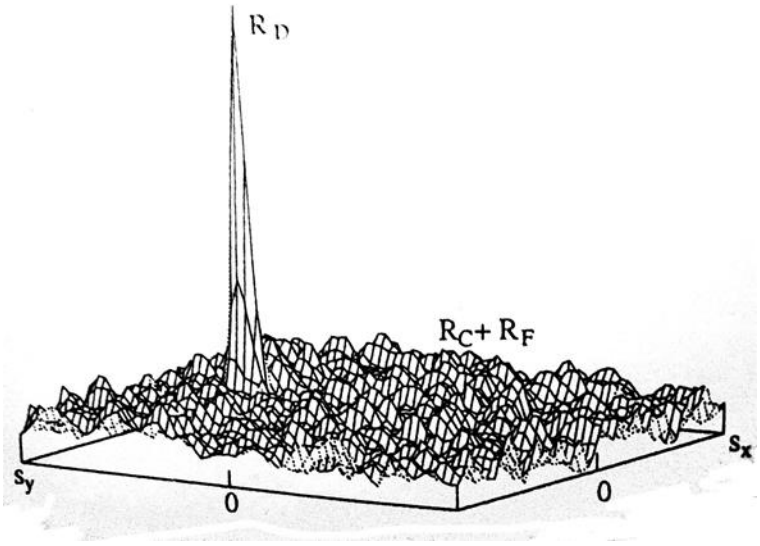

Figure 2.6 Composition of Peaks in Cross-Correlation Function

2.3.1.2 Experimental Set-up of LIF-PIV Technique

LIF-PIV technique has the advantage of yielding the particles fluorescent images with high light intensity and high resolution, without the impact of the scattering light from the other phases. Thus this technique has been proved to be superior for the measurement of the complicated multi-phase flow.

Figure 2.7 shows the schematic of the experimental set-up for measuring the ambient gas flow field of the non-evaporating spray, which mainly comprises mechanical high pressure fuel injection system, optical accessible constant volume vessel, timing control unit and LIF-PIV system. Three quartz windows with a diameter of 100mm were installed at the three sides of chamber respectively and the tracer injector was installed at the fourth side. The injection of the tracer droplets and the incidence of the laser sheet were from two opposite sides, while a CCD camera (PCO1600, PCO Inc.) was placed perpendicular to the laser sheet. Diesel fuel was injected into the high ambient gas density condition while the CCD camera captured the spray and the tracer images at a specific timing.

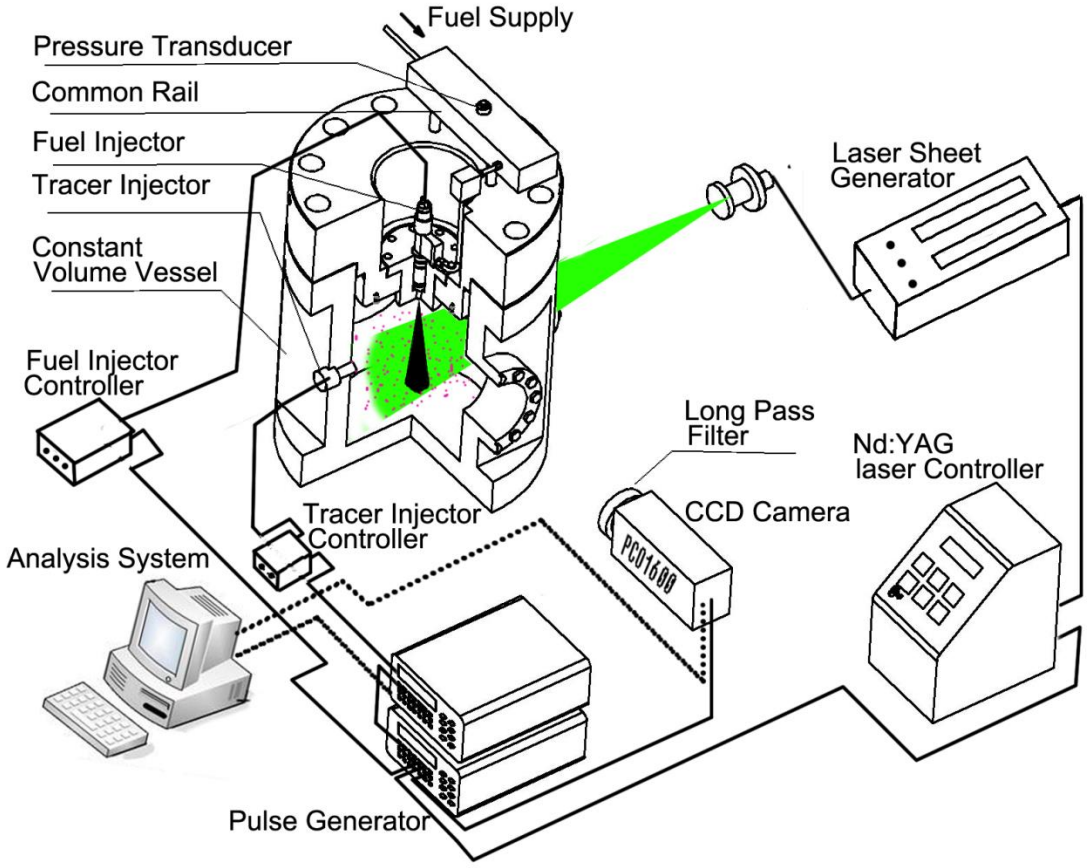

Figure 2.7 LIF-PIV Experimental Setup for Measuring Ambient Gas Flow

The LIF-PIV technique is capable of measuring the motion of the tracers very close to spray vicinity accurately by providing high contrast tracer image and cutting off the scattering light from the high-number-density droplets in the spray. Figure 2.8 shows the experimental time chart. Two delay generators (DG535, Stanford Inc.) synchronized the pulses for the tracer

injection, fuel injection, laser shot and image capture. Firstly, the water solution of Rhodamine B reagent which was used as the fluorescent tracing particle was injected into high pressure chamber from left side by a swirl type injector with an injection pressure of 9MPa. After a certain interval when the tracing particles had been distributed uniformly in the whole chamber (Δt_{inj}=1300ms in Fig. 2.8), the fuel injection pulse was triggered. At desired timing after the start of injection (SOI), an Nd:YAG laser sheet with a wavelength of 532nm and thickness of 1mm was incident from the right side of the vessel thus making the spray plume illuminated, the tracing particles emitted the fluorescent light at wavelength of longer than 590nm. Meanwhile the CCD camera mounted with the long pass filter (>560nm) was synchronized to capture two images with high spatial resolution of 1600×1200 pixels during a short time interval (Δt_{shot}=40μs in Fig. 2.8). The scattering signal of the spray droplets was cut off and only the fluorescent light from the tracing particles was recorded. Figure 2.9 shows the principle of the image capturing process using the LIF-PIV technique in the previous work by Moon et al. [2010]. The two-dimensional ambient gas flow field was calculated based on the displacement of tracers in the two images by using the cross correlation algorithm.

For measuring the spray flow field and the ambient gas flow of the evaporating spray, the basic experiment set-up was similar, however the tracers supply, frame interval and interrogation window size varied. The detailed information will be introduced in the relevant chapters, respectively.

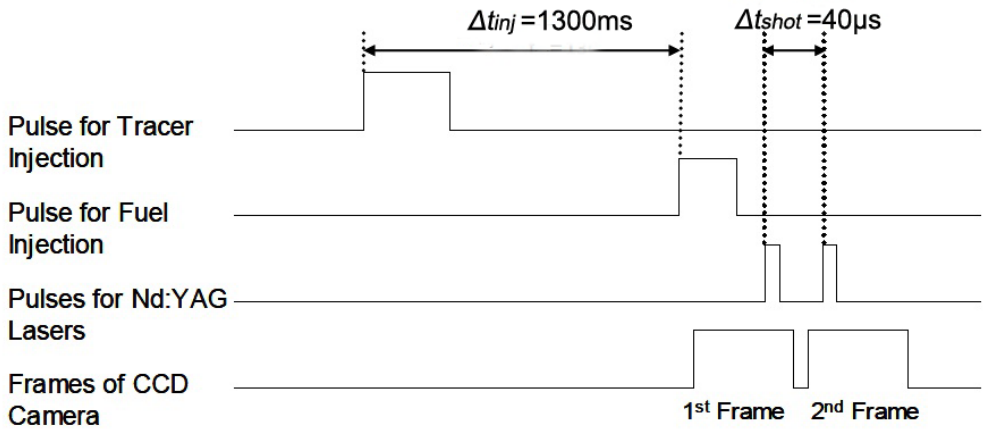

Figure 2.8 Time Chart of LIF-PIV Experiment

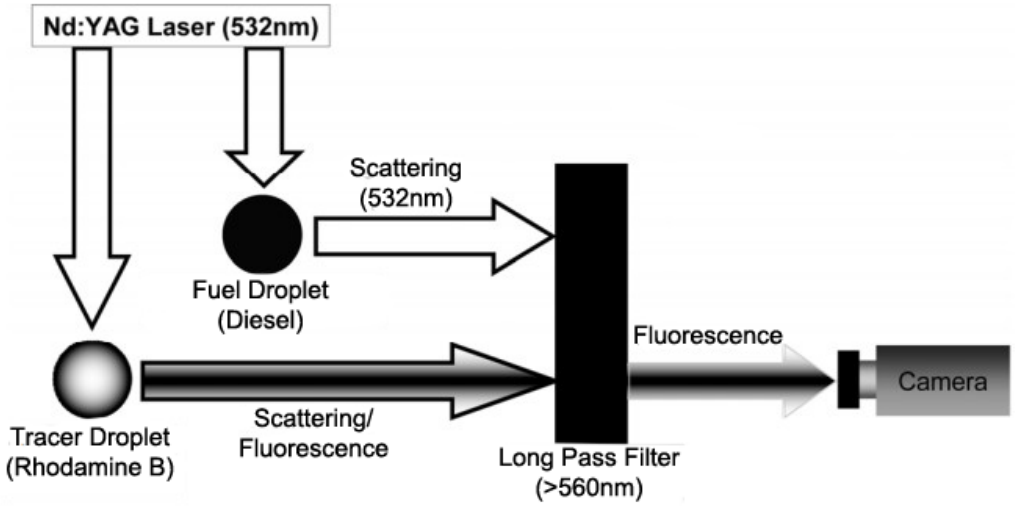

Figure 2.9 Principle of Image Capturing of Tracer Droplet with Long Pass Filter

2.3.1.3 Optimization of PIV Measurement

So many PIV experimental parameters need careful optimization, which directly impact the measurement accuracy. Zhao et al. [2001] summarized the main variables that need optimization in Table 2.1, which mainly involves three aspects:

- Laser source;
- Seeding property;
- Data processing.

The measurement error is weighted with $1/\Delta t_{shot}$, increases rapidly with decreasing the time interval of two frames [Raffel et al. 2000]. However, a larger frame interval leads to the measuring noise increase. In the two-dimensional PIV experiment, in order to limit the out-of-plane loss of correlation, the out-of-plane displacement of particles should not exceed 30% of the light sheet thickness [Keane et al. 1990]. The relevant equation is shown as follows:

$$\Delta z \geq 4 \cdot w \cdot \Delta t_{shot} \tag{2.4}$$

Where the w is out-of-plane velocity component and Δz is the laser sheet thickness. As a conclusion, a thicker laser sheet should be employed. Although it is also possible to include the out-of-plane velocity component which would confuses the 2-dimension measurement. The thickness of the laser sheet in this study was adjusted to approximately 1mm. The frame interval Δt_{shot} used for measuring the ambient gas flow of the non-evaporating spray was 40 μs.

Since the particle tracing velocity U_p follows an exponential function of time as shown in Eq.(2.5), in which t_s is relaxation time defined in Eq.(2.6), thus the smaller droplet size is favorable to rapidly attain velocity equilibrium with the surrounding gas. The d_p is the diameter of the tracer particle [μm]; ρ_l is the density of the tracer [kg/m^3]; μ is the kinetic viscosity [Pa*s] and *t* is the time after the tracer particles are exposed to the surrounding flow.

$$U_p = U\left[1 - exp\left(-\frac{t}{t_s}\right)\right] \tag{2.5}$$

$$t_s = {d_p}^2 \frac{\rho_l}{18\mu} \tag{2.6}$$

The tracing droplet size versus time investigation was conducted by using LDSA (Laser Diffraction Size Analyzer, LDSA-1400A, Tonichi Computer Inc.). The He-Ne laser beam illuminates the diluted droplets and the scattering and diffractive light is formed, the receiver analyzes the different patterns of the light and correlates it to the droplets size distribution.

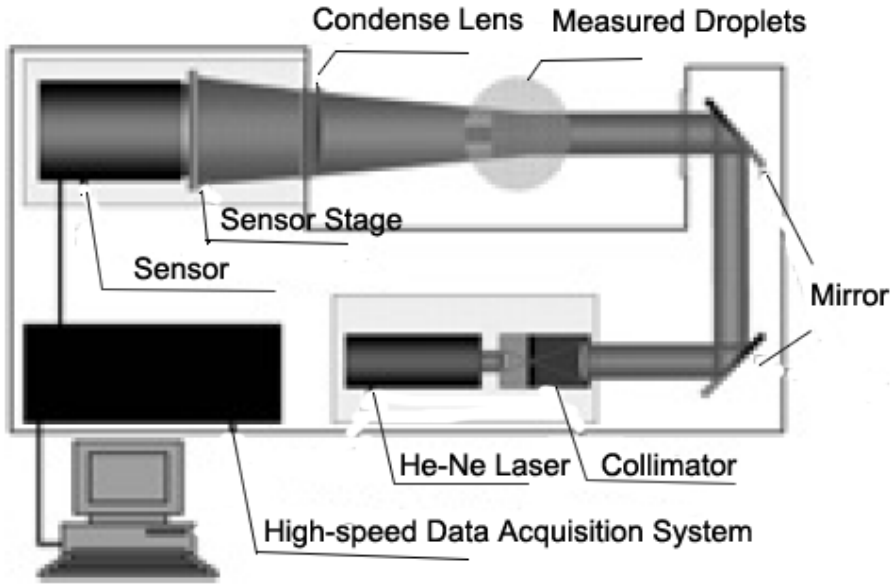

Figure 2.10 Schematic of Laser Diffraction Size Analyzer

The AMD (Arithmetic Mean Diameter) result with ambient pressure of 1.6MPa is shown in Fig.2.11, in which the coordinate represents the relative position from the nozzle tip. 1300ms after the tracer injection, the droplets with bigger size deposits in the lower region due to the gravitational effect, the average droplet size is 6-8μm.

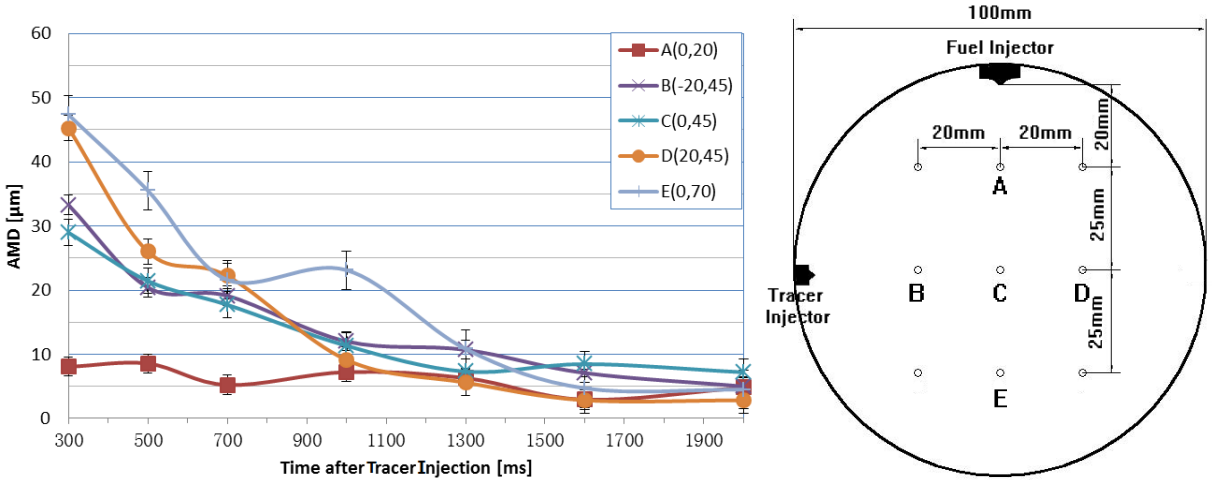

Figure 2.11 Temporal Variations of Tracer Droplets' Size at Various Locations

According to Eq.(2.6), t_s is approximately 0.15ms in this experiment. Based on the graph of tracing ability shown in Fig.2.12, it takes approximately 0.2ms for the tracer to attain 80% of the surrounding gas velocity. Assuming that the gas velocity along the spray surface ranges from 2 to 5m/s and is almost stable in the quasi-steady condition, the tracer particle has enough time for tracing the spray induced ambient gas motion since the first testing timing starts from 0.5ms ASOI.

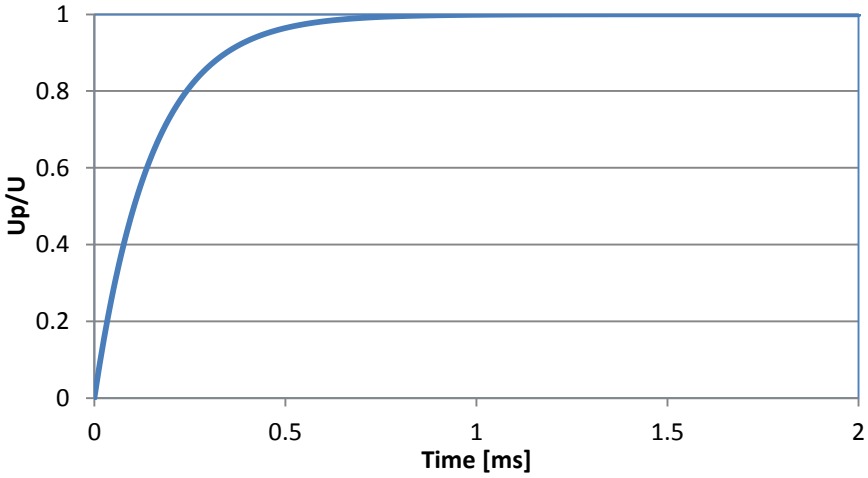

Figure 2.12 Tracing Ability of Tracer Droplet Relative to Ambient Gas Motion

(dp=7*10-6m, ρl=1000kg/m3, μ=1.82*10-5(Pa*s))

Meanwhile, the residual tracer velocity should be as low as possible in order to ensure the ambient gas almost static before the fuel injection. As shown in Fig.2.13, the average tracer velocity in the whole region before the fuel injection is lower than 0.1m/s. To achieve the

reliable PIV results, there should be enough detectable droplets inside the measuring region. Due to the deposition of tracer droplets, the time interval between the tracer injection and the fuel injection Δt_{inj} should not be too long.

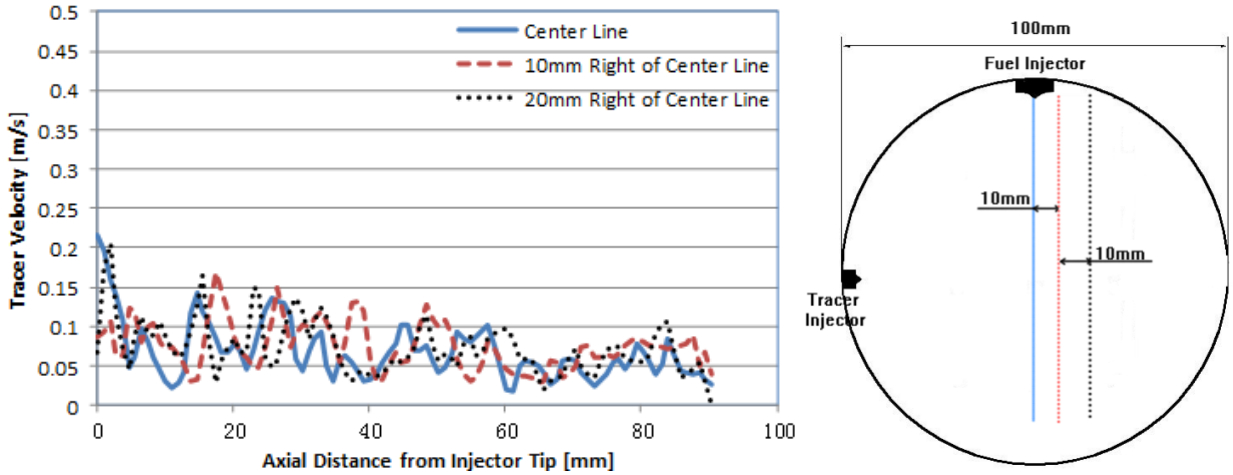

Figure 2.13 Spatial Distribution of Tracer Velocity at 1300ms after Tracer Injection

The displacement of tracer particles should not exceed half of the interrogation window size [Zhao et al., 2001]. This implies that a comparatively lager interrogation window and shorter frame interval is more favorable. Due to only the linear shift of particles in the interrogation window would be yield, the interrogation window size should be small enough to track velocity gradient especially in the unstable flow. On the other hand, the number of tracer droplets in one interrogation window need to be ensured and the recommended number is at least 5-8, the particles entering in or going out of the interrogation window will also contribute to the incurrence of the spurious vector [Raffel et al. 2000], which implies too small interrogation window may cause undesirable result. After predicting the magnitude of tracer particle velocity and comparing the effect of different interrogation size, the interrogation window of 16*16 pixels (1.55mm*1.55mm) with 50% overlap was selected for the ambient gas flow measurement.

Figure 2.14 shows an example of the tracer particles' distribution result, among which one interrogation window with 16*16 pixels is enlarged to show the particles' image in detail. Even though the real particle size is much smaller than the pixel size, as the smallest addressable screen element in a display device, the pixel is capable to capture the strong fluorescent light emitted from the droplets and record their displacement during the time interval with sufficient resolution. Thanks to the use of the long pass filter and the fluorescent property of the tracers, the influence of the strong scattering light from the fuel droplets can be eliminated.

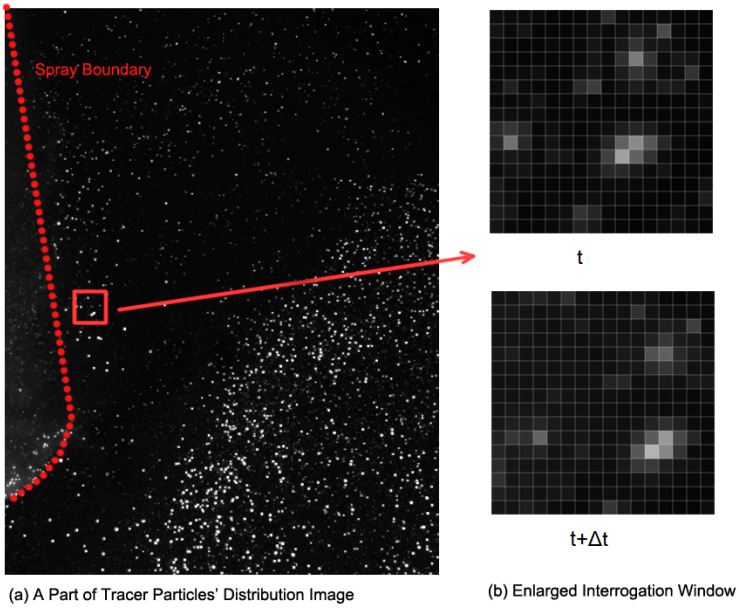

Figure2.14 Example of a Tracer Droplets Image and a Pair of Enlarged Interrogation Window using LIF-PIV Technique

Table 2.1 Summary of PIV System Variables and Their optimization

Laser source	Light sheet thickness (Δz):	$\Delta z \geq 4 \cdot w \cdot \Delta t_{shot}$; thicker sheet with sufficient spatial resolution.
	Pulse separation (Δt_{shot}):	Auto-correlaiton: $D_{max} \leq 0.25L$; Cross-correlaiton: $D_{max} \leq 0.5L$.
Seeding particles	Particle size (d_p):	1μm-10μm; small particle to follow turbulent flow, large particle to increase scattered light.
	Seeding density:	≈6 particles in the interrogation region for improved valid data rate (signal-to-noise ratio).
Imaging Optics	Magnification (M)	<0.1; smaller magnification for increased measurement area and reduced perspective error.
	f-number (f#)	Selected so that depth-of-field $\delta_z \geq \Delta z$ and particle image diameter $D_i \leq d_{pixel}$.

Cross-correlation CCD camera	Pixel size and No.:	The format of camera determines the spatial resolution of PIV recordings.
	Frame rate (30fps):	The number of PIV image pairs per second is half the frame rate.
Interrogation regions	Size (LxL):	Large L for increased dynamic range, smaller L for improved accuracy.
	Number:	Limited to the square matrix of $2^n x 2^n$ by FFT algorithms used in digital correlation calculations.
Evaluation scheme	Image shift between the two frames:	The two separately exposed images should be shifted by the estimated mean particle image displacement vector to reduce the in-plane loss of correlation.

2.3.2 OH* Chemiluminescence

A high speed video camera (Photron Co., ultima APX RS) was employed to measure the spray evolution and the natural luminosity of the Diesel flame. A 10-bit CMOS sensor with 17 μm pixels and a 16.7 ms to 2 μs global electronic shutter were used. This camera provided full mega 42 pixel resolution images at frame rates up to 3,000 frames per second (fps), 512 x 512 pixels resolution at 10,000 fps, and at reduced frame rates to the fastest frame rate of 250,000 fps. Figure 2.15 shows the experimental setup for direct imaging of the spray and the natural luminosity of Diesel flame. A Nikkor visible lens (Nikon, 70-210 mm, f/4-5.6) was mounted. When imaging the fuel spray, a Xenon lamp (Ushio Inc., SX-UID 510XAMQ) was used to illuminate the spray droplets.

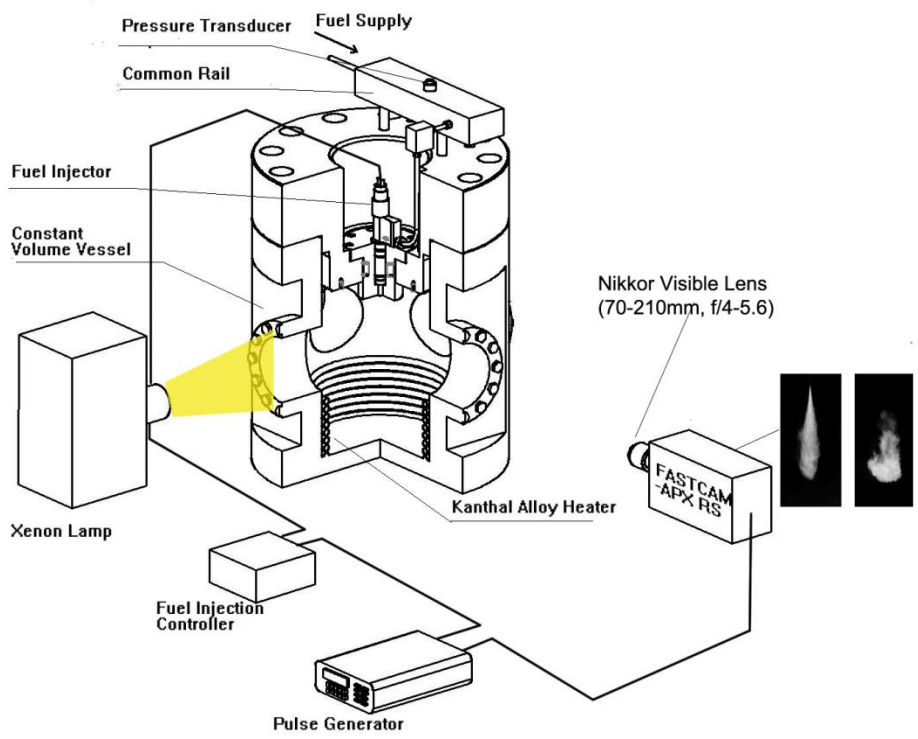

Figure 2.15 Experimental Setup for Direct Imaging of Spray and Natural Flame Luminosity

The imaging of the chemiluminescence from the OH* radical species was carried out to characterize the auto-ignition with high temperature and near stoichiometric mixture. Figure 2.16 shows the experimental setup for OH* chemiluminescence and two color pyrometry. Since the very weak light intensity of the OH* radicals, an image intensifier (LaVision Inc., HS-IRO) was mounted in front of the high speed video camera. The gain and gate of the image intensifier were adjusted carefully to the optimum values of 70 and 50 μs. A UV Nikkor lens (Nikon, 105 mm, f/4.5) coupled with a band pass filter with the wavelength of 310nm (10nm FWHM) was used. Figure 2.17 shows the light intensity distribution of the Diesel fuel flame measured by different band pass filters (10nm FWHM) [Siebers et al., 2000]. The horizontal dashed line in the figure represents the threshold used to define the lift-off length. It is found that for the band pass filter with the wavelength less than 310nm, the lift-off length is almost stable because the chemiluminescence in this range is strong enough compared with the soot incandescence. On the other hand, the soot incandescence becomes more dominant and masks the chemiluminescence with the wavelength more than 340nm due to the limit dynamic range of the camera, as a result, the lift-off length becomes longer because the chemiluminescence is not able to be detected. As a

conclusion, the 310nm was selected as the optimum value to observe the OH* chemiluminescence and determine the lift-off length and the ignition delay.

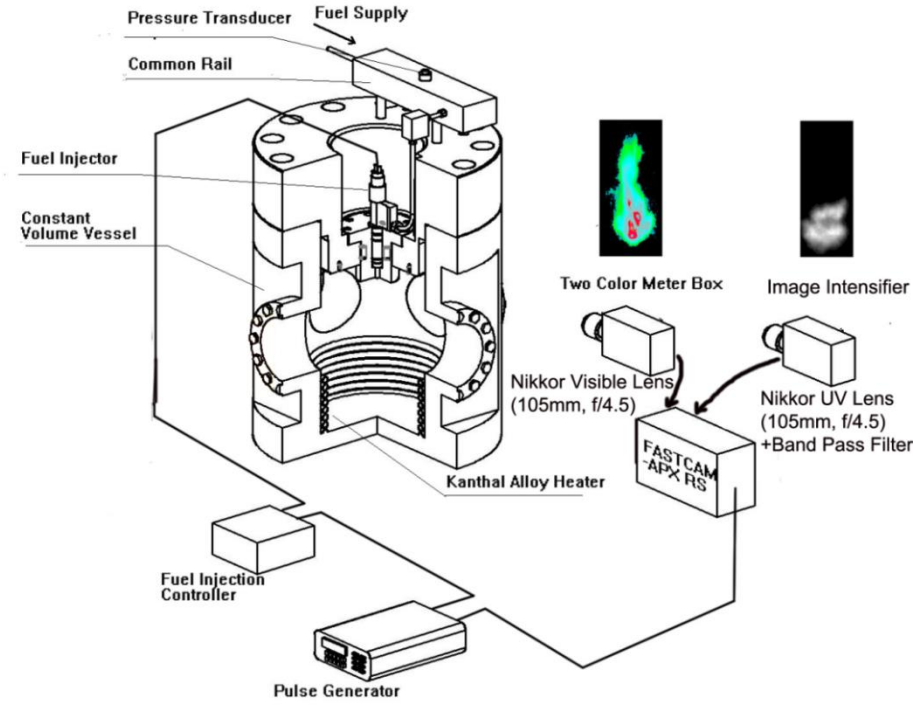

Figure 2.16 Experimental Setup for OH* Chemiluminescence and Two Color Pyrometry

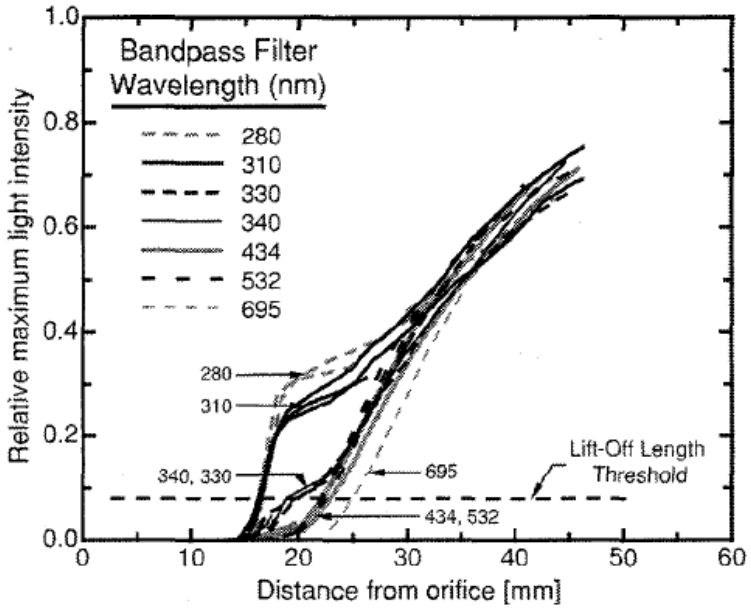

Figure 2.17 Light Intensity at Various Wavelengths as a Function of Axial Distance from Injector Orifice (D=100μm, P_{inj}=138MPa)

2.3.3 Two-Color Pyrometry

A two color meter box was mounted in front of the high speed video camera as shown in Fig. 2.16, the light emission of the sooting flame with two specific wavelengths (650nm and 800nm, 10FWHM) were split by the two color meter box, the instantaneous signals generated by the photodiodes were amplified and the resulting voltages at each wavelength were recorded by the camera. According to the Hottel and Broughton Law, the integrated line-of-sight information of the soot concentration and temperature can be computed. A Nikkor visible lens (Nikkon 105mm, f/4.5) was used.

2.3.3.1 Principle of Two Color Pyrometry

The intensity of radiation from a black body depends on the temperature of the black body and the specific wavelength, which is described by the Planck's equation:

$$E_{b,\lambda}(T) = \frac{C_1}{\lambda^5[e^{\left(\frac{C_2}{\lambda T}\right)} - 1]} \tag{2.7}$$

Where $E_{b,\lambda}$ is the monochromatic emissive power of a blackbody at actual temperature T (W m^{-3}), λ is the wavelength (μm), C1 and C2 are the Planck's constant, which are 3.7418*10^{-16} (W m^2) and 1.4388*10^{-2}(m K).

An apparent temperature T_a is defined as the temperature of a blackbody that will emit the same radiation intensity as a non-blackbody at temperature T. Thus the monochromatic emssivity ε_λ gives:

$$\varepsilon_\lambda = \frac{E_{b,\lambda}(T_a)}{E_{b,\lambda}(T)} \tag{2.8}$$

Combining Eq. (2.7) and Eq. (2.8), and using the empirical correlation developed by Hottel and Broughton [1932]:

$$\varepsilon_\lambda = \frac{e^{C_2/\lambda T} - 1}{e^{C_2/\lambda T_a} - 1} = 1 - e^{\left(-\frac{KL}{\lambda^\alpha}\right)} \tag{2.9}$$

Where K is an absorption coefficient which is proportional to the number density of soot particles, L is the geometric thickness along the line of sight. α is a constant which depends on the light wavelength, the soot particle size and the refractive index of soot.

The Eq. (2.9) can be transformed as follows:

$$KL = -\lambda^{\alpha} \ln\left[1 - \left(\frac{e^{\frac{C_2}{\lambda T}} - 1}{e^{\frac{C_2}{\lambda T_a}} - 1}\right)\right] \tag{2.10}$$

If there are two specific wavelengths λ_1 and λ_2 that are measured simultaneously, the value KL which is proportional to the integrated soot concentration can be eliminated:

$$\left[1 - \left(\frac{e^{\frac{C_2}{\lambda_1 T}} - 1}{e^{\frac{C_2}{\lambda_1 T_{a1}}} - 1}\right)\right]^{\lambda_1{}^{\alpha_1}} = \left[1 - \left(\frac{e^{\frac{C_2}{\lambda_2 T}} - 1}{e^{\frac{C_2}{\lambda_2 T_{a2}}} - 1}\right)\right]^{\lambda_2{}^{\alpha_2}} \tag{2.11}$$

Provided the two apparent temperature T_{a1} and T_{a2} at two specific wavelengths λ_1 and λ_2 can be obtained according to the calibration data, the actual temperature and the KL value can be calculated.

2.3.3.2 Calibration Process of Two Color Pyrometry

A standard two-color optical pyrometry system by using a tungsten lamp was used for the calibration. The photograph of the experiment setup is shown in Fig. 2.18. The correlation of the voltage and the apparent temperature at the wavelength of 662nm of the tungsten lamp was identified in advance. Then the corresponding apparent temperature at the wavelength of 650nm and 800nm can be calculated by Eq. (2.12):

$$T_{a1}(T_{a2}) = \frac{1}{\frac{1}{T_{a662}} + \frac{\lambda_{662} ln\varepsilon_{662} - \lambda_1(\lambda_2) ln\varepsilon_1(\varepsilon_2)}{C_2}} \tag{2.12}$$

The emissivity ε is function of the wavelength and the tungsten temperature, which can be calculated by the Larabee empirical equations as shown in Table 2.2.

With the aid of the Thermera software (Mitsui Optronics version 4.61), the correlation of the light intensity and the apparent temperature at the wavelength of 650nm and 800nm can be established. The calibration was carried out in wide temperature range from 1200K to 2600K, as a result the calibration database was formed. When measuring the sooting Diesel flame, the apparent temperature was obtained firstly by interpolation, then the actual temperature and the KL factor can be calculated according to Eq. (2.10) and Eq. (2.11). Figure 2.19 summarizes the main flow chart of the two color pyrometry measurement.

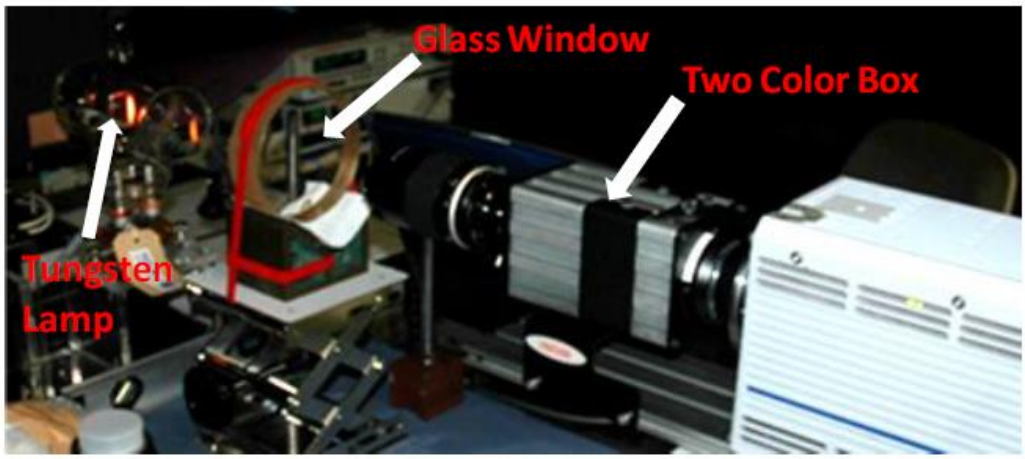

Figure 2.18 Calibration System of Two Color Pyrometry

Table 2.2 Larabee empirical equations for Calculating Emissivity

350 to 450 nm	$\varepsilon_{\lambda T} = 0.6075\text{-}0.3000\lambda\text{-}0.3265 \times 10^{-4}T + 0.5900 \times 10^{-4}\lambda T$
450 to 680 nm	$\varepsilon_{\lambda T} = 0.4655\text{-}0.01558\lambda\ 0.2675 \times 10^{-4}T - 0.7305 \times 10^{-4}\lambda T$
680 to 800 nm	$\varepsilon_{\lambda T} = 0.6552\text{-}0.2633\lambda\text{-}0.7333 \times 10^{-4}T + 0.7417 \times 10^{-4}\lambda T$
$\varepsilon_{\lambda T}$ is the emissivity at a particular wavelength and temperature, T is the tungsten temperature in K and λ is the wavelength in nanometer.	

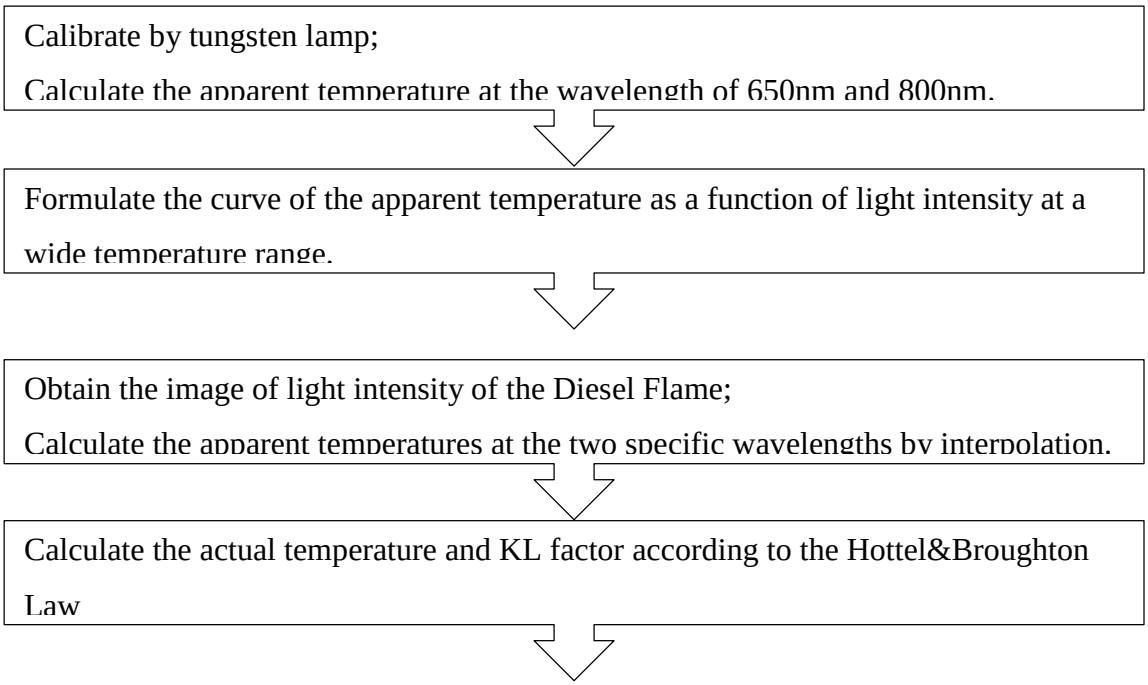

Figure 2.19 Flow Chart of Two Color Pyrometry Measurement

2.4 SUMMARY

1. The experiment was conducted in a wide range of injection pressure from the ordinary values in the current Diesel engines (100MPa, 200MPa) to the ultra-high (300MPa) value, which was achieved by using an air actuated liquid pump. A micro-hole nozzle (0.08mm) and a conventional nozzle (0.12mm) were applied as the test nozzles in this study.
2. A constant volume vessel was used for providing a quiescent atmosphere to investigate the spray and combustion evolution. The maximum temperature and pressure of 1000K and 6MPa of the atmosphere can be achieved.
3. Particle Image Velocimetry (PIV) and Laser Induced Fluorescence- Particle Image Velocimetry (LIF-PIV) techniques were used for measuring the spray flow and the ambient gas flow.
4. The direct photography using the high speed video camera was used to carry out the spray and the flame natural luminosity experiments. In order to understand the ignition, combustion, and soot formation processes, the OH* chemiluminescence and the two color pyrometry were utilized.

CHAPTER 3 FREE DIESEL SPRAY/AMBIENT GAS INTERACTION PROCESS

3.1 EXPERIMENTAL CONDITION

LIF-PIV technique was employed to measure ambient gas flow field of the non-evaporating free spray using the tracer droplets with Rhodamine B due to its fluorescent property. The detailed experimental process can be found in Chapter 2. Table 3.1 and Table 3.2 show the experimental conditions and the parameters for LIF-PIV system under the non-evaporating condition, respectively. The constant volume vessel was charged with nitrogen gas at room temperature (300K) to reach the desired pressure. In this study, three ambient gas densities 11 kg/m^3, $15kg/m^3$ and $20kg/m^3$ were used which also correspond to the typical in-cylinder ambient gas density condition at the fuel injection timing in the D.I. Diesel engine. The JIS#2 commercial Diesel fuel in the Japanese market was used as the test fuel in this work. Fuel injection duration of 2.2ms was selected to get a quasi-steady state spray. Several measurement timings during the fuel injection duration and after the end of injection (EOI) were selected. Two types of single-hole nozzle with the hole diameter of 0.08mm and 0.12mm were used to investigate the effect of nozzle hole-size on the spray-induced ambient gas motion. A wide range of injection pressure from 100, 200 to 300MPa were employed, which covers the current common rail diesel injection pressure and future probable ultra-high injection pressure conditions. The interrogation widow size of 16*16 pixel (1.55mm*1.55mm) and the frame interval of 40μs were selected according to the predicted velocity of the gas flow field.

Table 3.1 Experiment Conditions for Non-Evaporating Free Spray

Nozzle Type	Single Hole Nozzle
Hole Diameter (mm)	0.08; 0.12
Injection System	Common Rail System
Injection Pressure (MPa)	100; 200; 300
Injection Duration (ms)	2.2
Fuel Type	Diesel JIS #2
Density (g/cm^3,300K)	0.82~0.86
Kinematic Viscosity (cSt, 300K)	1.3~4.1
Surface Tension (N/m, 300K)	0.025
Ambient Gas	Nitrogen
Density/Temperature/Pressure (kg/m^3; K; MPa)	11/300/1.1 15/300/1.4 20/300/1.8
Measurement Timing	0.5, 1.0, 1.5, 2.0, 2.2, 2.5ms ASOI

Table 3.2 LIF-PIV System and Tracer Injection Parameters for Non-Evaporating Spray

LIF-PIV System	Analysis Algorithm	Cross-correlation Method
	Frame Interval	40 μs
	Interrogation Size	16*16 pixels (1.55mm*1.55mm)
	Windows Overlap	50%
	Laser Type	Nd:YAG Laser; 532nm; 120mJ
	Image Resolution	1600*1200 pixels
	Lens Type	Nikon Micro-Nikkor: 60 mm f/2.8D (With Long Pass Filter: >560nm)
Tracer Injection	Tracer Type	Water Solution of Rhodamine B
	Nozzle Type	Swirl Type
	Injection Pressure	9Mpa
	Injection Duration	2ms

For the evaporating spray condition, it is challenging to find an appropriate fluorescent matter that can endure the high temperature atmosphere, especially for the visible laser range. Alternatively, the MgO solid powder with the size of 2μm substituted the water solution of Rhodamine B as the tracer. The Mie scattering light from the MgO powder was directly recorded by the PIV system and used for analyzing. MgO solid powder was placed in front of the intake port prior to the pressurization, therefor it could be lifted and distributed inside the chamber. Unlike the LIF-PIV measurement for the non-evaporating spray in which the gas flow very closed to the spray boundary could also be obtained, the gas flow analysis for the evaporating spray starts from a certain distance away from the spray periphery due to the influence of the strong light scattered from the liquid core region and the existence of the vapor phase. Table 3.3 shows experimental conditions particularly for the evaporating spray. Meanwhile, the liquid length of the evaporating spray was measured by high speed video camera according to the Mie scattering light signal.

Table 3.3 Experimental Conditions for Evaporating Free Spray

Injector	Hole Diameter (mm)	0.08; 0.12
Ambient Gas	Density/Temperature/Pressure (kg/m^3; K; MPa)	11/797/2.6 15/885/4.0
Tracer Injection	Tracer Type	MgO Solid Powder
Measurement Method	PIV Technique	
	High Speed Video Camera	Frame Rate:10,000fps
		Resolution: 512*512

In order to eliminate the impact of shot to shot variation, in each specific timing the fuel shot was tried more than 10 times and the result of velocity measurement was obtained by averaging the value of 5-6 representative samples with good repeatability.

3.2 MEASUREMENT OF SPRAY INDUCED AMBIENT GAS FLOW FIELD

3.2.1 Non-Evaporating Condition

3.2.1.1 Spatial Distribution of Ambient Gas Flow

Figure 3.1 shows the examples of spatial distribution of ambient gas velocity vector synthesized with the spray image in the case of 0.08mm injector and 1.0MPa ambient pressure as a base condition. The spray tip penetration increases apparently with the injection pressure because of the larger momentum of the spray droplets. The high injection pressure keeps the spray tip an approximately hemispherical shape even near the end of injection if eliminating the shot by shot variation by averaging several spray samples. Only one side of the ambient gas flow is shown here because of the assumption of the axis-symmetric structure of the spray. The effect of fuel injection pressure, ambient gas density and nozzle hole size on the ambient gas flow is compared in Fig. 3.2. If only taking the air flow along the side periphery into account, there is no obvious change of air flow velocity when the ambient gas density rises from 15kg/m^3 to 20kg/m^3. The spray tip penetration decreases due to the increased air drag force, thus decelerating the spray development. The increase in both the injection pressure and the nozzle hole size significantly enhances the air flow velocity since more momentum transfers from the spray droplets to the ambient gas. It is assumed that there is a large amount of gas mass captured by the spray development at the tip periphery because the major spray momentum is still propagating downstream along the nozzle axis. The mean gas velocity at the tip periphery is 1-2m/s higher compared with that along the side periphery, which is still much lower than the spray penetrating velocity.

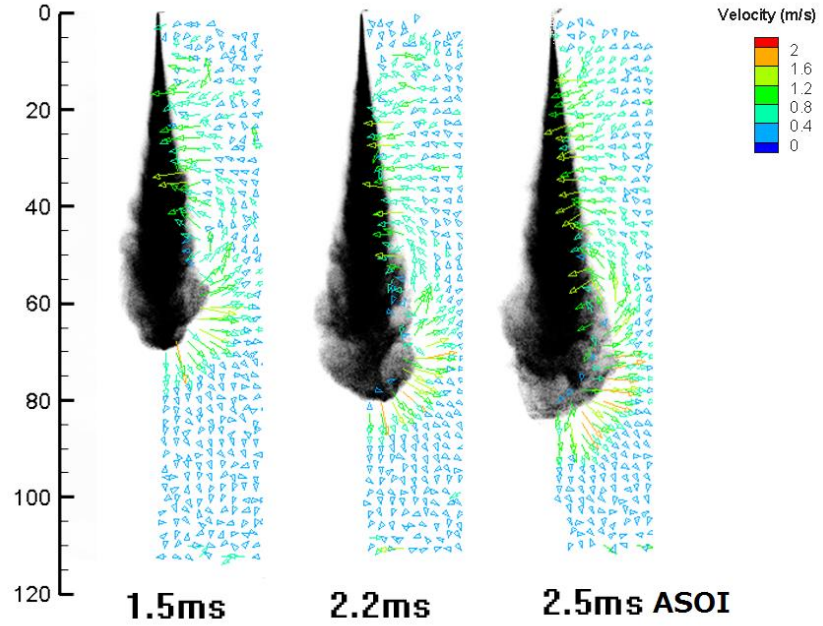

(a)P_{inj}=100MPa

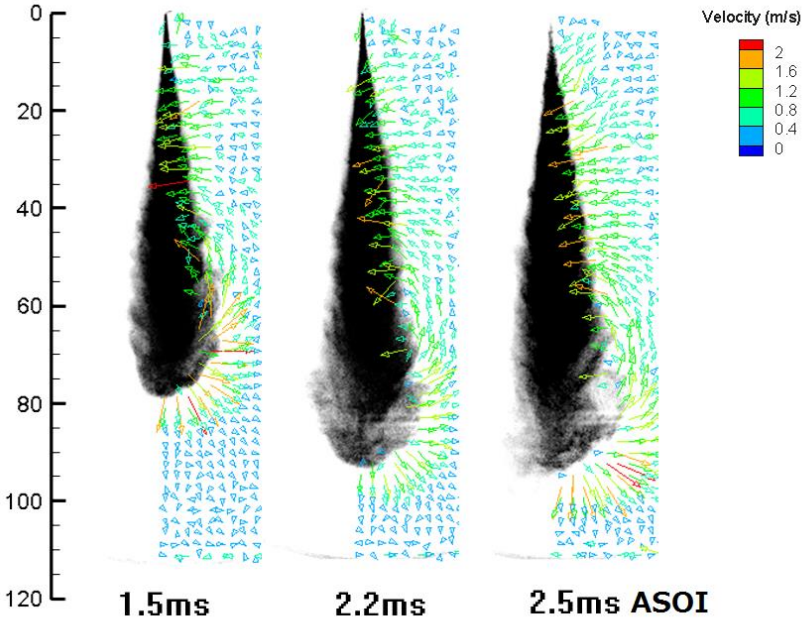

(b) P_{inj}=200MPa

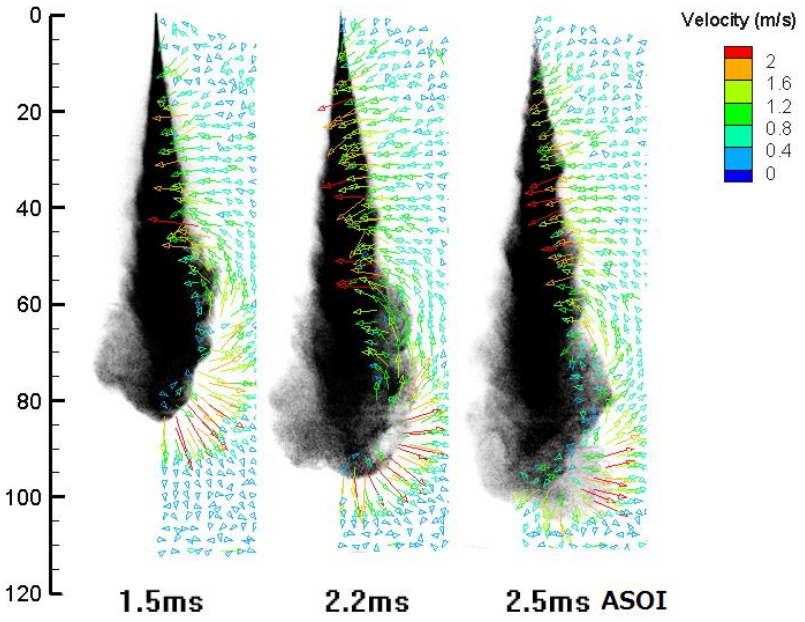

(c) P_{inj}=300MPa

Figure 3.1 Distribution of Ambient Gas Velocity Vector around Spray (ρ_a=11kg/m^3, d=0.08mm)

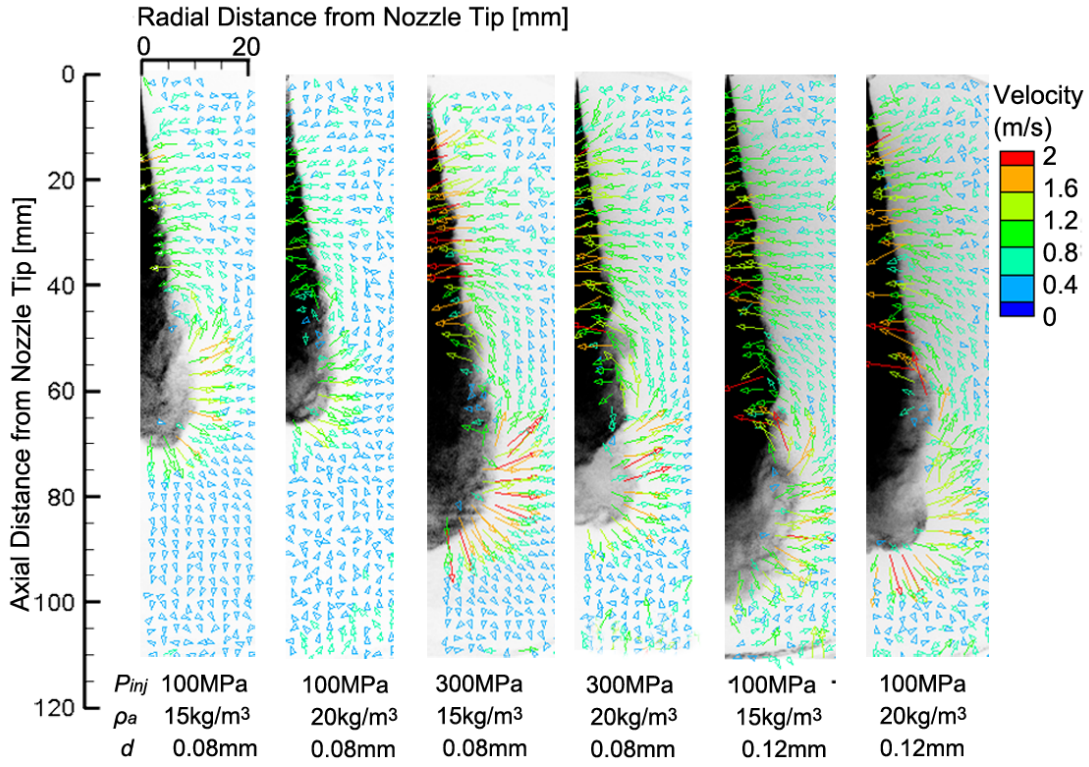

Figure 3.2 Spatial Distribution of Velocity Vectors of Ambient Gas Motion around Spray Periphery (2.2ms after Start of Injection)

3.2.1.2 Spray Tip Penetration

According to the Mie scattering light image illuminated by the laser sheet, the spray tip penetrations under the different conditions were measured and shown in Fig. 3.3. The position along the nozzle axis in which the light intensity is less than 10% of the maximum value was defined as the spray tip. The power fitted curve of the spray tip penetrations are also labeled, which will be used for calculating the spray tip penetrating velocity afterwards. The standard deviation of the sampling is less than 5% for all the cases. The spray tip penetration increases apparently when the injection pressure enhances from 100MPa to 200MPa, however, this trend becomes moderate when the injection pressure increases further. Several factors may contribute to this result, such as the increased air drag force and decreased cross-section area of the fuel mass flow inside the nozzle. Increased ambient gas density restricts the spray development due to the higher aerodynamic force. Larger nozzle hole size significantly increases the spray tip penetration, which is attributed to the larger initial droplets size with larger momentum.

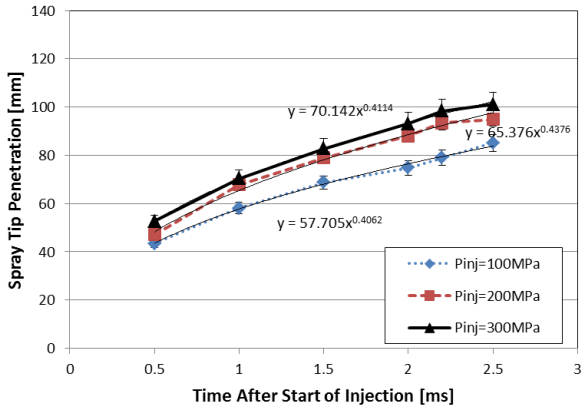

(a) ρ_a=11kg/m^3, d=0.08mm

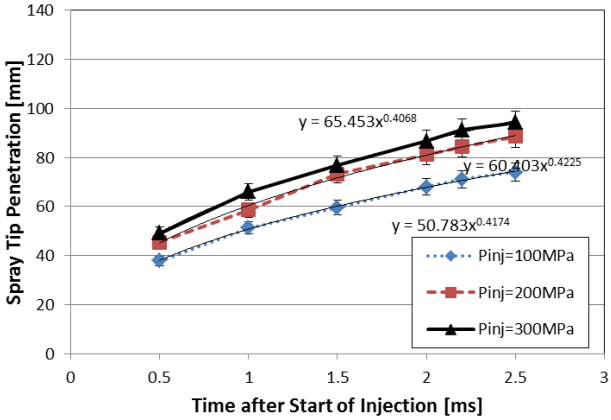

(b) ρ_a=15kg/m^3, d=0.08mm

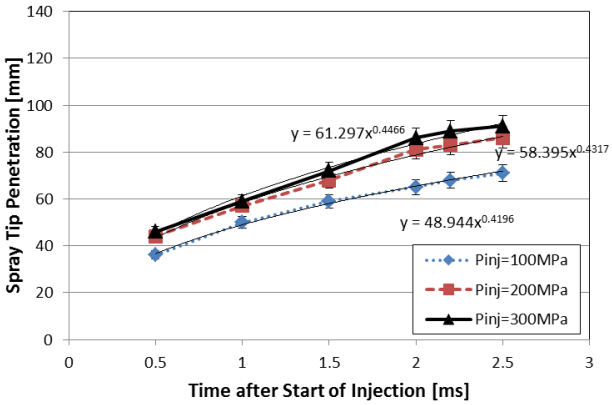

(c) ρ_a=20kg/m^3, d=0.08mm

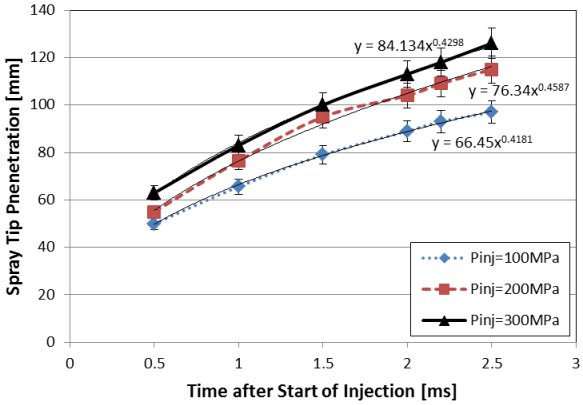

(d) ρ_a=20kg/m^3, d=0.12mm

Figure 3.3 Temporal Variation of Spray Tip Penetration

By recalling the predictive models proposed by Hiroyasu et al. [1990] and Siebers et al. [2009] shown in Chapter 1, Eq. (1. 4) and Eq. (1. 9), the spray tip penetrations measured by experiment and calculated by predictive models are compared in Fig. 3.4. In which C_a is the area contraction coefficient which is calculated based on the discharge coefficient of C_d and the cavitation number [Payri et al. 2004]. C_d is defined as the ratio of the fuel mass flow rate injected in the cylinder to the theoretical one computed from the Bernoulli equation. In this study, the value of both C_a and C_v are 0.85, since C_a can be regarded as almost constant though C_a decreases slightly with the increase in the injection pressure [Siebers., 1999]. It is found that both of the models tend to underestimate the spray tip penetration, with the increase of the injection pressure, the experiment results are in line with the predictive results gradually. Particularly, the model proposed by Naber and Siebers is able to predict the spray tip penetration more accurately, because it takes into account of the factor of the spray cone angle and the internal flow coefficient.

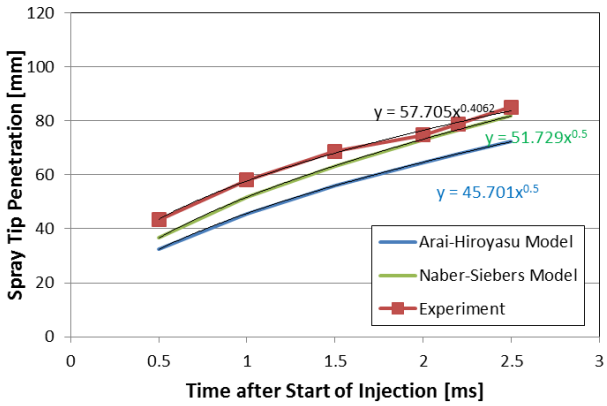

(a) P_{inj}=100MPa, ρ_a=11kg/m^3

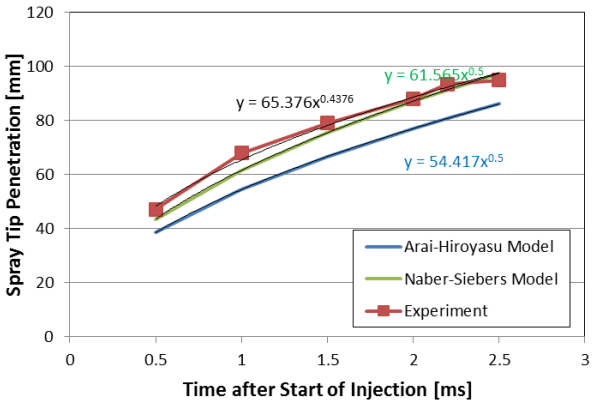

(b) P_{inj}=200MPa, ρ_a=11kg/m^3

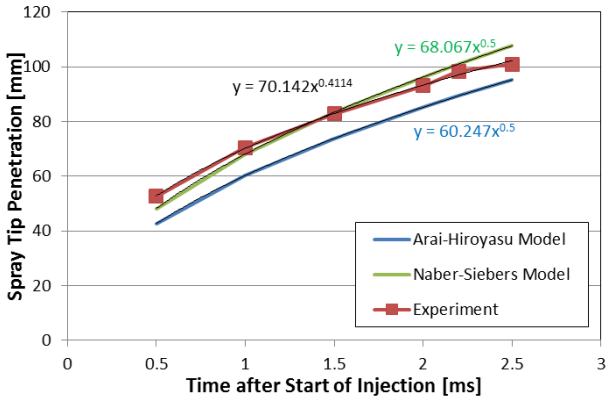

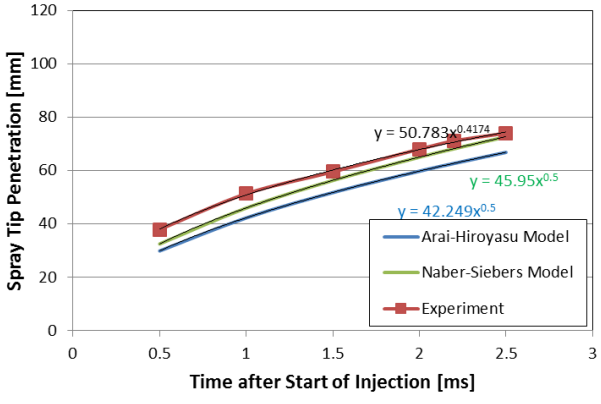

(c) P_{inj}=300MPa, ρ_a=11kg/m^3 (d) P_{inj}=100MPa, ρ_a=15kg/m^3

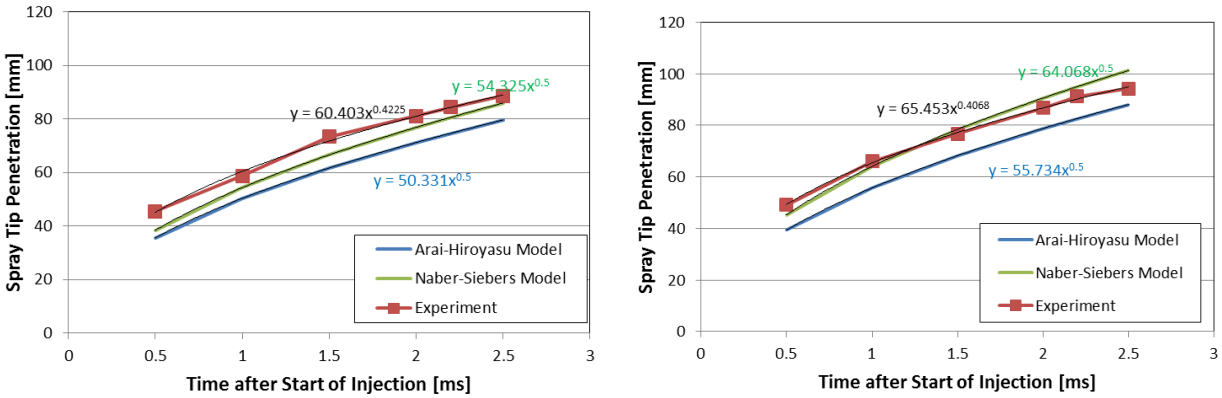

(e) P_{inj}=200MPa, ρ_a=15kg/m^3 (f) P_{inj}=300MPa, ρ_a=15kg/m^3

Figure 3.4 Comparison of Spray Tip Penetrations by Experiment and Models (d=0.08mm)

3.2.1.3 Ambient Gas Flow Velocity

As shown in Fig.3.5, the spatial distribution of spray-ambient gas interaction is categorized as three regions. Section 1: Entrainment section at the side periphery. Here the ambient gas is entrained into the spray periphery because of the pressure gradient from the surrounding air to the spray induced by fuel injection. The side periphery in this section is quite smooth and almost stable. Section 2: Capturing section at the spray tip periphery. The spray droplets at the spray tip region move downstream with sufficient momentum. A large amount of ambient gas is captured into the spray plume due to the substantial relative velocity of spray penetration and ambient gas motion. Section 3: Recirculation section downstream of the side periphery. In this section, the droplets at the spray tip gradually lose momentum and are pushed aside by the upstream droplets and ambient gas flow, resulting in the simultaneous movement of droplets and ambient gas in the radial direction. At the same time, due to the influence of the relatively lower pressure of the ambient gas outside of the entrainment section, the droplets and ambient gas flow towards the upstream direction. Ikegami et al.[2009] thought that in the Diesel combustion condition the pushed-out air movement would convey the soot formed in the spray tip region to the outside which improved soot oxidation. In the non-reacting spray case, the large vortex motion in this section implies strong turbulent mixing of fuel and air inside spray plume. In contrast, Cho et al. [1990] divided the spray periphery into two parts with smooth line: the penetration part and stagnation part. The current model refines the classification of the spray-ambient gas interaction according to the measurements of the instantaneous ambient gas flow field.

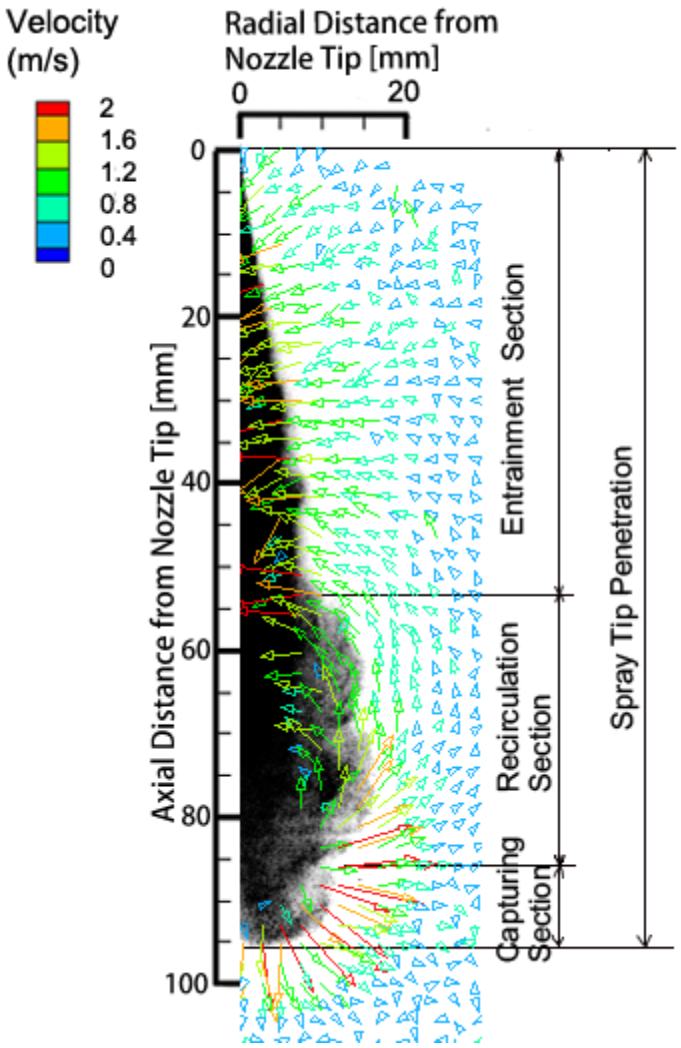

Figure 3.5 Description of Three Sections around Spray Periphery with Different Ambient Gas Motion feature (Pinj=300MPa, ρa=11kg/m3, d=0.08mm, t=2.2ms ASOI)

In order to identify the ambient gas flow velocity characteristics, a “control surface” is drawn along the spray spreading angle from the nozzle tip, and extended to far field straightly. The gas velocity component perpendicular to the control surface is defined as the “normal velocity”.

Figure 3.6 shows the spatial distribution of normal velocity along the control surface at the timing of EOI. The position with negative velocity value refers to the entrainment section, while the positive value refers to the pushed out flow at the recirculation section and a part of capturing section. The gas velocity shows very low value near the nozzle tip region and gradually increases downstream in the quasi-steady state. This is because the entrainment motion

is not fully developed near the nozzle due to the gas inertia. The smooth side periphery near the nozzle tip demonstrates the weak interaction in the interface of the spray and ambient gas. When go downstream, the large vortex motion at the recirculation section acts as the source to improve the gas entrainment upstream. It is evident that the higher injection pressure increases the gas flow velocity and the length of gas entrainment section along the side periphery. The increased gas flow velocity under the high injection pressures is attributed to the increased aerodynamic force along the side periphery. The spray atomization is improved with the increased injection pressure because of the more gas entrainment.

The maximum gas velocity at the entrainment section shows the similar value in all of the three gas density conditions. The similar result can also be found in the study by Sepret et al. [2010]. That is because the ambient gas drag force is linearly proportional to the gas density which tends to accelerate the gas flow, on the other hand, the increased gas density restrains the gas phase acceleration. Moreover, the entrainment section is considerably restrained in the high ambient gas density condition.

There is a considerable increase in air flow velocity and the length of entrainment section with the increase in nozzle hole size. Larger nozzle hole size results in the increase in the initial spray droplet size, the air drag force is proportional to the droplet size, which accounts for the increase in air flow velocity. The result of 300MPa injection pressure is not shown here because the spray exceeds the field of view.

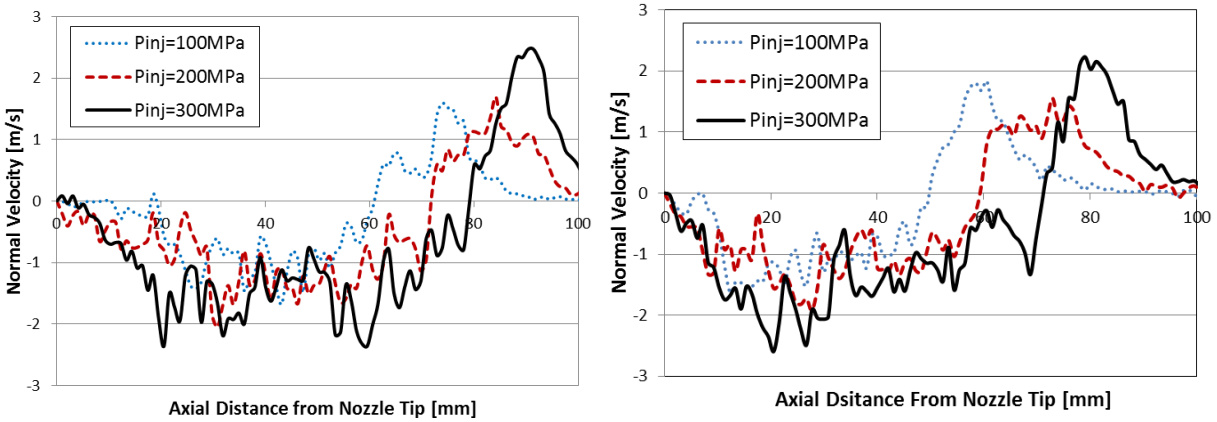

(a) ρ_a=11kg/m^3, d=0.08mm (b) ρ_a=15kg/m^3, d=0.08mm

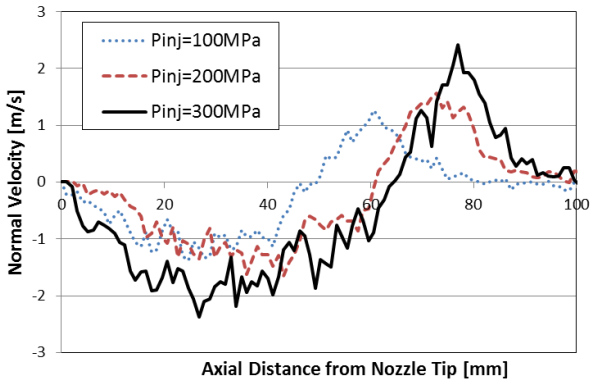

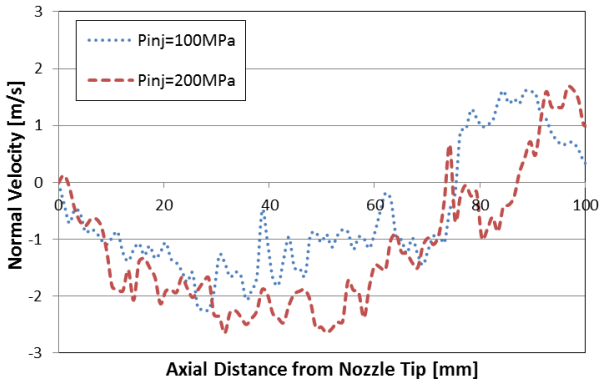

(c) ρ_a=20kg/m^3, d=0.08mm (d) ρ_a=15kg/m^3, d=0.12mm

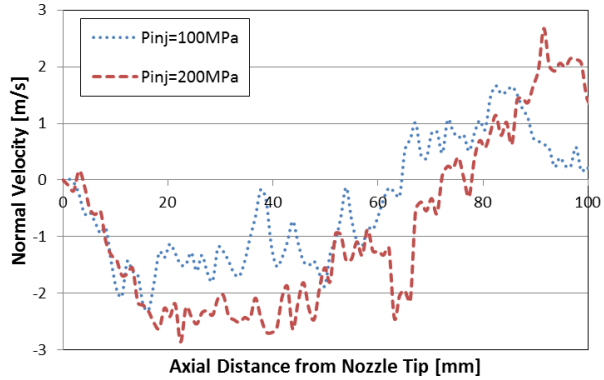

(e) ρ_a=20kg/m^3, d=0.12mm

Figure 3.6 Spatial Distribution of Normal Velocity along Control Surface (2.2ms ASOI)

3.2.2 Evaporating Condition

The evolution of the Diesel fuel spray under high ambient gas temperature condition was firstly investigated using the high speed video camera. The Mie scattering image of the liquid phase illuminated by the external Xenon lamp light source was used to determine the liquid length. It needs emphasize that the measured liquid length may defer a lot according to the different optical measuring methods. The diluted liquid droplets still exist downstream which may not be detected due to the limitation of the sensitivity of the optical system. In this study, a threshold value of 10% of the maximum intensity in an 8- bit dynamic range (0 to 255 grayscale range of images) of the camera was selected for determining the liquid phase boundary. Figure 3.7 shows the examples of the liquid phase images under the different conditions at the timing of 1.5ms ASOI. Generally, the liquid length decreases dramatically with the increase of the ambient gas

density and the decrease of the nozzle hole size, on the other hand, the fuel injection pressure has minor effect on the liquid length.

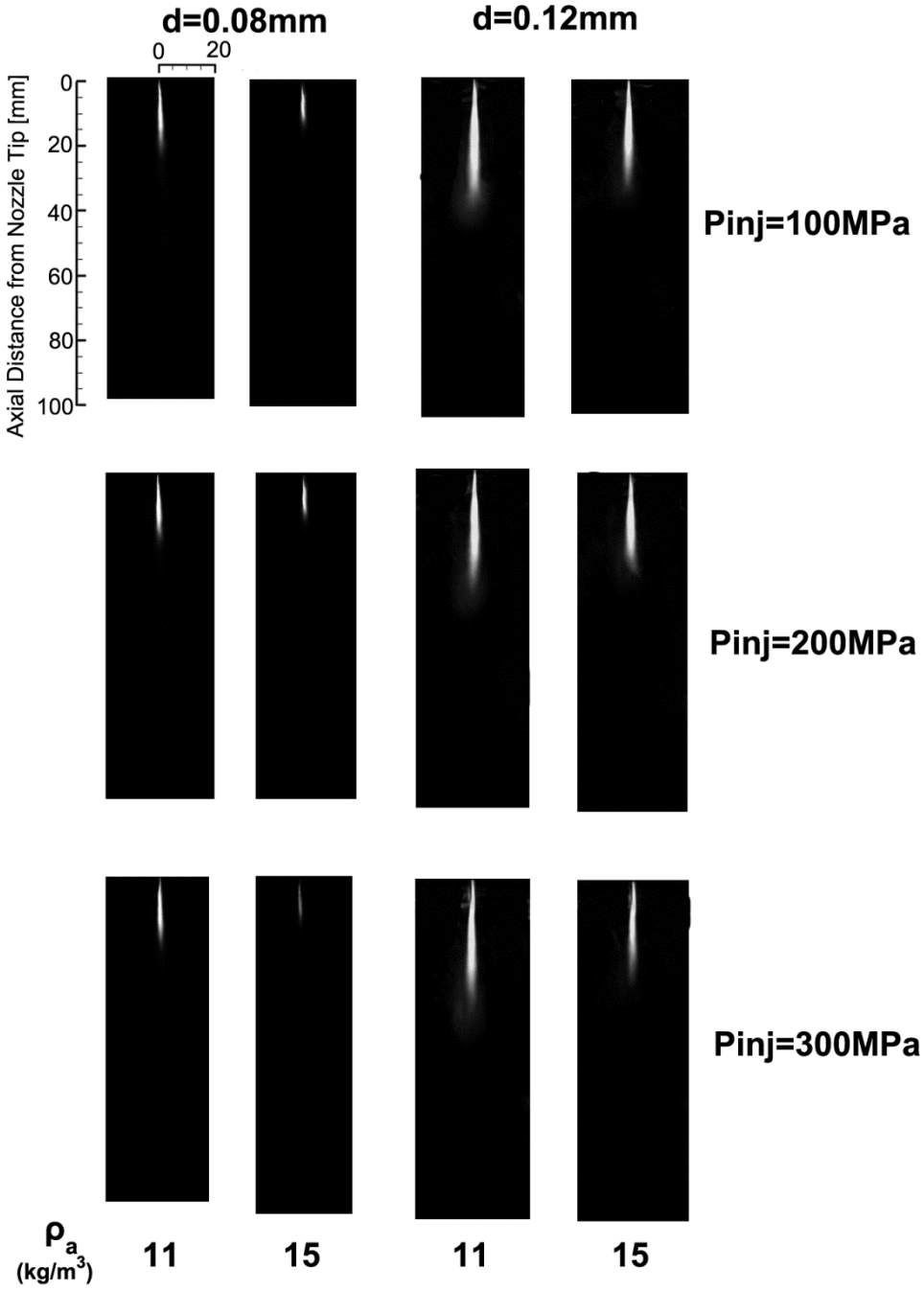

Figure 3.7 Mie Scattering Light Images of Liquid Phase (1.5ms ASOI)

Figure 3.8 shows the temporal variation of the liquid length under the different conditions. After 0.2ms ASOI, the liquid length reaches the peak value and keeps almost constant for all the

cases until the EOI. The liquid length reaches the steady state faster under the higher injection pressure. The position of the steady liquid phase is determined by the equilibrium of the total fuel evaporation rate in the spray and the fuel injection rate. The minor effect of fuel injection pressure on the liquid phase penetration is because the two opposing factors: the increased ambient gas entrainment and the increased injected fuel mass. Siebers et al. [1999] developed the mixing controlled vaporization law and concluded that the vaporization in a Diesel spray is controlled by mixing processes in the spray, as opposed to interphase transport rates of mass, momentum, and energy at droplet surfaces. Mixing processes refer to the entrainment of high temperature air into the spray and the overall transport and mixing of fuel and air throughout the spray cross-section.

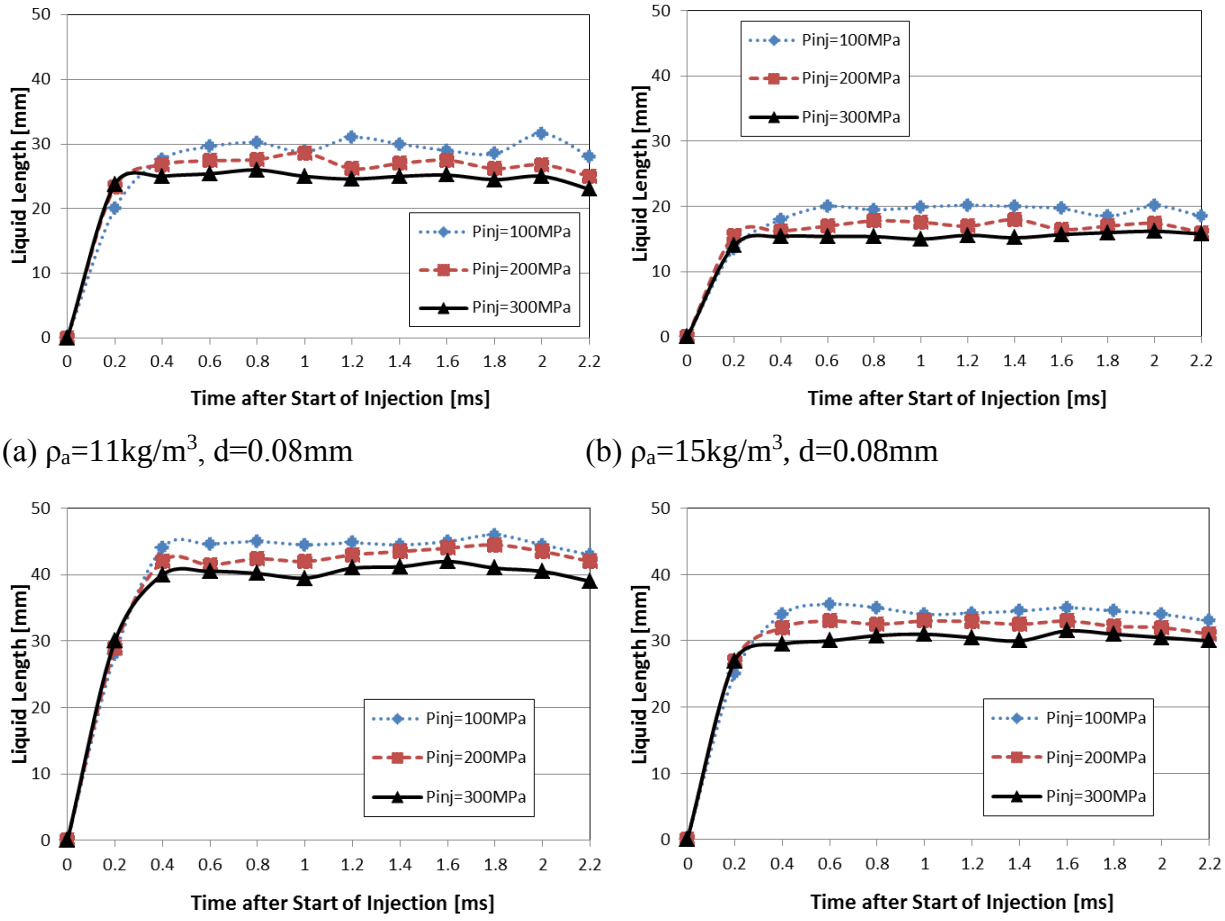

(a) ρ_a=11kg/m^3, d=0.08mm (b) ρ_a=15kg/m^3, d=0.08mm

(c) ρ_a=11kg/m^3, d=0.12mm (d) ρ_a=15kg/m^3, d=0.12mm

Figure 3.8 Temporal Variation of Liquid Length

Figure 3.9 shows the comparison of the spatial distribution of the ambient gas flow velocity at several timings after SOI in both (a) non-evaporating and (b) evaporating conditions

under the injection pressure of 100MPa, ambient gas density of 15kg/m^3 and the nozzle hole diameter of 0.08mm. Rather than the diluted spray droplets interact with the ambient gas in the non-evaporating condition, the liquid core region keeps almost constant after reaching the quasi-steady state in the evaporating condition, the vapor phase downstream pushes the ambient gas out.

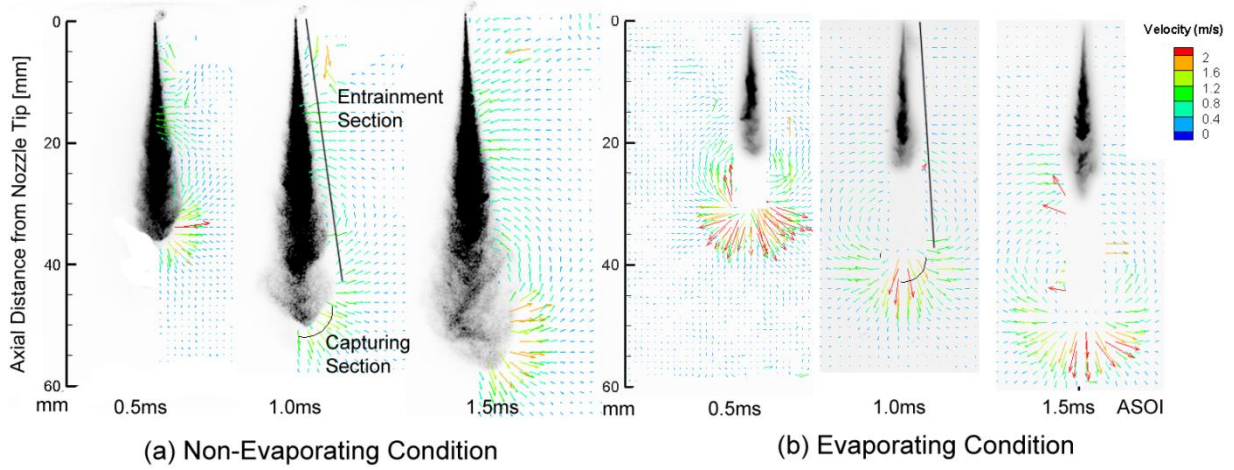

Figure 3.9 Spatial Distribution of Ambient Gas Flow Velocity

(Pinj=100MPa, ρa=15kg/m3, d=0.08mm)

Figure 3.10 shows the comparison of the normal velocity distribution at the entrainment section. It is worth emphasizing that the gas flow analysis for the evaporating spray starts from a certain distance away from the spray periphery, correspondingly, the control surface for the non-evaporating spray is also drawn with the same distance. Because of the square profile of the fuel injection rate, the maximum gas velocity keeps constant after reaching the quasi-steady state, while the entrainment section length increases with the time. The gas velocity for the non-evaporating case shows a slight larger value than that of the evaporating case. In contrast, Rhim et al. [2002] argued that the normal velocity for the evaporating case might increase by 0.5m/s due to the enhanced temperature gradient from the outside to the evaporating liquid region and the enhanced gas viscosity. On the other hand, the factors such as the reduced aerodynamic force on the spray/gas interface due to the relatively lower spray flow velocity, and the outward expansion of vapor phase tend to decrease the entrained gas flow velocity.

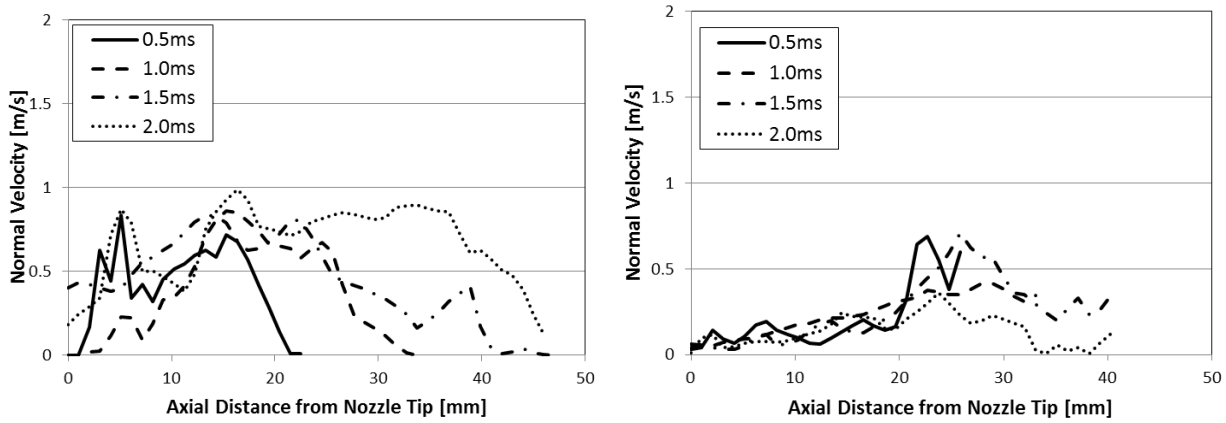

(a) Non-Evaporating Condition (b) Evaporating Condition

Figure 3.10 Comparison of Normal Velocity Distribution at Entrainment Section

The dominant factor lies in the tip region. Assuming that the spray tip region is a regular half sphere, the distribution of the axial component of the pushed out gas flow velocity along the quarter circle (90 deg. stands for the spray tip) at the capturing section is shown in Fig.3.11. The location along the nozzle axis where the maximum velocity appears is assumed to be spray boundary because the gas flow decelerates gradually when going out of the spray boundary. For comparison, the spray tip penetrating velocity at each timing is also denoted in the figure. A considerable increase of the pushed out gas velocity can be found in the evaporating case, in contrast, the spray penetrating velocity for the evaporating case decreases due to the faster momentum loss of the vapour phase. The increased gas flow velocity is attributed to the partial pressure taken by the fuel vapour, which restricts the amount of gas inside the spray plume, if the ambient density keeps the same. In the non-evaporating case, the whole spray volume consists of the ambient gas because the fuel vaporization is negligible. As an extreme condition, the much smaller velocity difference between the jet displacement and the ambient gas can be observed in the pure gas jet condition [Bruneaux et al., 2011]. The local fuel vapor/gas pressure is considered to determine the amount the ambient gas flow.

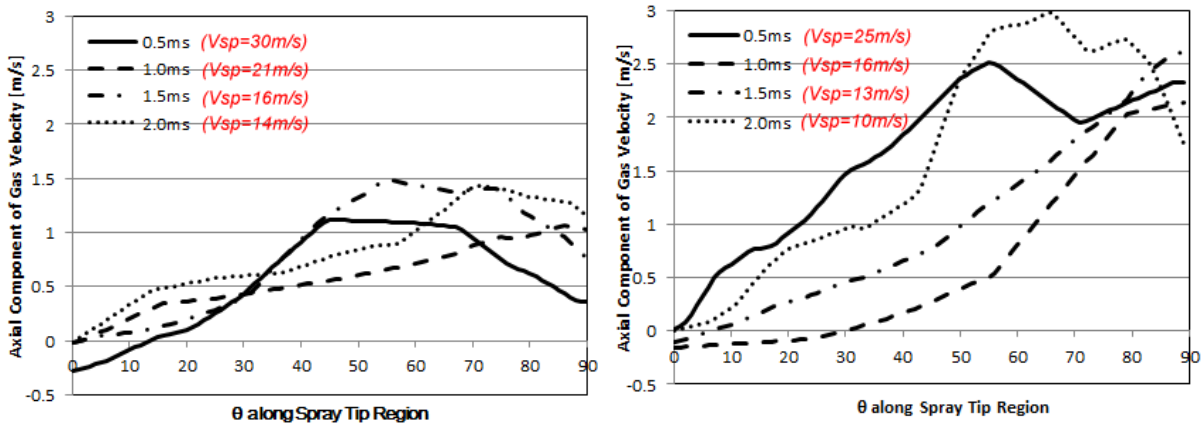

(a) Non-Evaporating Condition (b) Evaporating Condition

Figure 3.11 Comparison of Axial Velocity Component Distribution at Capturing Section

3.3 ANALYSIS OF AMBIENT GAS MASS FLOW RATE

3.3.1 Non-Evaporating Conditions

3.3.1.1 Model of Calculating Ambient Gas Mass Flow Rate

In order to analyze the gas mass flow rate around the side periphery and the tip periphery, a calculating model is introduced as shown in Fig.3.12. The mass flow rate calculation is based on the following assumption: (1) The spray plume is axisymmetric; (2) In the recirculation section downstream of the entrainment section, the ambient gas moves with the spray droplets under the same velocity. Koo et al. [1990] also found that the velocity of spray droplets decreases significantly along the radial coordinate. According to the laser illuminated spray image, the radial expanding speed of the width of the recirculation section (defined by the position where the upward gas velocity vector parallel to the nozzle axis locates) ranges from 2 to 4m/s since the main momentum propagation is in the axial direction, which also supports the assumption that the velocity of ambient gas and spray droplets are in the same order of magnitude. (3) The spray tip periphery is a half sphere whose radius is determined by the position where the spray periphery crosses the gas flow velocity vector perpendicular to the nozzle axis. The coordinate of spray periphery was obtained by averaging the images of several spray shots. The difference in distance between the ideal half sphere and the real irregular tip periphery is not greater than 3mm and the difference of the measured ambient gas velocity in this region is less than 0.4m/s. Therefore the assumption of the ideal half sphere is acceptable. The velocity vector along the

side periphery is subdivided into two components, the normal velocity $V_n(x, \alpha)$ which is perpendicular to the control surface and the tangential velocity which is parallel to the control surface. The normal velocity is used to quantify the gas mass flow rate through the side periphery. The control surface was drawn according to the spray spreading angle at different timings.

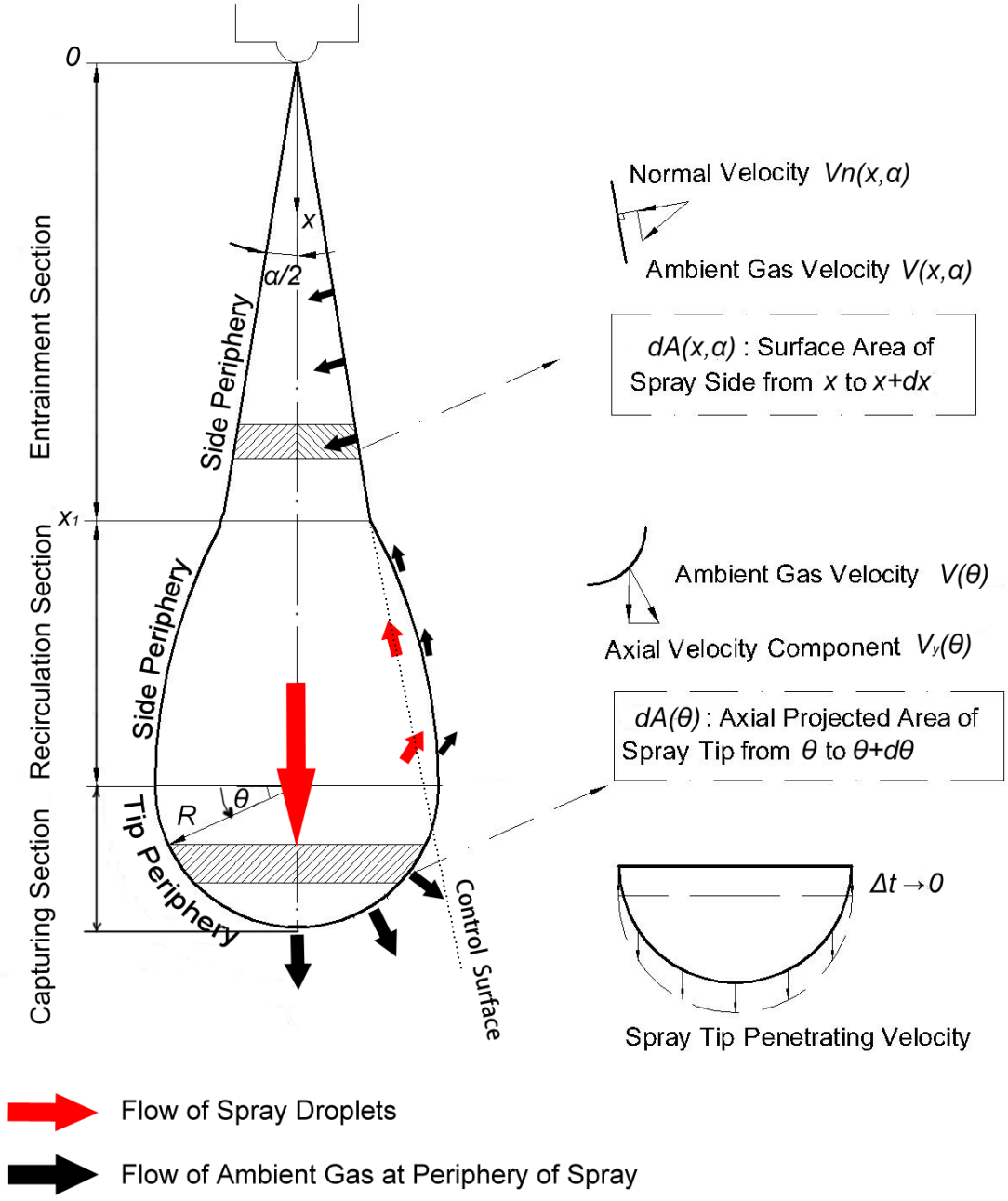

Figure 3.12 Definition of Velocity Components, Sections around Free Spray Periphery

Equations (3.1)-(3.3) show the process of calculating the gas mass flow rate entrained through the side periphery and captured by the spray tip periphery. The total gas mass flow rate was obtained by integrating the local gas mass flow rate with a series of discrete segments. The interval of each segment is 1mm at the side periphery and 1 degree at the spray tip. The calculation of gas mass flow rate at the entrainment section ($\dot{\mathrm{M}}\mathrm{a}_{\mathrm{ent}}$) focused only on the entrainment section while the recirculation section was in balance state—no gain or loss of ambient gas flow. The captured gas mass flow rate at the tip periphery ($\dot{\mathrm{M}}\mathrm{a}_{\mathrm{cap}}$) was obtained by subtracting ambient gas mass flow rate pushed out of the tip periphery ($\dot{\mathrm{M}}\mathrm{at}_{\mathrm{pushing}}$) from the ideal gas mass flow rate due to the spray penetration ($\dot{\mathrm{M}}\mathrm{at}_{\mathrm{penetrating}}$). Within a short time interval Δt_{shot}, the spray tip periphery was assumed to penetrate downwards without radial expansion, thus the spray volume change equals $\mathrm{V_{sp}}\,\pi\,\mathrm{R}^2$. The spray penetrating velocity $\mathrm{V_{sp}}$ was obtained by calculating the temporal change of the power fitting curve of the spray tip penetration length according to the spray images. The position along the nozzle axis in which the light intensity is less than 10% of the maximum value was defined as the spray tip. Correspondingly, $\dot{\mathrm{M}}\mathrm{at}_{\mathrm{pushing}}$refers to the integral of the local gas mass flow rate at different θ position based on the axial component of gas velocity $\mathrm{V_y}(\theta)$ and axial projected area of tip periphery $\mathrm{A}(\theta)$. The sum of the mass flow rate at the side periphery ($\dot{\mathrm{M}}\mathrm{a}_{\mathrm{ent}}$) and mass flow rate at the tip periphery ($\dot{\mathrm{M}}\mathrm{a}_{\mathrm{cap}}$) was considered to be the total gas mass flow rate through the whole periphery of the spray ($\dot{\mathrm{M}}\mathrm{a}$). The detailed definition of the variables is listed in the nomenclatures section.

Entrainment Section at Spray Side Periphery:

$$\dot{M}a_{ent} = \int_0^{X_1} \rho_a \; V_n(x,\alpha)\; dA(x,\alpha)\; dx \tag{3.1}$$

Capturing Section at Spray Tip Periphery:

$$\dot{M}a_{cap} = \dot{M}at_{penetrating} - \dot{M}at_{pushing} = \rho_a\, V_{sp}\, \pi\, R^2 - \int_0^{\theta_1} \rho_a\, V_y(\theta)\; dA(\theta)\; d\theta \tag{3.2}$$

At the Whole Spray Periphery:

$$\dot{M}a = \dot{M}a_{ent} + \dot{M}a_{cap} \tag{3.3}$$

3.3.1.2 Results of Ambient Gas Mass Flow Rate

Figure 3.13 shows the results of ambient gas mass flow rate into the spray entrainment section $\dot{\mathrm{M}}\mathrm{a}_{\mathrm{ent}}$ and the capturing section $\dot{\mathrm{M}}\mathrm{a}_{\mathrm{cap}}$ under the condition with the injection pressure from 100MPa to 300MPa, the ambient gas density of 11, 15, 20 kg/m^3 and nozzle hole size of 0.08mm and 0.12mm. The green dots show the ratio of instantaneous ambient gas and fuel mass flow rate ($\dot{M}_a/\dot{M}_f$). The instantaneous fuel mass flow rate $\dot{M}_f$ was obtained from the results of injection rate measurement. Due to the injection ends at 2.2ms, there is no $\dot{M}_a/\dot{M}_f$ value at the timing of 2.5ms ASOI.

A high portion of the gas mass flow rate into the spray is from the spray tip periphery. In the early stage of injection, for example under the ambient gas density of 15 kg/m^3 and nozzle hole size of 0.08mm, at the timing of 0.5ms ASOI, the proportion of gas mass flow rate at the side periphery account for 8%, 7.5% and 7% of the total value $\dot{M}_a$ under the injection pressure of 100MPa, 200MPa and 300MPa, respectively, because the entrainment motion at the side surface is not yet developed and the entrainment section length is short. With the gradual development of the spray-ambient gas momentum interaction, this ratio rises to 16%, 18% and 24% at the EOI timing under the injection pressure of 100MPa, 200MPa and 300MPa, respectively. In contrast, Cho et al. [1990] measured the ambient gas flow rate of the Diesel spray with much lower injection pressure (20~40MPa). Their conclusion was that almost 50% of the ambient gas mass flow was taken in from the side periphery. The spray with the increasing fuel injection pressure tends to capture more ambient gas through the tip periphery due to the larger velocity difference of the spray droplets and the ambient gas. As reported by Han et al. [2001], under the combustion condition, the proportion of gas entrainment at side periphery tends to be larger owing to the heat release at the tip periphery restricts the gas entrainment. The gas mass flow rate continues increasing even after the end of injection, this can be attributed to the spray plume with sufficient momentum developing downwards along the nozzle axis.

The total ambient gas mass flow rate $\dot{M}_a$ increases with the injection pressure significantly since the improved momentum interaction between the fuel spray and the ambient gas at the side periphery and the larger velocity difference at the tip periphery. However, the increase in instantaneous ratio of gas and fuel mass flow rate ($\dot{M}_a/\dot{M}_f$) becomes moderate when the injection pressure shifts from 200MPa to 300MPa. According to the Bernoulli equation, the fuel jet velocity from the nozzle orifice follows a square root function of the difference between

the fuel pressure inside the nozzle sac and the pressure of ambient gas. Moreover, higher injection pressure results in lower area contraction coefficient of nozzle and higher possibility of the cavitation flow inside the nozzle hole [Payri et al. 2004]. As a result, the increase in spray tip penetration becomes moderate in higher injection pressure, which suppresses the increase in gas mass flow rate captured by the spray penetration. Several studies [Zhu et al., 2011; Okude et al., 2004] reported the similar phenomena that the positive effect of ultra-high injection pressure on promoting fuel and air mixing process is gradually weaken after the pressure reaches a certain point. However, the effect of ultra-high injection pressure is still apparent in the reacting spray condition, because the air entrainment at the side periphery becomes more prominent under the evaporating condition, the higher injection pressure enhances the momentum transfer at the side periphery. The small scale turbulent mixing particularly in the head vortex region is improved with the rise of injection pressure, which leads to a lower soot level [Minato et al., 2005].

Figure 3.14 shows the ambient gas mass flow rate into the entrainment section $\dot{\mathrm{M}}\mathrm{a}_{\mathrm{ent}}$ and the gas mass flow rate through the whole spray periphery $\dot{M}_a$ as a function of injection pressure and gas density using the nozzle hole size of 0.08mm. It is clear that the higher ambient gas density leads to the larger ambient gas mass flow rate, which demonstrate that the gas density value is the key factor to determine the ambient mass flow rate even though the similar gas flow velocity and decreased spray periphery length in the high gas density condition. Considering the fuel injection rate is the same, the ratio of instantaneous gas and fuel mass flow rate increases apparently in the higher ambient gas density condition. The increasing drag force on the spray periphery enhances the ambient gas flow, which promotes the liquid phase disintegration into small droplets. It is also supposed that the fuel and air mixing process inside the spray plume is improved in the high ambient gas density condition. However the increase in $\dot{\mathrm{M}}\mathrm{a}_{\mathrm{ent}}$ becomes moderate in the high ambient gas density condition, which results from the influence of the decreased entrainment section length.

Figure 3.13 also shows the ambient gas mass flow rate and the ratio of instantaneous ambient gas and fuel mass flow rate ($\dot{M}_a/\dot{M}_f$) of the 0.12mm nozzle hole under 100MPa injection pressure. Comparing with the result of 0.08mm nozzle, the gas mass flow rates in both the entrainment section $\dot{\mathrm{M}}\mathrm{a}_{\mathrm{ent}}$ and the capturing section $\dot{\mathrm{M}}\mathrm{a}_{\mathrm{cap}}$ significantly increase. On the other hand, the ratio of instantaneous ambient gas and fuel mass flow rate decreases inversely due to the increase in fuel injection rate. This implies that the spray atomization deteriorates in

the larger nozzle hole size case. What's more, the dependency of the ratio of the ambient gas and fuel mass flow rate on the ambient gas density becomes insensitive under the larger nozzle hole size condition.

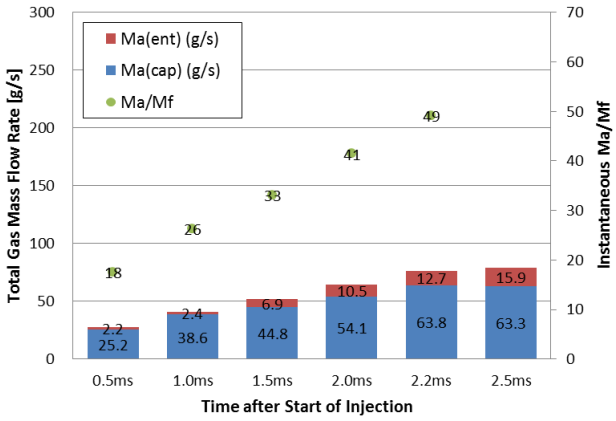

(a) P_{inj}=100MPa, ρ_a=11kg/m^3, d=0.08mm

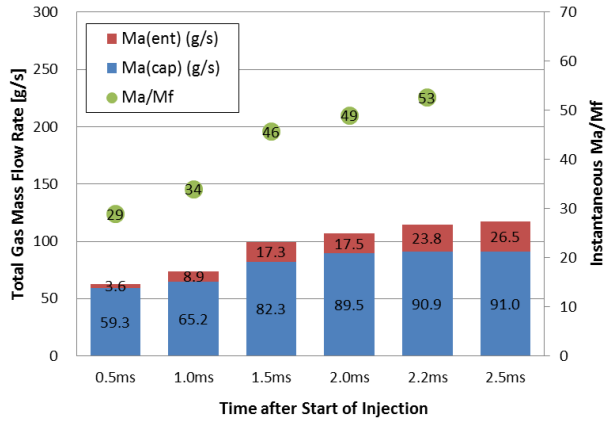

(b) P_{inj}=200MPa, ρ_a=11kg/m^3, d=0.08mm

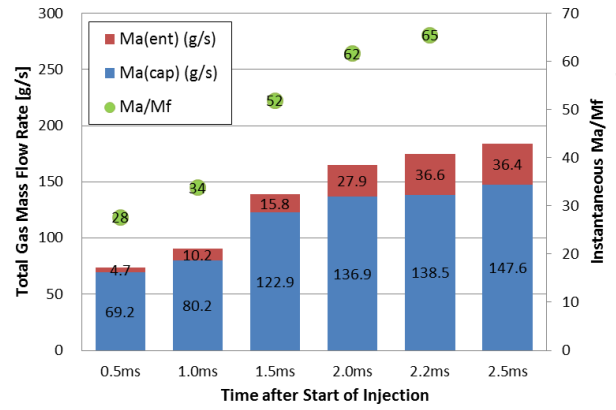

(c) P_{inj}=300MPa, ρ_a=11kg/m^3, d=0.08mm

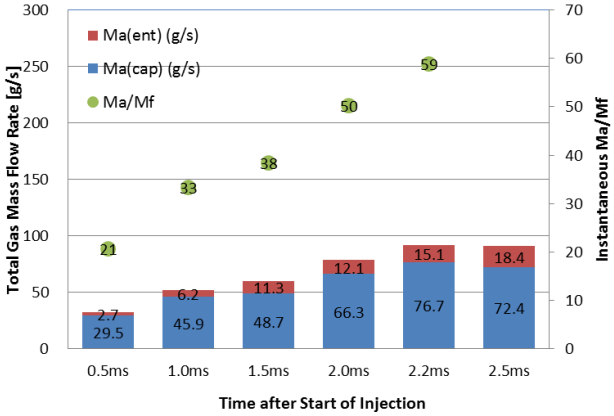

(d) P_{inj}=100MPa, ρ_a=15kg/m^3, d=0.08mm

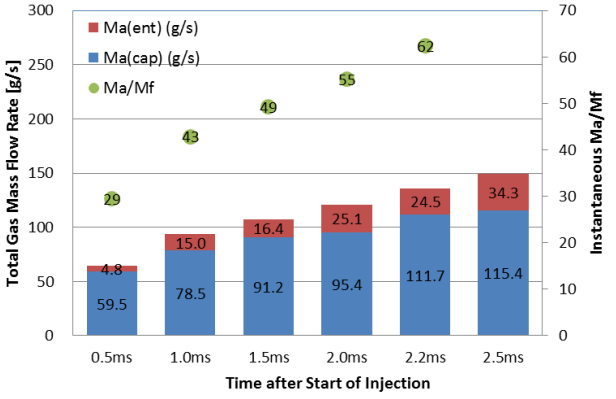

(e) P_{inj}=200MPa, ρ_a=15kg/m^3, d=0.08mm

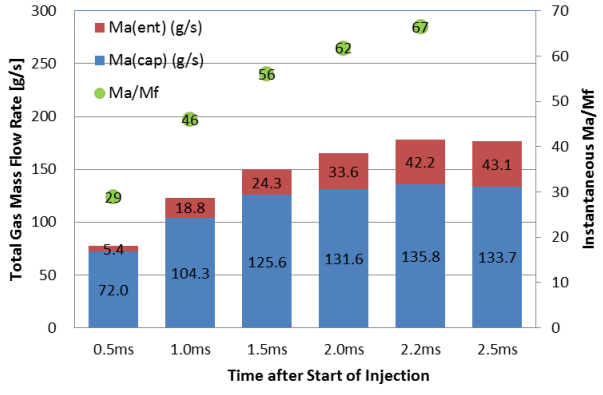

(f) P_{inj}=300MPa, ρ_a=15kg/m^3, d=0.08mm

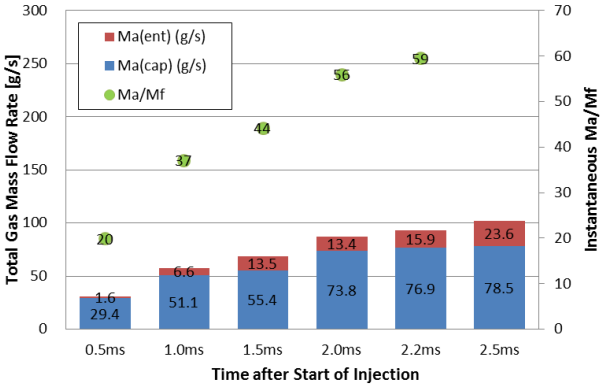

(g) P_{inj}=100MPa, ρ_a=20kg/m^3, d=0.08mm

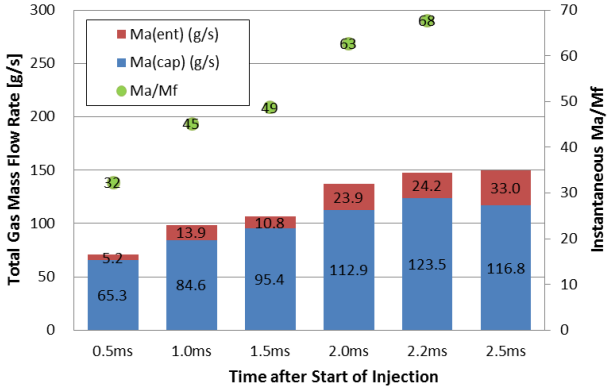

(h) P_{inj}=200MPa, ρ_a=20kg/m^3, d=0.08mm

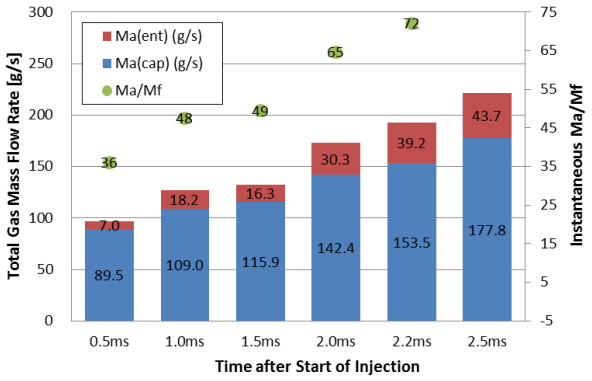

(i) P_{inj}=300MPa, ρ_a=20kg/m^3, d=0.08mm

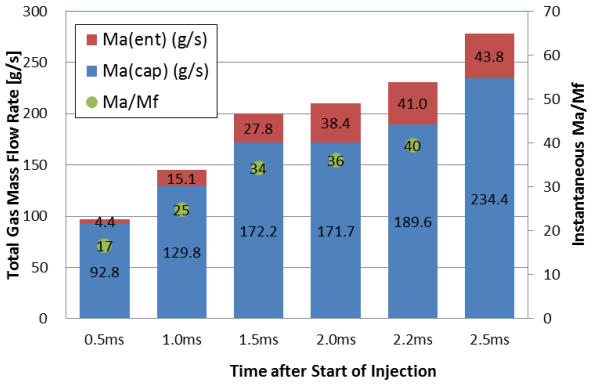

(j) P_{inj}=100MPa, ρ_a=15kg/m^3, d=0.12mm

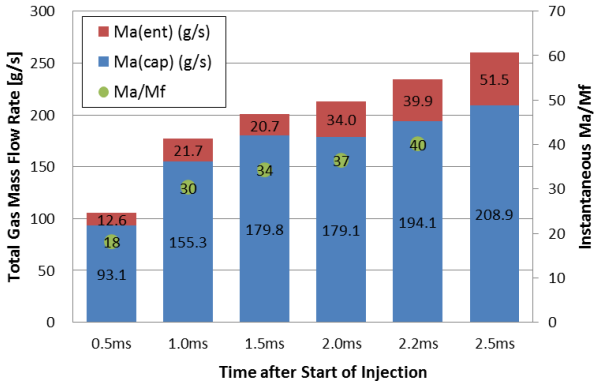

(k) P_{inj}=100MPa, ρ_a=20kg/m^3, d=0.12mm

Figure 3.13 Temporal Variation of Ambient Gas Mass Flow Rate

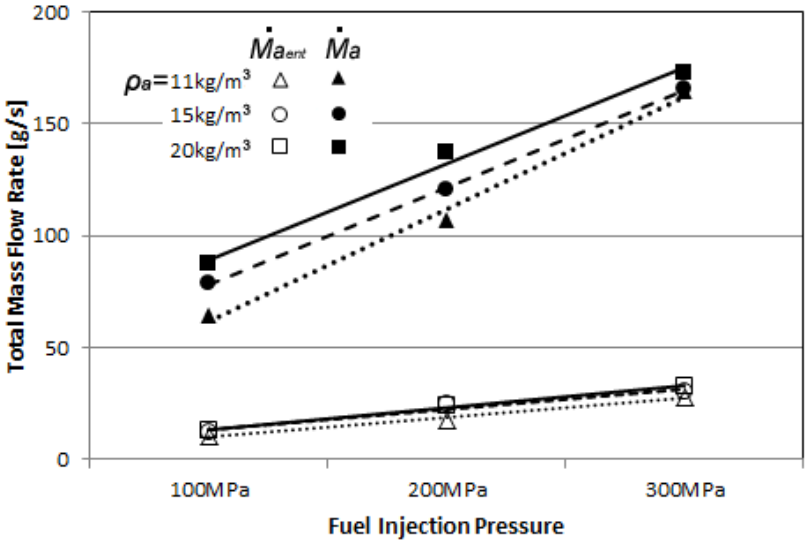

Figure 3.14 Ambient Gas Mass Flow Rate as a Function of Injection Pressure and Ambient Gas Density (d=0.08mm, 2.2ms ASOI)

3.3.1.3 Comparison with Predictive Model

The results of ambient gas mass flow rate measured by LIF-PIV technique using the nozzle hole size of 0.08mm under the ambient gas density of 15kg/m^3 were compared with the model for calculating the instantaneous equivalence ratio proposed by Wakuri et al. [1957] (Details can be found in Chapter 1). The equation of this model is shown as follows:

$$\emptyset_{inst} = \frac{L_{th}\sqrt{C_a}}{2\tan(\alpha/2)}\sqrt{\frac{\rho_l}{\rho_a}}\frac{D}{x} \tag{3.4}$$

where x is the distance of a certain cross section from the nozzle tip in the original model, here the spray tip penetration S was used to investigate the equivalence ratio of the whole spray body. The comparison of the instantaneous equivalence ratio $\emptyset_{inst}$ and the mean equivalence ratio $\emptyset_{mean}$ of the whole spray are taken into account in Figs.3.15 and 3.16, respectively. The instantaneous equivalence ratio was calculated from the instantaneous ambient gas and fuel mass flow rate by LIF-PIV results in Fig.3.15 (a) and from the predictive model suggested by Wakuri et al. [1957] in Fig.3.15 (b). The mean equivalence ratio $\emptyset_{mean}$ was calculated according to the temporal integration of instantaneous ambient gas flow rate by LIF-PIV result in Fig.3.16 (a) and the spray volume in Fig.3.16 (b).

For all the cases, the equivalence ratio decreases with the spray development, the high injection pressure has the potential to achieve the lean mixture more rapidly. The instantaneous equivalence ratio result from Wakuri's model shows the similar trend however a bit higher value compared with that from the PIV result. Two of the main assumptions regarding the deduction of Wakuri's model are: (1) In any cross section downstream of nozzle tip, the ambient gas and spray droplets flow together without relative velocity; (2) the initial momentum of the spray droplets transfers to the fuel and gas mixture downstream. The first assumption implies that all the gas inside the spray results from the entrainment at the side periphery, which differs from the actual spray behavior according to the PIV measurement in this study. Some other study [Naber et al., 1996] also argued that this assumption may be doubtful but stands for approximate prediction for the steady spray. Regarding the second assumption, some part of momentum of the droplets is also transferred to the ambient air outside the spray which causes the entrainment and pushed-out motion. As a conclusion, the predictive model tends to underestimate the ambient gas flow rate through the whole spray periphery. The mean equivalence ratio results in Figs.3.16 (a) and 3.16 (b) are in good agreement in both the results from the PIV measurement and the spray volume. The difference at the early stage of injection duration is supposed to result from the underestimation of the entrained gas mass in the entrainment section due to the inertia of the tracer particles. The accuracy can be improved by using smaller tracer particles with higher tracking ability and increasing the number of measurements. Generally, the calculation method proposed in this study was proved to have the ability to characterize the ambient gas flow into the spray accurately.

According to the spray tip penetration equation proposed by Hiroyasu and Arai [1990] shown as follows:

$$S = 2.95 \left(\frac{P_{inj} - P_a}{\rho_a}\right)^{0.25} (D\ t)^{0.5} \qquad t > t_{break} \tag{3.5}$$

The effect of injection pressure, ambient gas density and nozzle hole size on the instantaneous equivalence ratio can be summarized as follows (Provided C_a and θ keep constant):

$Injection\ Pressure: \emptyset_{inst} \propto (\Delta P)^{-0.25}$

$Ambient\ Gas\ Density: \emptyset_{inst} \propto (\rho_a)^{-0.25}$

$Nozzle\ Hole\ Diameter: \emptyset_{inst} \propto (D)^{0.5}$

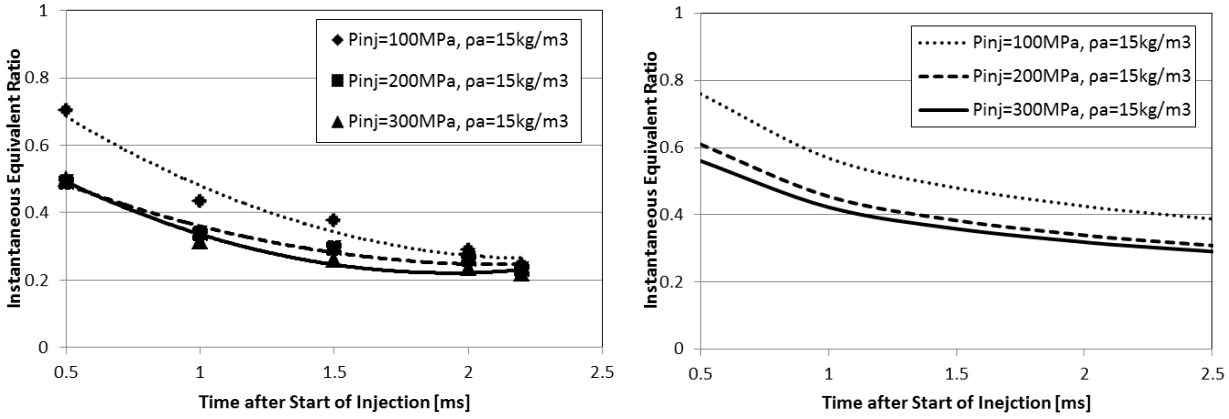

(a) from LIF-PIV Results (b) from Predictive Model

Figure 3.15 Comparison of Instantaneous Equivalence Ratio (d=0.08mm)

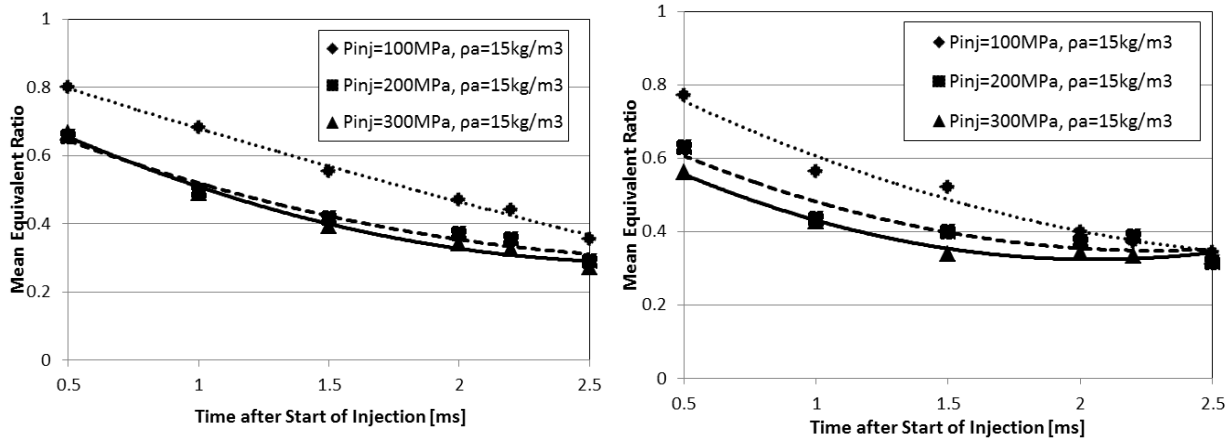

(a) from LIF-PIV Results (b) from Spray Volume

Figure 3.16 Comparison of Mean Equivalence Ratio (d=0.08mm)

The gas mass flow rate at series of cross sections with different distances from the nozzle tip can be obtained according to the above mentioned Wakuri theory. Because it is assumed that all the entrained gas comes from the side periphery, the local normal velocity along the side periphery can be calculated by dividing the difference of gas mass flow rate of the adjacent cross sections by the surface area of side periphery and the gas density. Equations (6) and (7) show the process:

$$\dot{M}a = \rho_a \, \pi \, d^2 \left[\frac{C_a \, V_0}{8} \left(\sqrt{\left(\frac{\rho_l}{\rho_a} - 1 \right)^2 + \frac{16 \, \rho_l}{C_a \, \rho_a} \left(\frac{x}{d} \right)^2 tan^2 \left(\frac{\alpha}{2} \right)} - \frac{\rho_l}{\rho_a} + 1 \right) - \frac{C_a}{4} V_0 \right] \qquad (3.6)$$

$$V_n(x,\alpha) = \frac{\dot{M}a(x+dx) - \dot{M}a(x)}{\rho_a \, dA(x,\alpha)} \tag{3.7}$$

V_0 is the initial fuel injection velocity at the orifice exit, which can be calculated according to the Bernoulli equation. The spray spreading angle α was obtained from the spray images. The interval of the adjacent sections was set to 1mm. Figure 3.17 shows the comparison of the normal velocity distributions from the Wakuri theory and the PIV measurement, respectively. In accordance with the definition in Fig.8, the entrained ambient gas velocity is marked positive, while the pushed-out gas velocity in the recirculation section is not shown here. The predictive result shows that the normal velocity starts with a much larger value from the nozzle tip due to the very small side area value, which conflicts with the break-up process of the actual spray. When go downstream to the quasi-steady state, both of the results are gradually consistent with each other. Because the Wakuri theory assumes a Diesel spray with extremely long injection duration, the pushed-out gas velocity downstream is not able to be predicted. Wakuri theory can properly reflect the gas entrainment feature if the spray reaches the quasi-steady state.

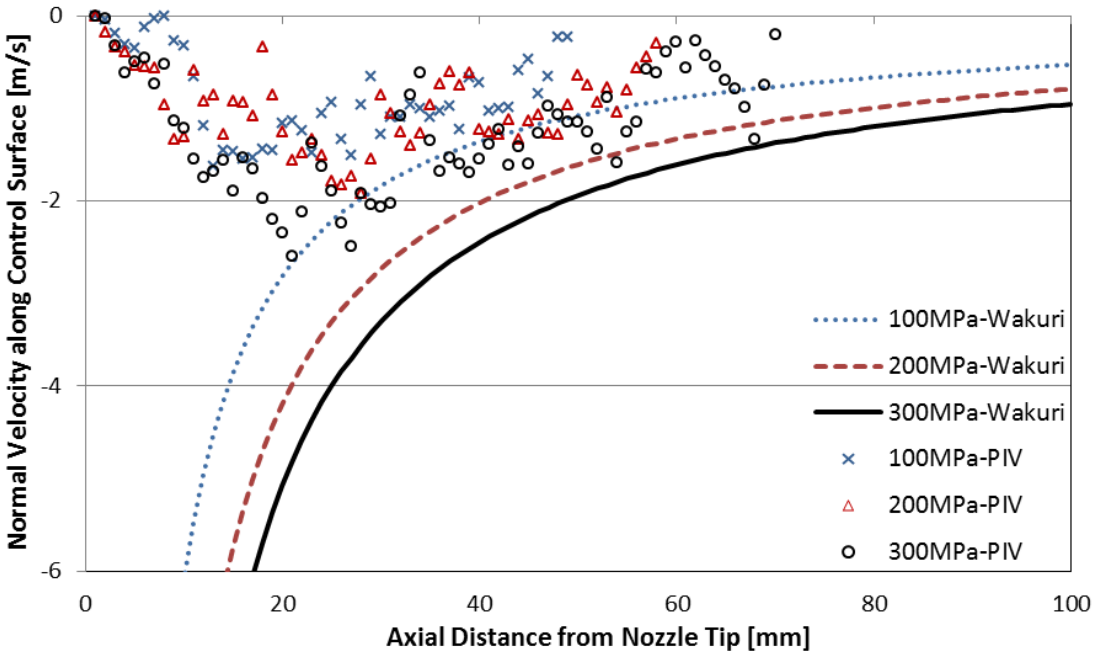

Figure 3.17 Comparison of Spatial Distribution of Normal Velocity along Control Surface (ρa=15kg/m3, d=0.08mm, 2.2ms ASOI)

3.3.2 Evaporating Condition

According to the calculating model proposed in Fig. 3.12, the total gas mass flow rate result under the injection pressure of 100MPa, ambient gas density of 15kg/m^3 and the nozzle hole diameter of 0.08mm is shown in Fig. 3.18. $\dot{M}a_{ent}$ indicates the gas flow at the entrainment section, while the $\dot{M}a_{cap}$ indicates that at the capturing section. The green dots show the instantaneous ratio of gas/fuel mass flow rate. In both the non-evaporating and evaporating cases, a large proportion of the ambient gas flow is attributed to that at the capturing section. However, because of the significant reduction of gas mass flow rate at the tip periphery, the proportion of the gas mass flow rate at the entrainment region in evaporating case rises to 10%-21%, compared with the 8%-18% in non-evaporating case, which implies that the gas flow along the side surface plays a more important role in the burning spray condition. The total ambient gas mass flow rate and the instantaneous $\dot{M}_a/\dot{M}_f$ for the evaporating case decrease remarkably especially in the later stage of the fuel injection duaration, since the vapor phase at the spray tip loses the momentum faster. Siebers et al. [2009] suggests that cooling effect of the ambient gas due to the spray vaporization at the tip region results in a relatively higher ambient gas density, which leads to the shorter spray penetration of the evaporating condition based on the conservation of the jet momentum. The total gas mass flow rate is also likely to be reduced by vaporization.

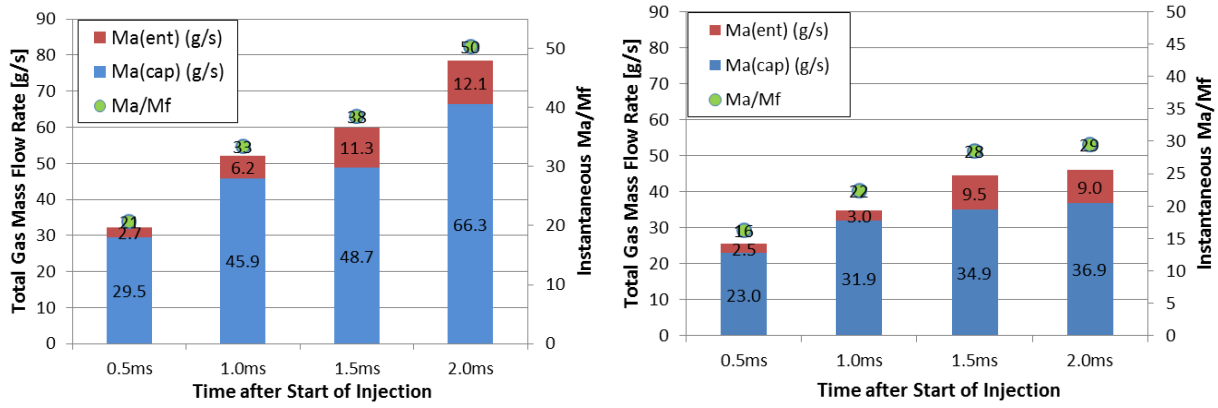

(a) Non-Evaporating Condition (b) Evaporating Condition

Figure 3.18 Comparison of Gas Mass Flow Rate Result

3.4 SUMMARY

The characteristics of the Diesel spray evolution and the spray induced ambient gas motion were measured quantitatively by using PIV, LIF-PIV and high speed video camera under both the

non-evaporating and the evaporating quiescent condition. The ambient gas velocity and mass flow rate into the spray through the whole spray periphery (spray side periphery and tip periphery) were investigated quantitatively.

Based on this study, the following can be concluded:

1. The effects of fuel injection pressure, ambient gas density and the nozzle hole size on the spray tip penetration and the liquid length are presented.
2. The LIF-PIV technique is capable of measuring the 2-dimensional gas flow field around the spray periphery with high resolution and eliminating the circumstance noise. The spray model proposed in the study divides the spray body into entrainment section, recirculation section and capturing section, which quantitatively describes the ambient gas flow field of a transient Diesel spray.
3. The ambient gas mass flow rate into the spray through the spray tip periphery is prominent in the whole periphery in non-evaporating spray condition and the proportion of the ambient gas entrainment along the side periphery increases as the spray developing.
4. Higher injection pressure improves the ambient gas mass flow rate into the spray, both at the spray side periphery due to the increased drag force and at the tip periphery due to the larger droplets/gas velocity difference. However the increase in total entrained gas-fuel ratio tends to be moderate when the injection pressure rises to the ultra-high level.
5. Higher ambient gas density suppresses the entrainment section length and the spray penetrating velocity, on the other hand, the ambient gas mass flow rate into the spray increases apparently. As a result, the equivalence ratio of the spray decreases under the higher ambient gas density condition.
6. The smaller nozzle hole size results in the significant decrease in the ambient gas mass flow rate into the spray, on the other hand, the ratio of the ambient gas and fuel mass flow rate increases.
7. The gas velocity along the side periphery for the non-evaporating case shows a slight larger value than that of the evaporating case. On the other hand, a considerable increase of the pushed out gas velocity at the tip periphery can be found in the evaporating case, in contrast, the spray tip penetration for the evaporating case decreases due to the faster momentum loss of the vapor phase.
8. A large amount of ambient gas flow mass is attributed to the flow at the tip region in both the

non-evaporating and the evaporating condition. The role of the gas flow along the side periphery becomes more important in evaporating spray condition. The total ambient gas mass flow rate for the evaporating case decrease remarkably.

CHAPTER 4 FLAT-WALL IMPINGING DIESEL SPRAY/AMBIENT GAS INTERACTION PROCESS

4.1 EXPERIMENTAL CONDITION

LIF-PIV technique was employed to measure ambient gas flow field of the non-evaporating wall impinging spray using the tracer droplets with Rhodamine B due to its fluorescent property. The basic selection of the parameters for LIF-PIV system is the same as what has been mentioned in Chapter 3 for the free Diesel spray. Table 4.1 shows the experiment conditions for the flat-wall impinging spray. Here one ambient gas density of 15 kg/m^3 and one nozzle hole size of 0.08mm were used. A flat stainless steel plate was placed beneath the nozzle tip with the distance of 30mm and 40mm which corresponds to the typical impingement distance from the nozzle tip to piston cavity wall in the heavy duty Diesel engines.

Table 4.1 Experiment Conditions for Flat-wall Impinging Spray

Nozzle Type	Single Hole Nozzle
Nozzle Diameter (mm)	0.08
Injection Pressure (MPa)	100, 200, 300
Injection Duration (ms)	2.2
Test Fuel	Diesel JIS #2
Ambient Gas	Nitrogen
Ambient Gas Density(kg/m^3)	15(300K, 1.4MPa)
Impingement Distance (mm)	30, 40

4.2 MEASUREMENT OF SPRAY INDUCED AMBIENT GAS FLOW FIELD

4.2.1 Spatial Distribution of Ambient Gas Flow

Figure 4.1 indicates the comparison of spatial distribution of ambient gas flow velocity under the fuel injection pressure of 100MPa at several specific timings after SOI in the case of free Diesel spray, the nozzle-wall distance of 30mm and 40mm, respectively. The ensemble averaged result from 5~6 samples with good repeatability was used in the analysis of the velocity filed to avoid the shot-by-shot variation. One typical spray image from these samples is selected as the background. It's presumed that the wall-impinging spray is axis-symmetric as the spray impinges

normally, thus half of the spray width is shown here. Generally, the region prior to the wall-impingement shows the similar tendency for both the free spray and impinging spray. The ambient gas is entrained into the spray plume due to the velocity difference induced pressure gradient. The spray periphery in this region is smooth, however, the length of the entrainment section is restrained under the impingement condition. After spray-wall impingement, a fraction of the spray droplets adhere to the wall and forms the liquid film, the left rebound or splash from the wall and enter the atmosphere again, the spray body moves towards the radial direction along the wall, the ambient gas ahead of the spray head is strongly pushed outside. It is evident that the pushed-out gas velocity for the impinging spray is larger than that for the free spray, the strong wall jet vortex forms at the spray head contributes to this result. Similar as the results of the free spray, a part of the pushed-out gas is recirculated to the upstream region, the strong turbulent mixing process can be found near downstream. The spray height enhances with the time.

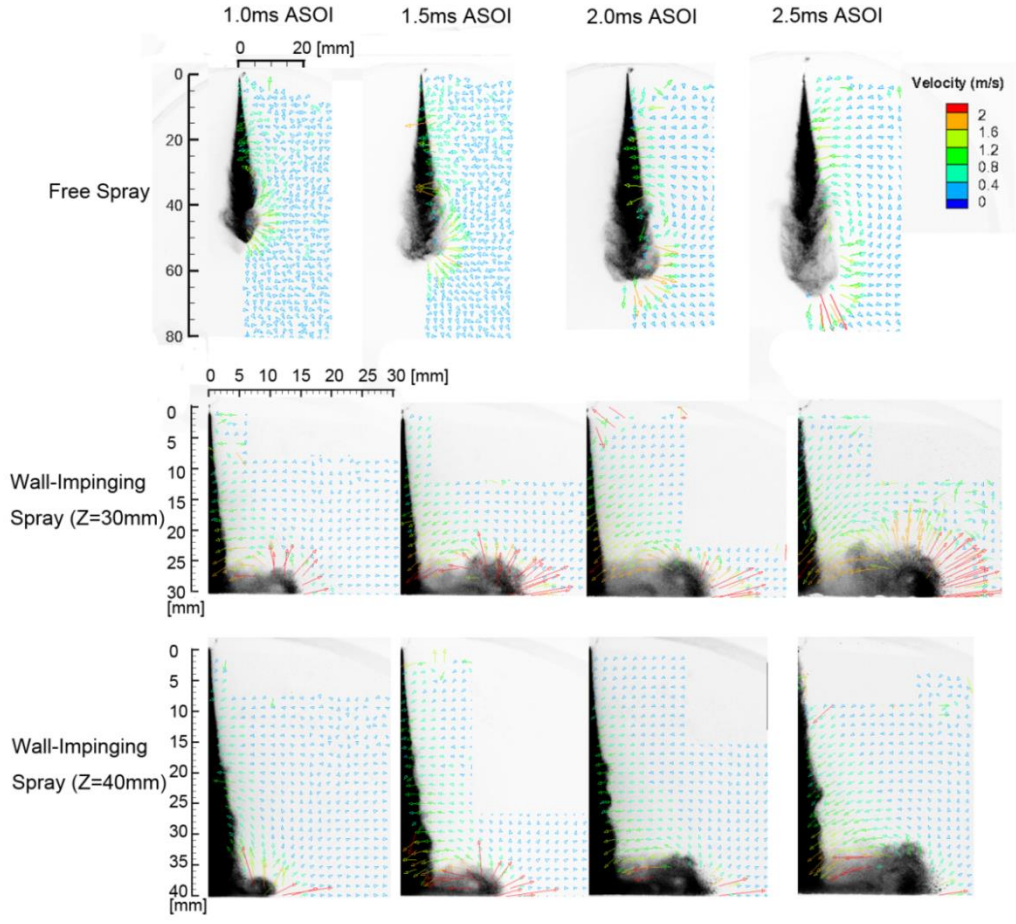

Figure 4.1 Comparison of Ambient Gas Flow Field of Free Spray and Wall-Impinging Spray (P_{inj}=100MPa, ρa=15kg/m^3, d=0.08mm)

Figure 4.2 shows the effect of fuel injection pressure on the evolution of the impinging spray with the impingement distance of 30mm and 40mm, respectively. Higher injection pressure extends the spray further along the radial direction and enhances the spray height, which implies that more spray droplets are splashed from the wall and move downstream with larger momentum. The pushed-out gas velocity at the spray head and the gas velocity as the recirculation region increase apparently with the increase of the injection pressure. It is predicted the wall-jet vortex intensity increases with the fuel injection pressure. Regarding the effect of wall impingement distance, the ambient gas flow is intensified with the decrease of the impingement distance, particularly in the post-impingement region.

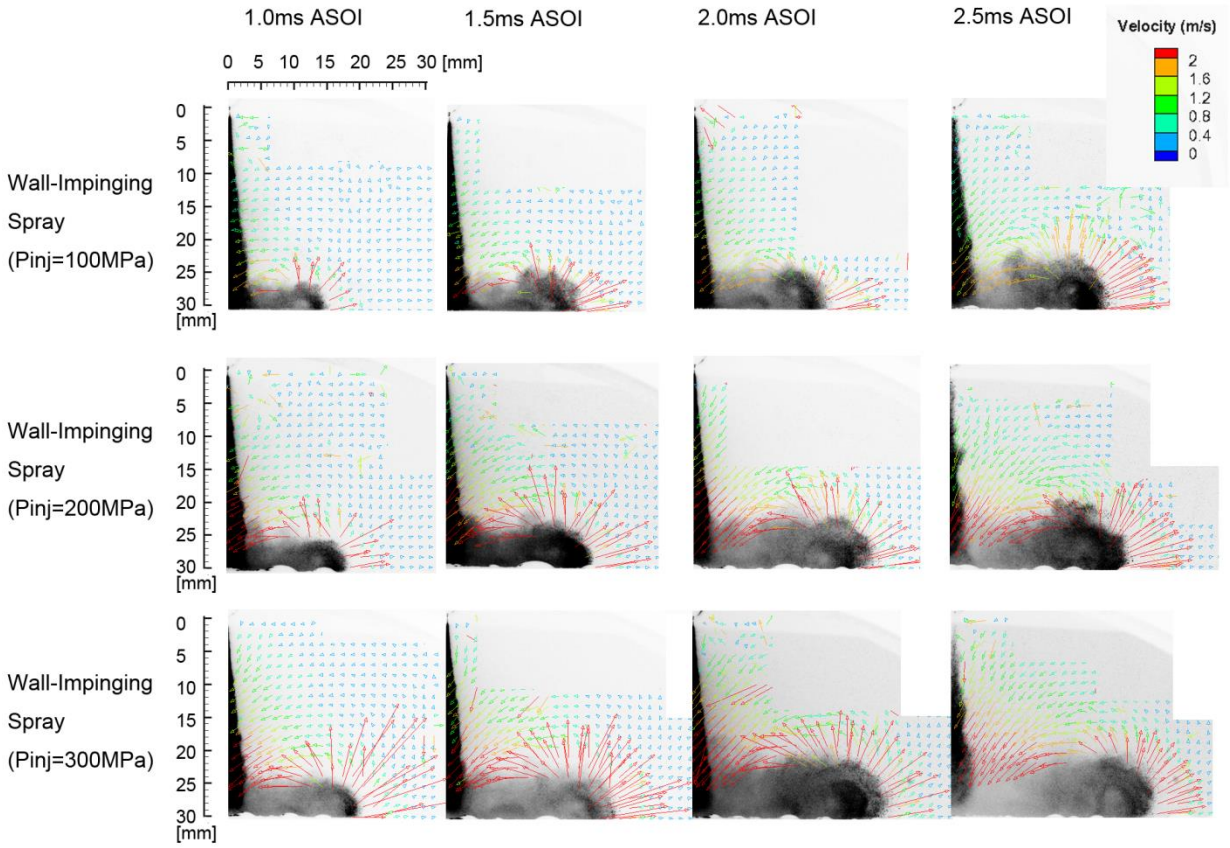

(a) Z=30mm

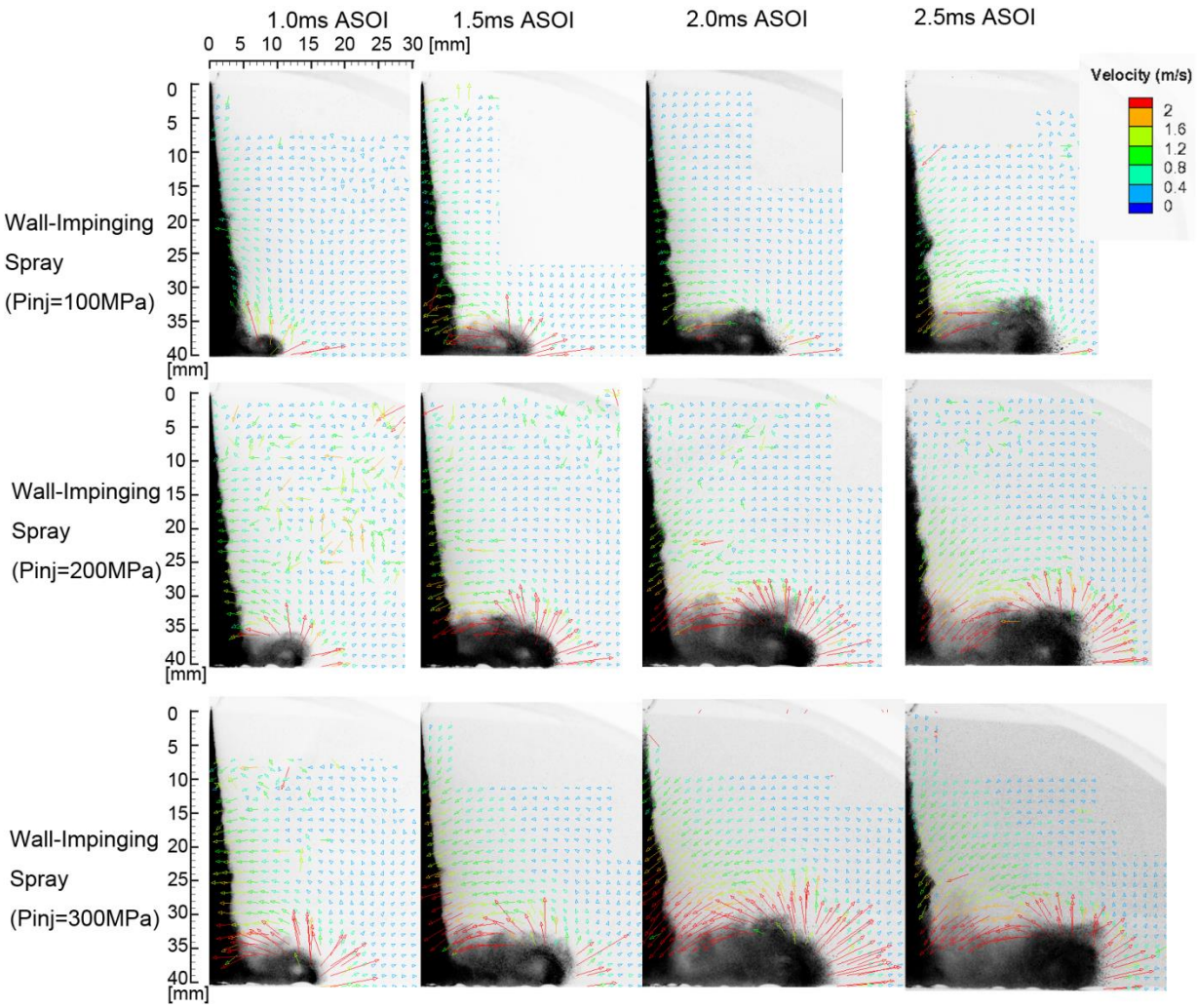

(b)=40mm

Figure 4.2 Effect of Fuel Injection Pressure on Wall-Impingement Spray (ρa=15kg/m3, d=0.08mm)

Figure 4.3 summarizes the comparison of spray tip penetration of the free spray and wall-impinging spray with different injection pressures. The spray tip penetration of the wall-impinging condition was defined as the summation of the impingement distance and the half of the radial spray length. The free spray shows the longest penetrating length, and the shorter the impinging distance is, the more the penetrating length is limited. The spray tip penetrating velocity obtained from the time rate of change of power fitted curve of the spray tip penetration will be used for the gas flow rate calculation subsequently. The spray tip penetrating velocity is apparently suppressed under the wall-impingement condition mainly due to the friction with the liquid film, which results in faster momentum loss.

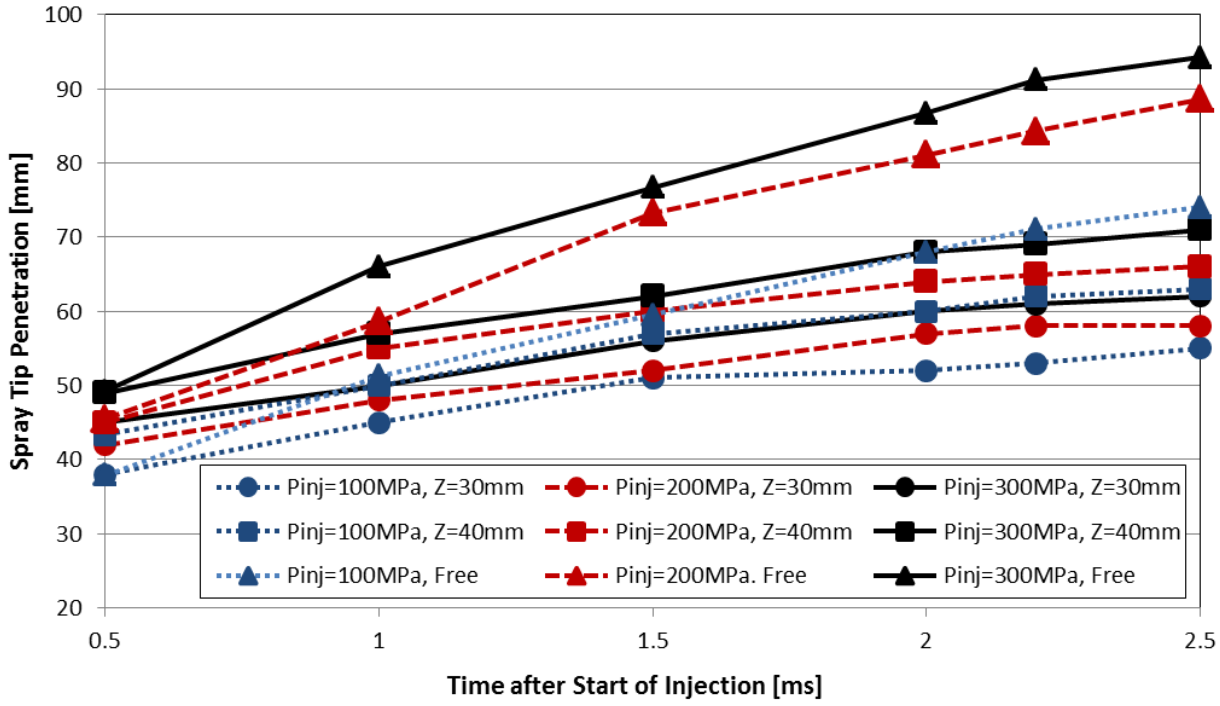

Figure 4.3 Comparison of Spray Tip Penetration of Free Spray and Wall-Impinging Spray

4.2.2 Ambient Gas Flow Velocity

In order to analyze the wall-impinging spray induced ambient gas flow quantitatively, a calculating model is proposed in Figure 4.4. The subsequent gas mass flow rate calculation is also carried out according to this model. The same as the model defined for the free spray, the spray periphery is divided into three sections. Firstly, the entrainment section is located in the free spray region. The entrained gas velocity is subdivided into two components, the normal velocity perpendicular to the side periphery and the tangential velocity. For the post-impingement spray region, the capturing section is located at the spray head, in which the ambient gas is pushed out and the gas velocity is subdivided into the radial component along the wall and axial component perpendicular to the wall. In order to neglect the shot-by-shot variation of the spray tip shape, a quarter circle is used to represents the spray tip for calculation, whose coordinate is determined by averaging several samples. The recirculation region is located between the impinging point and the capturing section, in which the ambient gas motion shifts to the upstream direction, especially the strong gas flow towards the impinging point can be observed. The boundary of the recirculation section and the capturing section is determined by the location where the gas velocity vector normal to the wall appears.

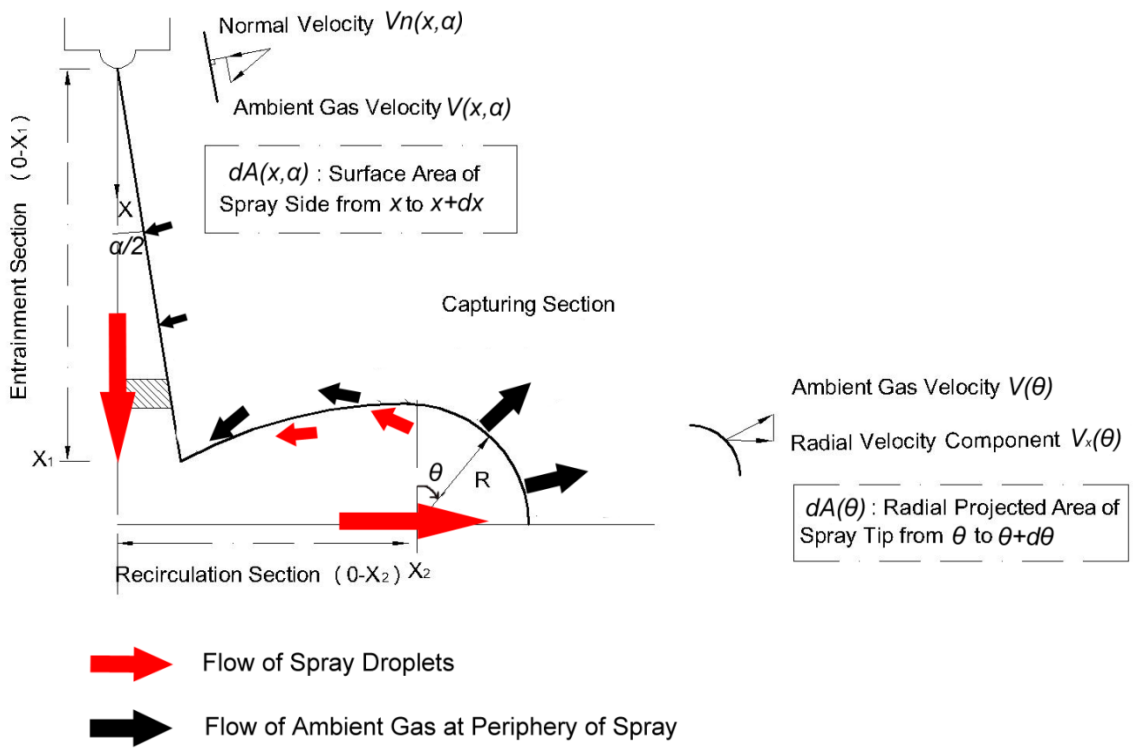

Figure 4.4 Definition of Velocity Components, Sections around Wall-impinging Spray Periphery

Figure 4.5 shows the comparison of the normal velocity along the side periphery of the free spray and the impinging spray with the impingement distance of 30mm and 40mm. The normal velocity near the nozzle tip region shows the similar results irrespective of the free spray and impinging spray. On the other hand, in the downstream of the free spray region particularly the position approaching to the impinging point, the normal velocity for the impinging spray increases abruptly. This tendency becomes more apparent with the reduction of the impingement distance and the increase of the injection pressure. The strong turbulent flow induced by the impingement results in the recirculation movement, which is considered to be the reason for the increased entrained gas velocity near the impinging point. The length of the entrainment section is restricted under the wall-impingement condition. Coghe et al. [2000] presented that the gas entrainment efficiency and the momentum transfer are promoted as the nozzle tip and the wall get closer. Mohammadi et al. [2002] studied a wall impinging non-evaporating spray and concluded that higher injection pressure increases the spray droplets velocity in the leading part due to the wall-jet vortex and promotes the air entrainment.

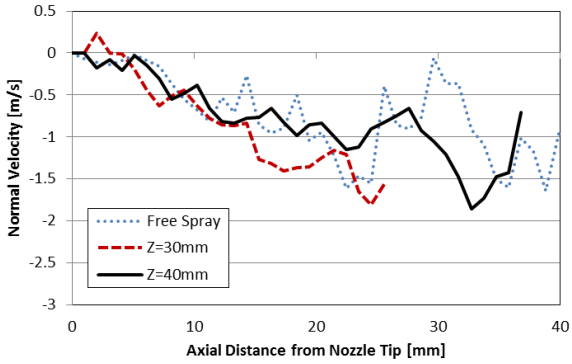

(a) P_{inj}=100MPa, 1.5ms ASOI

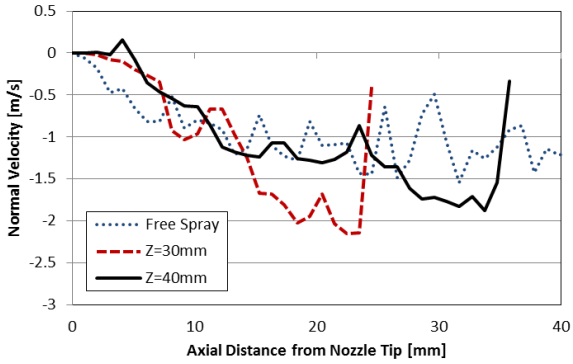

(b) P_{inj}=200MPa, 1.5ms ASOI

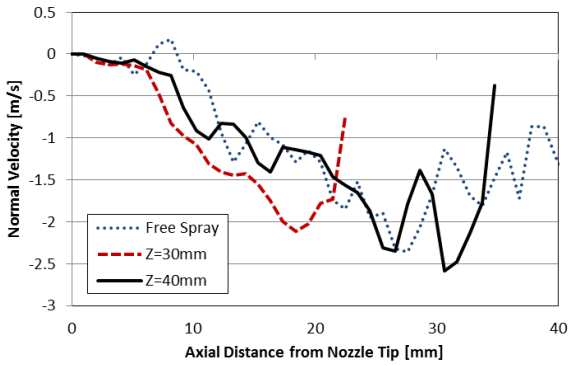

(c) P_{inj}=300MPa, 1.5ms ASOI

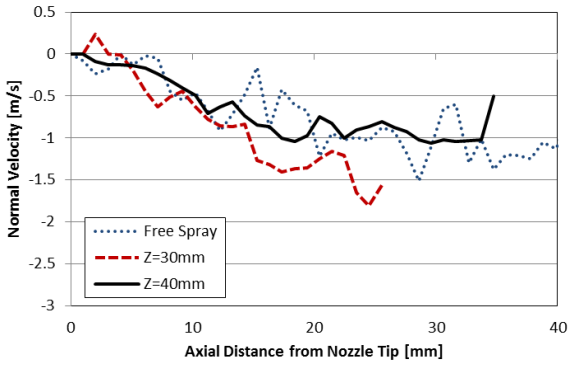

(d) P_{inj}=100MPa, 2.0ms ASOI

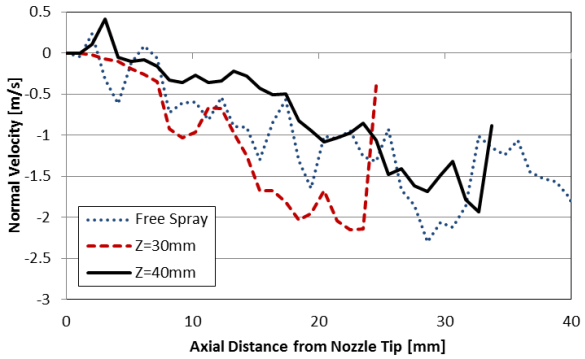

(e) P_{inj}=200MPa, 2.0ms ASOI

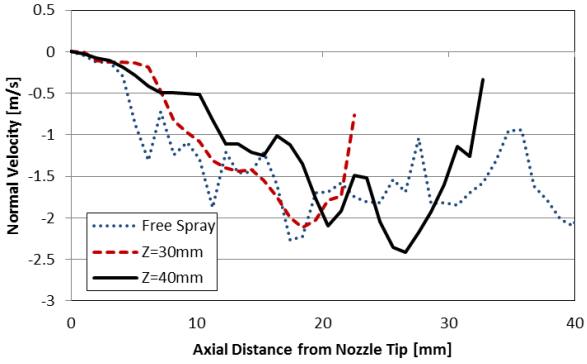

(f) P_{inj}=300MPa, 2.0ms ASOI

Figure 4.5 Comparison of Normal Velocity along Side Periphery

By extracting the axial component of gas velocity of the free spray and the radial component of gas velocity of the wall-impinging spray along the quarter circle at the tip periphery, the result of comparison of the pushed-out gas velocity is shown in Fig. 4.6. The value of θ indicates the angle from the vertical direction, thus 90 deg. indicates the vertex of spray tip. It is evident that spray-wall impingement significantly increases the push-out gas velocity particularly under the shortened impingement distance condition. The strong wall-jet vortex

formed in the spray tip periphery contributes to this result. It is worth emphasizing that the spray penetrating velocity is reversely restrained under the wall-impingement condition. Hence it is considered that more momentum is transferred from the spray to the ambient gas under the wall-impingement condition due to the improved turbulent flow. The pushed-out gas velocity increases slightly with the increase of the fuel injection pressure.

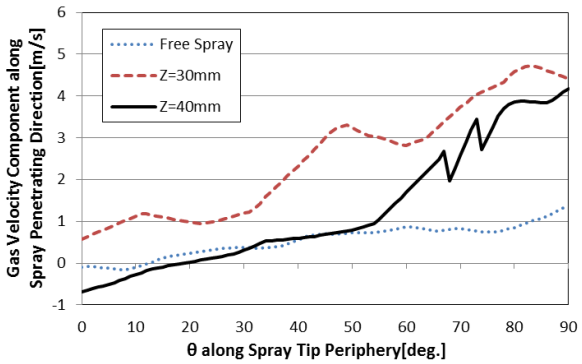

(a) P_{inj}=100MPa, 1.5ms ASOI

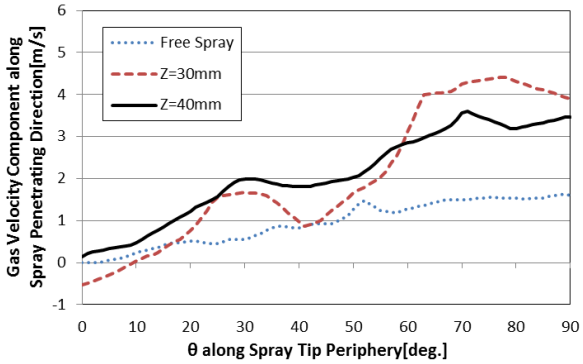

(b) P_{inj}=200MPa, 1.5ms ASOI

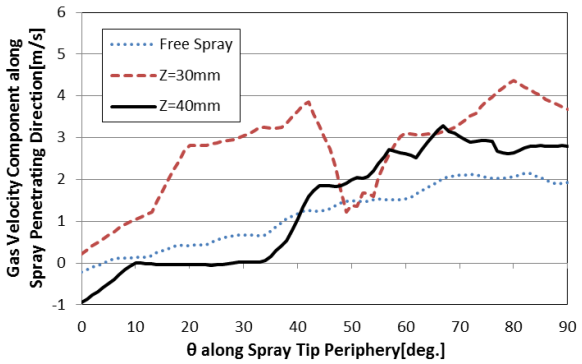

(c) Pinj=300MPa, 1.5ms ASOI

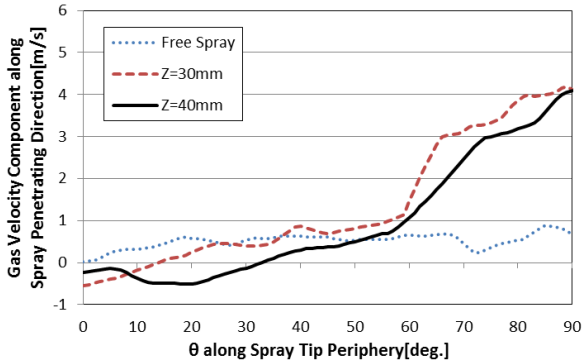

(d) Pinj=100MPa, 2.0ms ASOI

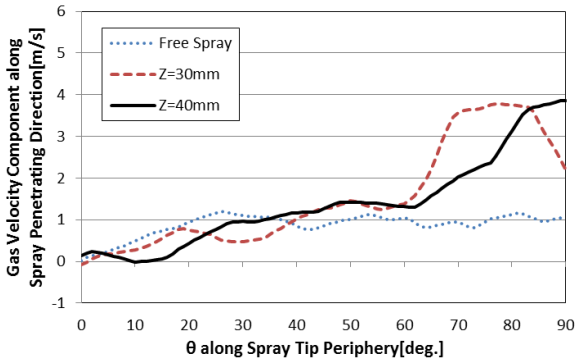

(e) P_{inj}=200MPa, 2.0ms ASOI

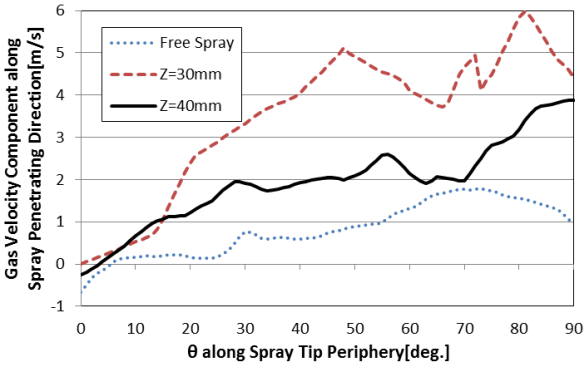

(f) P_{inj}=300MPa, 2.0ms ASOI

Figure 4.6 Comparison of Gas Velocity Component along Spray Penetrating Direction

4.3 ANALYSIS OF AMBIENT GAS MASS FLOW RATE

Equation (4.1-4.4) presents the process for calculating the ambient gas mass flow rate of a wall-impinging spray according to the model proposed in Fig. 4.4. (1).The entrainment section along the side surface has the same definition and principle as that in the free spray case. The total gas mass flow rate at the side surface region ($\dot{M}a_{ent}$) is defined in Eq.4.1, which is obtained by integrating the local gas mass flow rate in a series of discrete segments from nozzle tip to the coordinate of x_1. The spray boundary in this section is constant. (2). In the downstream recirculation section, the spray height increases with the time, on the other hand, the strong vortex motion leads to a large amount of ambient gas entering the spray boundary especially near the impinging point. Thus rather than the assumption for the free spray, the gas flow rate in this region is not negligible in the impinging spray case. This section spans from the nozzle axis to the coordinate of x_2, which is also the boundary of the recirculation section and the capturing section at the tip. x_2 is defined according to the position where the perpendicular gas velocity vector appears. The upper boundary of recirculation section is defined by averaging the Mie-scattering image of several spray samples. The increasing rate of the spray height V_{upward} is calculated according to the displacement of the upper boundary during a very short time interval. The gas flow rate in recirculation section $\dot{M}a_{pushing}$ is obtained by considering the axial component of gas flow velocity $V_y(x)$and the axial projected area $dA(x)$ along the spray upper boundary. The total ambient gas mass flow $\dot{M}a_{rec}$ is obtained by subtracting the $\dot{M}a_{pushing}$ from the ideal gas mass flow due to the upper boundary movement $\dot{M}a_{upward}$ as shown in Eq.4.2. (3). In the capturing section, the spray head moves radially away from the nozzle axis with the velocity of V_{sp}, a large amount of ambient gas is also captured due to the velocity difference of spray penetration and ambient gas motion. Due to the fluctuation of the shape of the spray head, a quarter of the circle with the radius of R is considered as the boundary of the spray head, which is defined by averaging images of several samples. The gas mass flow rate in capturing section $\dot{M}a_{pushing}$ is obtained by considering the radial component of gas flow velocity $V_x(\theta)$ and the radial projected area $dA(\theta)$ along the circle boundary. The total ambient gas mass flow $\dot{M}a_{cap}$ is obtained by subtracting the $\dot{M}a_{pushing}$ from the ideal gas mass flow due to the spray tip penetration $\dot{M}a_{penetrating}$ as shown in Eq.4.3. Finally, the total ambient gas flow rate around the

whole spray periphery $\dot{M}_a$ is obtained by summating the results from each section as shown in Eq.4.4.

Entrainment Section:

$$\dot{M}a_{ent} = \int_0^{x_1} \rho_a \cdot V_n(x,a) \cdot dA(x,a) \quad (4.1)$$

Recirculation Section:

$$\dot{M}a_{rec} = \dot{M}a_{upward} - \dot{M}a_{pushing} = \rho_a \cdot V_{upward} \cdot \pi \cdot {x_2}^2 - \int_0^{x_2} \rho_a \cdot V_y(x) \cdot dA(x) \quad (4.2)$$

Capturing Section:

$$\dot{M}a_{cap} = \dot{M}a_{penetrating} - \dot{M}a_{pushing} = \rho_a \cdot V_{sp} \cdot 2\pi \cdot x_2 \cdot R - \int_0^{\theta_1} \rho_a \cdot V_x(\theta) \cdot dA(\theta) \quad (4.3)$$

At the Whole Spray Periphery:

$$\dot{M}_a = \dot{M}a_{ent} + \dot{M}a_{rec} + \dot{M}a_{cap} \quad (4.4)$$

Figure 4.7 indicates the results of total ambient gas mass flow around the whole periphery and the instantaneous gas/fuel ratio of the wall-impinging spray with the impingement distance of 30mm and 40mm, respectively. Compared with the corresponding gas mass flow rate result of the free spray shown in Chapter 3, Fig. 3.13, the gas mass flow rate captured in the tip periphery of the free spray accounts for 70-85% of the total value due to the large velocity difference of the spray droplets and the ambient gas. The proportion of gas flow from the side surface increases with the development of the spray due to the extension of the length of the entrainment section and the increased entrained gas velocity. On the other hand, under the condition of the impinging spray, the entrained gas mass from side periphery takes up much lower proportion because of the restrained entrainment section. With the radial expansion of the spray, the velocity difference between the spray head and the ambient gas decreases, resulting in the reduction of the proportion of the total gas mass flow from the tip region. At the same time, due to the extension of the length of the recirculation section and the increased gas flow velocity, the proportion of the gas flow from the recirculation section increases. The proportion of the gas flow from capturing section and the recirculation section is approximately the same when reaching the end of fuel injection.

The increase of the injection pressure significantly improves the gas flow at both side periphery and the tip periphery under the free spray condition, as a result, leaner mixture can be achieved due to the enhanced air/fuel ratio. While under the impinging spray condition, the higher injection pressure mainly improves the ambient gas flow at the recirculation section and the capturing section. As a result, the instantaneous ratio of gas/fuel mass flow rate increases with increasing the injection pressure. It is noteworthy that compared with that of the free spray, less effect of higher injection pressure on the improvement of gas/fuel ratio under the impinging spray condition can be observed. The increased liquid film mass as the increase of fuel mass flow rate and more energy dissipation due to the splashing after the wall impingement are supposed to be the reasons. The general tendency is that regardless of the injection pressure, the wall impingement restrains the development of the fuel spray and the ambient gas mass flow rate, compared with the free spray condition. The shorter the nozzle-wall distance is, the more the ambient gas mass flow rate is supressed. It can be found that increasing rate of ambient gas mass flow rate with time becomes moderate and even decreases reversely near EOI, which demonstrates the a large amount of momentum loses due to the friction with wall. If taking into account of the liquid film formed on the flat wall, the real ratio of the ambient gas /fuel mass in the spray plume tends to be larger than the results shown in Fig. 4.7.

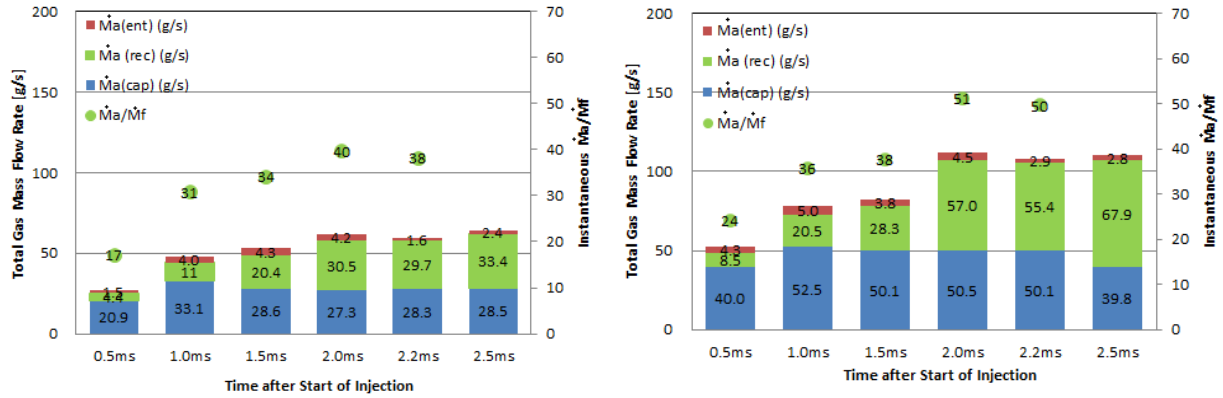

(a) P_{inj}=100MPa, Z=30mm (b) P_{inj}=200MPa, Z=30mm

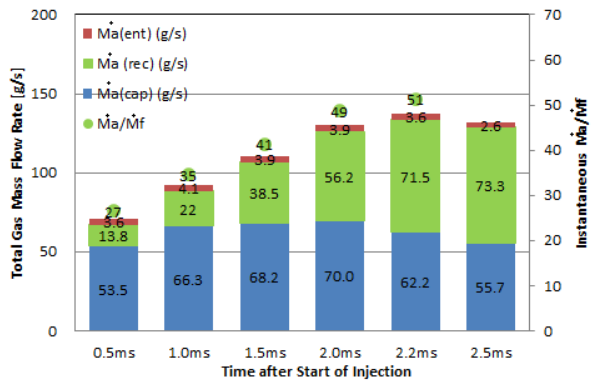

(c) P_{inj}=300MPa, Z=30mm

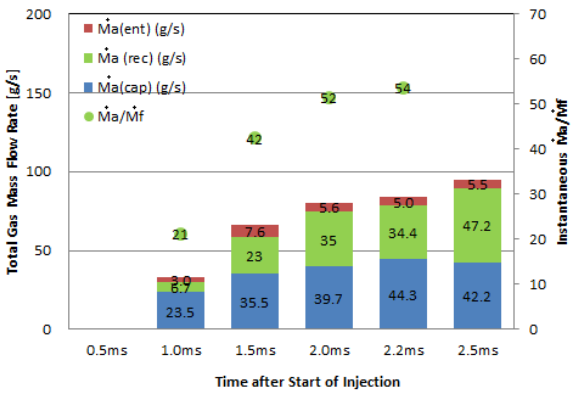

(d) P_{inj}=100MPa, Z=40mm

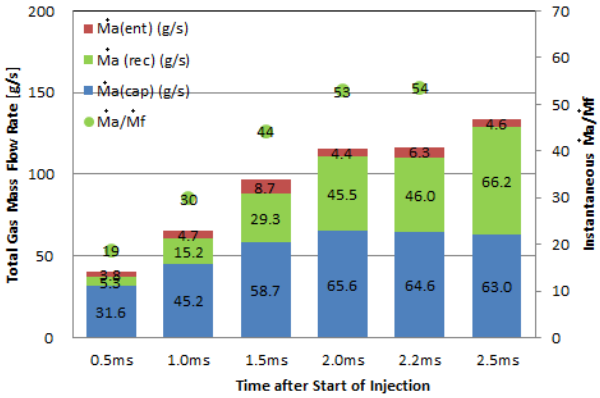

(e) P_{inj}=200MPa, Z=40mm

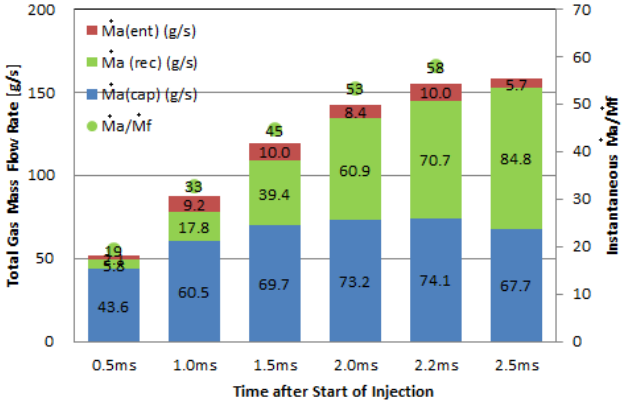

(f) P_{inj}=300MPa, Z=40mm

Figure 4.7 Ambient Gas Mass Flow Rate of Wall-Impinging Spray

The temporal integration of the ambient mass flow rate is compared with the spray volume for the free spray and the impinging spray in Fig.4.8 in order to validate the accuracy of the calculation model. The result shows that total ambient gas mass calculated from the LIF-PIV result and from the spray volume are in good agreement, the largest difference at some timings is less than 10%. The impinging spray volume is smaller than that of the free spray, which demonstrates that the ambient gas mass flow rate is restrained for the wall-impinging spray condition. Song et al. [2003] studied a gas jet experimentally and compared with the computational results, the result shows that the loss of momentum to the walls reduces the rate of jet penetration of the wall-impinging jet. In the wall-impinging jet, the fuel becomes ‘‘flammable’’ almost as fast as it does in the free jet but that the formation of “lean mixture” appears to be slower.

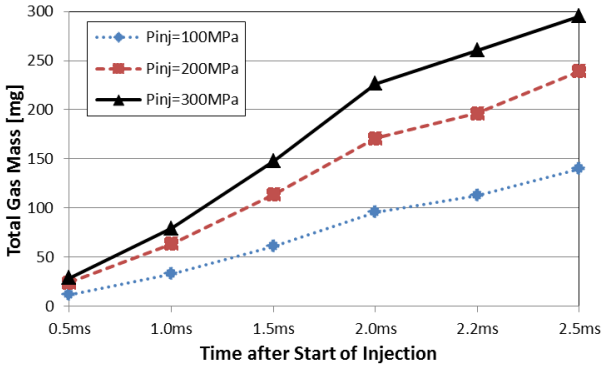

(a) Free Spray (From LIF-PIV Result)

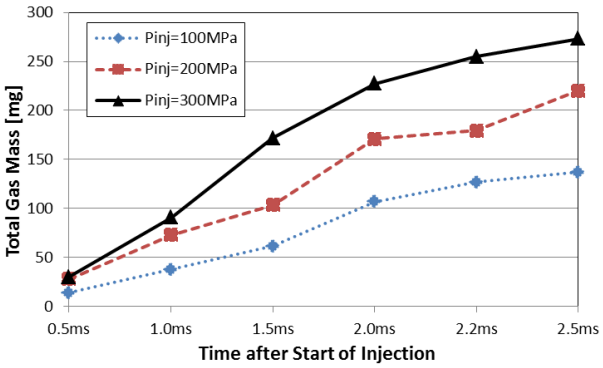

(b) Free Spray (From Spray Volume)

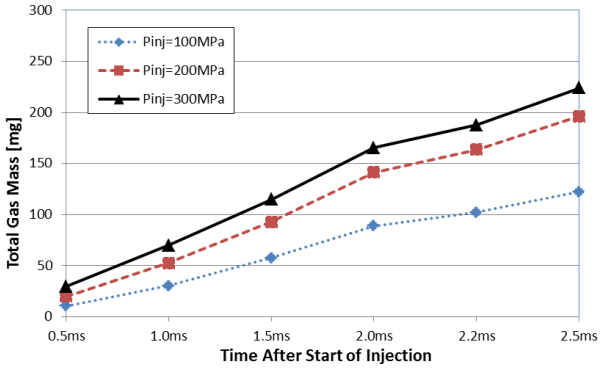

(c) Impinging Spray (From LIF-PIV Result)

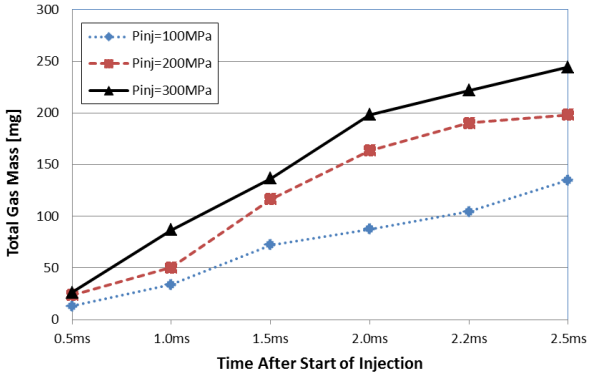

(d) Impinging Spray (From Spray Volume)

Figure 4.8 Comparison of Total Ambient Gas Mass (ρa=15kg/m3, Z=30mm)

4.4 SUMMARY

The characteristics of the ambient gas flow field of the non-evaporating wall-impinging spray were measured quantitatively by using LIF-PIV technique. The ambient gas velocity and mass flow rate into the spray through the whole spray periphery were investigated quantitatively.

Based on this study, the following can be concluded:

1. The spray-wall impingement restricts the spray penetration and the increase of the spray volume under the non-evaporating condition. The shorter the impinging distance is, the more the penetrating length is limited.
2. It is evident that the pushed-out gas velocity for the impinging spray is larger than that for the free spray, the strong wall jet vortex forms at the spray head contributes to this result. The pushed-out gas velocity at the spray head and the gas velocity at the recirculation region increase apparently with the increase of the injection pressure. The ambient gas flow is

intensified with the decrease of the impingement distance, particularly in the post-impingement region.

3. Under the condition of the impinging spray, the entrained gas mass from side periphery takes up much lower proportion because of the restrained entrainment section. With the radial expansion of the spray, the velocity difference between the spray head and the ambient gas decreases, resulting in the reduction of the proportion of the total gas mass flow from the tip region. At the same time, due to the extension of the length of the recirculation section and the increased gas flow velocity, the proportion of the gas flow from the recirculation section increases.
4. The instantaneous ratio of gas/fuel mass flow rate increases with increasing the injection pressure. Compared with that of the free spray, less effect of higher injection pressure on the improvement of gas/fuel ratio under the impinging spray condition can be observed.
5. The wall impingement restrains the development of the fuel spray and the ambient gas mass flow rate, compared with the free spray condition. The shorter the nozzle-wall distance is, the more the ambient gas mass flow rate is suppressed.

CHAPTER 5 INTERNAL FLOW FIELD OF FREE DIESEL SPRAY

5.1 EXPERIMENTAL CONDITION

For the measurement of the droplets flow of non-evaporating spray, a localized photography of the spray droplets particularly focusing on the downstream region with the diluted spray was applied. The time interval between the double frames and the size of the interrogation window need to be carefully adjusted compared with that of the ambient gas flow measurement due to the significant difference of the velocity scale. After careful comparison, the interrogation window of 16*16 pixels (0.94mm*0.94mm) and the double frames interval of 5μs were adopted. The spray droplets themselves were treated as the tracer to calculate the spray droplets movement.

Due to the unclear physical properties especially the boiling point of the diesel fuel, the mixture of dodecane and silicon oil was selected as the surrogate fuel for measuring the vapor phase flow of the evaporating spray. Firstly, the pure dodecane reagent was injected into the prescribed high temperature and high pressure atmosphere to determine the liquid length and the complete vaporization location. In the formal experiment, 95%/vol. of the dodecane was mixed with 5%/vol. of the silicon oil which has remarkable higher boiling point, thus It is proper to consider that the remaining droplets downstream of the complete vaporization location of the dodecane spray are composed of the silicon oil. Kosaka, H. et al. [1992] concluded that the investigation of the scattering light from silicon droplets is capable of relating to the vapor phase concentration as long as the several conditions can be met: (1). the component of residual liquid droplets are composed of silicon oil; (2). the silicon oil droplets follow the turbulence; (3). uniform distribution of silicon oil droplets; (4). multiple scattering of silicon droplets are negligible. The fluorescent image from TMPD mixed in the vapor phase was in good agreement with the Mie scattering image from the silicon droplets as long as the silicon droplets were small enough. In this study, we directly make use of the conclusion that the fully atomized silicon droplets can be employed to trace the vapor phase flow of the evaporating spray. Several options of the percentage of the silicon oil were tested and 5% was selected at last according to the scattering light intensity and distributing number density of the silicon droplets and the physical property of the mixing fuel.

Table 5.1 shows the experimental conditions of the internal spray flow measurement under the non-evaporating and evaporating conditions, respectively. By comparing the physical property, the blended fuel of the 5%/vol. silicon oil (KF-95-50cs) and 95%/vol. dodecane is able

to represent the flow property of the Diesel spray. In both the non-evaporating condition and the evaporating condition, the ambient gas density of 15 kg/m^3 was kept the same.

Table 5.1 Experimental Conditions of Free Spray Internal Flow Measurement

Measuring Method	PIV	
Interrogation Window Size	16*16 pixels (0.94mm*0.94mm)	
Frame Interval	5μs	
Nozzle Diameter (mm)	0.08	
Injection Pressure (MPa)	100, 200, 300	
Injection Duration (ms)	2.2	
Ambient Gas	Nitrogen	
Ambient Gas Density (kg/m^3)	15	
Ambient Condition	Non-Evaporating	Evaporating
Ambient Temperature (K)	300	770
Ambient Pressure (MPa)	1.4	3.5
Test Fuel	Diesel JIS#2	5%/vol. Silicon Oil (KF-95-50cs) + 95%/vol. Dodecane
Fuel Density (kg/m^3)	~860	760
Kinematic Viscosity (mm^2/s)	5-6	4.2
Boiling Point (K, 1bar)	450~630	~520

In order to preserve the velocity fluctuation information which varies in the different shots, the results of velocity distribution from several single samples are shown together with the ensemble averaged results.

5.2 FLOW FIELD IN NON-EVAPORATING CONDITION

Figure 5.1 shows the several samples of the fuel droplets flow field under the injection pressure of 100MPa at different timings. Only the downstream part of the spray is magnified and analyzed to avoid the impact of the strong scattering light from the upstream part. The Mie scattering spray images of the corresponding samples are also shown together to take into account of the result of fuel mass concentration distribution, because the Mie scattering light

intensity is related to the number and size of local droplets. Meanwhile, the ensemble averaged velocity distribution of approximately 10 samples is shown together on the right side. The maximum velocity usually locates along the centerline of the spray, while attenuates gradually with the radial direction. In particular, the droplets near the spray side periphery downstream tends to be pushed aside and move upward, which corresponds to the recirculation region observed in the ambient gas flow measurement, as a result the large scale vortex motion forms. The intermittent distribution of the droplets velocity can be found in all the samples, which is owing to the turbulent fluctuation in the flow field, the numerical simulation result with LES turbulent model is capable of showing the similar flow field characteristics [Hori et al., 2006]. It is believed that the spray penetration is based on such process: the spray droplets parcel injected in advance loses the momentum, then is surpassed and pushed aside by the successive parcel with higher velocity. This process results in the incoherent velocity distribution and mass concentration distribution. It is found that the spray droplets velocity decelerates gradually with time, especially in the downstream region.

Due to the ambient gas resistance, the spray droplets movement usually bifurcates at the tip region, rather than moving straightforward. The magnified A region in Fig.5.2 highlights such behavior, it can be also observed in region A that the parcel with larger droplet size or more fuel mass has more momentum to develop further downstream. Such kind of parcels at the tip region determines the whole spray development. On the other hand, the vortex like motion appears on both sides of the main flow path, the lower fuel mass concentration can be found in the centre of the vortex structure due to the centrifugal force impact.

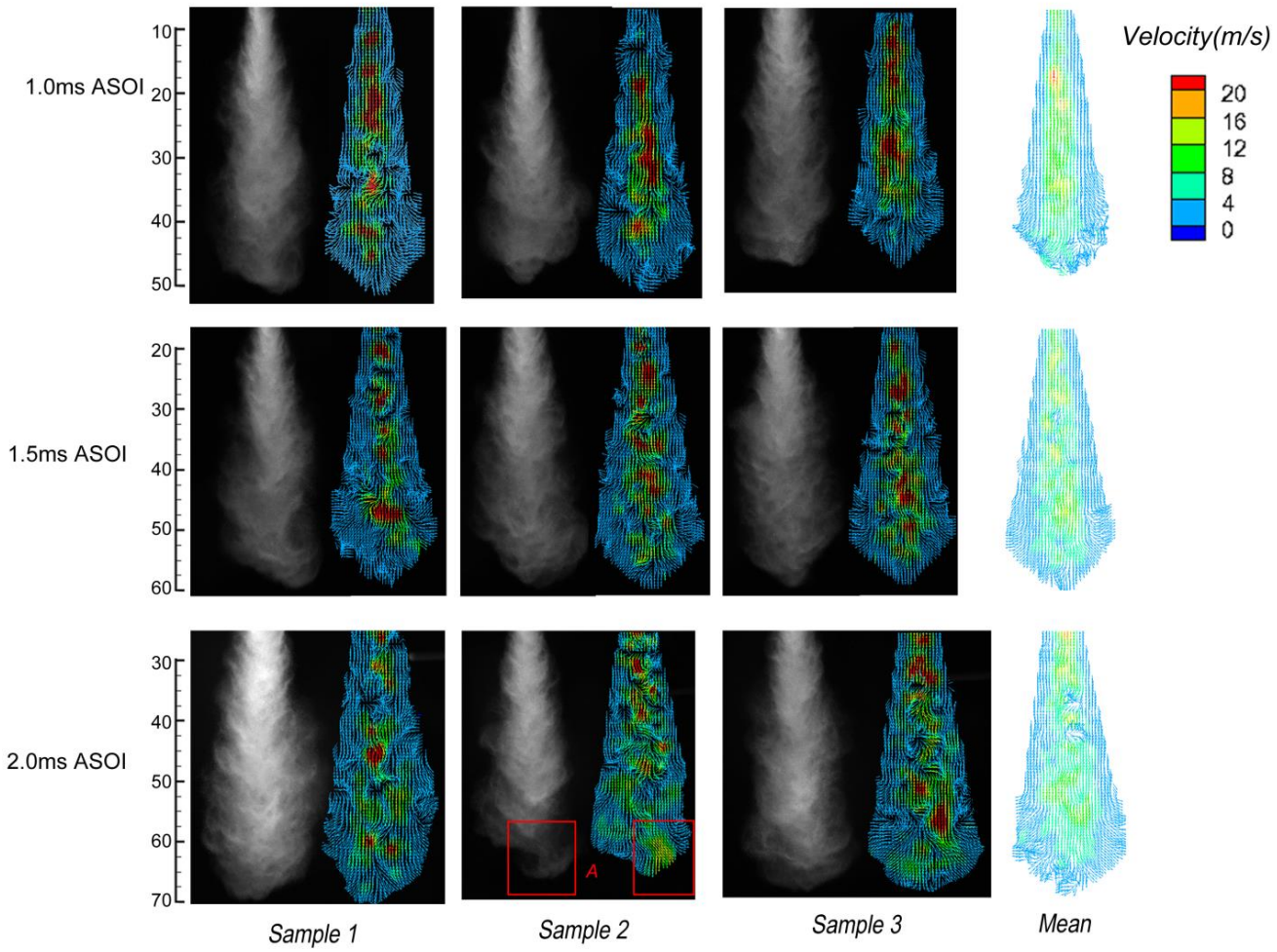

Figure 5.1 Flow Field of Spray Droplets in Non-Evaporating Condition (P_{inj}=100MPa)

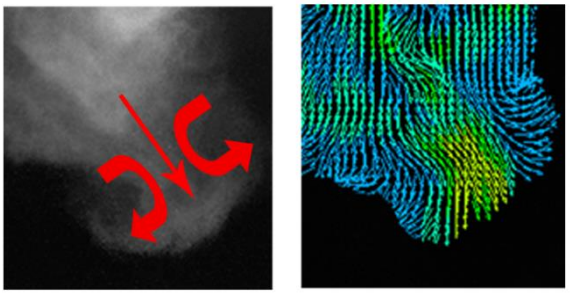

Figure 5.2 Magnified Region A Shown in Figure 5.1

Figure 5.3 shows the effect of fuel injection pressure on the droplets flow field at the timing of 2.0ms ASOI, in which the spray is considered to reach the quasi-steady state. By selecting one sample from one injection pressure respectively, the comparison of count of velocity distribution is shown in Figure 5.4. It is evident that the mean value of the droplets

velocity increases with the fuel injection pressure especially at the spray tip region, which leads to the longer penetration length. The small scale vortex motion, in other word, the fluctuation of the velocity distribution becomes more considerable in the whole region, which accounts for that the small scale turbulent mixing can be effectively enhanced with the increase of fuel injection pressure, as a result, the fuel/gas mixing process is promoted.

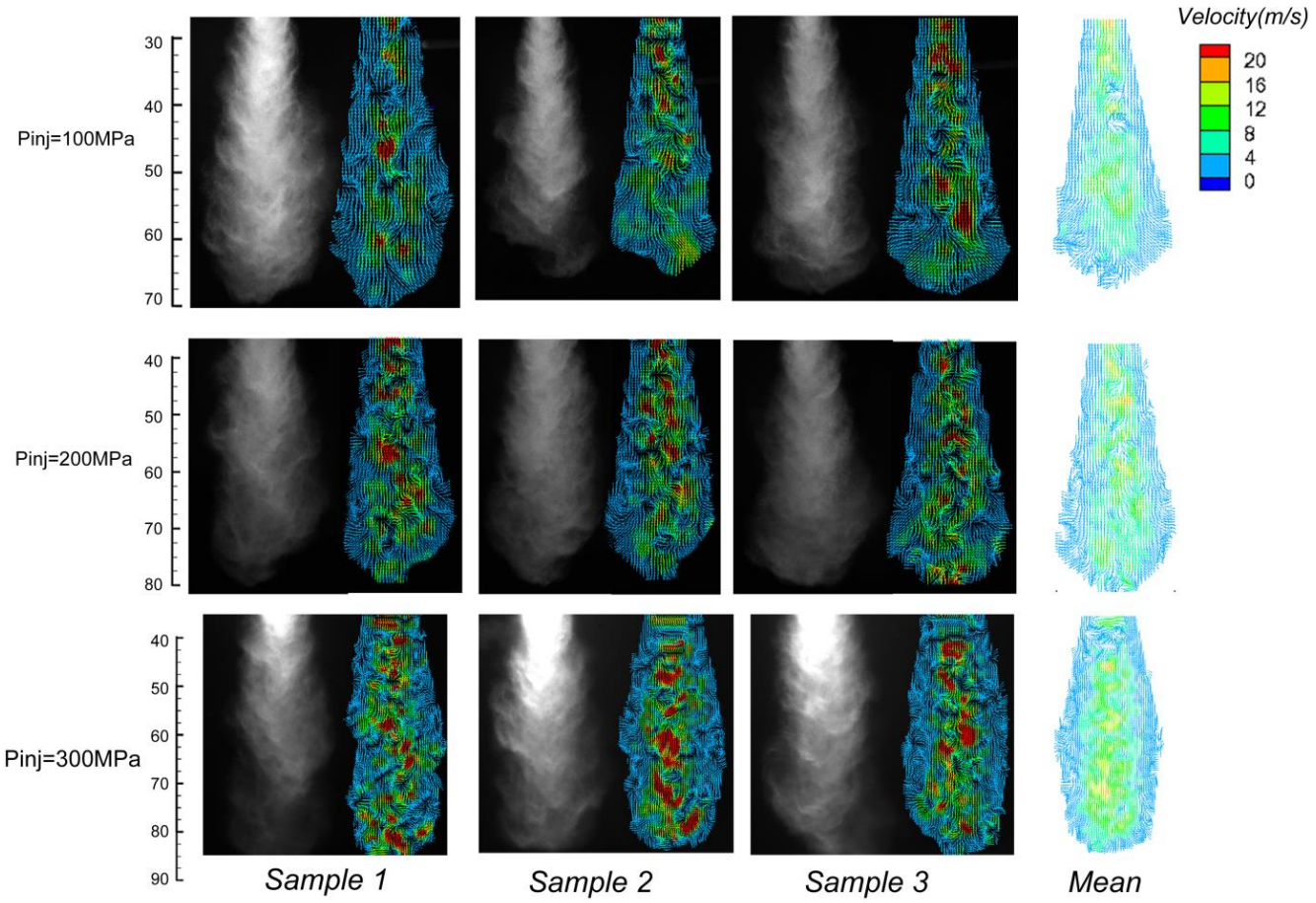

Figure 5.3 Effect of Fuel Injection Pressure on Droplets Flow Field (2.0ms ASOI)

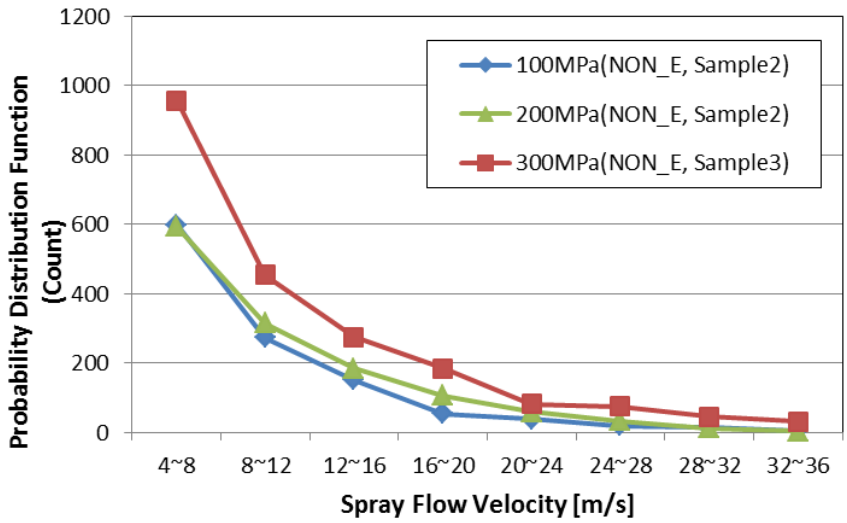

Figure 5.4 Probability Distribution Function of Spray Velocity (2.0ms ASOI)

The vorticity distribution of the flow field was calculated according to the following equation (5.1):

$$\omega_{ij} = \frac{du_{ij}}{dy_{ij}} - \frac{dv_{ij}}{dx_{ij}} \qquad (5.1)$$

where the u, v stand for radial and axial component of the flow velocity respectively, the x, y are the co-ordinate of the flow field, i, j are the index of the interrogating point. The vorticity distribution provides the quantitative information of the vortex motion and the turbulent mixing process. The results of vorticity distribution under the different injection pressures are shown in Fig.5.5. The sequence of the samples corresponds to that in Fig. 5.3. It is notable that the vortex intensity enhances with the increase of the fuel injection pressure. Particularly, the significantly high vortex intensity extends to the tip region under the high injection pressure condition, which implies the tendency to improve the fuel/gas mixing process. The magnified region A, B shown in Fig. 5.6 indicates that larger fuel mass concentration usually locates along the streamline of the vortex motion, the smaller fuel mass concentration locates at the center of the vortex structure due to the centrifugal force effect. As a conclusion, the vorticity distribution corresponds to the resultant heterogeneity of the fuel concentration distribution. Figure 5.7 quantitatively indicates the probability distribution of the vorticity intensity by selecting one sample from each injection pressure, respectively, which proves the significant increase of mean vortex with the increase of injection pressure.

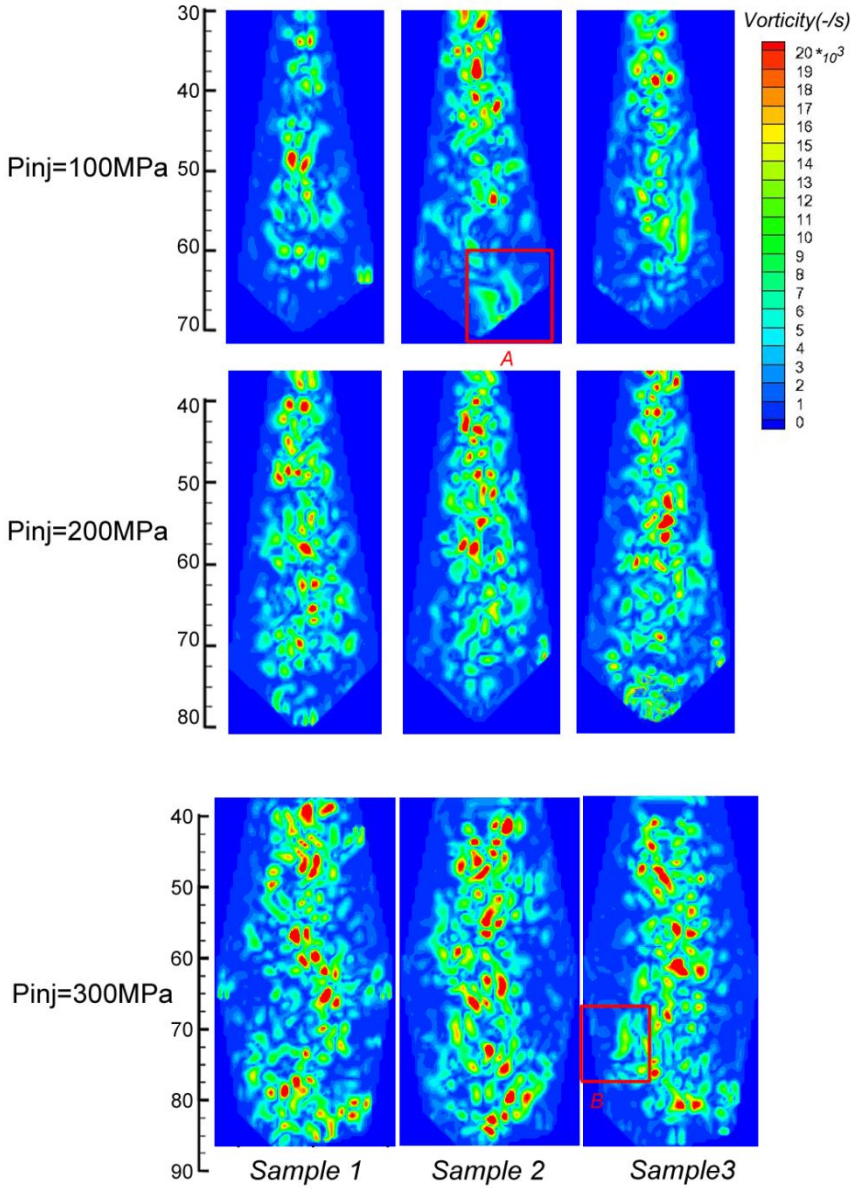

Figure 5.5 Vorticity Distribution of Non-Evaporating Spray (2.0ms ASOI)

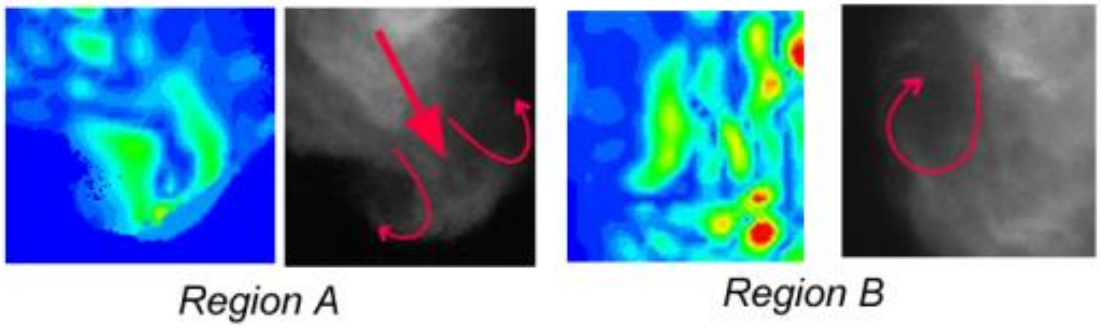

Figure 5.6 Magnified Region A and B Shown in Figure 5.4

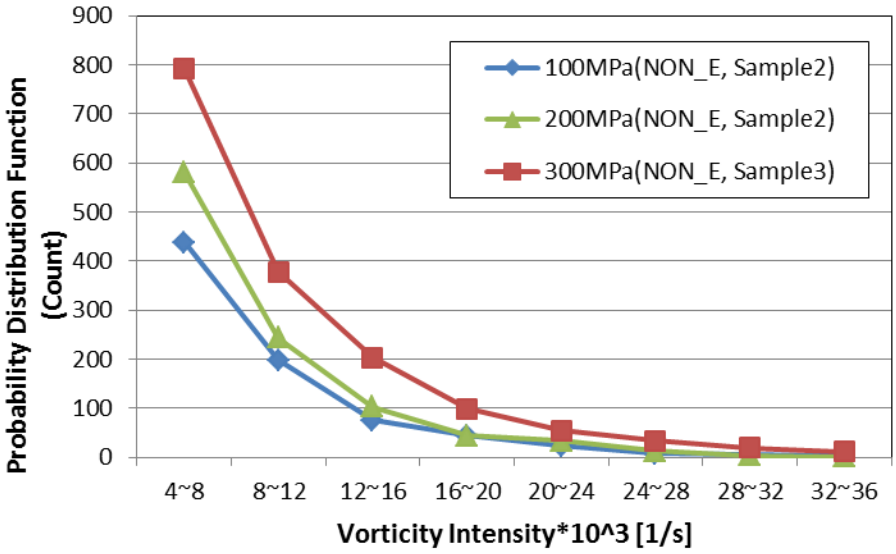

Figure 5.7 Probability Distribution Function of Vorticity Intensity (2.0ms ASOI)

It is noteworthy that there is significant fluctuation of the velocity distribution shot by shot, which will apparently influence the subsequent mixture formation result and combustion characteristics. Hence it makes sense to identify the velocity fluctuation characteristics under the different injection pressure and ambient gas conditions.

Equation (5.2) is used to calculate the deviation of the velocity distribution of several samples:

$$\sigma = \sqrt{\frac{1}{n}\sum_{1}^{n}(u-\bar{u})^2 + \frac{1}{n}\sum_{1}^{n}(v-\bar{v})^2} \tag{5.2}$$

Where the σ is the deviation of the velocity distribution, $\bar{u}$ and $\bar{v}$ are the mean velocity in the radial direction and axial direction, n is the number of the samples. In this study, 10 representative samples were selected for calculation under each injection pressure condition. Figure 5.8 shows the results of the deviation of the velocity distribution at the timing of 2.0ms ASOI. Figure 5.9 shows the quantitative results of probability distribution function of deviation of velocity. It shows that under the lower injection pressure condition (100MPa), the velocity fluctuation mainly concentrates in the upstream region, most of droplets downstream lose the momentum and the comparatively stable mixture can be formed. With the increase of the fuel injection pressure, the fluctuation of the velocity spreads radially and axially towards the spray tip region. The proportion of the deviation of velocity with larger value increases significantly

with the increase of injection pressure. Such kind of high velocity fluctuation implies the strong turbulent mixing occurs throughout the spray plume, which is favorable to the uniform and lean mixture formation. On the other hand, the uncertainty of the fuel/gas mixture formation also increases.

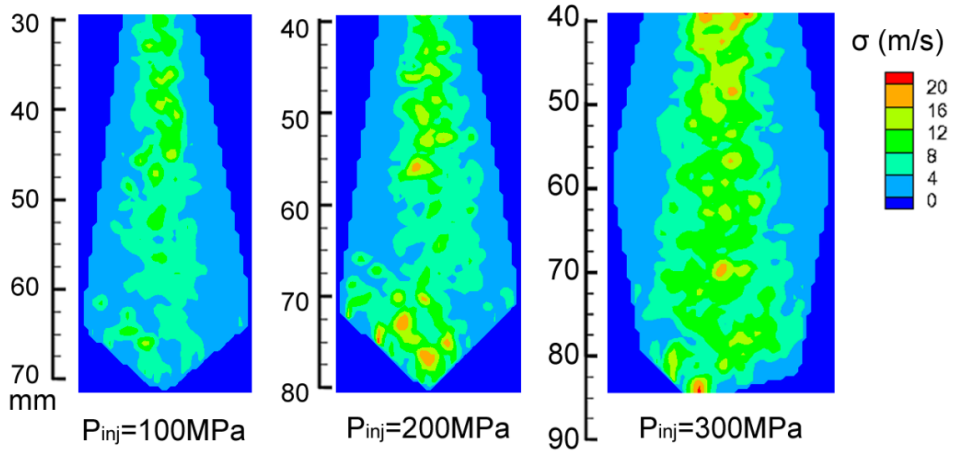

Figure 5.8 Deviation of Velocity Distribution (2.0ms ASOI)

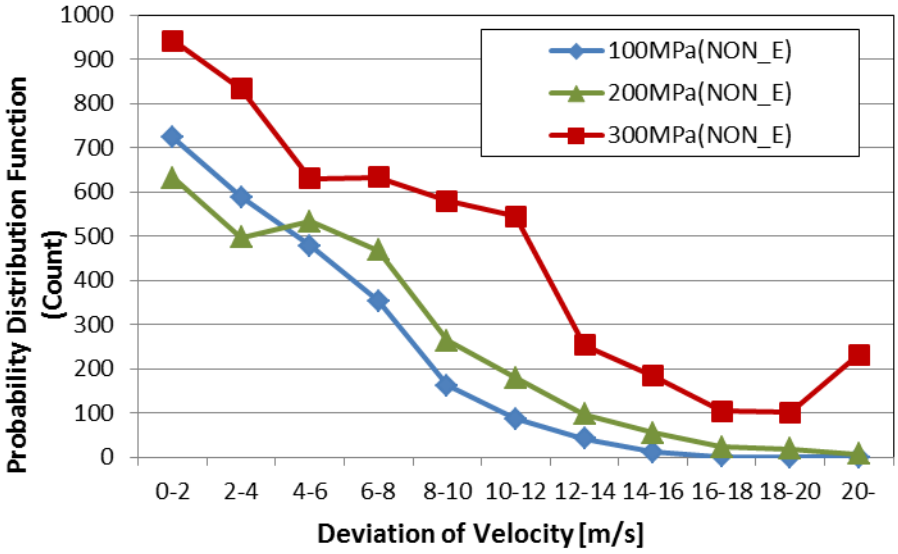

Figure 5.9 Probability Distribution Function of Deviation of Velocity (2.0ms ASOI)

5.3 FLOW FIELD IN EVAPORATING CONDITION

Several samples of the vapor phase flow field in the evaporating condition coupled with the Mie scattering signal image of the silicon droplets are shown in Fig.5.10. Figure 5.11 shows the comparison of probability distribution of mean velocity between the non-evaporating spray and

evaporating spray. The ambient density was kept constant as that in the non-evaporating conditions. Compared with the non-evaporating spray, the evaporating spray periphery fluctuates remarkably with different shots, which also corresponds to the shot-by-shot variation of the flow field. Especially at the spray tip region, unlike the flow field shown in Fig.5.3, the irregular vapor phase even flows towards the radial direction. This is because that the vapor phase with less momentum is subjected to the resistance of the surrounding gas at the tip region much easier. Even though the spray flow velocity shows the similar value as the non-evaporating condition upstream, as a result, the evaporating spray penetrates shorter than non-evaporating spray under the same ambient gas density condition.

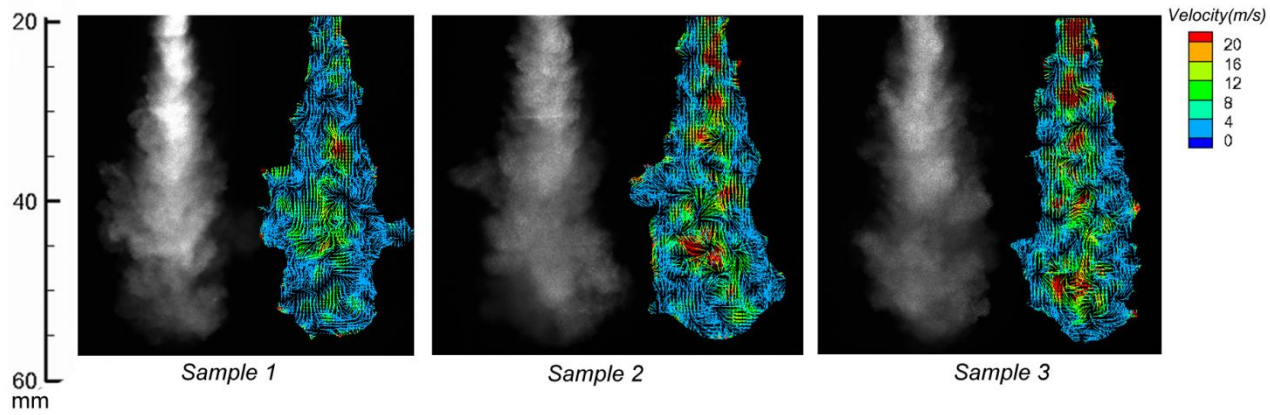

Figure 5.10 Flow Field of Spray Vapor Phase in Evaporating Condition (P_{inj}=100MPa, 2.0ms ASOI)

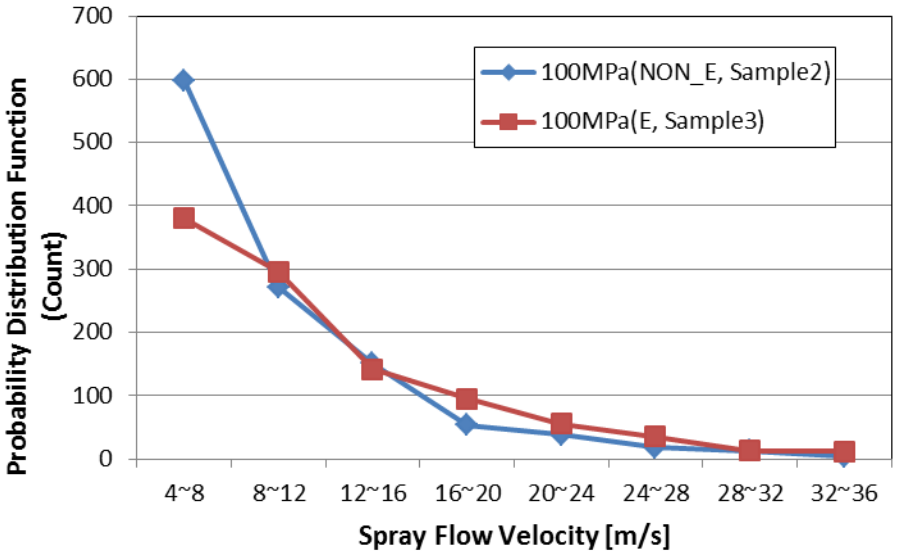

Figure 5.11 Comparison of Probability Distribution of Mean Velocity

Corresponding to the Equation. (5.1) and (5.2), Figure 5.12 and 5.13 show the vorticity distribution and the deviation of the velocity value, respectively. Correspondingly, the comparisons of probability distribution function of vorticity and velocity derivation with the non-evaporating case are shown in Fig. 5.14 and 5.15. Compared with the results of the non-evaporating condition under the injection pressure of 100MPa, it is found that the vapor phase flow features much stronger vorticity intensity and velocity fluctuation, in other word, the turbulent mixing is improved in the evaporating condition. However, the shot-by shot variation also increases under the evaporating condition. Several dynamic and thermodynamic reasons can be considered such as the increased gas viscosity, the strong gas density gradient and the heat transfer.

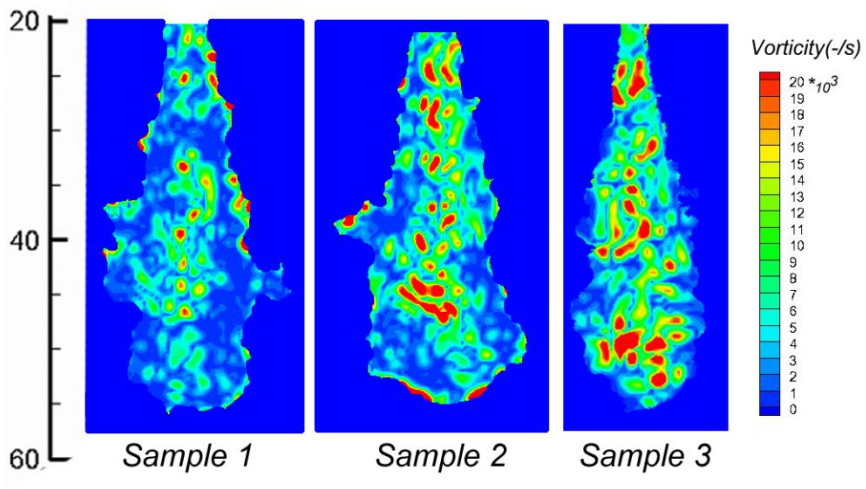

Figure 5.12 Vorticity Distribution of Evaporating Spray (P_{inj}=100MPa, 2.0ms ASOI)

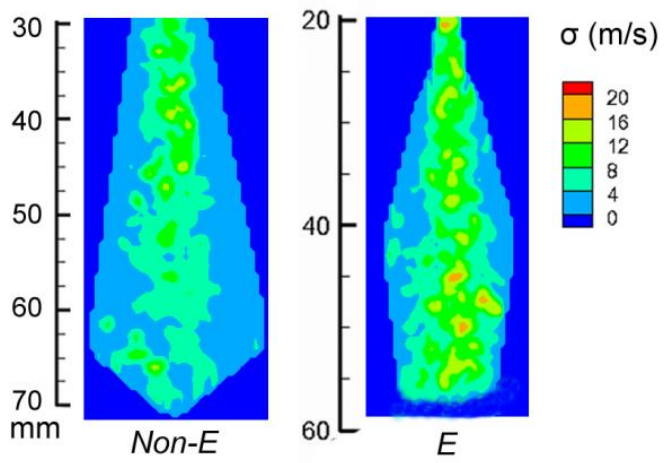

Figure 5.13 Deviation of Velocity Distribution (P_{inj}=100MPa, 2.0ms ASOI)

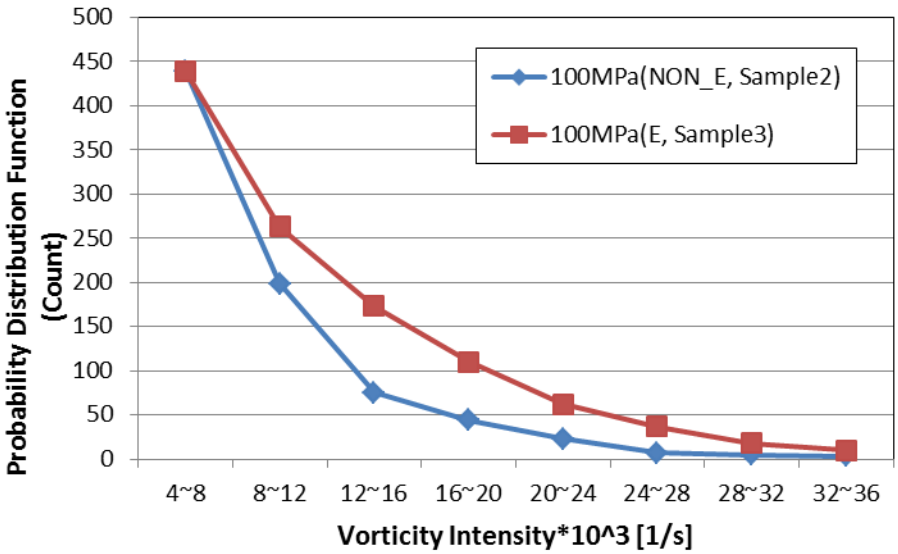

Figure 5.14 Comparisons of Probability Distribution Function of Vorticity Intensity

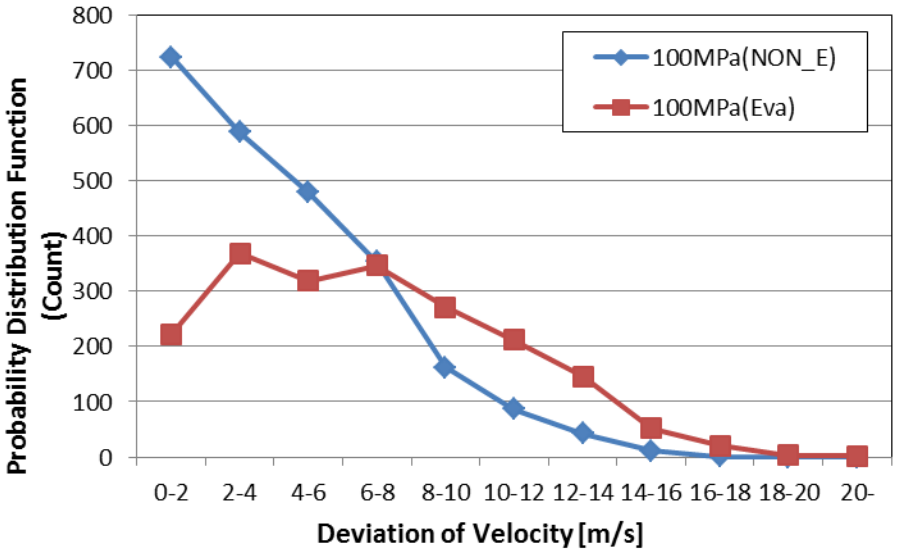

Figure 5.15 Comparisons of Probability Distribution Function of Deviation of Velocity

5.4 DISCUSSION

It is worth clarifying the phenomenon of the ambient gas flow and the internal flow in non-evaporating spray, evaporating spray and ultimately the gas jet especially at the tip region. To the authors' knowledge, there have been very few studies that provided enough evidence to explain that. In Chapter 3, The LIF-PIV and PIV measurement results indicate that large amount of ambient gas flow mass is attributed to the flow at the tip region regardless of the non-evaporating or evaporating condition. However, the detailed proportion changes according to the physical

and thermodynamic condition. It is found that the spray droplets still move downwards smoothly in Fig.5.1 and Fig. 5.2, because the ambient gas can easily enters the interval among the discrete droplets, as a result, a large velocity difference between the spray tip penetrating and the pushed-out gas was measured under the evaporating condition. On the other hand, the strong velocity fluctuation shown in Fig.5.8 and 5.9 indicates that the vapor phase at the tip region is subjected to the strong resistance from the outside gas, as a result, the ambient gas is pushed aside with higher velocity under the evaporating condition. The exact gas flow velocity and the gas mass flow rate at the tip region depend on the local fuel vapor pressure, the vapor flow velocity and the vortex intensity.

5.5 SUMMARY

The characteristics of the droplets flow of the non-evaporating spray and the vapor flow of the evaporating spray were measured quantitatively by using PIV technique. Several conclusions are summarized and presented as follows:

1. The incoherent velocity distribution and mass concentration distribution can be found inside the spray. The spray droplets velocity decelerates gradually with time, especially in the downstream region.
2. The vorticity distribution inside the spray corresponds to the resultant heterogeneity of the fuel mass concentration distribution. Correspondingly, the fuel parcel with different mass concentration also determines flow velocity distribution and the spray development.
3. Higher injection pressure enhances the mean flow velocity and the vorticity intensity in the whole region, which implies the promotion of the fuel/gas mixing process.
4. With the increase of the fuel injection pressure, the fluctuation of the velocity spreads radially and axially towards the spray tip region. Such kind of high velocity fluctuation implies the strong turbulent mixing occurs throughout the spray plume, which is favorable to the uniform and lean mixture formation. On the other hand, the uncertainty of the fuel/gas mixture formation also increases.
5. The much stronger vorticity and flow fluctuation inside the spray can be observed in the evaporating case. This is because that the vapor phase with less momentum is subjected to the resistance of the surrounding gas at the tip region much easier.
6. The ambient gas flow velocity and the gas mass flow rate at the tip region depend on the local fuel vapor pressure, the vapor flow velocity and the vortex intensity.

CHAPTER 6 INTERNAL FLOW FIELD OF FLAT-WALL IMPINGING DIESEL SPRAY

6.1 EXPERIMENTAL CONDITION

This Chapter will introduce the measurement of the internal flow field of the flat-wall impinging spray. As what has been mentioned in Chapter 5, the PIV setting was the same as what has been used for the free spray measurement. Three fuel injection pressures (100MPa, 200MPa, 300MPa) and two impingement distances (30mm, 40mm) were selected. The ambient gas density of 15 kg/m^3 was kept the same under the non-evaporating condition and the evaporating condition.

Table 6.1 Experimental Conditions of Wall-impinging Spray Internal Flow Measurement

Measuring Method	PIV	
Interrogation Window Size	16*16 pixels (0.94mm*0.94mm)	
Frame Interval	5μs	
Nozzle Diameter (mm)	0.08	
Injection Pressure (MPa)	100, 200, 300	
Injection Duration (ms)	2.2	
Impingement Distance (mm)	30, 40	
Ambient Gas	Nitrogen	
Ambient Gas Density (kg/m^3)	15	
Ambient Condition	Non-Evaporating	Evaporating
Ambient Temperature (K)	300	770
Ambient Pressure (MPa)	1.4	3.5
Test Fuel	Diesel JIS#2	5%/vol. Silicon Oil (KF-95-50cs) + 95%/vol. Dodecane
Fuel Density (kg/m^3)	~860	760
Kinematic Viscosity (mm^2/s)	5-6	4.2
Boiling Point (K, 1bar)	450~630	~520

6.2 FLOW FIELD IN NON-EVAPORATING CONDITION

Figure 6.1 shows the several samples of the fuel droplets flow field under the injection pressure of 100MPa and the impinging distance of 30mm at different timings. The flat wall impinging spray is considered to be axis-symmetric, hence only left half of the droplets velocity distribution and the corresponding Mie scattering spray image are shown, the mean value of the droplets velocity distribution from approximate 10 samples is shown on the right side. In the free spray region prior to the wall impingement, the spray droplets move downwards straightly with high velocity. After wall impingement the spray droplets move towards the radial direction, it is found that the droplets lose the momentum significantly when developing radially. Particularly near the impinging point, there are some vectors direct to the nozzle tip, which indicates that the spray droplets rebound or splash from the wall and enter the atmosphere again. In the lower part of the post-impingement spray region, the droplets still move straightly along the wall, these droplets are considered to be responsible of the resultant spray penetration. On the other hand, a large scale wall-jet vortex motion can be found in the upper part of the post-impingement spray region. Especially at the periphery of the spray, the droplets velocity shifts to the nozzle axis direction. As a result, the “recirculation section” mentioned in Fig. 4.4 of Chapter 4 forms in this region, in which a large amount of ambient gas move back towards the impinging point with the spray droplets. Correspondingly, a relatively lower fuel droplets concentration can be found in the center of the vortex structure due to the centrifugal force effect. The vortex structure moves forward with time and meanwhile the spray height increases.

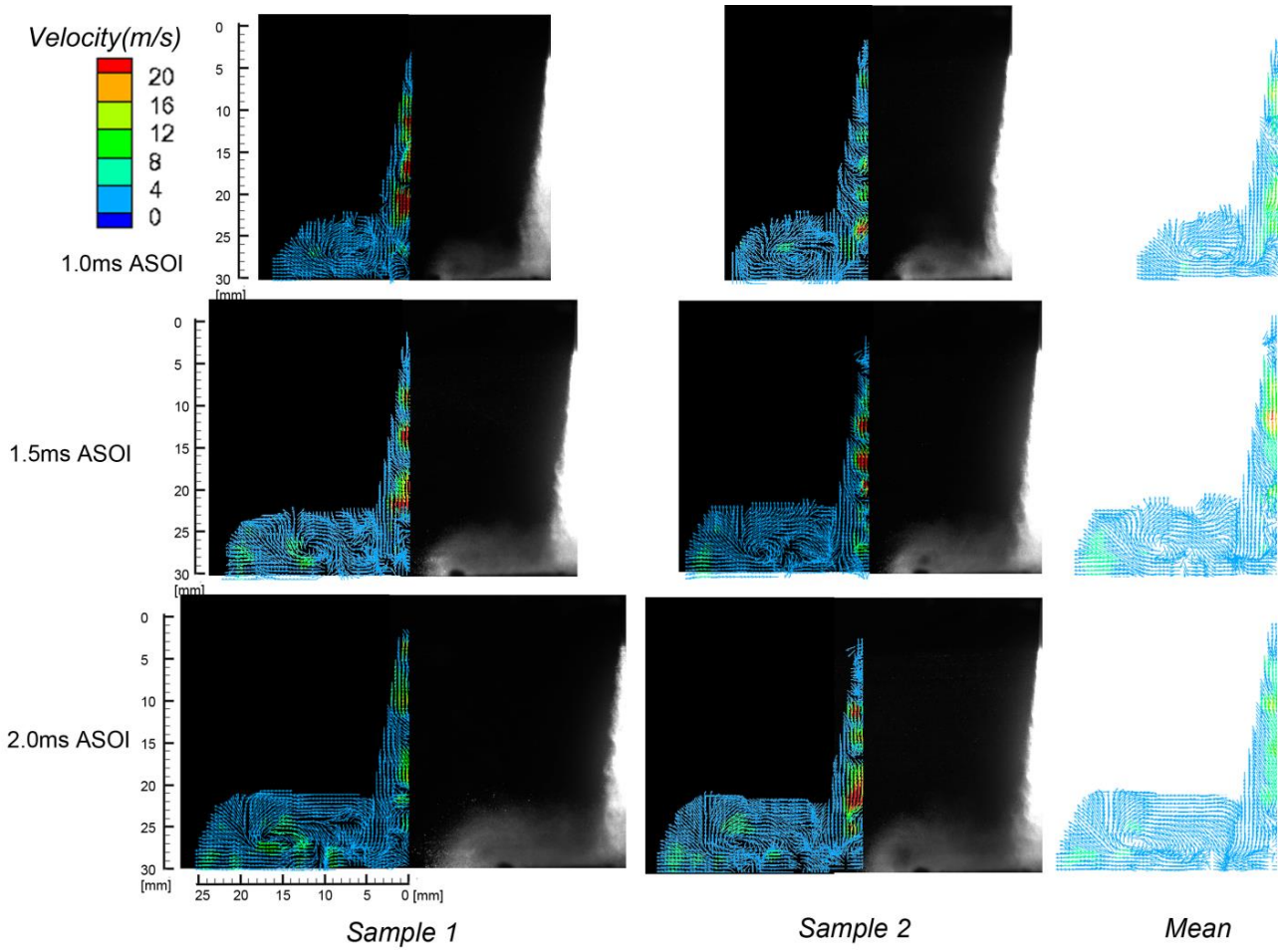

Figure 6.1 Droplets Flow Field of Wall-impinging Spray under Non-evaporating Condition (P_{inj}=100MPa)

Figure 6.2 shows the effects of injection pressure and impingement distance on droplets flow field. Figure 6.3 indicates quantitative results of the probability distribution function of spray flow velocity. It is evident that the mean droplets velocity increases with the increase of the injection pressure. The small scale vortex motion, in other word, the fluctuation of the velocity distribution becomes more considerable especially at the recirculation section, which implies that the small scale turbulent mixing can be effectively enhanced with the increase of fuel injection pressure. The radial length of the post impingement region is slightly longer when the impingement distance decreases, however, the total spray tip penetration decreases under the shorter impingement distance condition. Correspondingly, the increased mean flow velocity can be found under the longer impingement distance condition. The similar large vortex structure can be found in both of the impingement distance conditions.

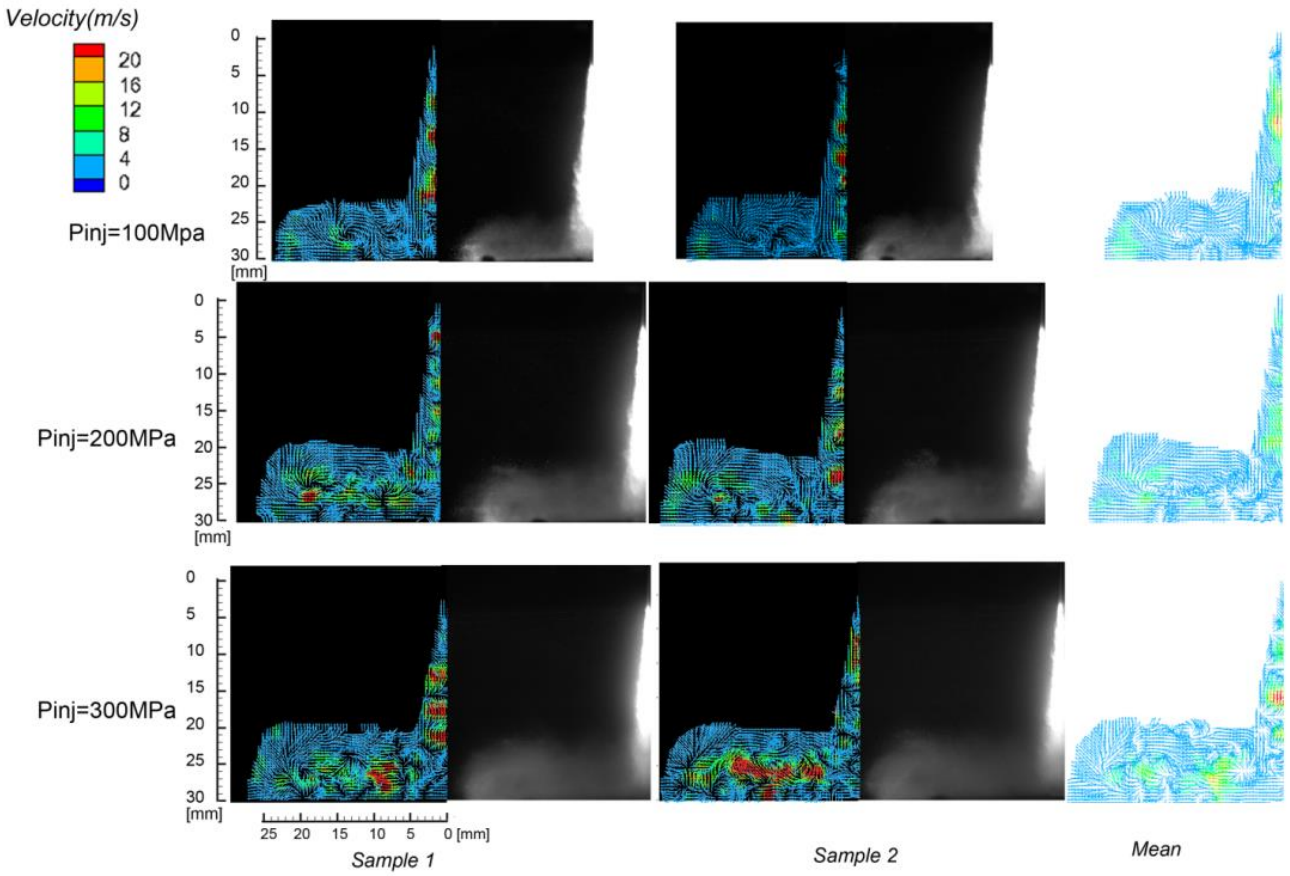
Velocity(m/s)
20
16
12
8
4
0
Pinj=100Mpa
Pinj=200MPa
Pinj=300MPa
0
5
10
15
20
25
30
[mm]
25 20 15 10 5 0 [mm]
Sample 1
Sample 2
Mean

(a) Z=30mm

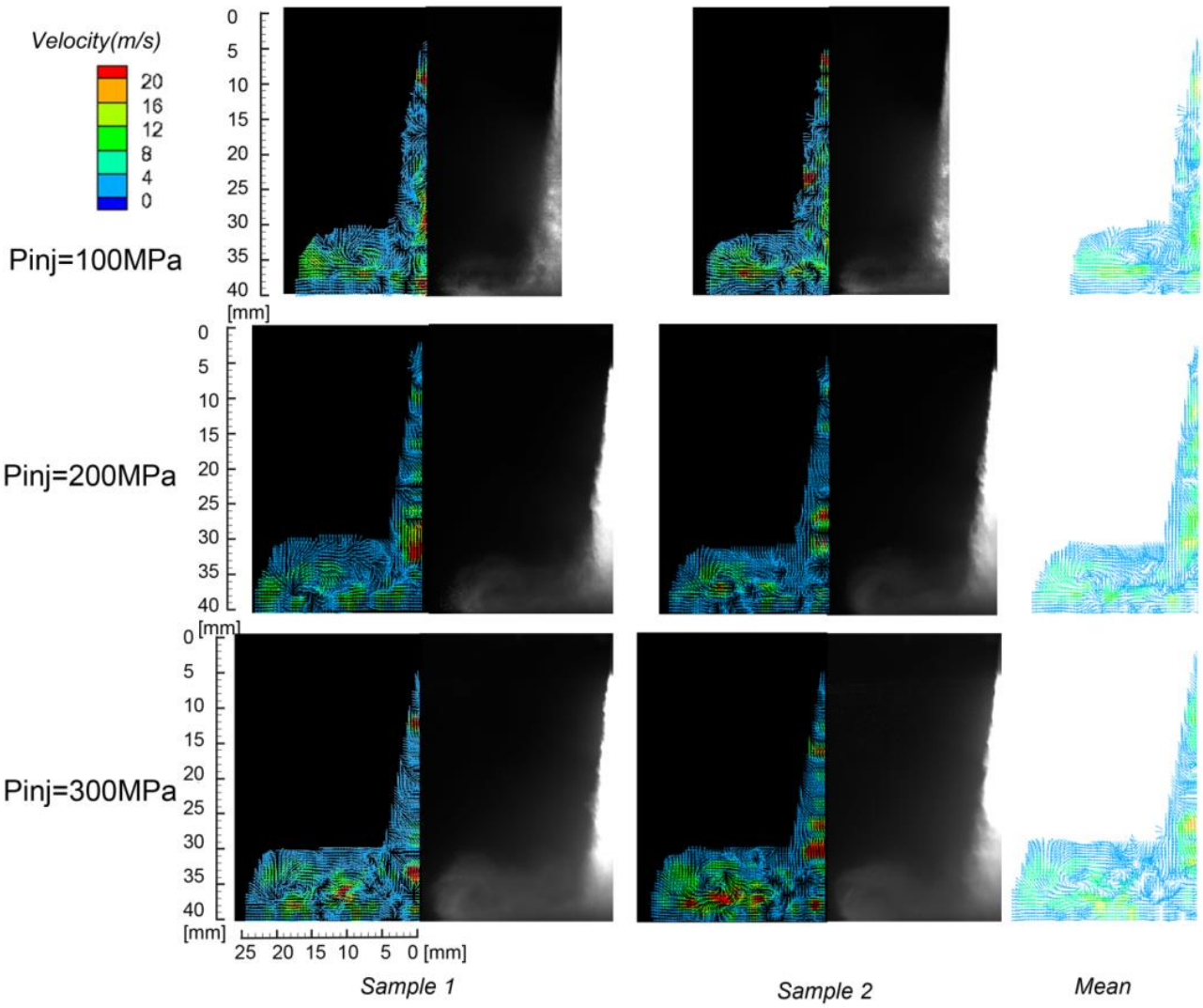

(b) Z=40mm

Figure 6.2 Effects of Injection Pressure and Impingement Distance on Droplets Flow Field (1.5ms ASOI)

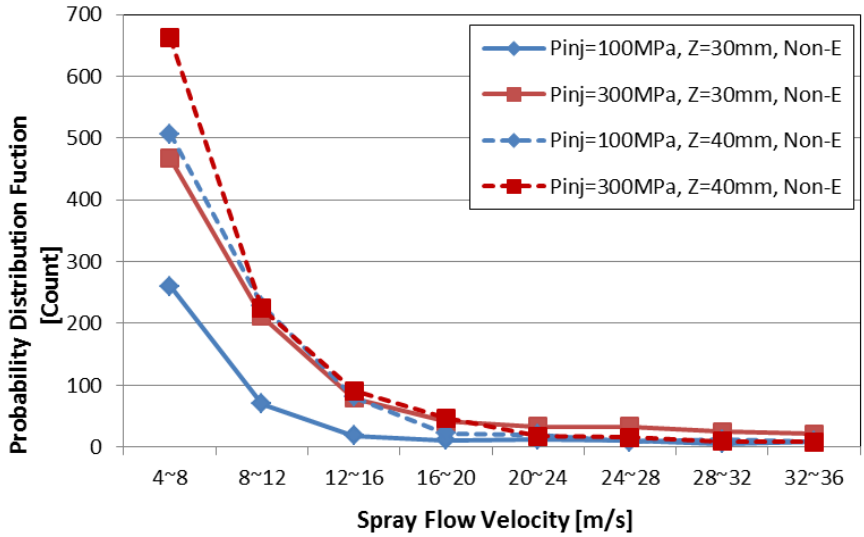

Figure 6.3 Probability Distribution Function of Flow Velocity (1.5ms ASOI)

By using the equation (5.1) proposed in Chapter 5, the results of vorticity intensity distribution of the wall-impinging spray are shown in Fig. 6.4. Figure 6.5 summarizes the probability distribution function of vorticity intensity. As mentioned above, the increase of fuel injection pressure effectively improves the vorticity intensity, which implies the promotion of the turbulent mixing process of the fuel/gas mixture. The vorticity intensity tends to be improved with the decrease of the impingement distance especially at the post-impingement spray region. This is considered to be related to the larger pushed-out ambient gas velocity at the tip region under the shorter impingement distance condition. The stronger vorticity motion will also result in the restricted spray penetration length. Figure 6.6 summarizes the comparison of probability distribution function of flow velocity and vorticity intensity between free spray and impinging spray. The impinging spray results in a decreased mean flow velocity distribution due to the restrain of the wall. On the other hand, the mean vorticity intensity increases with the reduction of impingement distance. Compared with the previous ambient gas flow measurement, the impinging spray restricts the total ambient gas flow, however, the increased vorticity intensity implies that the turbulent mixing and mixture formation tend to be improved.

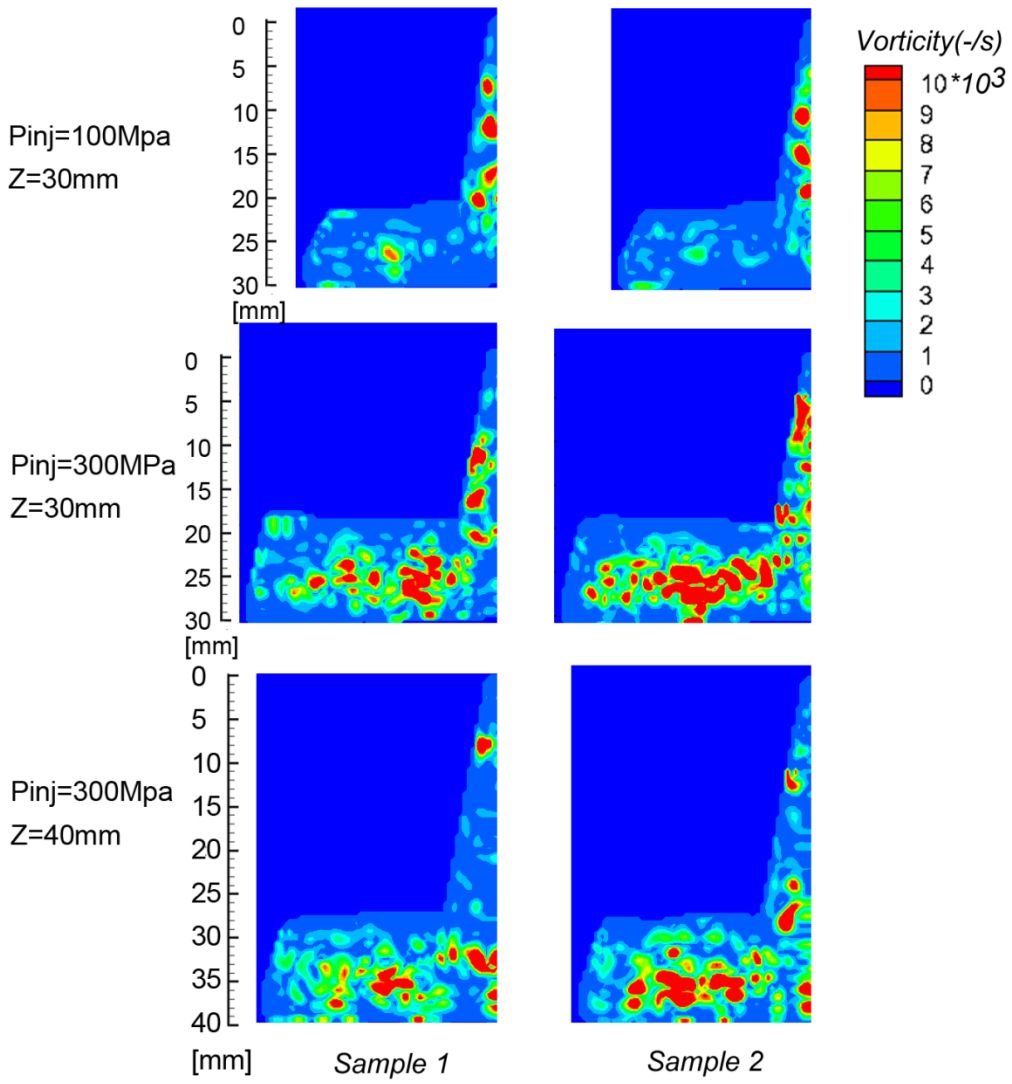

Figure 6.4 Vorticity Intensity Distribution of Wall-Impinging Spray (1.5ms ASOI)

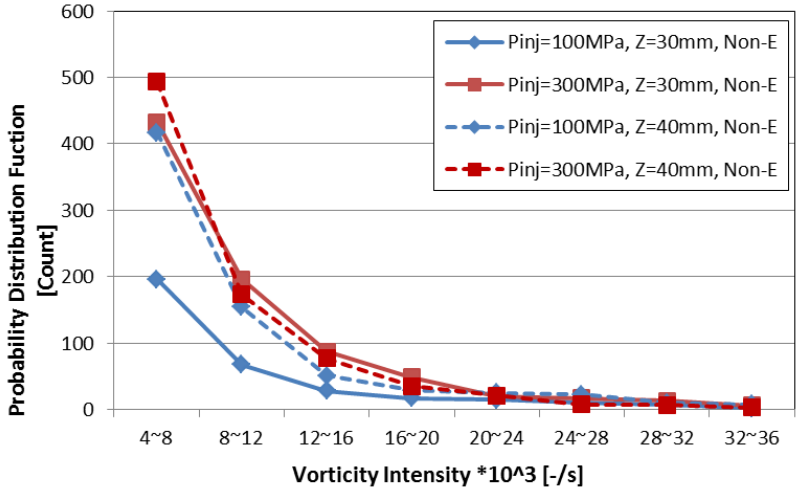

Figure 6.5 Probability Distribution Function of Vorticity Intensity (1.5ms ASOI)

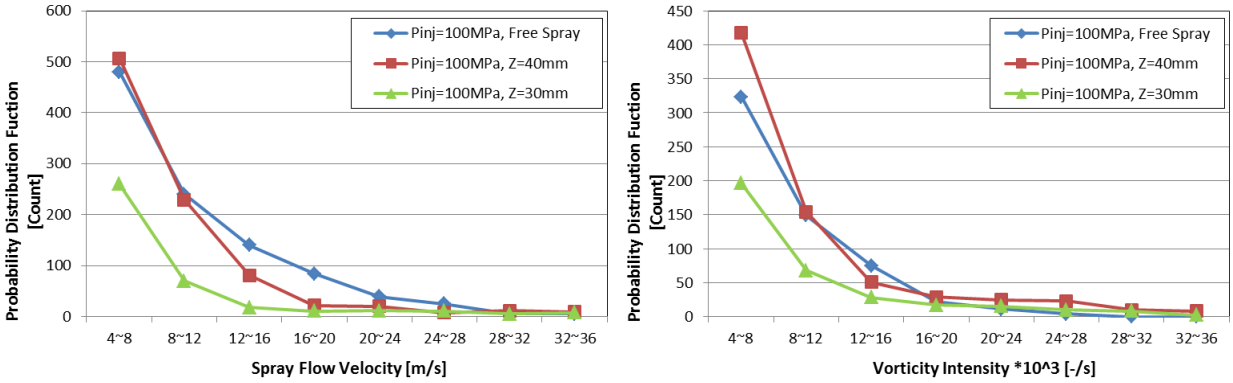

(a) PDF of Flow Velocity (b) PDF of Vorticity Intensity

Figure 6.6 Comparisons between Free Spray and Impinging Spray (1.5ms ASOI)

6.3 FLOW FIELD IN EVAPORATING CONDITION

Figure 6.7 shows the vapor phase flow of the wall-impinging spray under evaporating condition under the injection pressure of 100MPa. Figure 6.8 shows the comparison of probability distribution function of velocity and vorticity intensity with the non-evaporating impinging spray. Compared with the results of mean velocity distribution under non-evaporating condition in Fig. 6.1, the evaporating condition shows a higher value especially near the wall, the friction from the flat wall should be lower than the non-evaporating condition because of the less influence of the liquid film. The same as the result of the free spray, it is found that vorticity intensity or the small scale turbulent mixing is considerably improved under the evaporating condition, which would restrain the spray development but improve the uniform mixture formation.

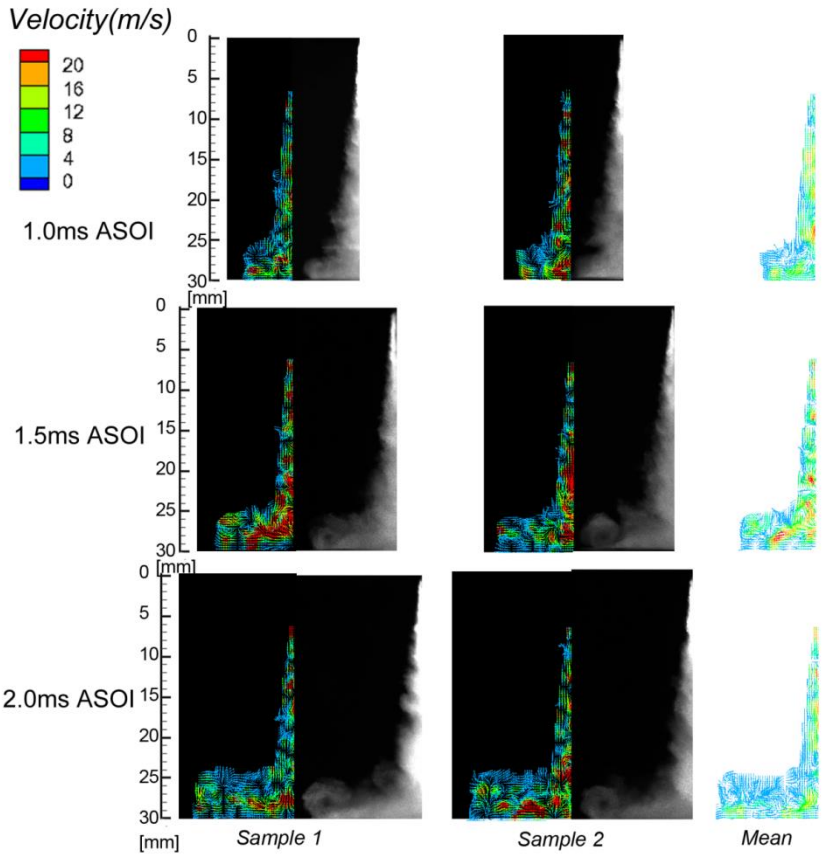

Figure 6.7 Vapor Phase Flow of Wall-impinging Spray under Evaporating Condition (P_{inj}=100MPa)

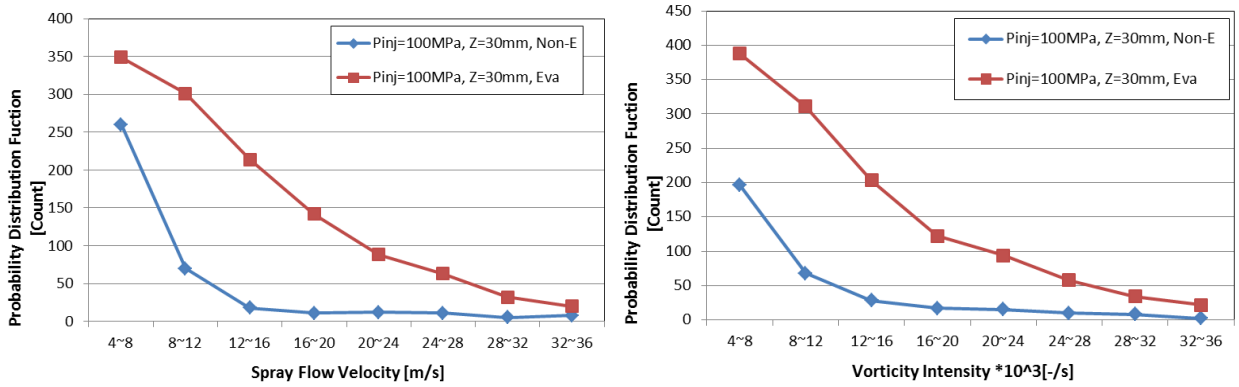

(a) PDF of Flow Velocity (b) PDF of Vorticity Intensity

Figure 6.8 Comparisons between Free Spray and Impinging Spray (1.5ms ASOI)

6.4 SUMMARY

The internal flow field of the flat-wall impinging spray was measured using PIV technique under the non-evaporating and evaporating conditions. Several conclusions are summarized and presented as follows:

1. In the free spray region prior to the wall impingement, the spray droplets move downwards straightly with high velocity. After wall impingement the spray droplets move towards the radial direction and lose the momentum gradually due to the friction with the liquid film.
2. A large scale wall-jet vortex motion can be found in the upper part of the post-impingement spray region. As a result, the "recirculation section" forms in this region, in which a large amount of ambient gas move back towards the impinging point with the spray droplets.
3. The increase of fuel injection pressure improves the mean velocity value, the vorticity intensity, which implies the promotion of the turbulent mixing process of the fuel/gas mixture.
4. The vorticity intensity tends to be improved with the decrease of the impingement distance especially at the post-impingement spray region. This is considered to be related to the larger pushed-out ambient gas velocity at the tip region under the shorter impingement distance condition. Compared with the previous ambient gas flow measurement, the impinging spray restricts the total ambient gas flow, however, the increased vorticity intensity implies that the turbulent mixing and mixture formation tend to be improved.
5. The evaporating condition shows a higher value of mean flow velocity especially near the wall, the friction from the flat wall should be lower than the non-evaporating condition because of the less influence of the liquid film.
6. The vorticity intensity or the small scale turbulent mixing is considerably improved under the evaporating condition, which would restrain the spray development but improve the uniform mixture formation.

CHAPTER 7 IGNITION AND COMBUSTION PROCESS OF DIESEL SPRAY

7.1 EXPERIMENTAL CONDITION

The characteristics of the combustion process of the Diesel spray were investigated using the direct imaging of natural flame luminosity, OH* chemiluminescence imaging and two color pyrometry techniques. The combustion behaviors were related to the previously mentioned spray evolution and ambient gas motion features. Table 7.1 shows the experimental conditions in the spray flame measurements. Two nozzle hole sizes (0.08mm and 0.12mm), three injection pressures (100MPa, 200MPa and 300MPa) were used. The three ambient gas densities (11, 15 and 20 kg/m^3) corresponds to the real engine in-cylinder conditions at the -20deg.ATDC, -10deg.ATDC, -5deg.ATDC in which the fuel injection starts. For all the measurements the injection duration was kept the same (2.2ms) to get the quasi-steady state spray.

The setting of camera parameters was adjusted according to the light intensity level. The natural flame luminosity is particularly sensitive under the different ambient conditions, to avoid the saturation of the dynamic range of the 8 bit image (with the maximum value of 256), the exposure time was set to 1/10,000s under the ambient density of 11 kg/m^3, and 1/1,000,000s under the ambient density of 15 and 20 kg/m^3. The visible lens aperture was set to f/4. For the OH*chemiluminescence, the UV lens aperture was set to f/4.5. The exposure time was set to 1/10,000s. The gain and width value of the image intensifier control unit were set to 60-70 and 40-90μs. For the two color pyrometry, the 50mm visible lens was connected to the two color box. The aperture of f/8 was used, which had been used for the calibration in advance. The exposure time was set to 1/10,000s. For all the measurement, the image resolution of 512*512 pixels and the frame rate of 10,000 (1/s) were selected.

Table 7.1 Experimental Conditions

Nozzle Diameter (mm)	0.08, 0.12		
Injection Pressure (MPa)	100, 200, 300		
Injection Duration (ms)	2.2		
Spray Type	Free Spray	Flat Wall-Impingement Spray (Z=30mm; Z=40mm)	
Ambient Gas	Air		
Ambient Gas Density (kg/m^3)	11	15	20
Ambient Temperature (K)	797	885	900
Ambient Pressure (MPa)	2.6	4	5.5

7.2 FREE DIESEL SPRAY MEASUREMENT

7.2.1 Direct Photography of Spray Flame

The flame natural luminosity comes primarily from the soot incandescence and chemiluminescence. In the highly sooting flames like those in the typical Diesel engine, the natural luminosity is dominated by the thermal radiation from combustion-heated soot particles in the flame with a broadband emission spectrum. The contribution of the luminous soot at various depths along the line of sight of the natural luminosity image depends on the soot concentration and temperature in the plume.

Figure 7.1 shows the natural flame luminosity as a function of time after the start of fuel injection with the different injection pressures. Correspondingly, the Mie-scattering images of the non-evaporating spray at the same timing are shown above the flame images. The fuel emerging from the nozzle orifice atomizes and vaporizes, and the vapor undergoes immediately thermal cracking, generating a number of saturated and unsaturated split hydrocarbons. Some of them decompose and form the poly-aromatic hydrocarbons (PAH), which are known as the soot precursor [Kitamura et al., 2002]. The appearance of the soot incandescence is determined by the position where the soot formation becomes dominant over the soot oxidation. It is evident that the positions of the soot luminosity are around the spray tip region for all the cases. Most of the soot will be oxidized at the thin periphery of spray tip due to the strong turbulent mixing with

ambient gas. The soot luminosity region moves downstream together with the spray development. Aizawa et al. [2002] studied the young soot formation by LII technique and concluded that the soot precursor exists mainly in the central and upstream region of the spray, the young soot particles are thinly distributed in the spray periphery.

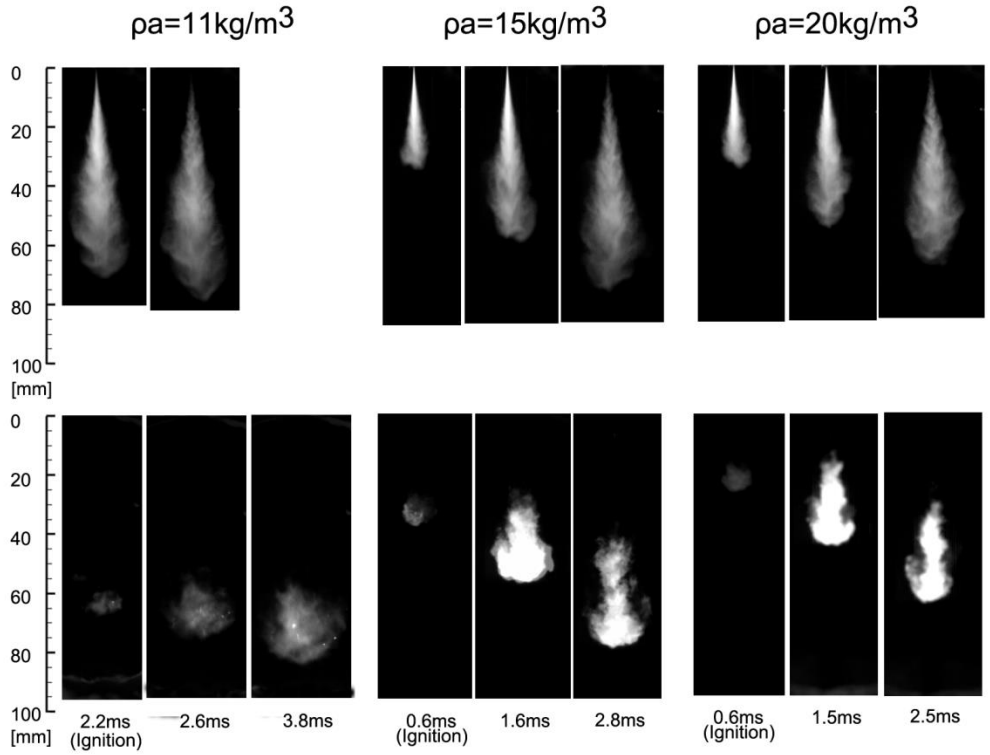

(a) P_{inj}=100MPa

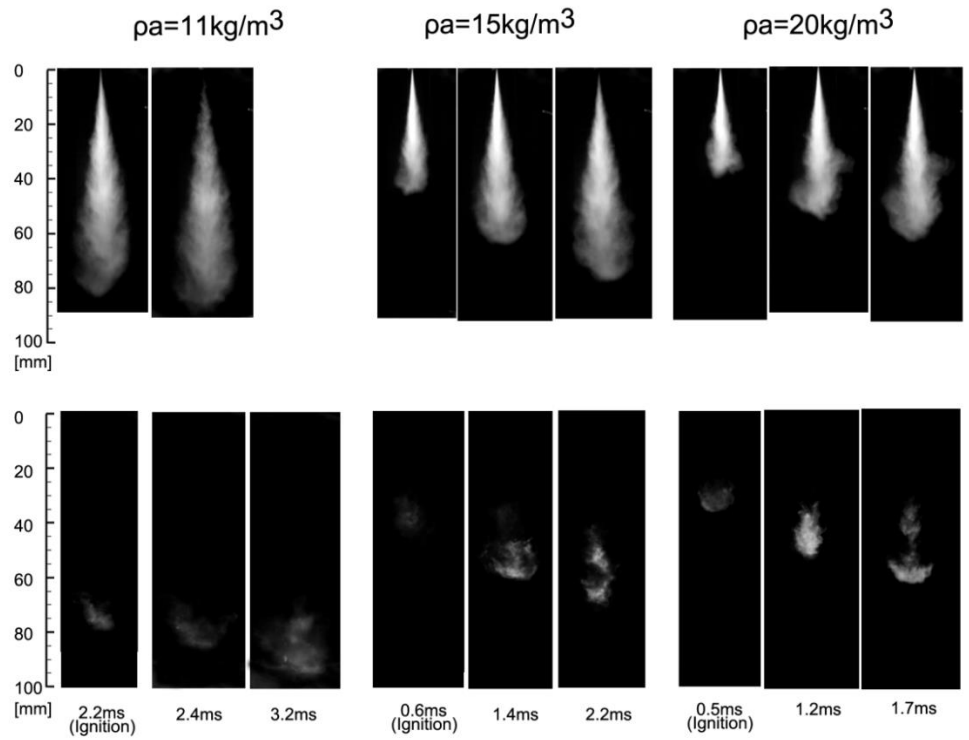

(b) P_{inj}=200MPa

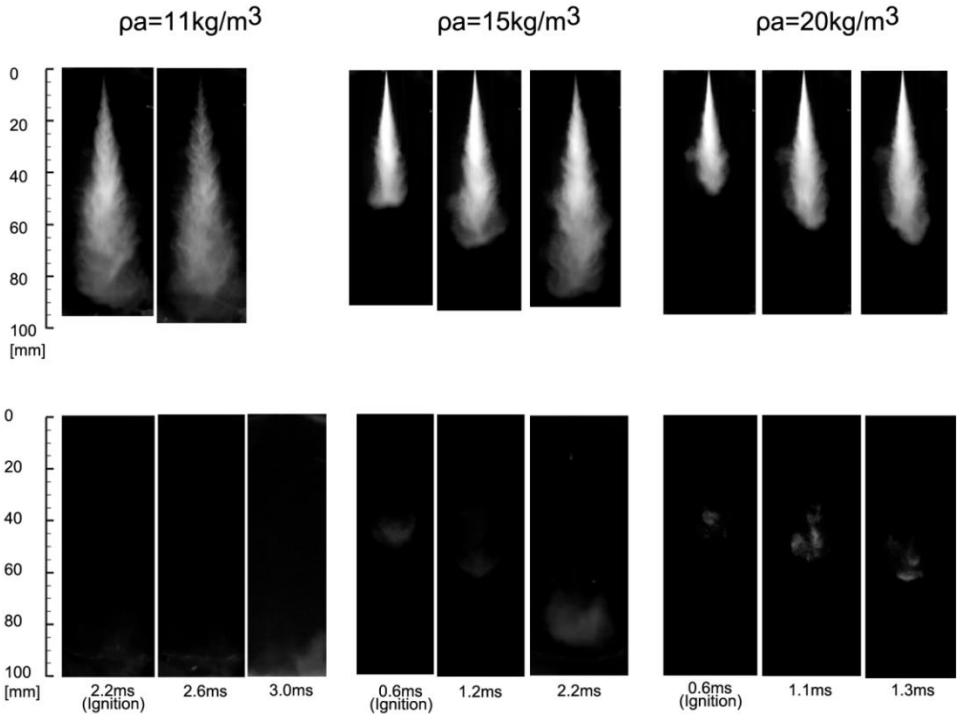

(c) P_{inj}=300MPa

Figure 7.1 Distribution of Natural Flame Luminosity (D=0.08mm)

Figure 7.2 quantitatively indicates the temporal variation of the integrated natural flame luminosity under the three ambient density conditions with the nozzle hole size of 0.08mm. All the data used in this analysis are the averaged results from at least four shots of spray flame samples. In order to eliminate the possible image noise, a threshold (10-256) was applied to extract the light intensity information.

Generally, the lower ambient gas density significantly decreases the flame luminosity value. In this study, the lower ambient gas density, which corresponds to the lower ambient pressure and temperature, significantly postpones the inception of the soot formation even after EOI, which provides enough time for forming the lean fuel/air mixture, as a result, the formation of soot is restrained. Bobba et.al [16] studied that the first soot formation timing is roughly coincident with the premixed Heat Release Rate peak in the fuel rich premixed combustion phase. If the premixed HRR peak occurs near or after EOI, that means a much longer time for the mixing process of injected fuel and surrounding air, the leaner combustible mixture leads to lower soot concentration level and lower soot temperature. Meanwhile, the visible flame area is constrained in the upstream under the higher ambient gas density condition due to the shorter spray tip penetration, which implies that less ambient gas can be entrained from the side periphery. The ambient gas mass entrained form the side periphery is critical to the premixed combustion phase. Even though the higher ambient gas density leads to the higher soot temperature, which also enhances the flame luminosity level, the soot concentration is still believed to be the prominent factor to determine the flame luminosity value.

Meanwhile, the flame luminosity value and area also decrease with the increase of fuel injection pressure. However, the injection pressure value tends to have little impact on the appearance timing of the soot incandescence. Particularly in the case of 300MPa, the flame luminosity is almost invisible in the three ambient conditions. Although the duration from the start of injection to the inception of soot luminosity under the higher ambient gas density condition is much shorter as mentioned above, the soot formation still keeps the low level, which implies the advantage of ultra-high injection pressure for improving the fuel/air mixing rate. The combination of high injection pressure and micro-hole nozzle considerably reduces the time required for forming a lean mixture. As the fuel/gas mixing is proceeding in the diffusive combustion, soot is oxidized gradually after reaching the peak value.

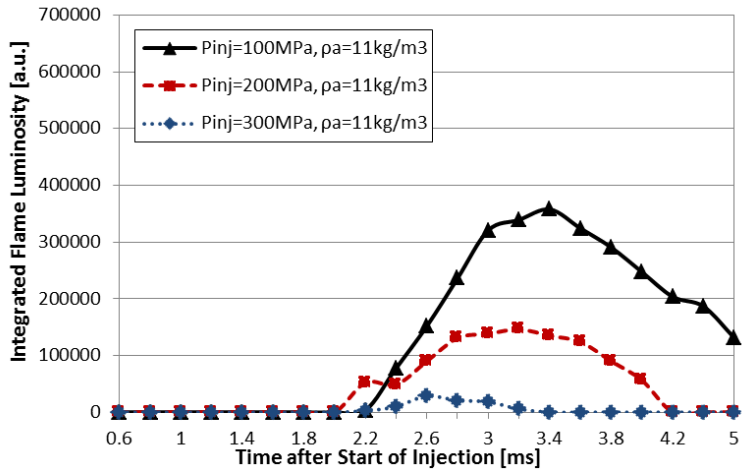

(a) ρ_a =11 kg/m^3

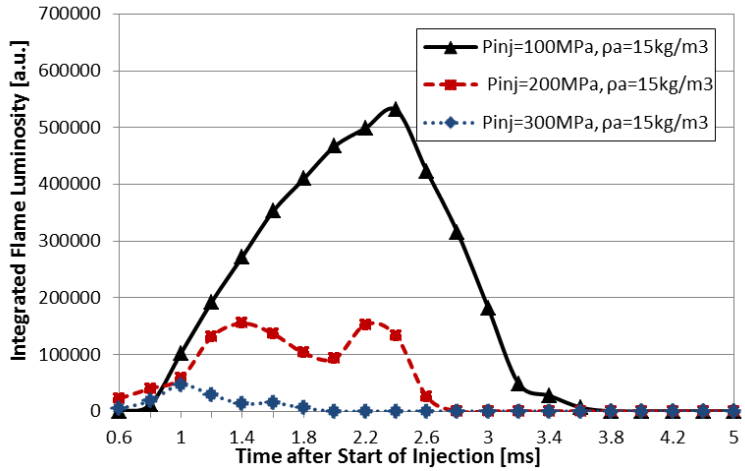

(b) ρ_a =15 kg/m^3

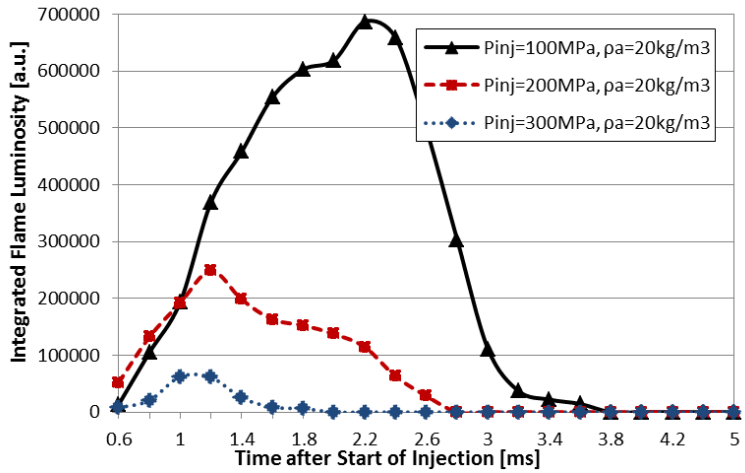

(c) ρ_a =20 kg/m^3

Figure 7.2 Temporal Variation of Integrated Natural Flame Luminosity (D=0.08mm)

7.2.2 OH* Chemiluminescence Results

As mentioned in Chapter 2, the light emission with the wavelength of 310nm is dominated by the chemiluminescence from exited-state OH (OH*). OH* is short-lived and results from the exothermic chemical reactions in near-stoichiometric, high heat release region [Gaydon, 1974], which is used as a marker to identify the initiation of the auto ignition. Several studies [Tinaut et al., 2010; Price et al., 1968] concluded that the maximum value of OH* emission coincides with the peak of heat release ratio. Tinaut et al. [2010] also pointed out that the OH*/CH* ratio is linearly dependent on the local equivalent ratio. Ikegami et al. [2009] concluded that the intermediate OH* radical is highly reactive in such reactions as soot oxidation and NO formation.

Figure 7.3 shows the OH* chemiluminescence images as a function of time after the start of fuel injection with the different injection pressure and nozzle hole size. Correspondingly, the Mie-scattering images of the non-evaporating spray at the same timing are shown above the flame images. The timing of the first flame image shown in Fig. 7.3 is referred to as the initiation of the auto ignition. The increase of the fuel injection pressure and the ambient gas density reduces the ignition delay due to the rapid fuel/gas mixing (physical process) and exothermic reaction (chemical process). Because the difference of ambient gas temperature for the ambient gas density of 15 and 20 kg/m^3 is not so much, the ignition delay does not differ a lot. It is predicted that the ignition delay of lower ambient gas density (11 kg/m^3) would be much longer. Compared with the timing shown in Fig.7.2, it is found that the appearance of flame natural luminosity is 0.2-0.3ms earlier than that of OH* chemiluminescence. Dec et al. [1998] studied the spectra of the sooting flame chemiluminescence and suggested that in the early combustion stage, the CH (peak at 430nm) CH_2O (368-470nm) are dominant, the OH signal (310nm) is weak. Actually, the mixture downstream in the cool chemical reaction range is too rich (with high equivalence ratio 2-4) to produce significant OH [Dec, 1997]. The OH chemiluminescence becomes active when reaching the early sooting combustion stage. As a conclusion, the natural luminosity appears at the early stage is originated from other radicals, the low OH* signal is masked. However, OH* is proper to mark the high temperature exothermic reaction. It is worth noticing that upper boundary of the OH* signal keeps stable after the spray reaches the quasi-steady state. The upper boundary is determined by the equilibrium of the upstream turbulent mixing rate and the downstream chemical reaction rate. While the lower boundary of the OH*

signal moves downstream with the spray development, the position almost overlaps with the natural luminosity.

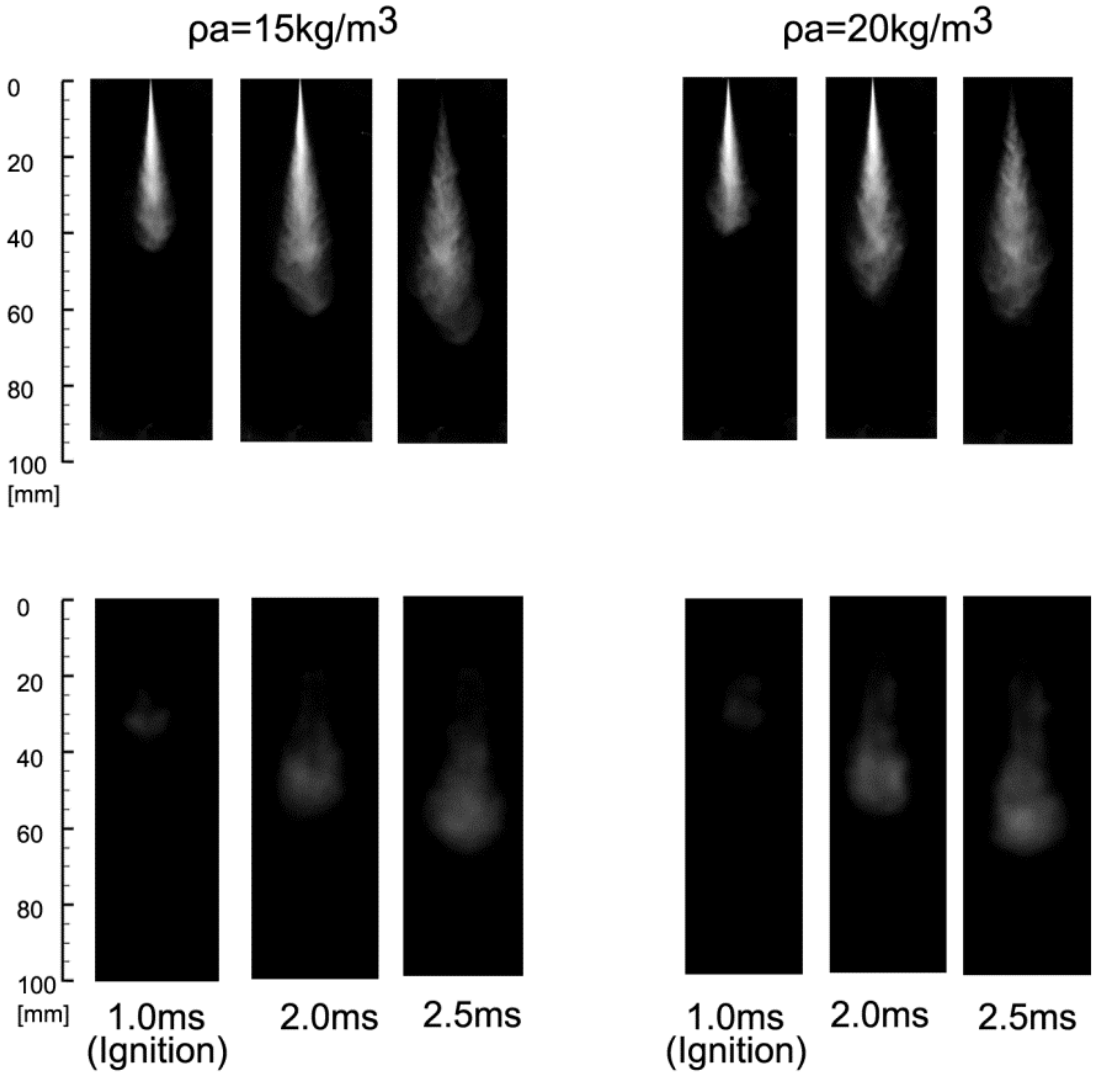

(a) P_{inj}=100MPa, D=0.08mm

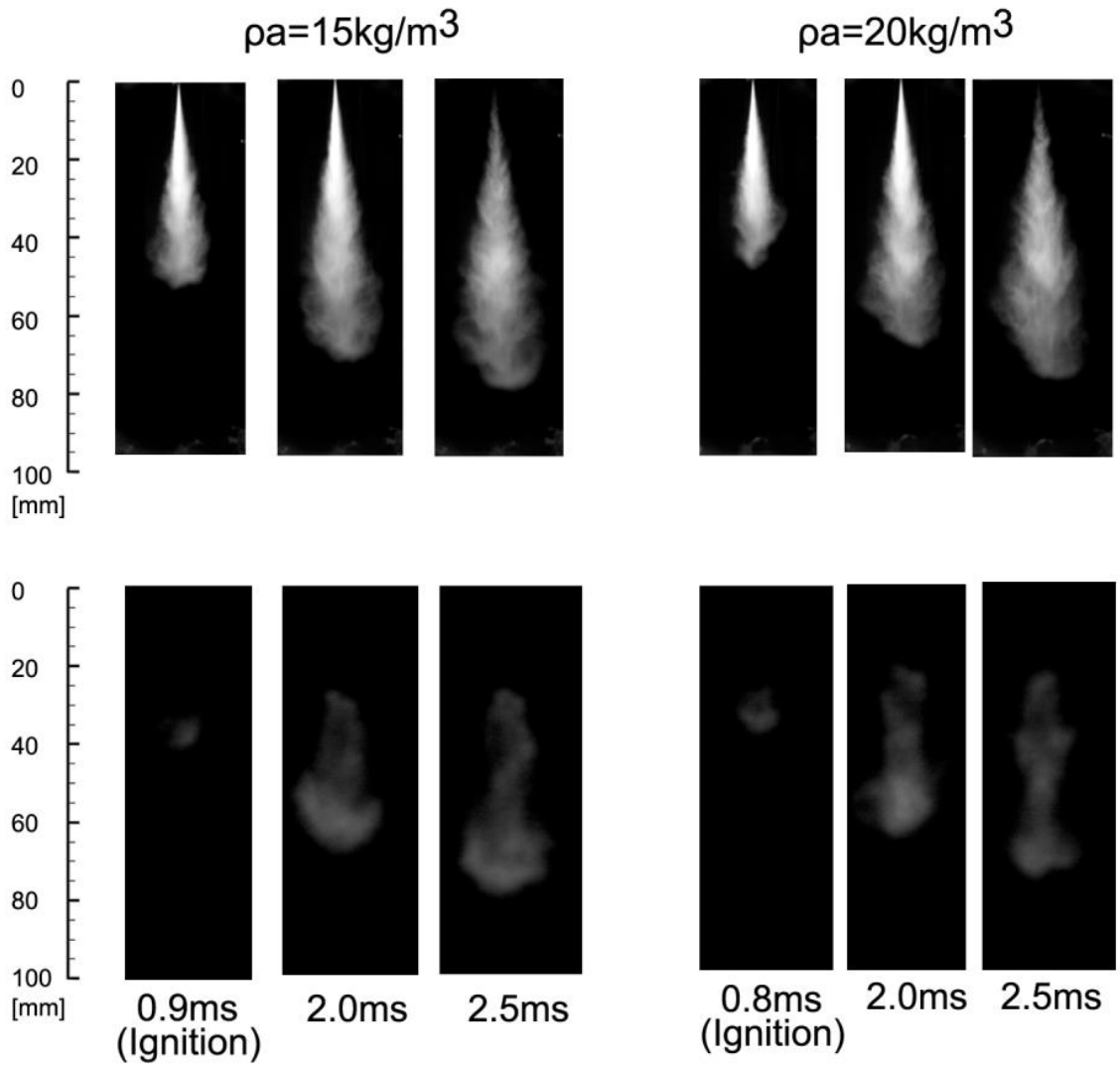

(b) P_{inj}=200MPa, D=0.08mm

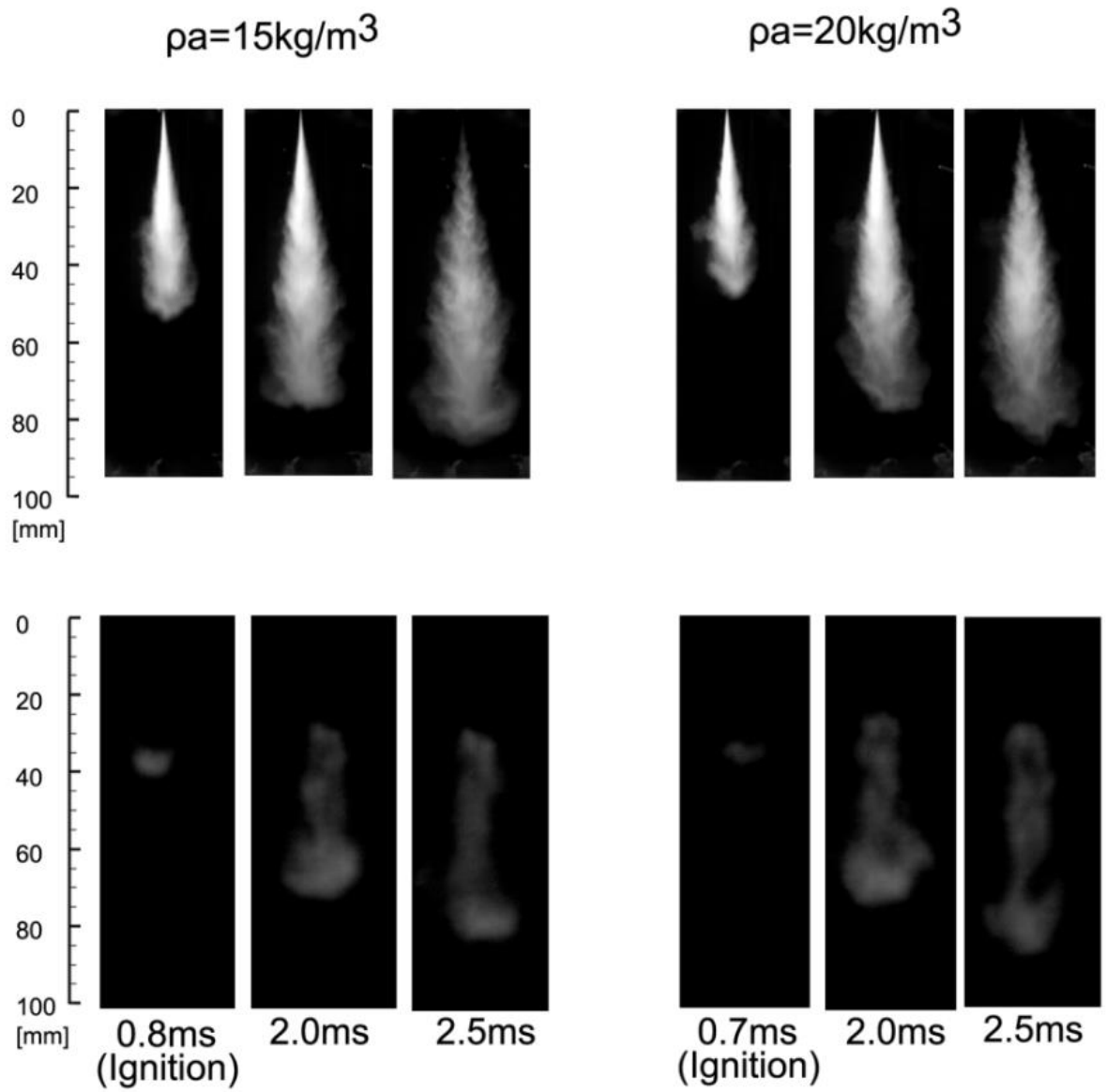

(c) P_{inj}=300MPa, D=0.08mm

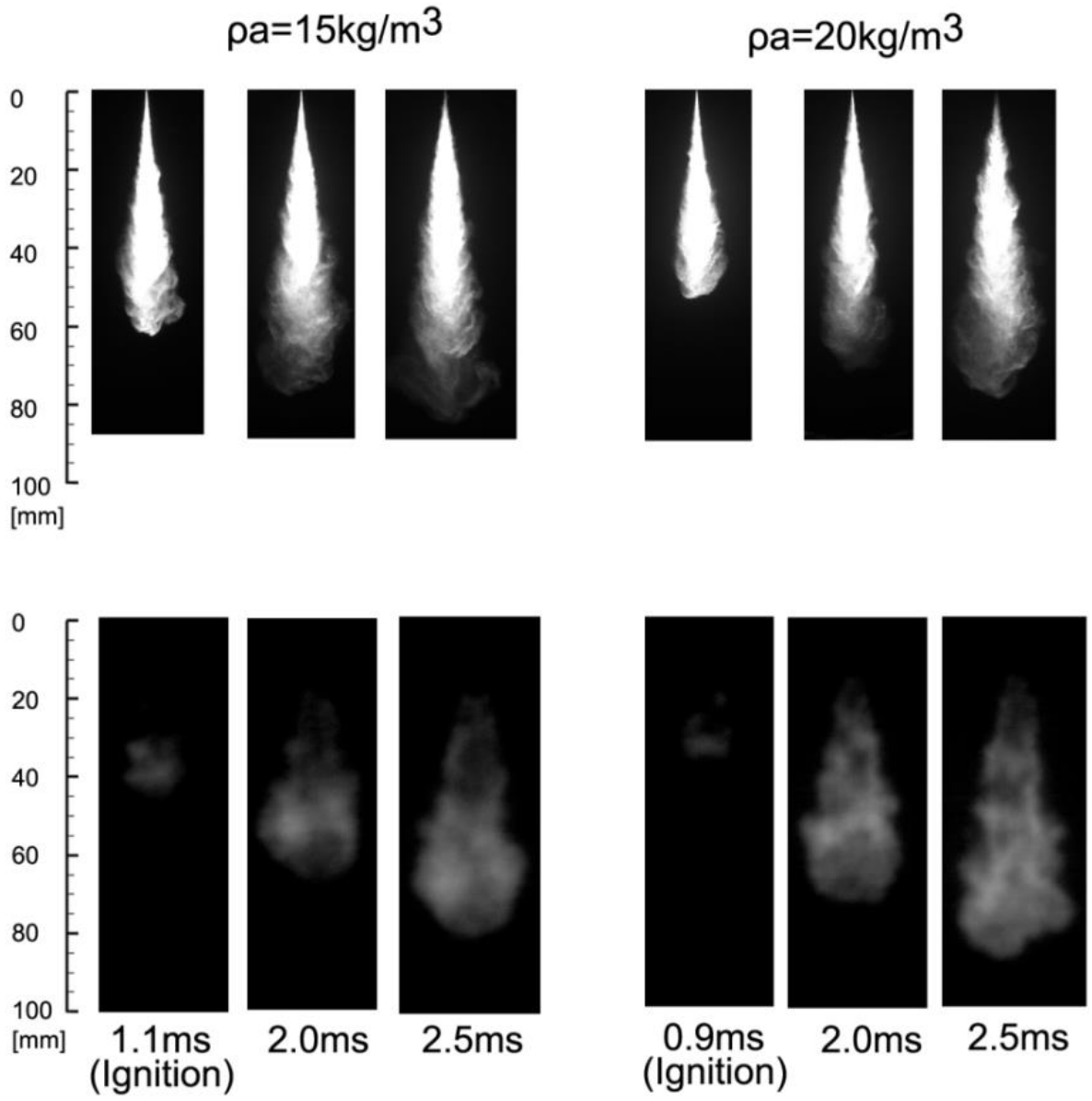

(d) P_{inj}=100MPa, D=0.12mm

Figure 7.3 Spatial Distribution of OH* Chemiluminescence

Figure 7.4 quantitatively indicates the temporal variation of the OH* chemiluminescence intensity. Generally, the increase of the fuel injection pressure and the decrease of the ambient gas density tends to slightly reduce the OH* intensity since the formation of the leaner mixture reduces the combustion temperature. On the other hand, the increase of nozzle hole size significantly increases the ignition delay and the OH* signal intensity. More time is required for fuel atomization and vaporization due to the increased fuel mass flow rate and larger droplets

size. Two reasons for the high OH* intensity: the relatively rich fuel/gas mixture results in higher combustion temperature; the injected fuel mass for 0.12mm is much larger.

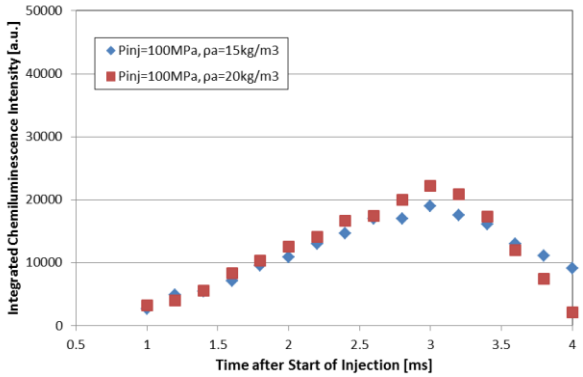

(a) P_{inj}=100MPa, D=0.08mm

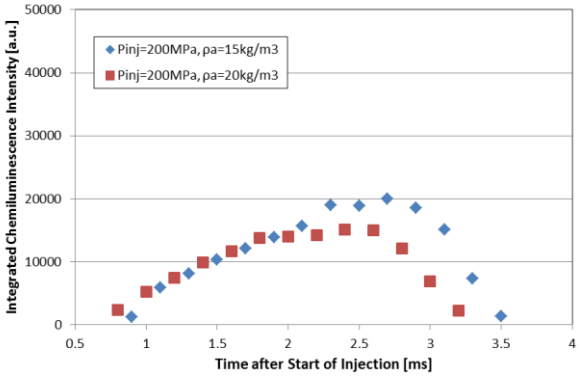

(b) P_{inj}=200MPa, D=0.08mm

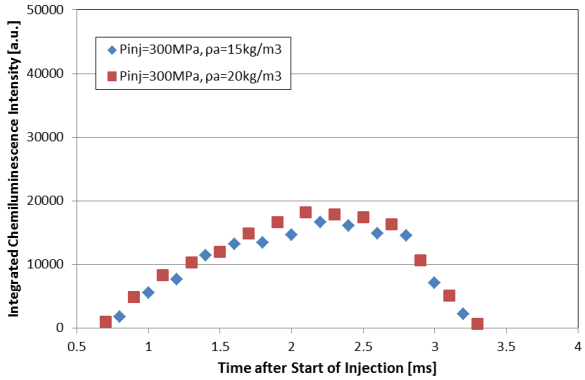

(c) P_{inj}=300MPa, D=0.08mm

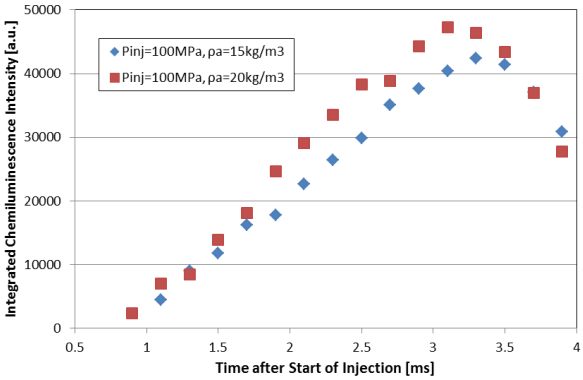

(d) P_{inj}=100MPa, D=0.12mm

Figure 7.4 Temporal Variation of OH* Chemiluminescence Intensity

The lift-off length is defined as the distance between the fuel injector tip and the upstreammost extent of combustion in the fuel jet. The rich, partially premixed combustion is believed to occur in the central region of the fuel jet just downstream of the lift-off length [Dec, 1997; Chomiak et al., 1996]. The air entrainment upstream of the lift-off length impacts the behavior of the rich, central reaction process. Siebers et al. [2001] applied the OH* signal to measure the lift-off length on a DI Diesel fuel jets under quiescent conditions. In this study, the same method was used on a quasi-steady Diesel spray.

Figure 7.5 indicates the comparisons of the lift-off length and the liquid length. The increase of injection pressure pushes the stable flame region further downstream and reduces the liquid length. Especially in the case of 0.08mm, when the injection pressure increases up to 200MPa, the lift-off length is longer than the liquid length, which implies that fuel vaporization

is complete before any combustion zone is reached. Therefore, no interaction will occur between the fuel vaporization process and combustion processes. For the larger nozzle hole size condition (0.12mm), the lift-off length is shorter than the liquid length, the central zone of the spray will have a relatively cool core that contains vaporizing liquid-phase fuel. This vaporizing core is surrounded most closely by the rich reaction zone which is believed to occur downstream of the lift-off length which in turn will be surrounded by the stoichiometric diffusion flame at the periphery of the burning spray [Dec, 1997; Kosaka et al., 1996]. The vaporization cooling will likely influence the combustion rate, especially at the flame stabilization location and combustion will most likely enhance the fuel vaporization rate. The vaporization cooling on the lift-off length will also lead to the reduction of the laminar flame speed and lengthening of the lift-off length. The soot formation is likely to be promoted due to the cooling effect. The increase of ambient gas density reduces the lift-off length and the liquid length simultaneously, thus its effect on the interaction of the combustion zone and the liquid zone becomes ambiguous.

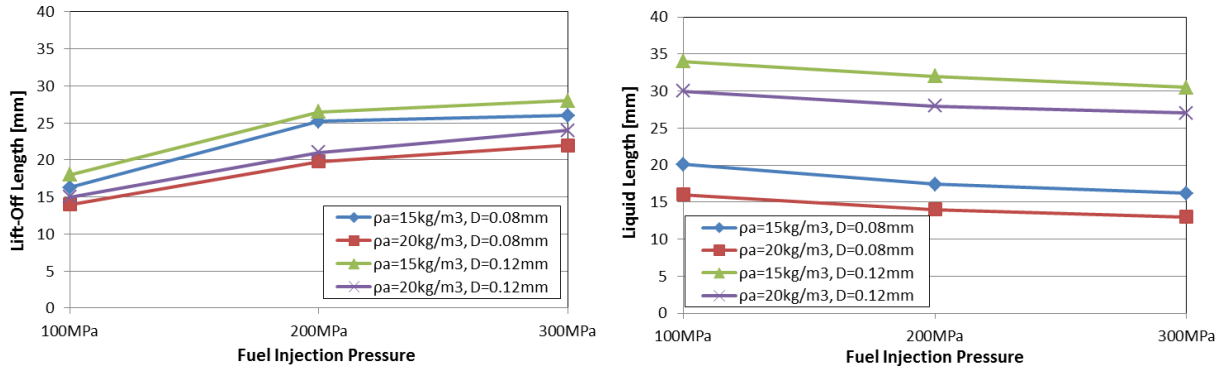

(a) Lift-off Length (b) Liquid Length

Figure 7.5 Comparisons of Lift-off Length and Liquid Length

By recalling the equations (7.1) and (7.2) which have been introduced in Chapter 1, Siebers et al. [2004] proposed a method to analyze the air entrained flow rate to the lift-off length as a percentage of the total air required to burn the fuel being injected according to the expression for the axial variation of the cross-sectional average equivalence ratio $\emptyset_{inst}$, which is shown in Eq. (1.15) in Chapter 1.

$$\zeta_{st}(\%) = \frac{100}{\emptyset_{inst}} = \frac{10}{3} \cdot \left(\sqrt{1 + 16 \cdot \left(\frac{L_0}{x^+} \right)^2} - 1 \right) \tag{7.1}$$

Where the L_0 is the lift-off length and x^+ is the characteristic length scale for the spray, defined as:

$$x^+ = \sqrt{\frac{\rho_l}{\rho_a}} \frac{\sqrt{C_a} \cdot D}{0.66 \cdot \tan(\alpha/2)} \tag{7.2}$$

Figure 7.6 compares the air entrainment percentage upstream of lift-off length from the predicted model and PIV results. The ambient gas entrainment upstream of the lift-off length at the timing of 2.0ms from the PIV measurement was used because it approaches the quasi-steady state. More air is entrained upstream of the lift-off length with the increase of injection pressure, the decrease of nozzle hole size and ambient gas density. The PIV result shows the similar trend but relatively larger value, because the ultra-high injection pressure effectively improves the air entrainment and forms the lean mixture much faster.

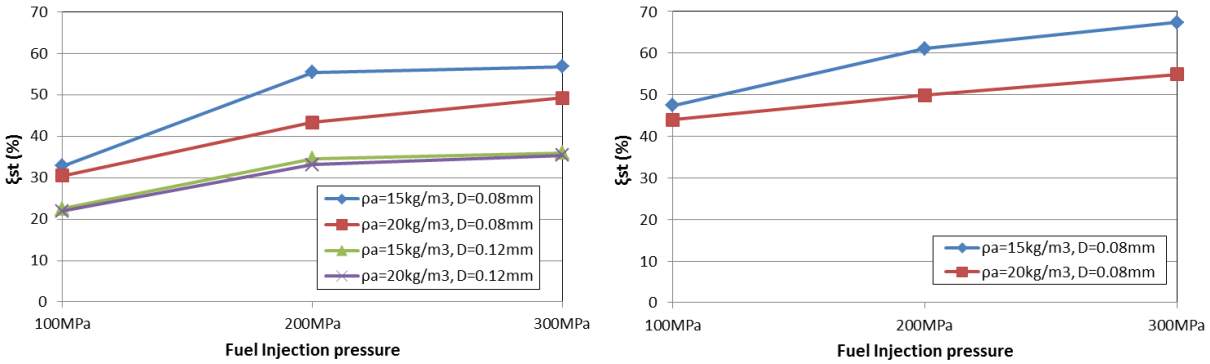

(a) Results from Predicted Model (b) Results from PIV Measurement

Figure 7.6 Comparison of Air Entrainment Percentage upstream of Lift-off Length

7.2.3 KL factor and Temperature Distribution of Spray Flame

The results of two color pyrometry provide the quantitative line-of-sight information of the soot formation and temperature distribution of a Diesel spray flame. Figure 7.7 shows the KL factor and the temperature distribution under the different conditions.

The maximum KL factor distributes near the flame tip region, which is consistent with the location where the natural luminosity appears. It implies large amount of soot clouds form in the inner region of the turbulent diffusive flame phase. While along the spray periphery especially at the spray tip, the relatively lower soot level can be observed, which coincides with the suggestion that most of soot will be consumed on the thin layer of the diffusive flame front during the strong mixing process with the ambient gas.

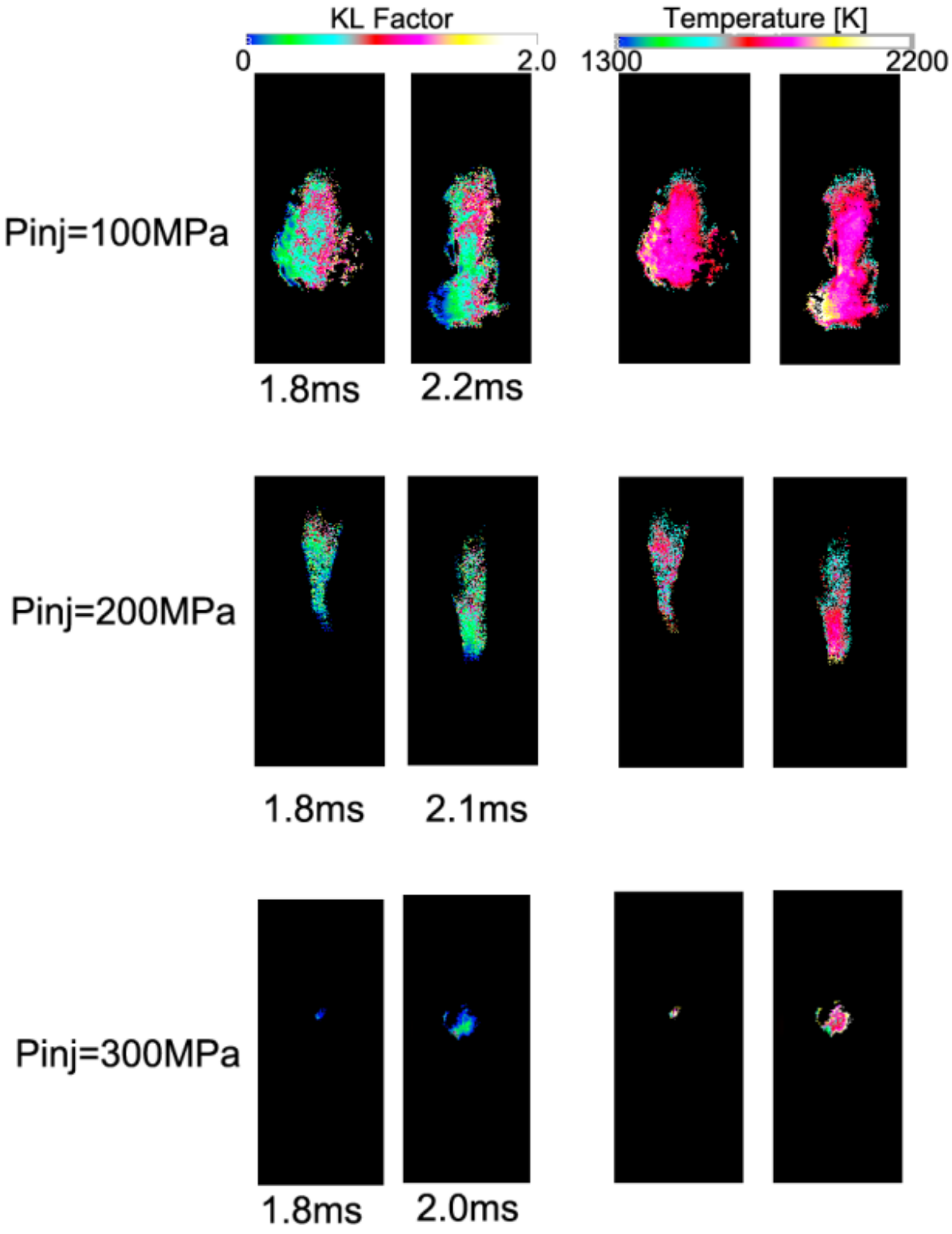

(a) ρ_a =15kg/m^3, D=0.08mm

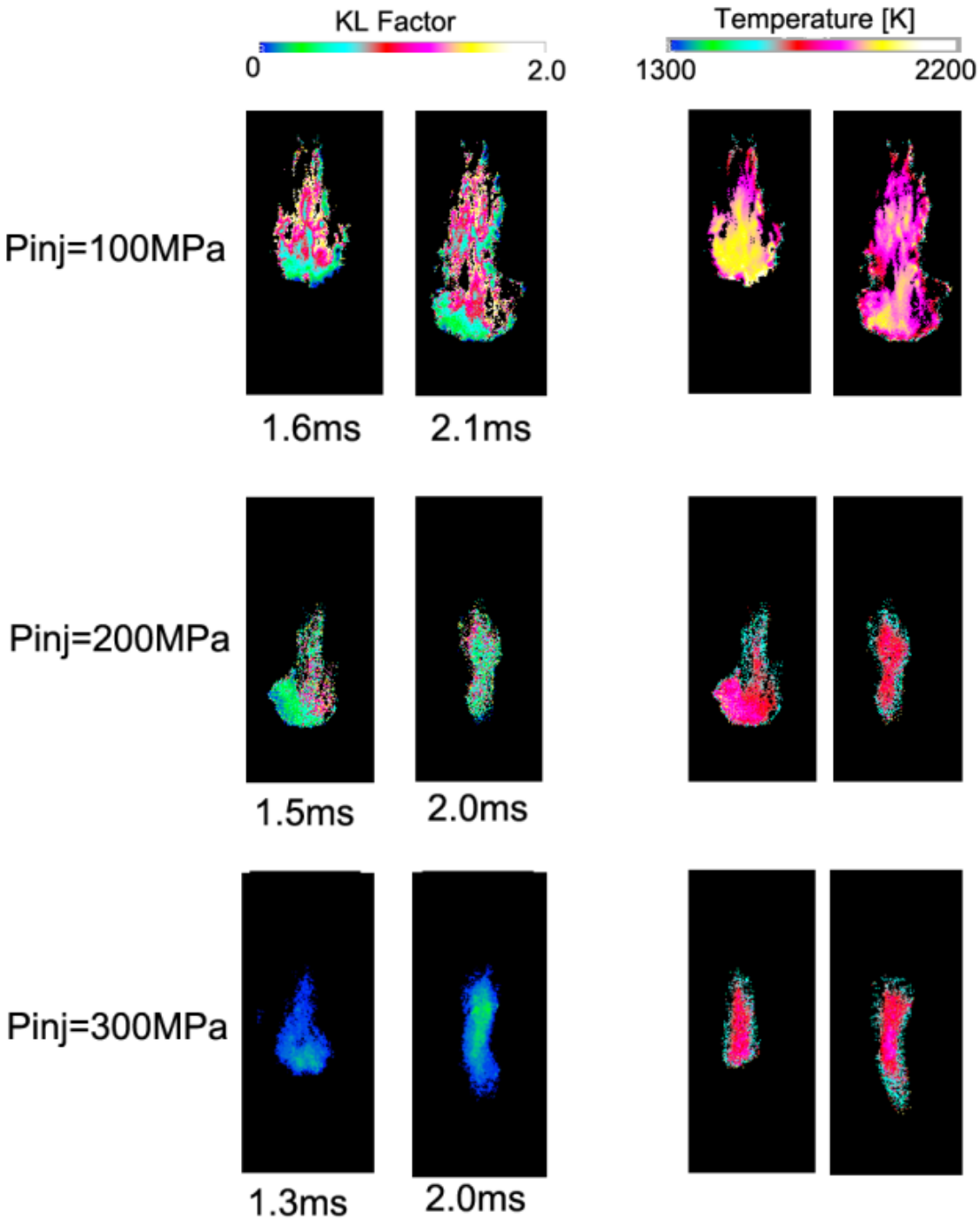

(b) ρ_a =20kg/m^3, D=0.08mm

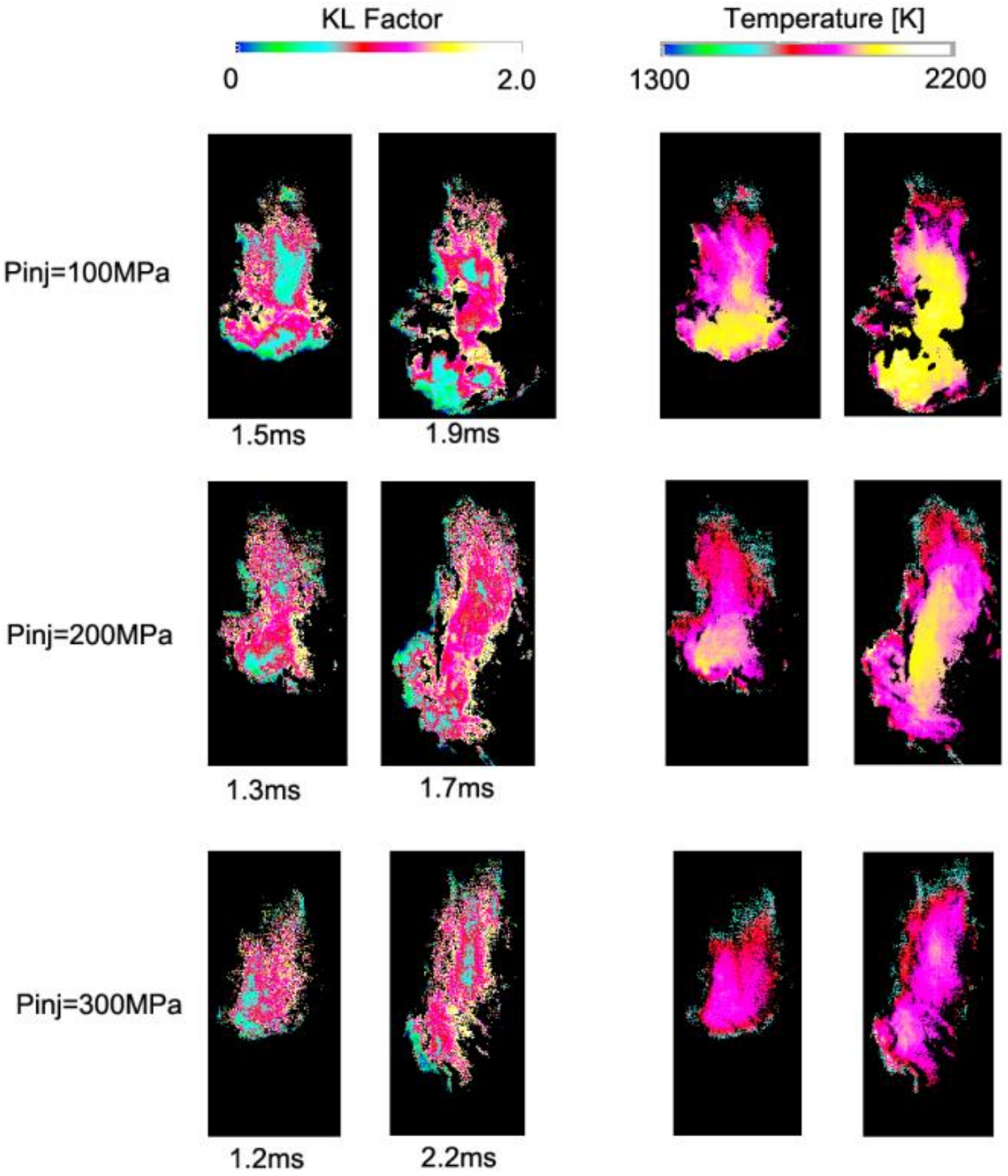

(c) ρ_a =15kg/m^3, D=0.12mm

Figure 7.7 Spatial Distributions of Flame KL Factor and Temperature

The temporal variation of flame integrated KL factor and temperature is shown in Fig.7.8. The reduction of ambient gas density apparently lowers the soot level of the flame, which is

attributed to the longer ignition delay. It allows the formation of leaner fuel/gas mixture prior to the auto-ignition. Correspondingly, the flame temperature also decreases with the reduction of ambient gas density. Regardless of the ambient gas density, the ultra-high injection pressure significantly reduces the soot level and flame temperature. Especially under the injection pressure of 300MPa, the visible luminous flame region becomes very small. It almost achieves the non-sooting combustion. The decrease of the flame temperature due to the higher injection pressure and the lower ambient density is also believed to be the reason for the lower OH* signal intensity, as mentioned in Sec. 7.2.2. On the other hand, the use of larger nozzle hole size evidently increases the soot level, even though the ultra-high injection pressure was applied. As mention previously, the direction interaction of the liquid phase and the initial combustion phase under the larger nozzle hole size condition results in the rich fuel/gas mixture in the premixed combustion phase and larger amount of unburned or partially oxidized fuel fraction. As a result, the soot formation downstream will by promoted. It implies that combined usage of high injection pressure and small nozzle hole size is necessary to achieve the ultra-low soot emission level.

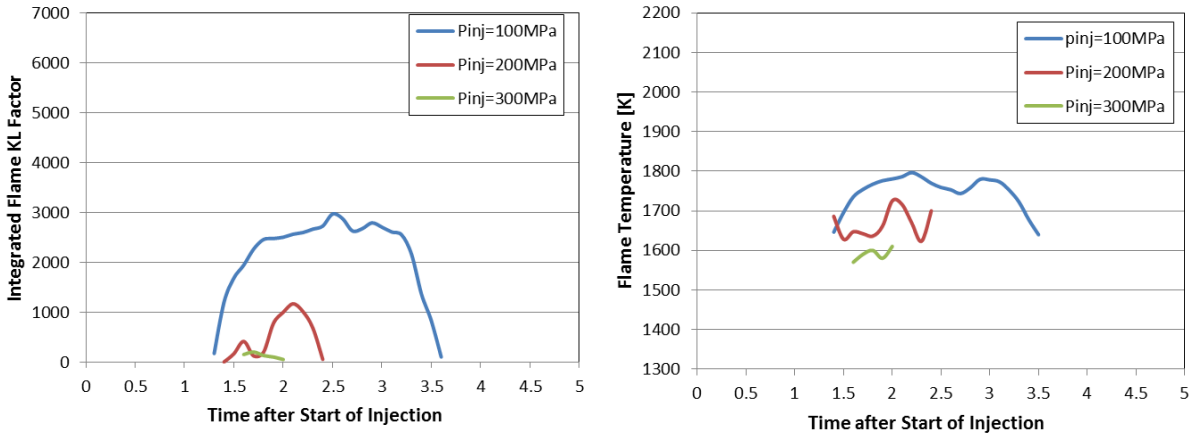

(a) ρ_a =15kg/m^3, D=0.08mm

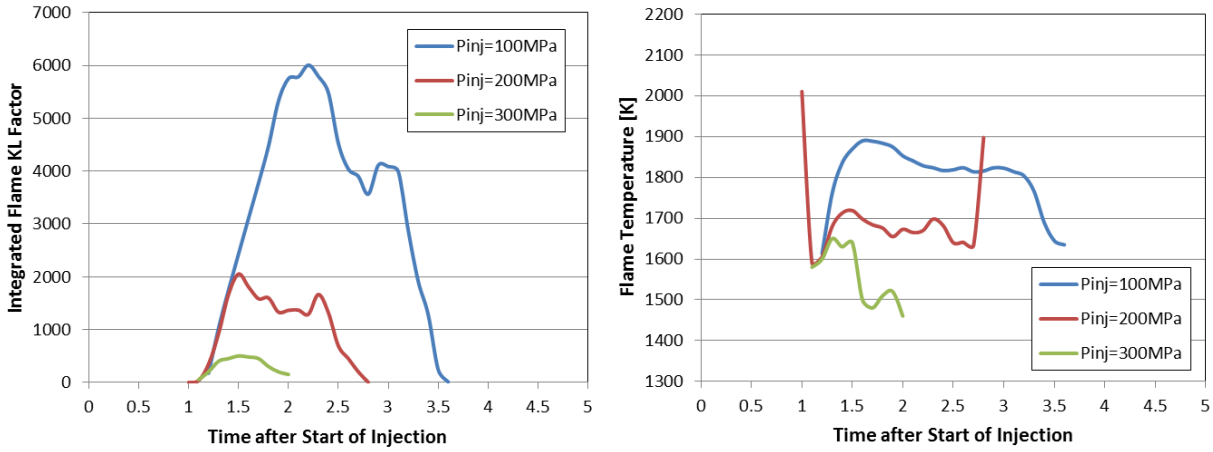

(b) ρ_a =20kg/m^3, D=0.08mm

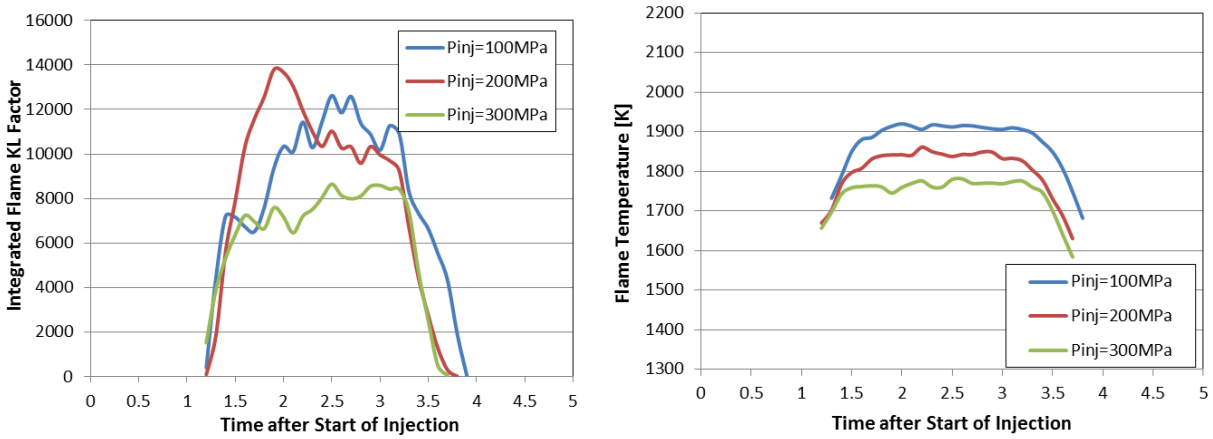

(c) ρ_a =15kg/m^3, D=0.12mm

Figure 7.8 Temporal Variation of Flame Integrated KL Factor and Temperature

7.2.4 Discussion of Relationship of Ambient Gas Entrainment and Combustion Feature

Even though the measurement of the ambient gas flow by LIF-PIV technique was carried out under the non-evaporating condition, it is still feasible to characterize the general relationship of the ambient gas entrainment and combustion feature.

Figure 7.9 summarizes the correlation of the ambient gas entrainment and the soot formation level. The horizontal axis is the ratio of ambient gas/fuel mass flow rate ($\dot{M}_a/\dot{M}_f$) upstream of the lift-off length. The lift-off length was obtained from the OH* signal, while the gas mass flow rate was the results of LIF-PIV measurement on the non-evaporating spray under the quasi-steady state. The vertical axis is the ratio of the integrated flame KL factor (at the

timing of 2.0ms ASOI) and the fuel injected mass. There is the tendency that the total soot mass decreases if more air is entrain from side periphery upstream of the lift-off length.

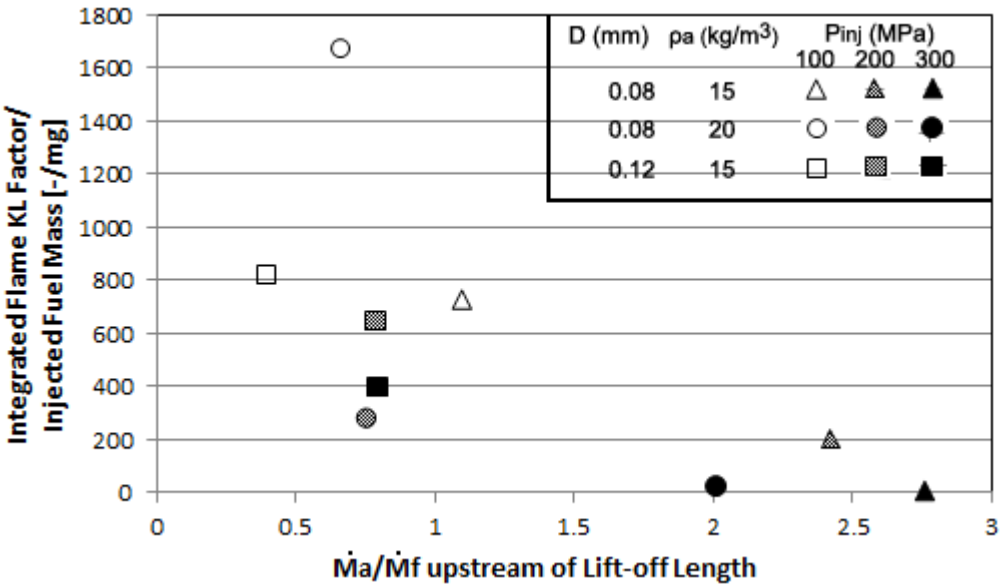

Figure 7.9 Correlation of $\dot{M}_a/\dot{M}_f$ Upstream of Lift-off Length and Integrated Flame KL Factor

Higher injection pressure promotes the break-up of the liquid droplets due to the increased aerodynamic force. As a result, more ambient gas is entrained from the side periphery, which leads to the shorter liquid phase and less rich central reaction region. The ultra-high injection pressure provides necessary turbulent kinetic energy for fuel/air mixing, which promotes the soot oxidation in the diffusive combustion.

The effect of ambient gas density on the resultant soot formation is more complicated. On one hand, the higher ambient gas density improves the ambient gas mass flow rate even though the restrained entrainment section. However, the $\dot{M}_a/\dot{M}_f$ upstream of Lift-Off Length decreases due to the evident reduction of the lift-off length. Furthermore, the significant reduction of the ignition delay also impacts the preparation of the leaner fuel/air mixture. As a result, higher soot level can be observed.

The larger nozzle hole size results in the decreased ratio of ambient gas/ fuel mass flow rate under the non-evaporating spray condition. Furthermore under the combustion condition, the larger nozzle hole size leads to the direct interaction of the liquid phase and the initial combustion phase. The vaporization cooling will likely influence the combustion rate and result in the poor fuel/gas mixing. As a result, the soot emission level is significantly enhanced.

Figure 7.10 summarizes the effects of injection pressure, ambient gas density and nozzle hole size on the spray vaporization and flame soot level. The white background represents the periphery of non-evaporating spray under the quasi-steady state. The arrows on the right side surface represent the ambient gas flow whose size corresponds to the relative velocity value. The green segments represent the liquid phase length and the yellow dashed lines denote the region with OH* chemiluminescence signal. The line-of-sight soot level images measured by two color method are also shown. Although the strengthened turbulent flow in the real engine condition may cause the difference in fuel vaporization and soot formation, the relative relationship is assumed to be the same as the current study. It's evident that the combination of higher injection pressure and smaller nozzle hole size is necessary to shorten the mixing period and promote the soot oxidation, particularly under the high boosting intake charge or late injection timing conditions.

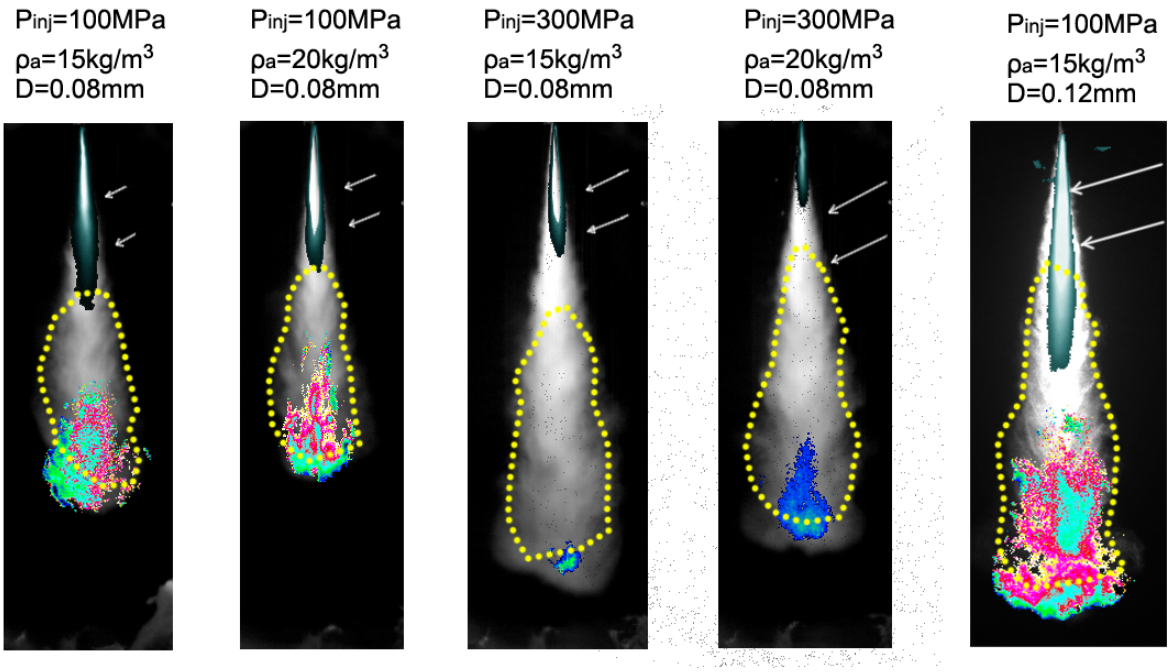

Figure 7.10 Schematics of Spray Flame Evolution

7.3 FLAT-WALL IMPINGING DIESEL SPRAY MEASUREMENT

7.3.1 OH* Chemiluminescence Results

Figure 7.11 shows the spatial distribution of the OH* chemiluminescence signal under the different conditions. Since the structure of the flat-wall impinging spray flame is considered to be axis-symmetric, only the right side from the nozzle axis is shown. The OH* signal can only

be detected near the wall, compared with lift-off-length measured for the free spray flame (20-25mm for 0.08mm nozzle; 20-30mm for 0.12mm nozzle), the lift-off length for the impinging spray tends to be longer. One of the main reasons are that the lower ambient gas mass flow rate for impinging spray (measured by LIF-PIV technique) delays the fuel/gas mixing, as a result, the much longer ignition delay for the impinging spray allows the spray to extend further and mix with the ambient gas with longer period prior to the auto-ignition. The longer lift-off length for the impinging spray also implies more air entrainment from side periphery, which promotes the premixed combustion in the central reaction zone.

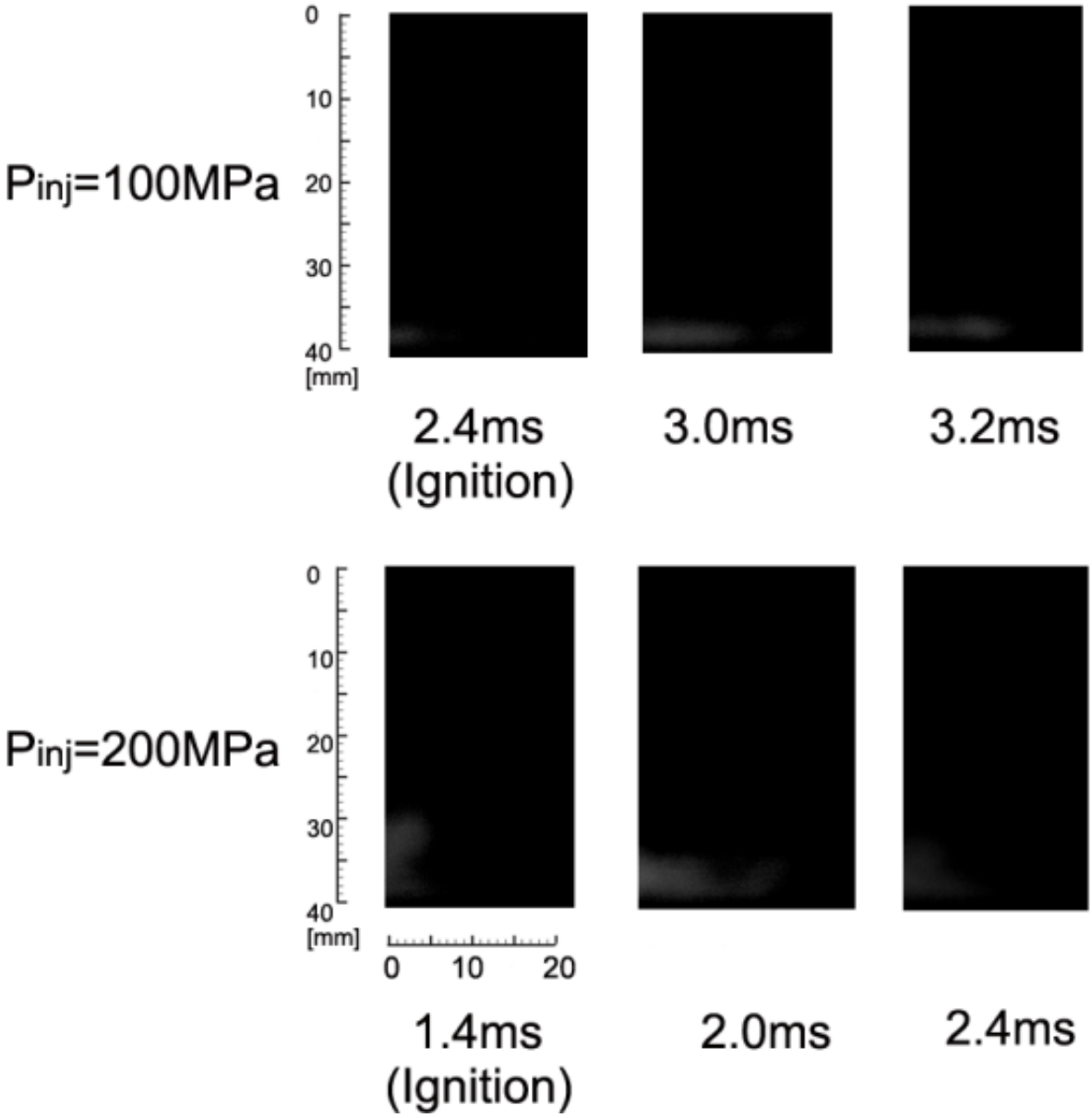

(a) D=0.08mm, ρ_a =15kg/m^3, Z=40mm

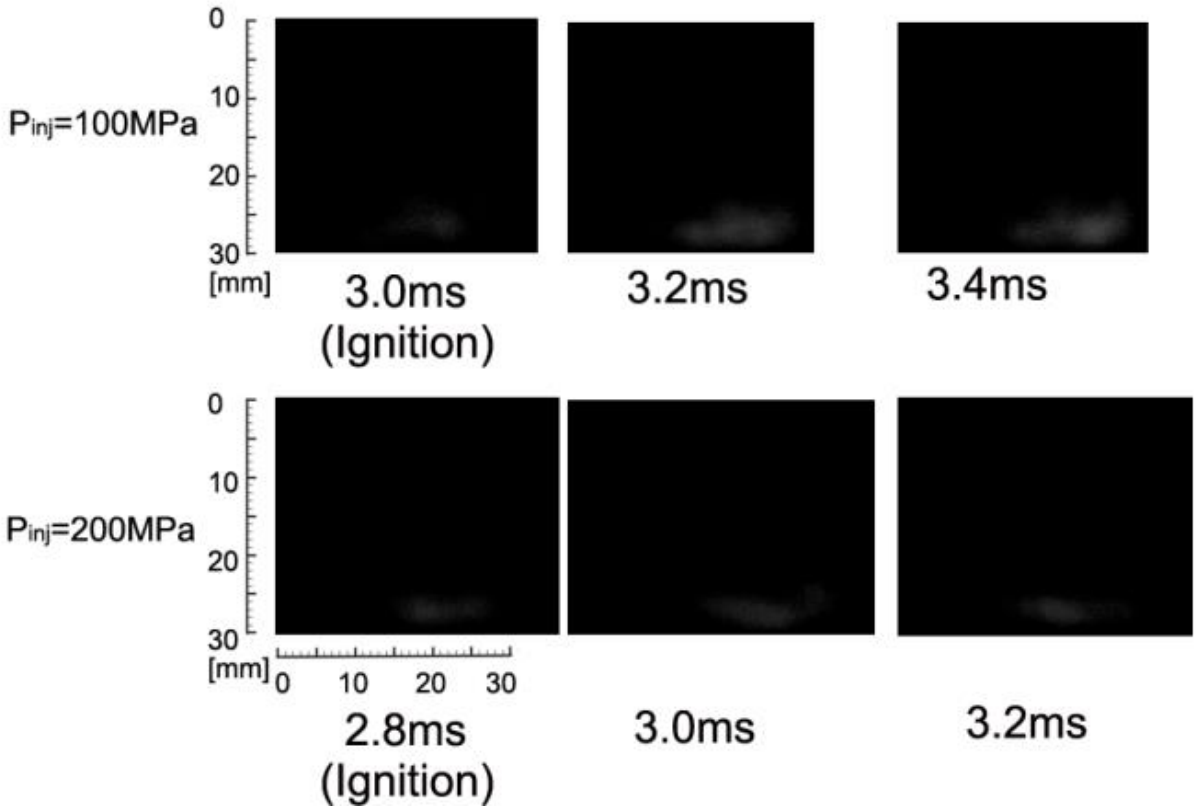

(b) D=0.12mm, ρ_a =15kg/m^3, Z=30mm

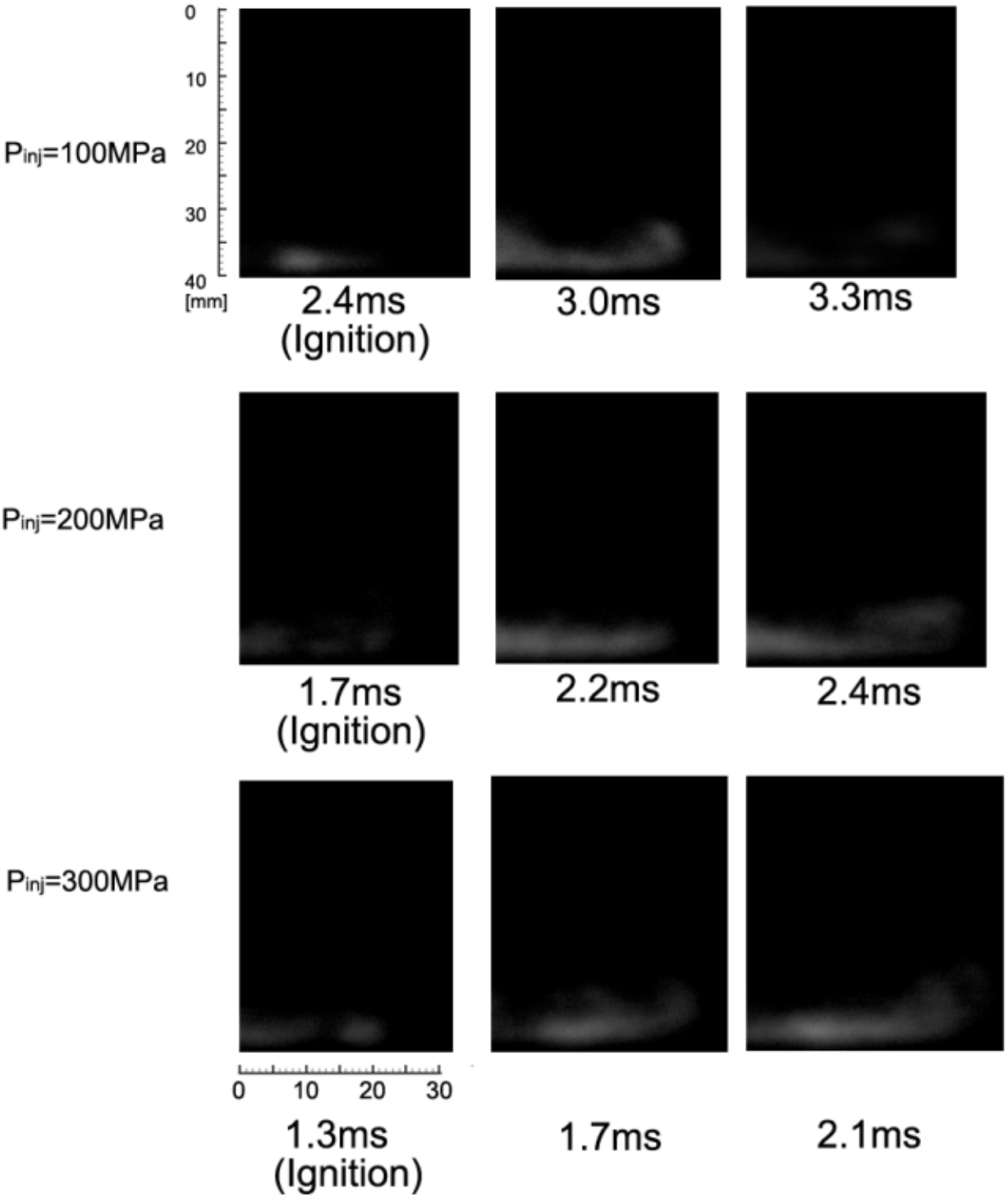

(c) D=0.12mm, ρ_a =15kg/m^3, Z=40mm

Figure 7.11 Spatial Distribution of OH* Chemiluminescence

The temporal variation of OH* chemiluminescence intensity is shown in Figure 7.11. It is found that the ignition delay is considerably prolonged for the impinging spray, this results from the decreased ambient gas mass flow rate into the spray under the impingement condition. The longer ignition delay may facilitate the fuel/gas mixing; On the other hand, the much longer ignition delay (especially for the short impingement condition) may also result from the poor fuel/gas mixture due to the direct liquid-wall impingement. The higher injection pressure and the smaller nozzle hole size advances the ignition inception, which has the same tendency as the free spray. The OH* intensity analysis for the impinging spray tends to be complicated because it depends on the correlation of the droplets size, liquid film, wall temperature and so on.

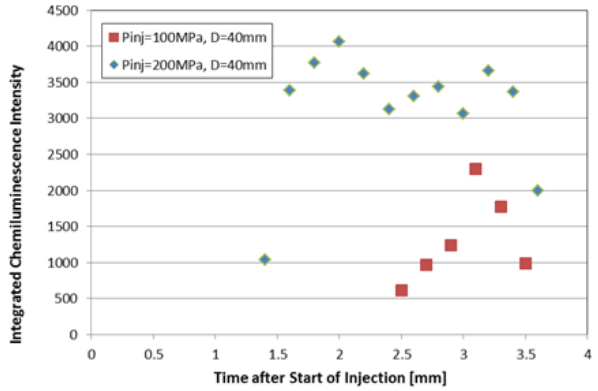

(a) D=0.08mm, ρ_a =15kg/m^3, Z=40mm

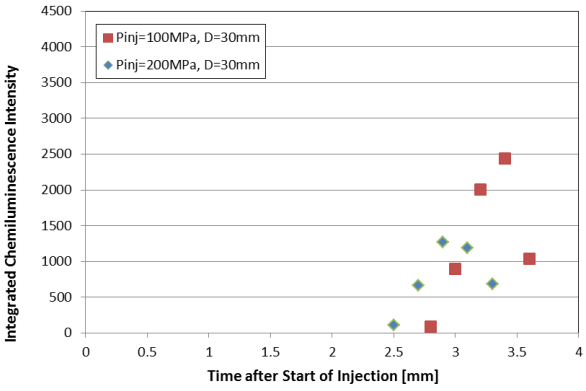

(b) D=0.12mm, ρ_a =15kg/m^3, Z=30mm

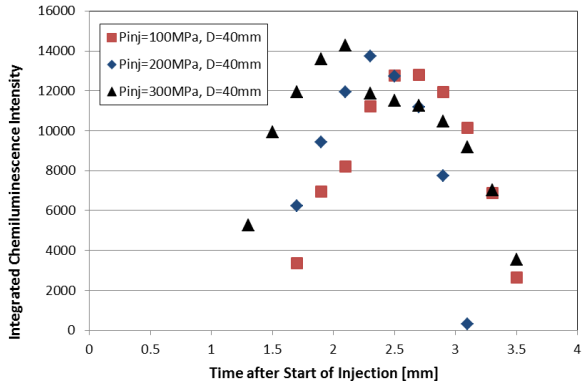

(c) D=0.12mm, ρ_a =15kg/m^3, Z=40mm

Figure 7.12 Temporal Variation of OH* Chemiluminescence Intensity

7.3.2 KL factor and Temperature Distribution of Spray Flame

Figure 7.13 shows the spatial distributions of the flame KL factor and the temperature of the flat-wall impinging Diesel spray. For the smaller nozzle hole 0.08mm, only the results with

the injection pressure of 100MPa are shown here because the sooting flame images were hardly detected by using higher injection pressures. The same as the free spray, the lower soot concentration can be observed at the spray tip due to the strong turbulent mixing with the ambient gas promotes the soot oxidation in this region. What should be emphasized is that in this study, the thickness of the stainless plate used to simulate the impinging spray was only 3mm, and the electric heater supplied the heat transfer from the bottom of the plate, thus it is assumed that the temperature gradient from the ambient gas to the plate is very small. As a result, the flame quenching effect due to the liquid film and the relatively lower wall temperature does almost not occur in this study. It can be found that the temperature of the lower boundary of the flame near the wall shows higher value, correspondingly, the soot level near the wall decreases.

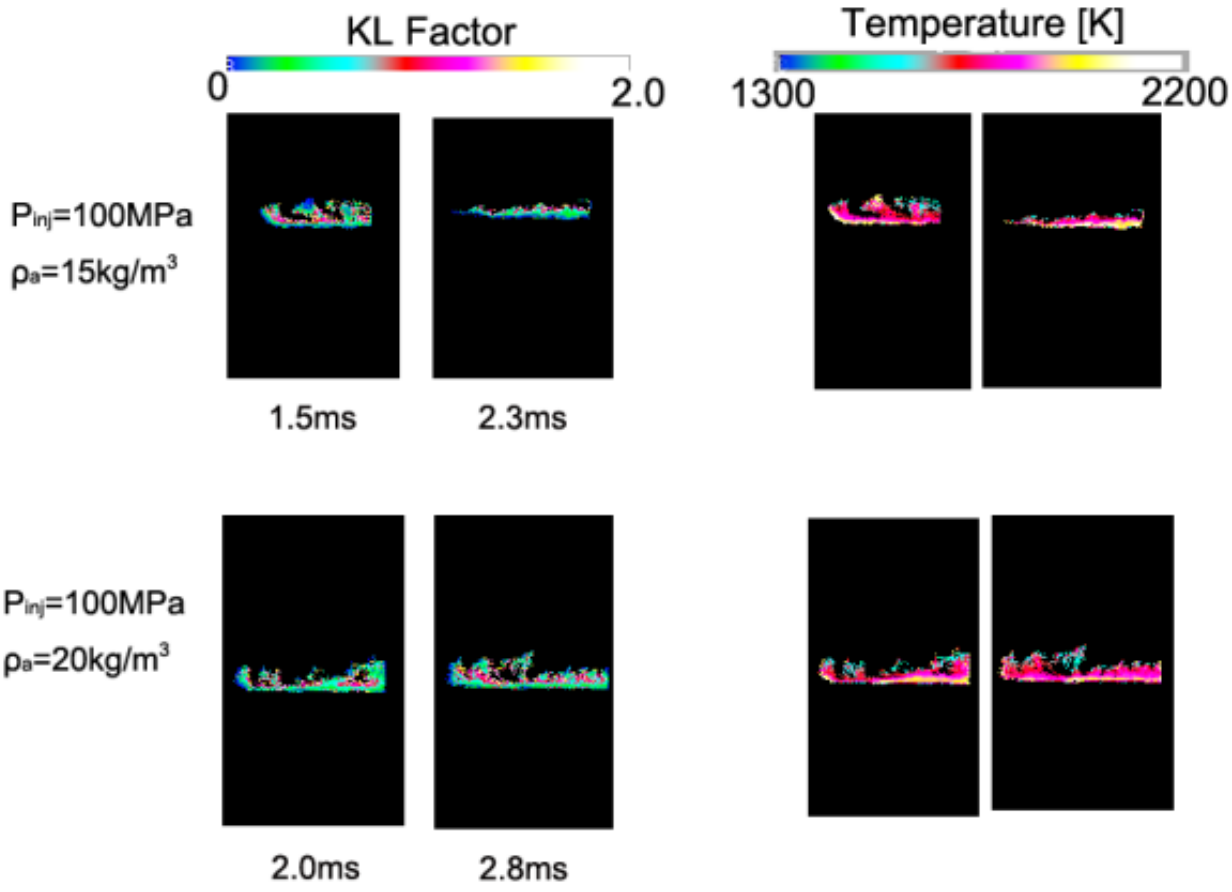

(a) D=0.08mm, P_{inj}=100MPa, Z=30mm

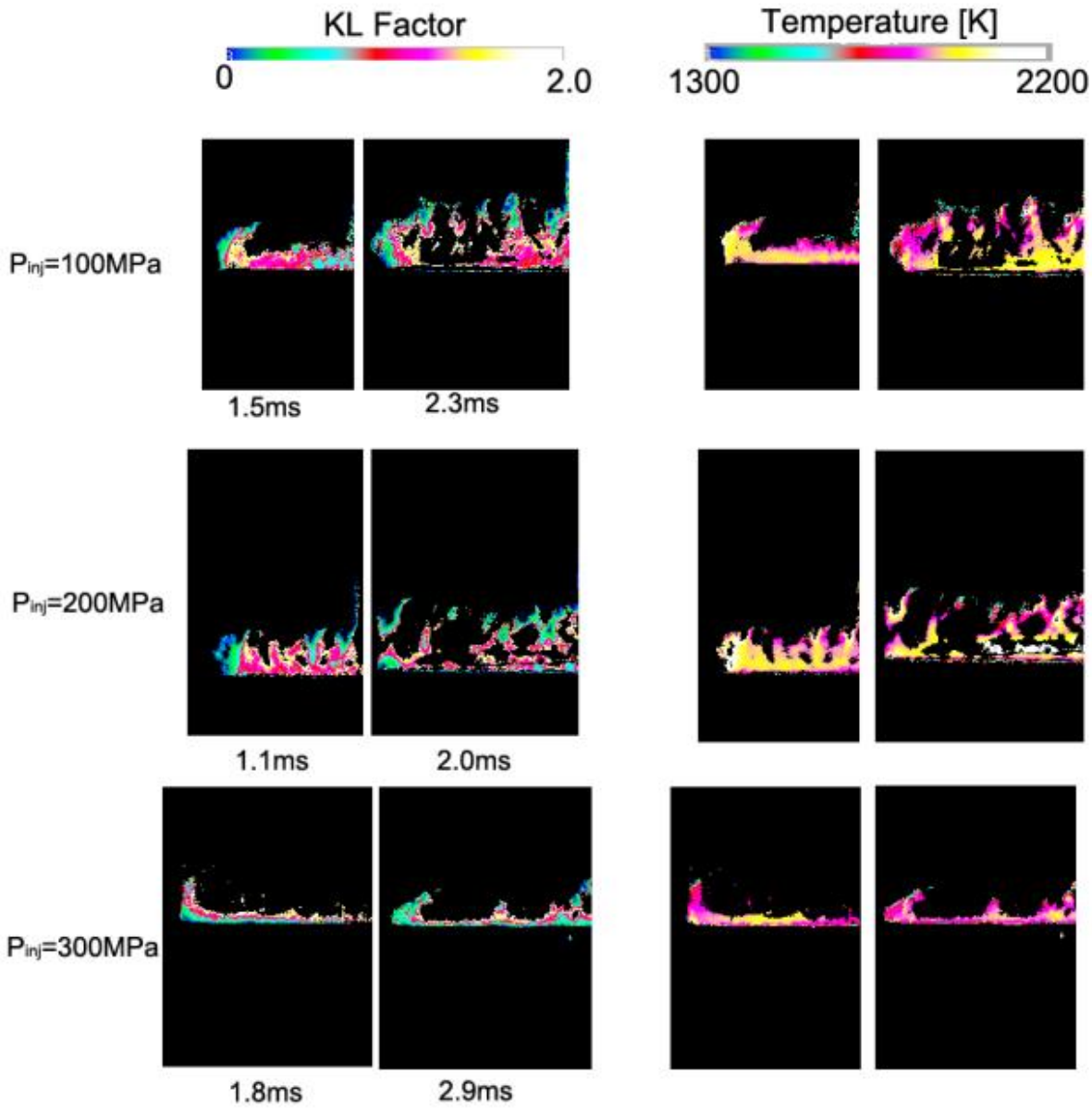

(b) D=0.12mm, ρ_a =15kg/m^3, Z=30mm

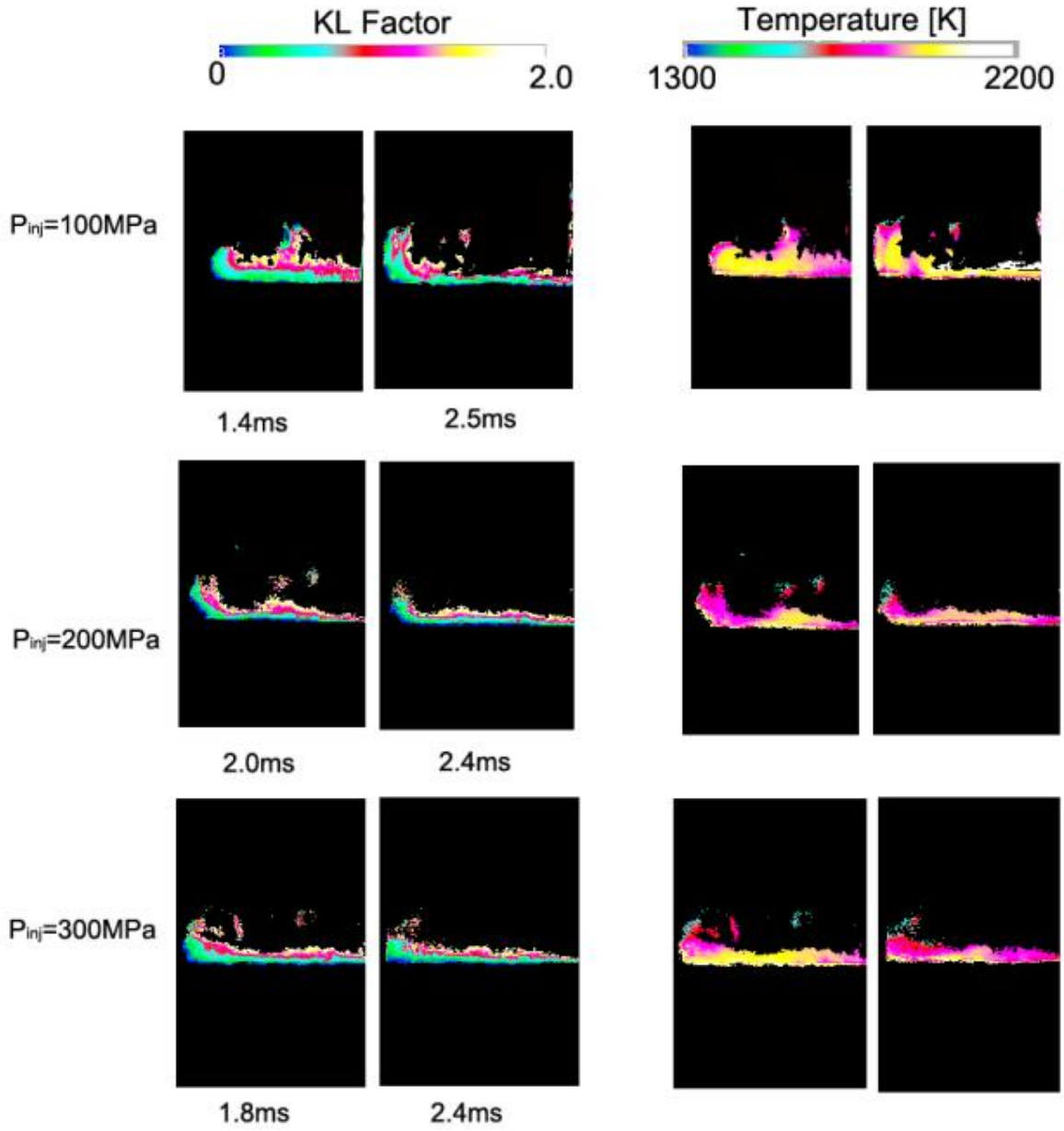

(c) D=0.12mm, ρ_a =15kg/m^3, Z=40mm

Figure 7.13 Spatial Distributions of Flame KL Factor and Temperature

Figure 7.14 shows the temporal variation of the integrated flame KL factor and the temperature. The same as the free spray, the increased injection pressure and decreased nozzle hole size effectively reduces the soot formation level due to the enhanced turbulent mixing process and larger ratio of ambient gas/fuel mass flow rate. The results in Fig.7.14 (b) and (c) indicate that the shorter impingement distance tends to increase the soot level. Several reasons

can be considered: (1). The ambient gas entrainment is further restrained with the decrease of the impingement distance according to PIV measurement; (2). More possibility of the direct impingement of the liquid phase to the wall, which results in the poor fuel/gas mixing. This can be demonstrated by comparing with the Fig.7.14 (a), with the same impingement distance, the use of smaller nozzle hole size may achieve the much lower soot level because the larger ratio of ambient gas/fuel mass flow rate and less liquid phase reaching the wall. Compared with the two color meter results of the free spray shown in Fig.7.8, it is found that spray-wall impingement considerably reduces the soot formation level if the proper injection pressure and nozzle hole size are selected. Even though the ambient gas entrained mas flow rate is restrained for the impinging spray (as shown in Chapter 4), the increased turbulent mixing (as shown in Chapter 6) and the prolonged ignition delay yields better fuel/gas mixing before the auto-ignition. Numerous studies [Pickett et al., 2005; Bruneaux et al., 2005] have the same conclusion that wall impinging spray improves the fuel vaporization and reduces the soot formation. On the other hand, if the liquid film forms on the wall such as in the cold start condition of the Diesel engine or the larger nozzle hole size/ lower injection pressure were applied, the soot formation reversely increases [Wang et al., 2011; Dec et al., 2001]. As a conclusion, the resultant fuel vaporization and combustion characteristics of the wall impinging spray depend on the combined effects of the liquid length, impingement distance, turbulent mixing intensity, wall temperature and so on.

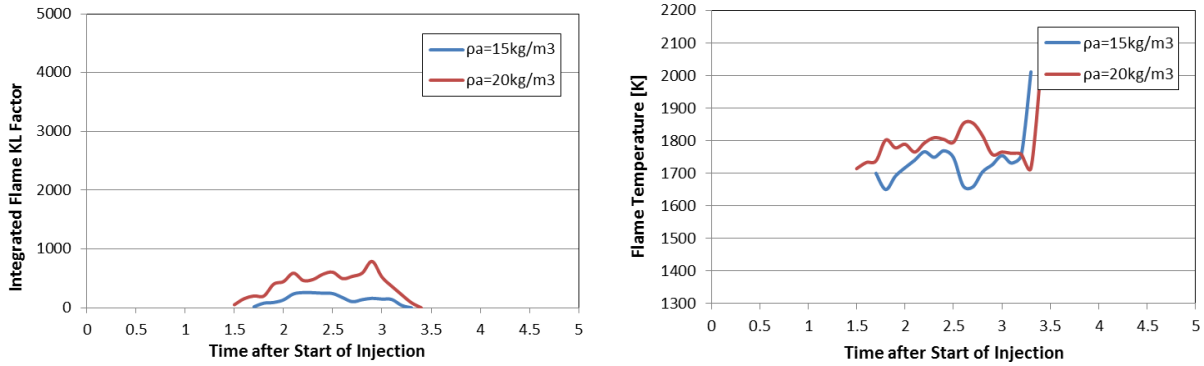

(a) D=0.08mm, P_{inj}=100MPa, Z=30mm

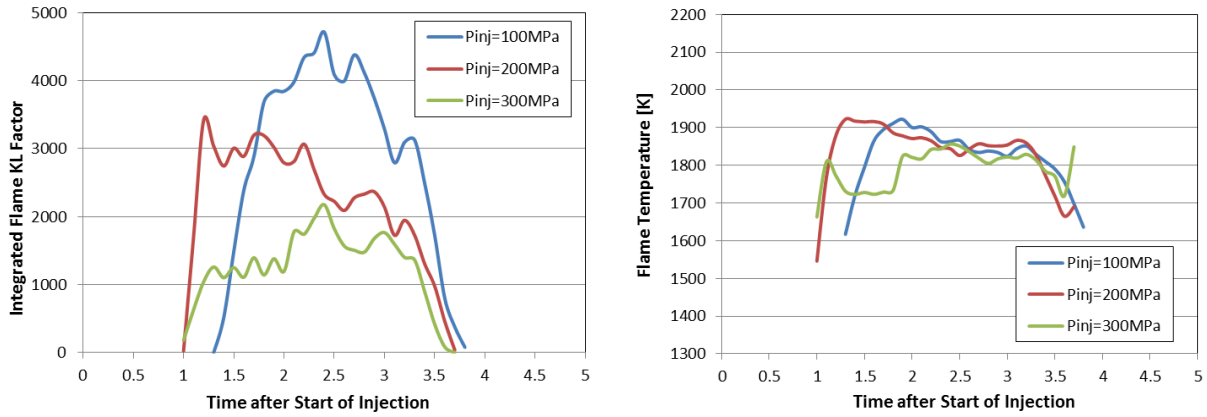

(b) D=0.12mm, ρ_a =15kg/m^3, Z=30mm

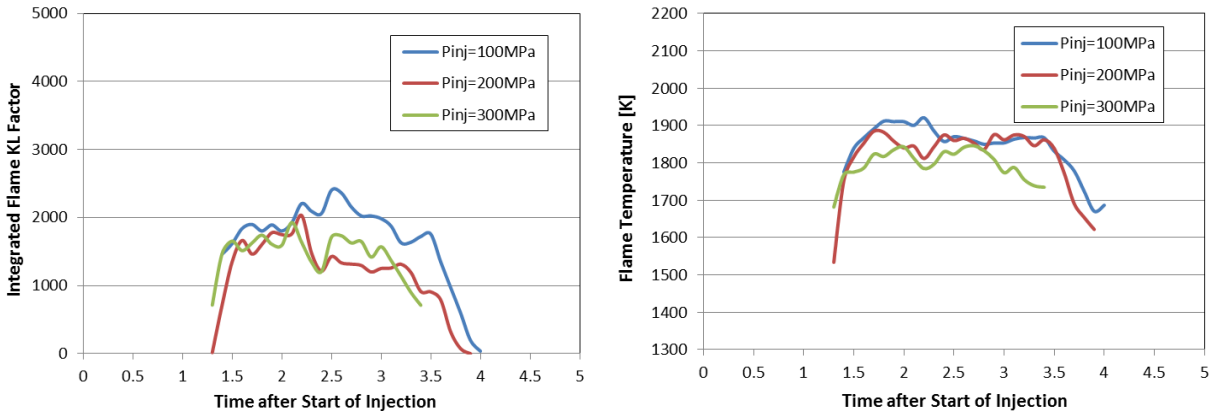

(c) D=0.12mm, ρ_a =15kg/m^3, Z=40mm

Figure 7.14 Temporal Variations of Integrated Flame KL Factor and Temperature

7.4 SUMMARY

The characteristics of the combustion process of the Diesel spray were investigated using the direct imaging of natural flame luminosity, OH* chemiluminescence imaging and two color pyrometry techniques, with respect to the free spray condition and the flat-wall impinging spray condition, respectively.

Based on this study, the following can be concluded:

1. The position of the soot luminosity is around the spray tip region for all the cases. Most of the soot will be oxidized at the thin periphery of spray tip due to the strong turbulent mixing with ambient gas. The soot luminosity region moves downstream together with the spray development.
2. The lower ambient gas density, which corresponds to the lower ambient pressure and

temperature, significantly postpones the inception of the soot formation even after EOI, which provides enough time for forming the lean fuel/air mixture, as a result, the formation of soot is restrained. The ultra-high injection pressure improves the fuel/air mixing rate, resulting in a low flame luminosity level even in the high ambient gas density condition. As the fuel/gas mixing is proceeding in the diffusive combustion, soot is oxidized gradually after reaching the peak value.

3. According to the OH* chemiluminescence results, the increase of the fuel injection pressure and the ambient gas density reduces the ignition delay due to the rapid fuel/gas mixing (physical process) and exothermic reaction (chemical process). The upper boundary of the OH* signal keeps stable after the spray reaches the quasi-steady state. The natural luminosity appears at the early stage is originated from other radicals, the low OH* signal is masked. However, OH* is proper to mark the high temperature exothermic reaction.
4. The increase of the fuel injection pressure and the decrease of the ambient gas density tends to slightly reduce the OH* intensity since the formation of the leaner mixture reduces the combustion temperature. On the other hand, the increase of nozzle hole size significantly increases the ignition delay and the OH* signal intensity.
5. More air is entrained upstream of the lift-off length with the increase of injection pressure, the decrease of nozzle hole size and ambient gas density. The relative location of the liquid length and the lift-off length is related to the combustion behavior.
6. The maximum KL factor distributes near the flame tip region, which implies large amount of soot clouds form in the inner region of the turbulent diffusive flame phase. While along the spray periphery especially at the spray tip, the relatively lower soot level can be observed, which coincides with the suggestion that most of soot will be consumed on the thin layer of the diffusive flame front during the strong mixing process with the ambient gas.
7. The reduction of ambient gas density apparently lowers the soot level of the flame, which is attributed to the longer ignition delay. Regardless of the ambient gas density, the ultra-high injection pressure significantly reduces the soot level and flame temperature. On the other hand, the use of larger nozzle hole size evidently increases the soot level even though the ultra-high injection pressure was applied, due to the direct interaction of the liquid phase and the initial combustion phase.
8. The correlation of the ratio of ambient gas/fuel mass flow rate ($\dot{M}_a/\dot{M}_f$) upstream of the lift-

off length and the total integrated flame KL factor and the schematics of spray flame evolution were presented.

9. For the wall impinging spray, the OH* signal can only be detected near the wall, the lift-off length for the impinging spray tends to be longer. One of the main reasons are that the lower ambient gas mass flow rate for impinging spray (measured by LIF-PIV technique) delays the fuel/gas mixing, as a result, the much longer ignition delay for the impinging spray allows the spray to extend further and mix with the ambient gas with longer period prior to the auto-ignition.
10. The longer ignition delay may facilitate the fuel/gas mixing; On the other hand, the much longer ignition delay (especially for the short impingement condition) may also result from the poor fuel/gas mixture due to the direct liquid-wall impingement.
11. Compared with the free spray, the spray-wall impingement is likely to reduce the soot formation level if the proper injection pressure and nozzle hole size are selected. The shorter impingement distance tends to increase the soot level.
12. The resultant fuel vaporization and combustion characteristics of the wall impinging spray depend on the combined effects of the liquid length, impingement distance, turbulent mixing intensity, wall temperature and so on.

CHAPTER 8 NUMERICAL SIMULATION OF DIESEL SPRAY

8.1 BASIC EQUATIONS

The fuel spray was analyzed based on Lagrangian spray module which involves the multi-phase flow phenomenon and implements the conservation equations for liquid phase and vapor phase simultaneously. The liquid phase simulation is carried out in a statistical Discrete Droplet Method (DDM) way [Huethorst et al., 1991; Liu et al., 1993], in which a group of droplets with the identical properties will be represented by a "parcel". The vapor of evaporating droplets was used as a source term of an additional transport equation for the vapor void fraction in Eulerian formulation.

In the Lagrangian description, all the flow quantities F are given as function particle and time. Hence it is appropriate to describe the dispersed phase (e.g. sprays consisting of liquid droplets).

$$F = F(particle, t) \tag{8.1}$$

The Eulerian description is used to describe the continuous flow field as a function of a point in space (related to a fixed coordinate system) and time,

$$F = F(\vec{x}, t) \tag{8.2}$$

In the following, the conservation equations of mass, momentum and energy for the multi-dimensional flows are shown:

$$Continuity\ Equation: \frac{D\rho}{Dt} + \rho\frac{\partial u_i}{\partial x_i} = 0 \tag{8.3}$$

$$Conservation\ of\ Momentum: \rho\frac{Du_j}{Dt} = \rho\left(\frac{\partial u_j}{\partial t} + u_i\frac{\partial u_j}{\partial x_i}\right) = -\frac{\partial P}{\partial x_j} + \frac{\partial \tau_{ij}}{\partial x_i} + f_j \tag{8.4}$$

$$Conservation\ of\ Energy: \rho\frac{De}{Dt} = \nabla\cdot(\lambda\nabla T) - P(\nabla\cdot\vec{u}) + \mu\varphi + \frac{\dot{Q}_s}{dx_1 dx_2 dx_3} \tag{8.5}$$

In which: x_i, x_j: Coordinates in the different direction (s);

u_i, u_j: Velocity Components in the different direction (m/s);

τ_{ij}: Stress tensor (N);

f_j: Body force (N);

e: Internal energy (J);

λ: Heat transfer coefficient (w/(m·K));

T: Temperature (K);

μ: Dynamic Viscosity (Pa s);

φ: Dissipation function;

$\dot{Q}_S$: Heat flux (J).

The basic Navier-Stokes equations can be used directly (DNS: direct numerical simulation) without averaging or using the turbulent models if the grid spacing is fine enough to resolve the smallest eddies in a flow field. However, it requires high performance of the processor and much longer calculating time. Thus in this study, basic RANS (Reynolds averaged Navier-Stokes) governing equations were used. The RANS equations are obtained by substituting the Reynolds decomposition terms into the instantaneous conservation equations, and then by averaging the entire equations over time. Due to the appearance of the additional terms: the Reynolds stresses and the turbulent heat flux as shown in Eq. (8.6) and (8.7), which have to be described by a turbulence model in order to close the system equation.

$$Turbulent\ Stress\ Tensor\text{:}\ \bar{\tau}_{ij,t} = -\rho\overline{u_i' u_j'} \tag{8.6}$$

$$Turbulent\ Heat\ Flux\text{:}\ \bar{q}_{i,t} = \rho C_P \overline{u_i' T'} \tag{8.7}$$

In which C_P is the heat capacity (J/(g K)). The superscript (′) denotes the fluctuating component.

The task of a turbulent model is to provide a relation for the turbulent eddy viscosity of a flow field in order to close the RANS equations. In this study, the standard $k-\varepsilon$ model was used which was proposed by Launder and Spalding [1974], which provides the description of the turbulent kinetic energy and its dissipation rate.

8.2 SELECTION OF SUB-MODELS

In this study, the numerical simulation of the spray was carried out using CFD code AVL FIRE®. The sub models for describing the spray break-up, droplets interaction, evaporation, wall interaction and the selection of the models parameters will be introduced.

There are mainly two models used for the primary break-up process, the “Blob Injection” and “Core Injection”. “Blob Injection” model introduces a series of large blobs of approximately nozzle diameter, the diameter is subsequently reduced according to the mass detachment rate calculated from the primary break-up model. Hence the initial liquid flow velocity and concentration distribution information from the nozzle file is necessary. “Core Injection” calculates the core erosion within a separate model and releases the parcels downstream the nozzle on the core surface. The main equations are shown as follows:

$$\tau_A = C_1\tau_T + C_3\tau_w \tag{8.8}$$

$$L_A = D_d = C_2 C_u \frac{k^{1.5}}{\varepsilon} \tag{8.9}$$

$$V_{drop} = \frac{L_A}{\tau_A} \tag{8.10}$$

In which the where τ_A is breakup time (subscript T for the turbulent part and subscript W for the aerodynamic part), L_A stands for turbulent length scale, D_d represents the initial droplet diameter, and V_{drop} is the droplets' initial velocities. Pogorevc et al. [2008] discussed the selection of the parameters for the "Core Injection" model in detail.

For the secondary break-up process, the "standard WAVE" model [Liu et al., 1993] was selected. The approach for the radius reduction of the parent drops is applied:

$$\frac{dr}{dt} = -\frac{r - r_{stable}}{\tau_A} \tag{8.11}$$

$$\tau_A = \frac{3.726 \cdot C_2 \cdot r}{\Lambda \cdot \Omega} \tag{8.12}$$

$$r_{stable} = C_1\Lambda \tag{8.13}$$

In which r_{stable} is the droplet radius of the product droplet, Λ and Ω are the wave length and the wave growth rate on the liquid surface. C_1 is a constant of 0.61 which determines the stable droplet size and break up time. The constant C_2 corrects the characteristic break-up time and varies from one injector to another, which exerts great impact on the spray characteristics. Liu et al. [2008] systematically studied the effect of C_2 constant on the spray development and the combustion.

In addition, the "Diesel Nozzle Flow" model offers a simple way to correct the injection velocities and initial droplet diameters due to cavitation by introducing the geometry information such as the orifice length to diameter ratio L/D and the inlet radius to diameter ratio R/D. More precise information such as the orifice outlet velocity and mass distribution can also be supplied by introducing the "Nozzle File" generated from the nozzle internal multiphase flow simulation.

The computational modeling offers a promising opportunity to obtain detailed information on the spray–wall impingement and wall-film build-up. FIRE® provides a number of models for the spray-wall interaction process. There are three methods available to treat the spray wall interaction:

(1). Use a wall interaction model within the spray module without activating the wallfilm module (possible for Walljet0/1/2, O'Rourke-Amsden, Bai-Gosman and Mundo-Sommerfeld model). In this case the wallfilm is approximated by droplets reflected under a small angle propagating close to the wall after impingement.

(2). Use the wallfilm module without activating a wall interaction model. In this case the wallfilm module takes care of the splashing of the impinged mass according to certain criteria. None of the Walljet0/1/2 models should be activated, otherwise the wallfilm will not get any sources.

(3). Use a wall interaction model plus the wallfilm module. In this case the standard splashing model within the wallfilm is deactivated automatically and the subdivision of deposited and splashed mass is calculated from the wall interaction model. This method is applicable with the Mundo-Sommerfeld, Bai-Gosman, O'Rourke-Amsden and Maichle-Weigand models.

After careful comparison of the different models with the experiment results, "Mundo-Sommerfeld" model [Mundo et al., 1994] and "Bai-Gosman" model [Bai et al., 1995] were found to reproduce the impinging spray geometry well if high injection pressure were applied.

For evaporation process, heat and mass transfer coefficients are set-up according to the model physics, but for fine tuning and matching with experimental data, two adjustment parameters (E1, E2) for the heat and mass transfer coefficients are provided for each model. In this study, "Dukowicz model" [Dukowicz, 1979] was employed.

Table 8.1 summarizes the parameters selection for the main models used in this study.

Table 8.1 Parameters Selection for Main Models

Process	Model	Index of Coefficients	Description	Selected Value
Primary Break-up	Core Injection	C1	Specify turbulent time scale (critical to spray tip penetration)	10-50 (According to the different injection pressure)
		C2	Specify atomization length scale (critical to spray spreading angle)	5-10 (According to the different injection pressure)

		C3	Specify aerodynamic time scale (critical to spray shape)	0-2
	Diesel Nozzle Flow	C1	R/D	0.075
		C2	L/D	15
Secondary Break-up	WAVE Standard	C1	Constant	0.61
		C2	Adjust break-up for different nozzle (critical to spray tip penetration)	60
		C3	Take liquid viscosity of the fuel into account	1
Evaporation	Dukowicz	E1	Heat transfer parameter	1
		E2	Mass transfer parameter	1
Wall Interaction	Bai Gosman	W1	Coefficient for splashing parameter	50
		W2	Rebound Weber number	5
		W3	Smooth/rough flag (0/1)	0
		W4	Dry/wet flag (0/1)	1
	Mundo Sommerfeld	W1	Splashing parameter (determine the ratio of splash/deposition)	57.5
		W2	Smooth/rough flag (0/1)	0
		W3	Diameter ratio lower limit	0.06

8.3 FREE DIESEL SPRAY SIMULATION

A cylindrical computational domain with the height of 100mm and the radius of 30mm was formed as shown in Fig.8.1. The cell size in the central region was refined to 1mm. In

accordance with the experiment carried out in the constant volume vessel, the “static wall” was used as boundary condition.

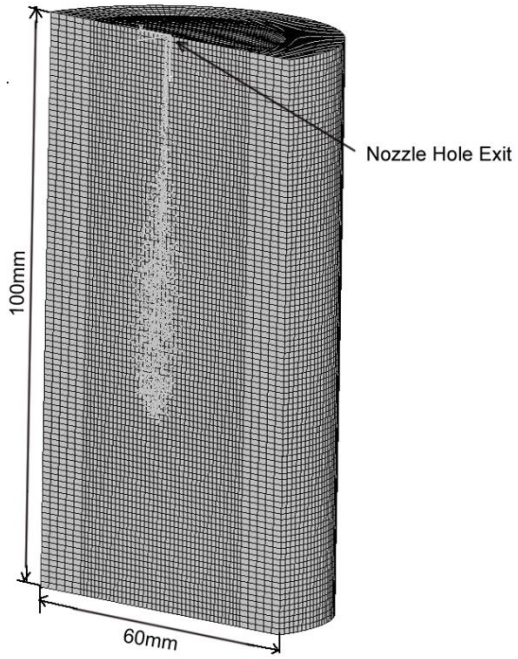

Figure 8.1 Computational Mesh for Free Spray

Figure 8.2 shows the comparison of spray Mie scattering images from the experiment and the droplets distribution by using the RANS model, in which the color level denotes the velocity value and the size scale denotes the droplets size level. The spray shape including the tip penetration and spray angle of the CFD result was carefully adjusted in order to be in line with the experimental result. The droplets flow velocity of non-evaporating spray from the PIV measurement was shown on the right side. It is evident that spray droplet velocity dramatically decreases when reaching the far field due to the break-up process.

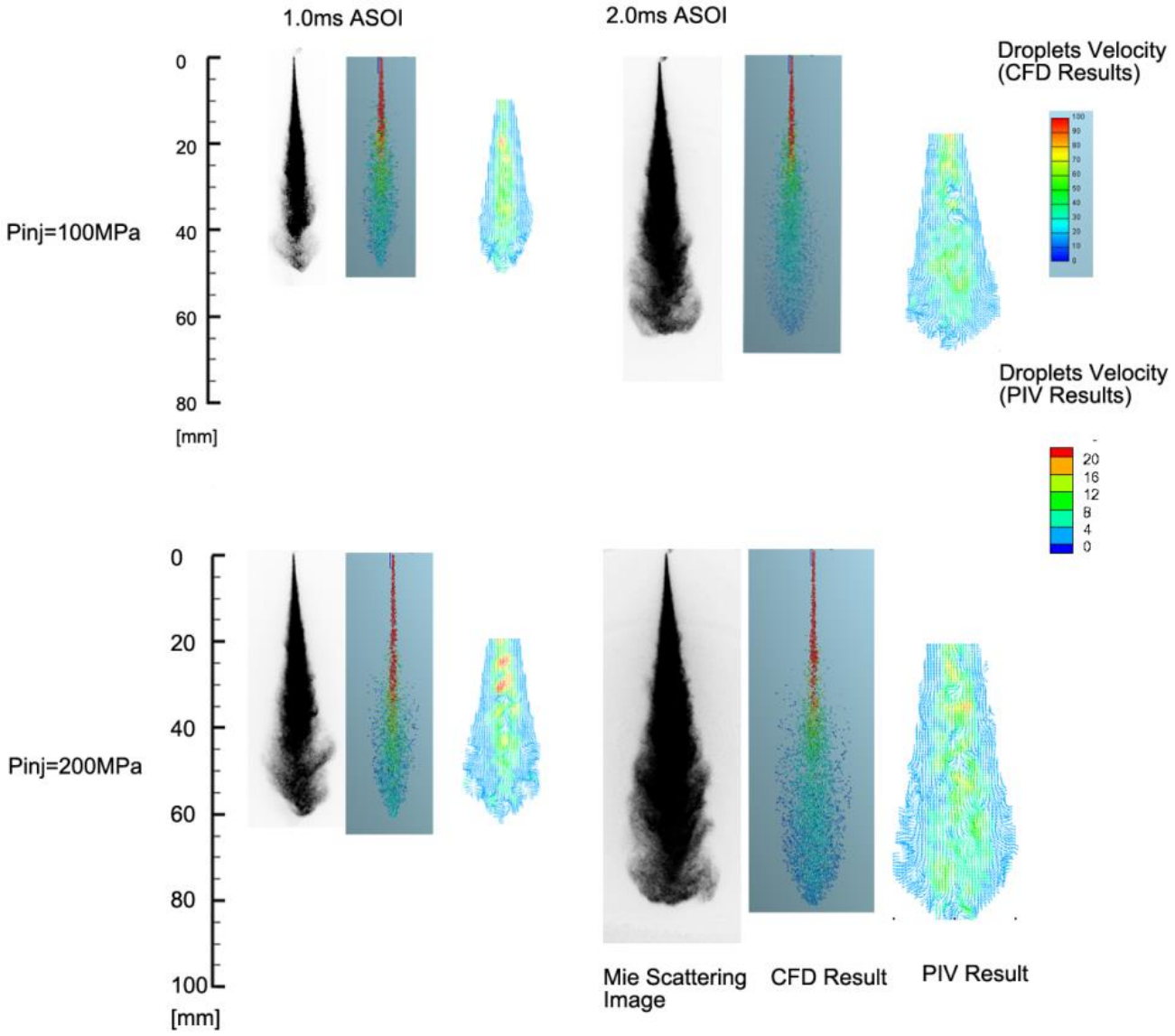

Figure 8.2 Comparison of Droplets Flow from CFD and PIV Results (ρa=15kg/m^3, D=0.08mm)

Figure 8.3 shows an example of gas flow field inside and outside the spray and the absolute pressure distribution which is not possible to be measured using the LIF-PIV method. The result suggests that the velocity of entrained gas is accelerated to a high value after entering the spray periphery due to the existence of pressure gradient from the spray periphery to the center line. On the other hand, a comparatively higher pressure region can be observed at the tip periphery, which leads to the pushed-out gas motion. Tanabe et al. [1985] measured the total pressure and static pressure distribution inside a gas jet and predicted the gas flow feature. That study shows the similar trend as the simulation result.

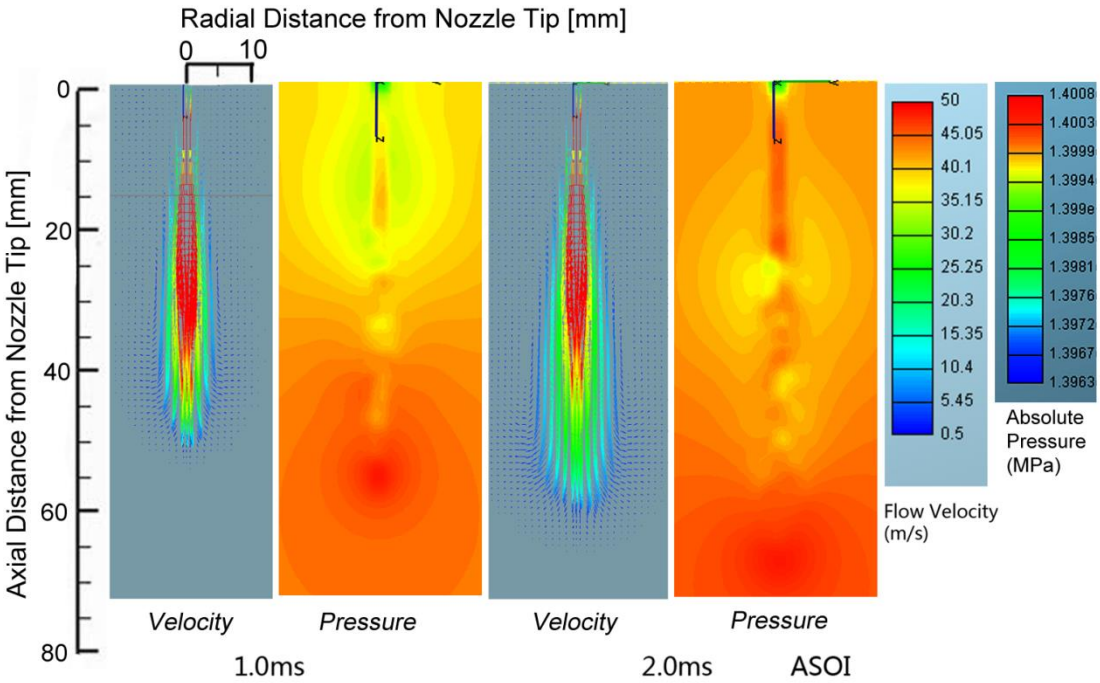

Figure 8.3 CFD Results of Spatial Distribution of Gas Flow Velocity and Absolute Pressure (Pinj=100MPa, ρa=15kg/m^3, d=0.08mm)

The comparison of gas flow fields from the CFD results and the LIF-PIV measurement under the non-evaporating condition and evaporating condition is shown in Fig. 8.4. The ambient gas flow field of CFD result shows the similar structure, three sections: “entrainment”, “recirculation” and “capturing” surrounding the spray periphery can also be found. The maximum gas flow velocity can be observed along the nozzle axis, and the gas flow gradually decelerates after going downstream.

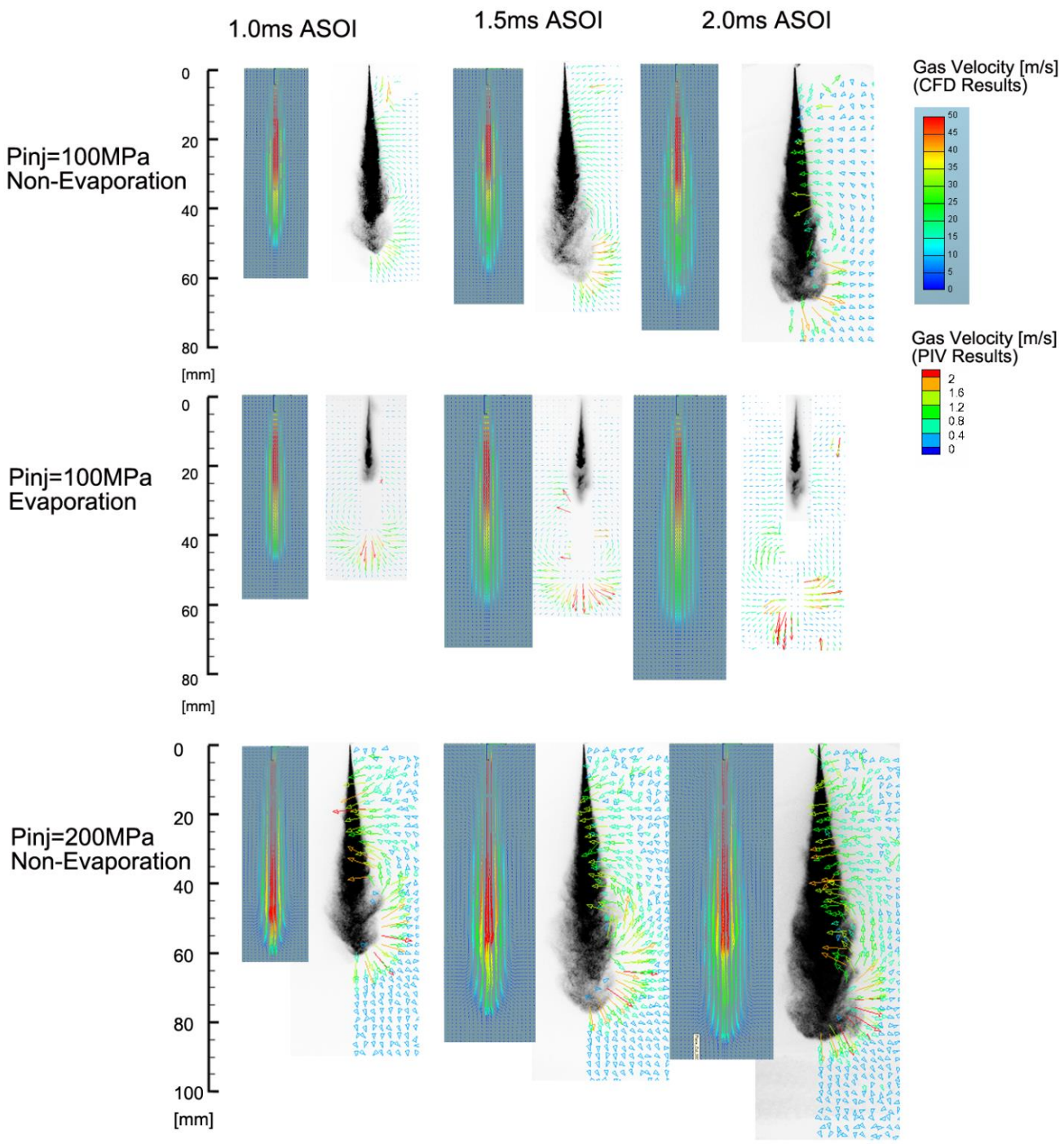

Figure 8.4 Comparison of Ambient Gas Flow from CFD and PIV Results (ρa=15kg/m^3, D=0.08mm)

The PIV results were compared with the CFD results quantitatively to identify the measurement accuracy from Fig. 8.5 to Fig. 8.7. Figure 8.5 shows comparison of the droplets

flow velocity along the nozzle axis. Due to the fuel droplets were simulated using Lagrangian method, the CFD result is shown as discrete dots here, one dot indicates the velocity of a droplets parcel. According to the CFD result, the droplets flow velocity can be accelerated up to 300m/s in the near field, however, it is difficult to measure the droplets flow in this region using PIV technique due to very dense droplets distribution. Thus the PIV measurement of the spray droplets flow only focused on the downstream region. When going downstream, the PIV results gradually approaches to the CFD results. It can be concluded that the velocity measurement results in the downstream region are reliable. The difference may result from the PIV parameters influence, and the neglect of the strong turbulence by using RANS model.

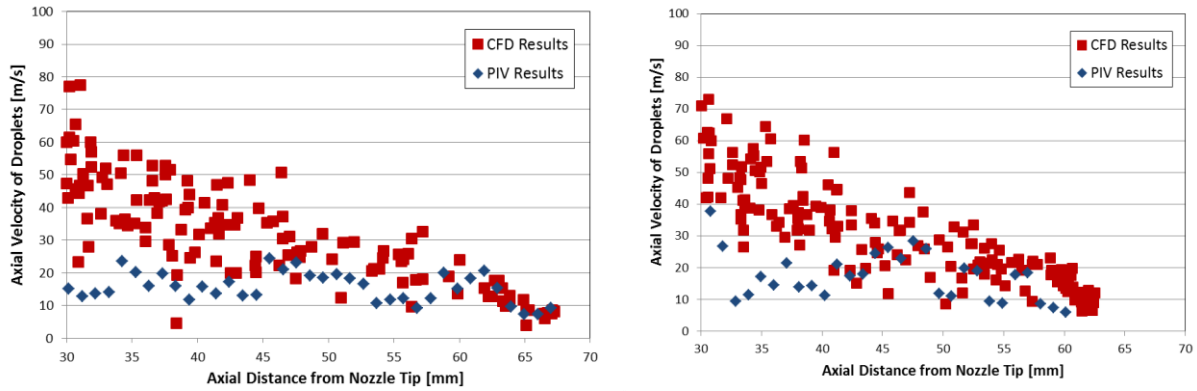

(a) 1.5ms ASOI (b) 2.0ms ASOI

Figure 8.5 Comparison of Droplets Flow Velocity along Nozzle Axis (Pinj=100MPa, ρa=15kg/m^3, D=0.08mm)

Figure 8.6 indicates the comparison of ambient gas flow velocity along nozzle axis. The black dashed line shows the spray tip penetration at the timing of 2.0ms ASOI. Due to the influence of the dense fuel droplets, the ambient gas flow filed inside the spray plume can hardly be observed in LIF-PIV measurement, on the other hand, the ambient gas flow outside the spray periphery obtained by LIF-PIV and CFD is in good agreement. The difference of velocity on the periphery results from the loss of fluorescence signal of tracers in LIF-PIV measurement. The difference between CFD and PIV results in evaporating condition seems to be larger, however the CFD results show the same tendency that the pushed-out gas velocity increases in evaporating condition.

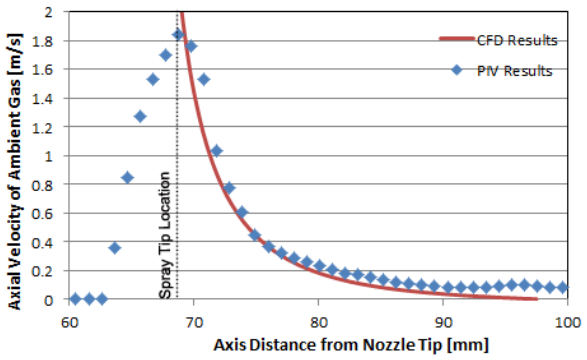

(a) P_{inj}=100MPa, Non-evaporating

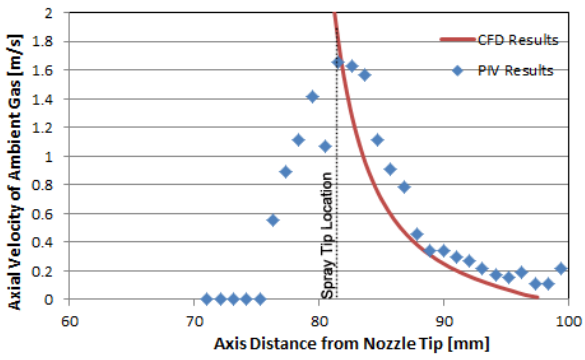

(b) P_{inj}=200MPa, Non-evaporating

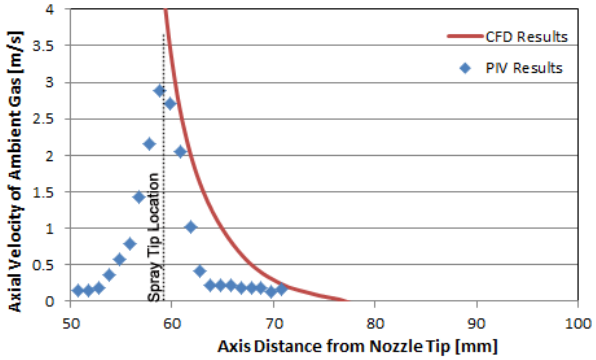

(c) P_{inj}=100MPa, Evaporating

Figure 8.6 Comparison of Ambient Gas Flow Velocity along Nozzle Axis (ρa=15kg/m^3, D=0.08mm, 2.0ms ASOI)

The comparison of radial velocity of the ambient gas is shown in Fig. 8.7, which is able to represent the tendency of the normal velocity along the spray side periphery due to the small spray spreading angle. The distances from the nozzle tip 20mm, 40mm and 60mm correspond to the typical positions in the entrainment section, recirculation section and capturing section, respectively. At 20mm axial distance, the radial velocity of ambient gas outside the spray periphery is towards the nozzle hole axis due to the entrainment flow (Negative radial velocity for radial distance >2mm or <-2mm). Then the gas flow shifts to the reverse direction when entering the spray because the gas flows together with the spray droplets whose velocity vectors are in the outward and downward directions (Positive radial velocity for radial distance <2mm and >-2mm). While at 40mm and 60mm axial distance, the ambient gas tends to be merely pushed out of the spray periphery, which shows different radial velocity distribution.

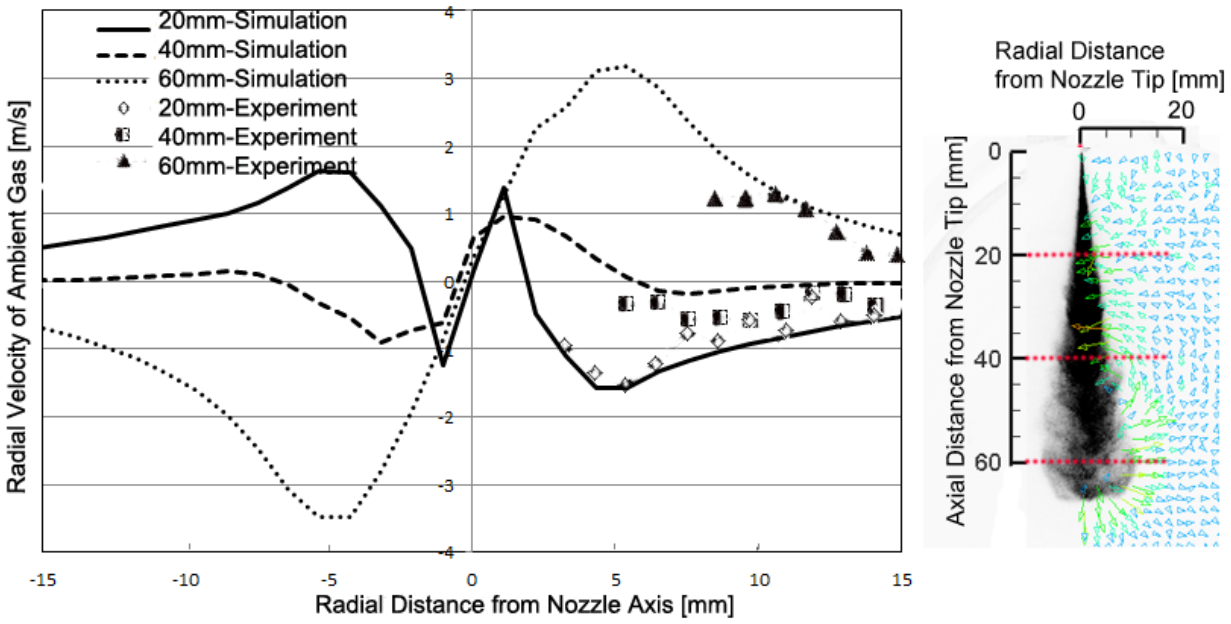

Figure 8.7 Radial Velocity of Ambient Gas along Cross Sections with Different Distance from Nozzle Tip (Pinj=100MPa, ρa=15kg/m^3, d=0.08mm, 2.0ms ASOI)

By extracting the droplets velocity and ambient gas velocity along the nozzle axis from the CFD results, the relationship of them at the tip region is shown in Fig. 8.8. It is found that the gas flow decelerate with the droplets simultaneously. At the same axial distance, the droplets parcels with different velocity exist. Especially at the tip periphery, the mean droplets velocity shows higher value than that of ambient gas, and the different tends to be larger with the increase of the injection pressure. This implies that spray droplets will capture large amount of ambient gas at the tip region. Particularly, the spray tip penetrating velocity V_{sp} at corresponding timing is also shown aside, that proves that the actual spray development will be determined by the droplets with relatively higher velocity a little bit upstream of the spray tip.

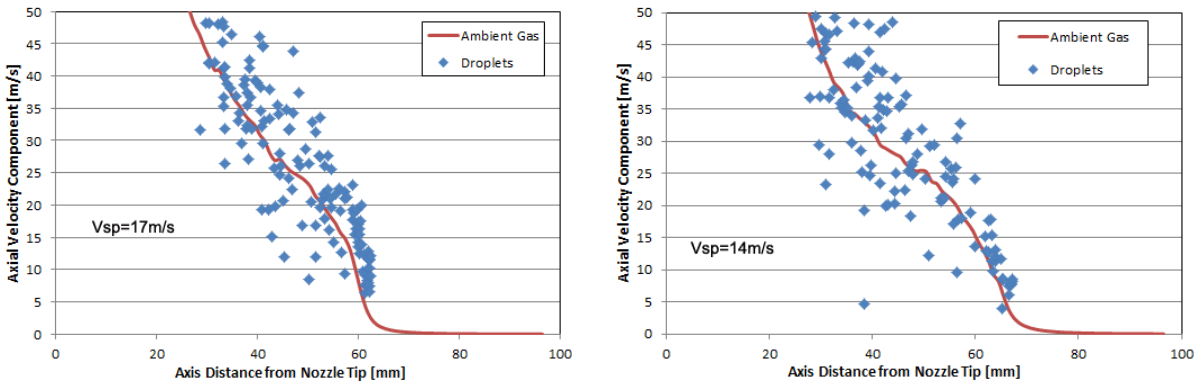

(a) P_{inj}=100MPa, 1.5ms ASOI

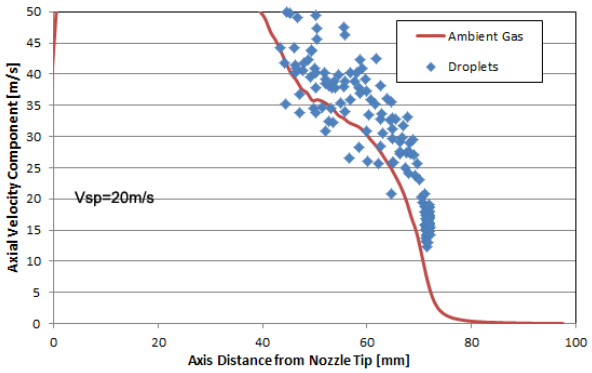

(b) P_{inj}=100MPa, 2.0ms ASOI

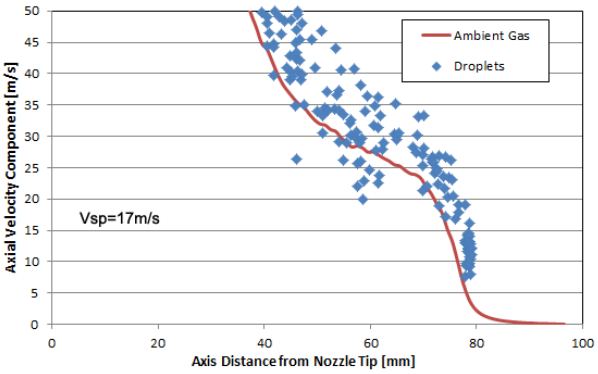

(c) P_{inj}=200MPa, 1.5ms ASOI

(d) P_{inj}=200MPa, 2.0ms ASOI

Figure 8.8 Comparisons of Droplets Velocity and Ambient Gas Velocity along Nozzle Axis From CFD Results

8.4 FLAT-WALL IMPINGING DIESEL SPRAY SIMULATION

The simulation of flat-wall impinging spray with the impingement distance of 30mm and 40mm was carried out. The computational meshes were shown in Fig. 8.9. The grid size of both of the meshes is 1mm.

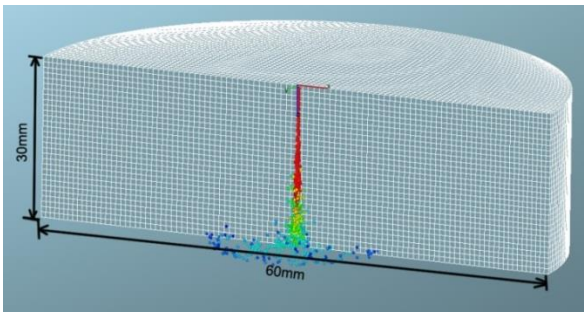

(a) Z=30mm

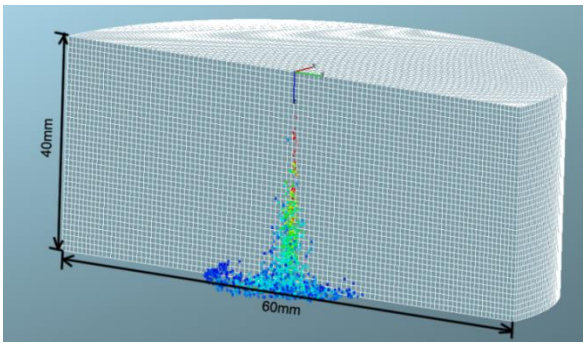

(b) Z=40mm

Figure 8.9 Computational Meshes for Impinging Spray

Figure 8.10 shows the comparison of the impinging spray between the CFD results (Bai_Gosman Model and the Mundo_Sommerfeld Model) and the Mie scattering images. The parameters as shown in Table8.1 were carefully adjusted to make the spray tip penetration and spray angle coincide with the experimental results. The Mundo_Sommerfeld Model seems to reproduce the spray height better by adjusting the splash parameter. The same as the PIV measurement results in Chapter 6, the spray droplets decelerate considerably after wall impingement. During the post wall-impingement development, the droplets near the wall have relatively higher velocity, while the droplets near the upper boundary show lower velocity due to the influence of recirculation motion.

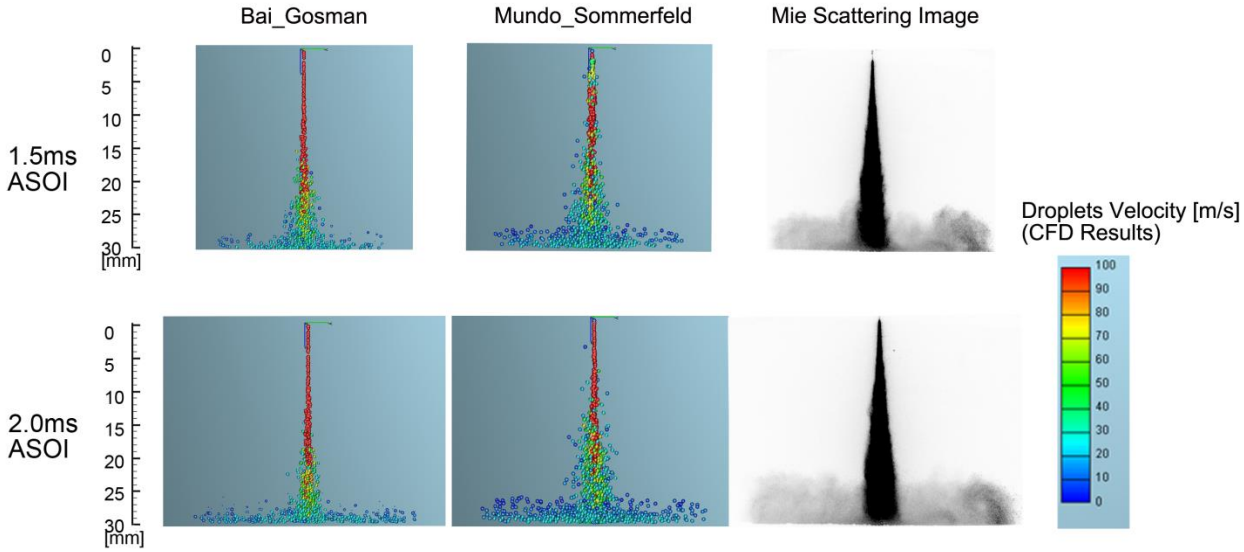

Figure 8.10 Comparison of Impinging Spray between CFD Results and Mie Scattering Images (Pinj=100MPa, ρa=15kg/m^3, d=0.08mm)

Figure 8.11 shows the effects of injection pressure and impingement distance on the gas flow and droplets flow from CFD and LIF-PIV results. The same as the LIF-PIV results, the large vortex motion forms at the tip periphery can also be observed in the CFD results, it tends to be stronger with the increase of injection pressure and the decrease of impingement distance. Due to the influence of recirculation motion in the impingement spray region, the gas entrainment near the impingement point shows a larger value than upstream.

Figure 8.12 shows the effect of wall temperature on the impinging spray development under the evaporating condition. The ambient gas temperature was set to 885K, and the ambient

gas density was kept as 15kg/m^3. Two types of wall temperature, 273K and 885K were employed. It is clear that due to the less influence from the wall liquid film, the higher wall temperature results in faster fuel vaporization, the higher equivalence ratio distribution can be observed. Meanwhile, the gas flow velocity shows higher value and the spray penetration increases.

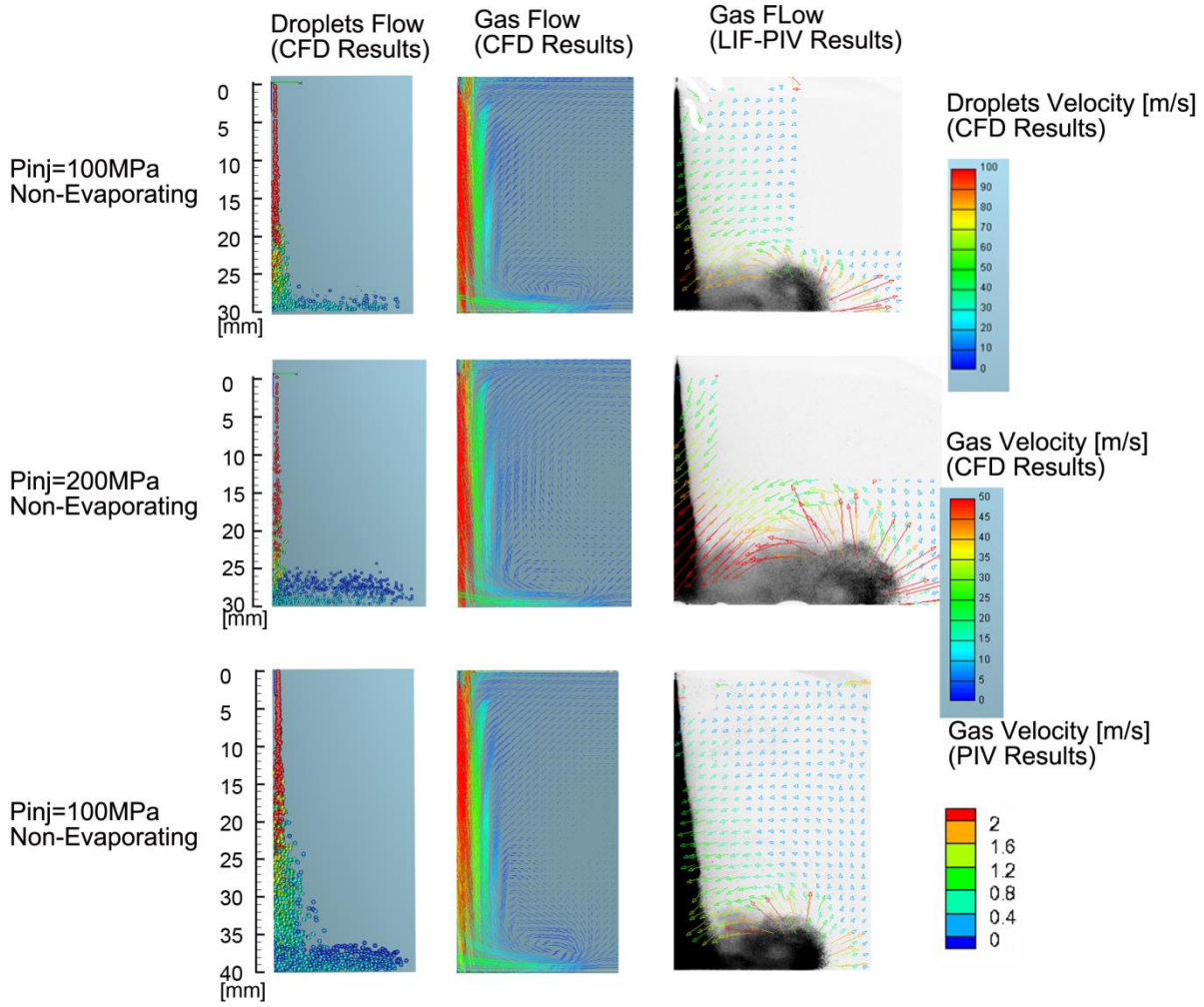

Figure 8.11 Effects of Injection Pressure and Impingement Distance on Gas Flow and Droplets Flow (ρa=15kg/m^3, d=0.08mm, 2.0ms ASOI)

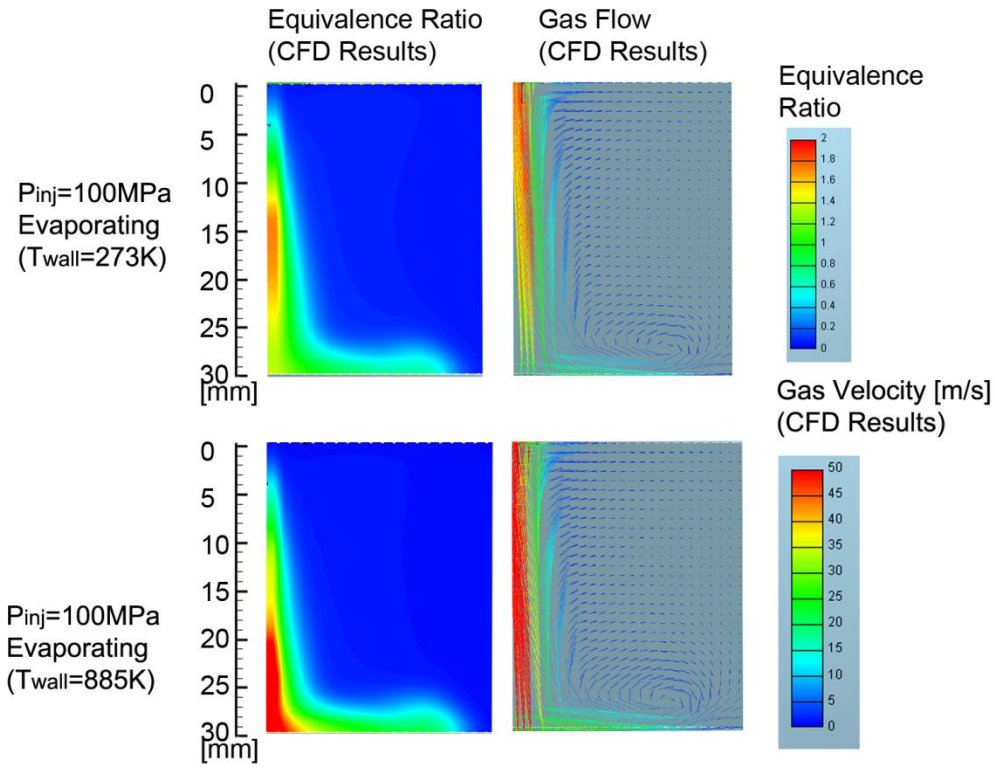

Figure 8.12 Effect of Wall Temperature on Impinging Spray Development (Pinj=100MPa, ρa=15kg/m^3, d=0.08mm, 2.0ms ASOI)

Due to the significant influence of the liquid wall film on the impinging spray evolution, the formation of liquid wall film under the different conditions is shown in Fig. 8.13. The effect of impingement distance is shown in Fig. 8.13(a) and (b), more than 80% of the fuel will stick to the wall under the impingement distance of 30mm, and this proportion will reduce to 60% if the impingement distance of 40mm was used. More liquid fuel suspends in the ambient gas, which results in long spray penetration and higher ambient gas flow velocity. Figure 8.13(c) and (d) show the effect of impinging wall temperature. Almost all the fuel will be vaporized after EOI if the wall temperature is the same as the ambient gas temperature, very few liquid film is left. As shown in Fig. 8.13 (e), the increase of injection pressure almost does not change the proportion of the liquid film mass to the total mass. As a conclusion, it proves the considerable influence of impingement distance and wall temperature on the liquid film formation, which will further impact the fuel vaporization and combustion characteristics, as presented in the previous chapters.

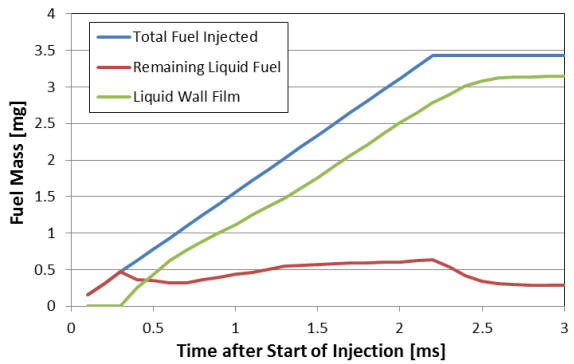

(a) P_{inj}=100MPa, Z=30mm, Non-E

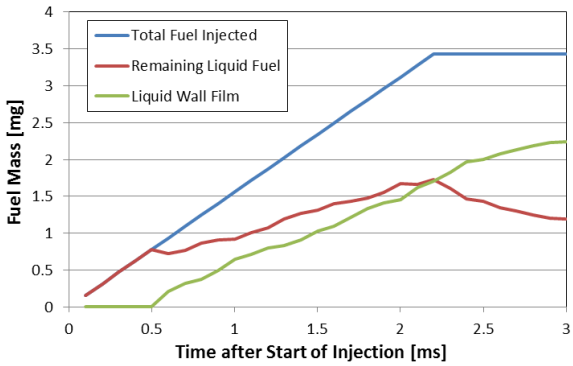

(b) P_{inj}=100MPa, Z=40mm, Non-E

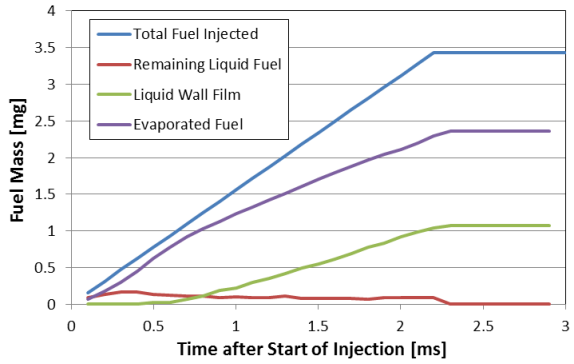

(c) P_{inj}=100MPa, Z=30mm, E (T_{wall}=273K)

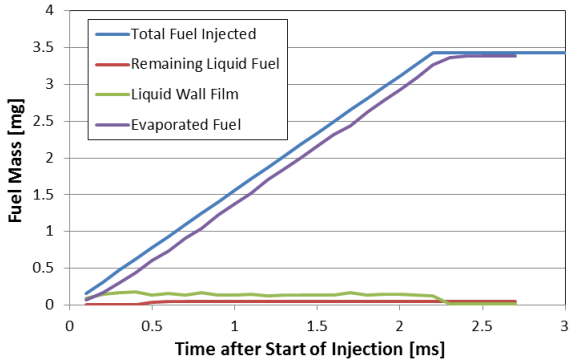

(d) P_{inj}=100MPa, Z=30mm, E (T_{wall}=885K)

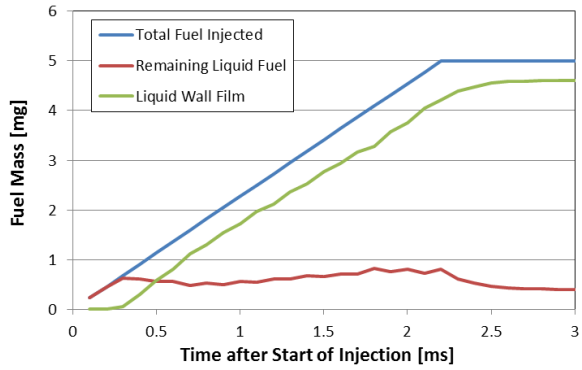

(e) P_{inj}=200MPa, Z=30mm, Non-E

Figure 8.13 Formation of Liquid Wall Film

8.5 SUMMARY

The numerical simulation of the Diesel spray was carried out using CFD code AVL FIRE® with RANS equations and standard $k-\varepsilon$ model. The CFD results are available to provide more profound understanding of the spray characteristics.

Based on this study, the following can be concluded:

1. The parameters of sub-models were adjusted carefully according to the experimental results, the selection of parameters is summarized.
2. For the free spray, the droplets flow and ambient gas flow from the CFD results were compared with the previous experiment results, which validate the accuracy of the measurement results.
3. The absolute pressure result suggests that the velocity of entrained gas is accelerated to a high value after entering the spray periphery due to the existence of pressure gradient from the spray periphery to the center line. On the other hand, a comparatively higher pressure region can be observed at the tip periphery, which leads to the pushed-out gas motion.
4. By extracting the droplets velocity and ambient gas velocity along the nozzle axis from the CFD results, it is found that the mean droplets velocity shows higher value than that of ambient gas, and the different tends to be larger with the increase of the injection pressure. This implies that spray droplets will capture large amount of ambient gas at the tip region. The actual spray development will be determined by the droplets with relatively higher velocity a little bit upstream of the spray tip.
5. For the flat-wall impinging spray, the Bai_Gosman Model and the Mundo_Sommerfeld Model are believed to be suitable for the high fuel injection pressure simulation.
6. The large vortex motion forms at the tip periphery can also be observed in the CFD results, it tends to be stronger with the increase of injection pressure and the decrease of impingement distance.
7. Due to the less influence from the wall liquid film, the higher wall temperature results in faster fuel vaporization, the higher equivalence ratio distribution can be observed. Meanwhile, the gas flow velocity shows higher value and the spray penetration increases.
8. The considerable influence of impingement distance and wall temperature on the liquid film formation is studied, which will further impact the fuel vaporization and combustion characteristics, as presented in the previous chapters.

CHAPTER 9 CONCLUSIONS

This study is aimed at clarifying the mixing process and the combustion characteristics of the high pressure D.I. Diesel spray in the quiescent condition. A wide range of injection pressure from the ordinary values in the current Diesel engines (100MPa, 200MPa) to the ultra-high (300MPa) value was selected. Three representative ambient gas density conditions (11, 15, 20 kg/m3) were selected. A micro-hole nozzle (0.08mm) and a conventional nozzle (0.12mm) were applied as the test nozzles in this study. The LIF-PIV (Laser Induced Fluorescence- Particle Image Velocimetry) and PIV (Particle Image Velocimetry) techniques were applied to measure the spray internal flow and ambient gas flow. The combustion features such as the natural luminosity of the reacting Diesel spray was visualized by using a high speed video camera. The OH chemiluminescence measurement and the soot concentration/temperature distribution measurement by two-color pyrometry provide the quantitative information of the Diesel flame. Numerical Simulation was conducted by AVL® FIRE commercial software.

The general findings in this research are summarized in this chapter.

9.1 FLOW FIELD OF AMBIENT GAS

The characteristics of the Diesel spray evolution and the spray induced ambient gas motion were measured quantitatively by using PIV, LIF-PIV and high speed video camera under both the non-evaporating and the evaporating quiescent condition. The ambient gas velocity and mass flow rate into the spray through the whole spray periphery (spray side periphery and tip periphery) were investigated quantitatively.

For the free spray, The spray model proposed in the study divides the spray body into entrainment section, recirculation section and capturing section, which quantitatively describes the ambient gas flow field of a transient Diesel spray. The ambient gas mass flow rate into the spray through the spray tip periphery is prominent in the whole periphery in non-evaporating spray condition and the proportion of the ambient gas entrainment along the side periphery increases as the spray developing. Higher injection pressure improves the ambient gas mass flow rate into the spray, both at the spray side periphery due to the increased drag force and at the tip periphery due to the larger droplets/gas velocity difference. However the increase in total entrained gas-fuel ratio tends to be moderate when the injection pressure rises to the ultra-high level. Higher ambient gas density suppresses the entrainment section length and the spray

penetrating velocity, on the other hand, the ambient gas mass flow rate into the spray increases apparently. As a result, the equivalence ratio of the spray decreases under the higher ambient gas density condition. The smaller nozzle hole size results in the significant decrease in the ambient gas mass flow rate into the spray, on the other hand, the ratio of the ambient gas and fuel mass flow rate increases. The gas velocity along the side periphery for the non-evaporating case shows a slight larger value than that of the evaporating case. On the other hand, a considerable increase of the pushed out gas velocity at the tip periphery can be found in the evaporating case, in contrast, the spray tip penetration for the evaporating case decreases due to the faster momentum loss of the vapor phase. A large amount of ambient gas flow mass is attributed to the flow at the tip region in both the non-evaporating and the evaporating condition. The role of the gas flow along the side periphery becomes more important in evaporating spray condition. The total ambient gas mass flow rate for the evaporating case decrease remarkably.

For the flat-wall impinging spray, the spray-wall impingement restricts the spray penetration and the increase of the spray volume under the non-evaporating condition. The shorter the impinging distance is, the more the penetrating length is limited. It is evident that the pushed-out gas velocity for the impinging spray is larger than that for the free spray, the strong wall jet vortex forms at the spray head contributes to this result. The pushed-out gas velocity at the spray head and the gas velocity at the recirculation region increase apparently with the increase of the injection pressure. The ambient gas flow is intensified with the decrease of the impingement distance, particularly in the post-impingement region. Under the condition of the impinging spray, the entrained gas mass from side periphery takes up much lower proportion because of the restrained entrainment section. With the radial expansion of the spray, the velocity difference between the spray head and the ambient gas decreases, resulting in the reduction of the proportion of the total gas mass flow from the tip region. At the same time, due to the extension of the length of the recirculation section and the increased gas flow velocity, the proportion of the gas flow from the recirculation section increases. The instantaneous ratio of gas/fuel mass flow rate increases with increasing the injection pressure. Compared with that of the free spray, less effect of higher injection pressure on the improvement of gas/fuel ratio under the impinging spray condition can be observed. The wall impingement restrains the development of the fuel spray and the ambient gas mass flow rate, compared with the free spray condition. The shorter the nozzle-wall distance is, the more the ambient gas mass flow rate is suppressed.

9.2 FLOW FIELD OF SPRAY

The characteristics of the droplets flow of the non-evaporating spray and the vapor flow of the evaporating spray were measured quantitatively by using PIV technique.

For the free spray, the incoherent velocity distribution and mass concentration distribution can be found inside the spray. The spray droplets velocity decelerates gradually with time, especially in the downstream region. The vorticity distribution inside the spray corresponds to the resultant heterogeneity of the fuel mass concentration distribution. Correspondingly, the fuel parcel with different mass concentration also determines flow velocity distribution and the spray development. Higher injection pressure enhances the mean flow velocity and the vorticity intensity in the whole region, which implies the promotion of the fuel/gas mixing process. With the increase of the fuel injection pressure, the fluctuation of the velocity spreads radially and axially towards the spray tip region. Such kind of high velocity fluctuation implies the strong turbulent mixing occurs throughout the spray plume, which is favorable to the uniform and lean mixture formation. On the other hand, the uncertainty of the fuel/gas mixture formation also increases. The much stronger vorticity and flow fluctuation inside the spray can be observed in the evaporating case. This is because that the vapor phase with less momentum is subjected to the resistance of the surrounding gas at the tip region much easier. The ambient gas flow velocity and the gas mass flow rate at the tip region depend on the local fuel vapor pressure, the vapor flow velocity and the vortex intensity.

For the flat-wall impinging spray, the spray droplets move downwards straightly with high velocity, in the free spray region prior to the wall impingement. After wall impingement the spray droplets move towards the radial direction and lose the momentum gradually due to the friction with the liquid film. A large scale wall-jet vortex motion can be found in the upper part of the post-impingement spray region. As a result, the “recirculation section” forms in this region, in which a large amount of ambient gas move back towards the impinging point with the spray droplets. The increase of fuel injection pressure improves the mean velocity value, the vorticity intensity, which implies the promotion of the turbulent mixing process of the fuel/gas mixture. Even though the mean droplets velocity does not change very much, the vorticity intensity tends to be improved with the decrease of the impingement distance especially at the post-impingement spray region. This is considered to be related to the larger pushed-out ambient gas velocity at the tip region under the shorter impingement distance condition. The vorticity

intensity or the small scale turbulent mixing is considerably improved under the evaporating condition, which would restrain the spray development but improve the uniform mixture formation.

9.3 IGNITION AND COMBUSTION PROCESS

The characteristics of the combustion process of the Diesel spray were investigated using the direct imaging of natural flame luminosity, OH* chemiluminescence imaging and two color pyrometry techniques, with respect to the free spray condition and the flat-wall impinging spray condition.

The position of the soot luminosity is around the spray tip region for all the cases. Most of the soot will be oxidized at the thin periphery of spray tip due to the strong turbulent mixing with ambient gas. The soot luminosity region moves downstream together with the spray development. The lower ambient gas density, which corresponds to the lower ambient pressure and temperature, significantly postpones the inception of the soot formation even after EOI, which provides enough time for forming the lean fuel/air mixture, as a result, the formation of soot is restrained. The ultra-high injection pressure improves the fuel/air mixing rate, resulting in a low flame luminosity level even in the high ambient gas density condition. As the fuel/gas mixing is proceeding in the diffusive combustion, soot is oxidized gradually after reaching the peak value.

According to the OH* chemiluminescence results, the increase of the fuel injection pressure and the ambient gas density reduces the ignition delay due to the rapid fuel/gas mixing (physical process) and exothermic reaction (chemical process). The upper boundary of the OH* signal keeps stable after the spray reaches the quasi-steady state. The natural luminosity appears at the early stage is originated from other radicals, the low OH* signal is masked. However, OH* is proper to mark the high temperature exothermic reaction. The increase of the fuel injection pressure and the decrease of the ambient gas density tends to slightly reduce the OH* intensity since the formation of the leaner mixture reduces the combustion temperature. On the other hand, the increase of nozzle hole size significantly increases the ignition delay and the OH* signal intensity. More air is entrained upstream of the lift-off length with the increase of injection pressure, the decrease of nozzle hole size and ambient gas density. The relative location of the liquid length and the lift-off length is related to the combustion behavior.

The maximum KL factor distributes near the flame tip region, which implies large amount of soot clouds form in the inner region of the turbulent diffusive flame phase. While along the spray periphery especially at the spray tip, the relatively lower soot level can be observed, which coincides with the suggestion that most of soot will be consumed on the thin layer of the diffusive flame front during the strong mixing process with the ambient gas. The reduction of ambient gas density apparently lowers the soot level of the flame, which is attributed to the longer ignition delay. Regardless of the ambient gas density, the ultra-high injection pressure significantly reduces the soot level and flame temperature. On the other hand, the use of larger nozzle hole size evidently increases the soot level even though the ultra-high injection pressure was applied, due to the direct interaction of the liquid phase and the initial combustion phase. The correlation of the ratio of ambient gas/fuel mass flow rate ($\dot{M}_a/\dot{M}_f$) upstream of the lift-off length and the total integrated flame KL factor and the schematics of spray flame evolution were presented.

For the wall impinging spray, the OH* signal can only be detected near the wall, the lift-off length for the impinging spray tends to be longer. One of the main reasons are that the lower ambient gas mass flow rate for impinging spray (measured by LIF-PIV technique) delays the fuel/gas mixing, as a result, the much longer ignition delay for the impinging spray allows the spray to extend further and mix with the ambient gas with longer period prior to the auto-ignition. The longer ignition delay may facilitate the fuel/gas mixing; On the other hand, the much longer ignition delay (especially for the short impingement condition) may also result from the poor fuel/gas mixture due to the direct liquid-wall impingement. Compared with the free spray, the spray-wall impingement is likely to reduce the soot formation level if the proper injection pressure and nozzle hole size are selected. The shorter impingement distance tends to increase the soot level. The resultant fuel vaporization and combustion characteristics of the wall impinging spray depend on the combined effects of the liquid length, impingement distance, turbulent mixing intensity, wall temperature and so on.

9.4 NUMERICAL SIMULATION OF DIESEL SPRAY

The numerical simulation of the Diesel spray was carried out using CFD code AVL FIRE® with RANS equations and standard k-ε model. The parameters of sub-models were adjusted carefully according to the experimental results, the selection of parameters is summarized.

For the free spray, the droplets flow and ambient gas flow from the CFD results were compared with the previous experiment results, which validate the accuracy of the measurement results. The absolute pressure result suggests that the velocity of entrained gas is accelerated to a high value after entering the spray periphery due to the existence of pressure gradient from the spray periphery to the center line. On the other hand, a comparatively higher pressure region can be observed at the tip periphery, which leads to the pushed-out gas motion. By extracting the droplets velocity and ambient gas velocity along the nozzle axis from the CFD results, it is found that the mean droplets velocity shows higher value than that of ambient gas, and the different tends to be larger with the increase of the injection pressure. This implies that spray droplets will capture large amount of ambient gas at the tip region. The actual spray development will be determined by the droplets with relatively higher velocity a little bit upstream of the spray tip.

For the flat-wall impinging spray, the Bai_Gosman Model and the Mundo_Sommerfeld Model are believed to be suitable for the high fuel injection pressure simulation. The large vortex motion forms at the tip periphery can also be observed in the CFD results, it tends to be stronger with the increase of injection pressure and the decrease of impingement distance. Due to the less influence from the wall liquid film, the higher wall temperature results in faster fuel vaporization, the higher equivalence ratio distribution can be observed. Meanwhile, the gas flow velocity shows higher value and the spray penetration increases. The considerable influence of impingement distance and wall temperature on the liquid film formation is studied, which will further impact the fuel vaporization and combustion characteristics, as presented in the previous chapters.

9.5 RECOMMENDATIONS FOR FUTURE WORKS

More fundamental experiments with more systematically varying parameters are recommended to provide data for calibrating the predicative models.

The precision of measurement of the ambient gas flow and vapor phase flow on the evaporating spray using PIV technique needs to be improved by introducing a more suitable tracer and more sensitive camera system. It would be more promising to employ a tracer matter with fluorescent property and enduring the high temperature atmosphere. Due to the fluctuation of spray development shot by shot especially at the spray tip region, the simultaneous investigation of spray/ambient gas flow at the magnified region of the tip region with PIV/LIF-PIV system would provide more understanding of the spray development.

The numerical simulation has the potential to provide more information of the spray evolution that is not able to be obtained by the experimental measurement. In the future, focus will be paid on the optimization of the parameters of the models for the ultra-high injection pressure, the multiphase-flow inside the nozzle orifice and the spray combustion process.

Although the strengthened turbulent flow in the real engine condition may cause the difference in fuel vaporization and soot formation, the relative relationship is assumed to be the same as the current study. It is recommended to study the spray and combustion characteristics using ultra-high injection pressure and micro-hole nozzle in the production optical engines.

REFERENCES

1. **Adrian, R.** (1991) Particle Imaging Techniques for Experimental Fluid Mechanics. *Annu. Rev. Fluid Mech.*, 23, 261-304.
2. **Aizawa, T., Kosaka, H.,** and **Matsui, Y.** (2002) 2-D Imaging of Soot Formation Process in A Transient Spray Flame by Laser-Induced Fluorescence Techniques. *SAE Paper* 2002-01-2669.
3. **Arcoumanis, C.,** and **Enotiadis, A. C.** (1991) In-Cylinder Fuel Distribution in A Port-Injected Model Engine Using Rayleigh Scattering. *Expts. Fluids*, 11, 375-387.
4. **Allocca, L., Andreassi, L.,** and **Ubertini, S.** (2007) Enhanced Splash Models for High Pressure Diesel Spray. *Journal of Engineering for Gas Turbines and Power*, 129, 609-621.
5. **Andresen, P., Meijer, G., Schliiter, H., Voges, H., Koch, A., Hentenschel, W., Oppermann, W., and Rothe, E.** (1990) Fluorescence Imaging inside An Internal Combustion Engine Using Tunable Excimer Lasers. *Applied Optics*, 29, 2392-2402.
6. **Andreassi, N., Ubertini, S.,** and **Allocca, L.** (2007) Experimental and Numerical Analysis of High Pressure Diesel Spray-wall Interaction. *International Journal of Multiphase Flow, 33, 742-765.*
7. **Aoyama, T., Hattori, Y., Mizuta, J.,** and **Sato, Y.** (1996) An Experimental Study on Premixed-Charge Compression Ignition Gasoline Engine. *SAE Paper* 960081.
8. **Arai, M., Shimizu, M.,** and **Hiroyasu, H.** (1991) Similarity between the Breakup Lengths of a High Speed Liquid Jet in Atmospheric and Pressurized Conditions. Los Alamos National Laboratory.
9. **Arifin, Y. M.,** and **Arai, M.** (2010) The Effect of Hot Surface Temperature on Diesel Fuel Deposit Formation. *J.Fuel*, 89, 934–942.
10. **Bai, C.,** and **Gosman, A. D.,** (1995) Development of Methodology for Spray Impingement Simulation. *SAE Paper* 950283.
11. **Baumgarten, C.** (2006) *Mixture Formation in Internal Combustion Engine*. Berlin Heidelberg, Springer-Verlag.
12. **Bo ödec, T.,** and **Simo ëns, S.** (2001) Instantaneous and Simultaneous Planar Velocity Field Measurements of Two Phases for Turbulent Mixing of High Pressure Sprays. *Exp. Fluids*, 31, 506-518.

13. **Bruneaux, G.,** and **Causse, M.** (2011) Air Entrainment in Diesel-Like Gas Jet by Simultaneous Flow Velocity and Fuel Concentration Measurements, Comparison of Free and Wall Impinging Jet Configurations. *SAE Paper* 2011-01-1828.
14. **Bruneaux, G.** (2005) Mixing Process in High Pressure Diesel Jets by Normalized Laser Induced Exciplex Fluorescence Part II: Wall Impinging Versus Free Jet. *SAE Paper* 2005-01-2097.
15. **Cao, M., Nishino, K., Mizuno, S.,** and **Torii, K.** (2000) PIV Measurement of Internal Structure of Diesel Fuel Spray. *Exp. Fluid*, 29, 211-219.
16. **Cho, I.Y., Fujimoto, H., Kuniyoshi, H., Ha, J.Y., Tanaba, H.,** and **Sato, G.T.** (1990) Similarity Law of Entrainment into Diesel Spray and Steady Spray. *SAE Paper* 900447.
17. **Chomiak, J.,** and **Karlsson, A.** (1996) Flame Lift-off in Diesel Spray. *26th symposium (international) on combustion.* The combustion institute, Pittsburgh, 557-2504.
18. **Chraplyvy, A. R.** (1981) Nonintrusive Measurements of Vapor Concentrations inside Sprays. *Applied Optics*, 20, 15.
19. **Collin, R., Nygren, J., Richter, M., Aldén, M., Hildingsson, L.,** and **Johansson, B.** (2003) Simultaneous OH- and Formaldehyde-LIF Measurements in an HCCI Engine. *SAE Paper* 2003-01-3218.
20. **Dandy, D. S.,** and **Vosen, S. R.** (1992) Numerical and Experimental Studies of Hydroxyl Radical Chemiluminescence in Methane-Air Flames. *Combust. Sci. Technol.* 82 (1), 131–150.
21. **Dec, J. E.** (1997) A Conceptual Model of DI Diesel Combustion Based on Laser-Sheet Imaging. *Transactions of the SAE*, 106, 3, 1319-1348.
22. **Dec, J. E.,** and **Espey, C.** (1995) Ignition and Early Soot Formation in a D.I. Diesel Engine Using Multiple 2-D Imaging Diagnostics. *SAE Paper* 950456.
23. **Dec, J. E.,** and **Espey, C.** (1998) Chemiluminescence Imaging of Autoignition in a DI Diesel Engine. *SAE Paper* 982685.
24. **Dent, J. E.** (1971) A Basis for the Comparison of Various Experimental Methods for Studying Spray Penetration. *SAE Paper* 710571.
25. **Dec, J. E.,** and **Tree, D. R.** (2001) Diffusion-Flame/Wall Interactions in a Heavy-Duty DI Diesel Engine. *SAE Paper* 2001-01-1295.
26. **Driscoll, K. D., Sick, V.,** and **Gray, C.** (2003) Simultaneous Air/fuel-phase PIV Measurements in a Dense Fuel Spray. *Exp. Fluids*, 35, 112-115.

27. **Düwel, I., Koban, W., Zimmermann, F. P., Dreier, T.,** and **Schulz, C.** (2009) Spectroscopic Characterization of The Fluorobenzene/DEMA Tracer System for Laser-Induced Exciplex Fluorescence for The Quantitative Study of Evaporating Fuel Sprays. *Appl. Phys. B*, 97, 909–918.
28. **Dukowicz, J.K.** (1979) Quasi-Steady Droplet Change in the Presence of Convection. *Informal report*. Los Alamos Scientific Laboratory, LA7997-MS.
29. **Espey, C., Dec, J., Litzinger, T. A.** and **Santavicca, A.** (1994) Quantitative 2-D Fuel Vapor Concentration Imaging in a Firing D.I. Diesel Engine Using Planar Laser-Induced Rayleigh Scattering. *SAE Paper* 940682.
30. **Endo, S.** (2011) Powertrain Technologies of Commercial Vehicles for Today and Future. *2011 SAE/JSAE International, Keynotes*. Kyoto, Japan.
31. **Fajardo, Claudia.**, and **Sick Volker.** (2009) Development of a high-speed UV particle image velocimetry technique and application for measurements in internal combustion engines. *Exp. Fluids*, 46:43-53.
32. **Flynn, P. F., Durrett, R. P., Hunter, G. L., Loye, A.O., Akinyem, O. C., Dec, J. E.,** and **Westbrook, C. K.** (1999) Diesel Combustion: An Integrated View Combining Laser Diagnostics, Chemical Kinetics, and Empirical Validation. *SAE Paper* 1999-01-0509.
33. **Gaydon, A. G.** (1974) *The Spectroscopy of Flames, 2nd Ed*. Chapman and Hall, London.
34. **Gao, J., Matsumoto, Y., Namba, M.,** and **Nishida, K.** (2007) Group-Hole Nozzle Effects on Mixture Formation and In-cylinder Combustion Processes in Direct-Injection Diesel Engines. *SAE Paper* 2007-01-4050.
35. **Gao, J., Moon, S., Zhang, Y., Nishida, K.,** and **Matsumoto, Y.** (2009) Flame Structure of Wall-Impinging Diesel Fuel Sprays Injected by Group-Hole Nozzle. *Combust. Flame*, 156, 1263-1277.
36. **Han, D.,** and **Mungal, M. G.** (2001) Direct Measurement of Entrainment in Reacting / Non-Reacting Turbulent Jets. *Combustion and Flame*, 124, 370–386.
37. **Huethorst, J. A. M.,** and **Marra, J.** (1991) Motion of Marangoni-Contracted Water Drops across Inclined Hydrophilic Surfaces. *Langmuir*, 7, 2756-2763.
38. **Higgins, B., Siebers, D.,** and **Aradi, A.** (2000) Diesel-Spray Ignition and Premixed-Burn Behavior. *SAE Paper* 2000-01-0940.

39. **Higgins, B., McQuay, M. Q., Lacas, F.,** and **Candel, S.** (2001) An Experimental Study on The Effect of Pressure And Strain Rate on CH Chemiluminescence of Premixed Fuel-Lean Methane/Air Flames. *J. Fuel*, 80 (11), 1583–1591.
40. **Hillamo, H., Kaario, O.,** and **Larmi, M.** (2008) Particle Image Velocimetry Measurements of a Diesel Spray. *SAE Paper* 2008-01-0942.
41. **Hill, B.J.** (1972) Measurement of local entrainment rate in the initial region of axysimmetric turbulent air jets. *J.Fluid Mech.*, 51, 773-779.
42. **Hiroyasu, H., Shimizu, M.,** and **Arai, M.** (1991) Breakup Length of a Liquid Jet and Internal Flow in a Nozzle. *Proc. ICLASS-91*, 275-282.
43. **Hiroyasu, H.,** and **Arai, M.** (1990) Structures of Fuel Sprays in Diesel Engines. *SAE Paper* 900475.
44. **Hottel, H.,** and **Broughton, F.** (1932) Determination of True Temperature and Total Radiation from Luminous Gas Flames. *Ind. And Eng. Chem.*, 4(2), 166-174.
45. **Hori, T., Senda, J., Kuge, T.,** and **Fujimoto, H.** (2006) Large Eddy Simulation of Non-Evaporative and Evaporative Diesel Spray in Constant Volume Vessel by Use of KIVALES. *SAE Paper* 2006-01-3334.
46. **Ikegami, M.,** and **Kamimoto, T.** (2009) Conventional Diesel Combustion. In: Arcoumanis, C., and Kamimoto, T., Editors. *Flow and Combustion in Reciprocating Engines*. Berlin Heidelberg, Springer-Verlag.
47. **Iida, N.** (1994) Combustion Analysis of Methanol-Fueled Active Thermo-Atmosphere Combustion (ATAC) Engine Using A Spectroscopic Observation. *SAE Paper* 940684.
48. **Jafarmadar, S., Khalilarya, S., Shafee, S.,** and **Barzegar, R.** (2009) Modeling the Effect of Spray/Wall Impingement on Combustion Process and Emission of DI Diesel Engine. *Thermal Science*, 13, 3, 23-34.
49. **Johnston, S. C.** (1980) Raman Spectroscopy and Flow Visualization Study of Stratified Charge Engine Combustion. *SAE Paper* 800136.
50. **Katura, N., Saito, M., Senda, J.,** and **Fujimoto, H.,** (1990) *JSME Trans.*, 56, 521, 227-234.
51. **Katsura, N., Saito, M., Senda, J.,** and **Fujimoto, H.** (1989) Characteristics of a Diesel Spray Impinging on a Flat Wall. *SAE Paper* 890264.
52. **Kawashima, J. I., Ogawa, H.,** and **Tsuru, Y.** (1998) Research on A Variable Swirl Intake Port for 4-Valve High-Speed DI Diesel Engines. *SAE Paper* 982680.

53. **Keane, R.D.,** and **Adrian, R.J.** (1990) Optimization of Particle Image Velocimeters, Part 1: Double Pulsed Systems. *Meas. Sci. Tech.*, 1(11), 1202-1215.
54. **Kimura, S., Aoki, O., Ogawa, H., Muranaka, S.,** and **Enomoto, Y.** (1999) New Combustion Concept for Ultra-Clean and High-Efficiency Small DI Diesel Engines. *SAE Paper* 1999-01-3681.
55. **Kitamura, T., Ito, T., Senda, J.,** and **Fujimoto, H.** (2002) Mechanism of Smokeless Diesel Combustion with Oxygenated Fuels Based on The Dependence of The Equivalence Ration and Temperature on Soot Particle Formation. *Int. J. Engine Res.*, 3(4), 223-248.
56. **Kobayashi, S., Sakai, T., Nakahira, T., Komori, M.,** and **Tsujimura, K.** (1992) Measurement of Flame Temperature Distribution in D.I. Diesel Engine with High Pressure Fuel Injection. *SAE Paper* 920692.
57. **Kosaka, H., Aizawa, T.,** and **Kamimoto, T.** (2005) Two-Dimensional Imaging of Ignition and Soot Formation Processes in a Diesel Flame. *International Journal of Engine Research*, 6(1), 21-42.
58. **Kosaka, H., Won, Y. H.,** and **Kamimoto, T.** (1992) A Study of the Structure of Diesel Sprays Using 2-D Imaging Techniques. *SAE Paper* 920107.
59. **Koo, J. A.,** and **Martin, J. K.** (1990) Droplet Sizes and Velocities in A Transient Diesel Fuel Spray. *SAE Paper* 900397.
60. **Kook, S., Le, M. K., Padala, S.,** and **Hawkes, E.** (2011) Z-type Schlieren Setup and its Application to High-Speed Imaging of Gasoline Sprays. *SAE Paper* 2011-01-1981.
61. **Kuniyoshi, H., Tanabe, H., Sato, G. T.,** and **Fujimoto, H.** (1980) Investigation on the Characteristics of Diesel Fuel Spray. *SAE Paper* 800968.
62. **Larrabee, R.D.** (1957) The Spectral Emissivity and Optical Properties of Tungsten. *Technical Report*. Research Laboratory of Electronics, Massachusetts Institute of Tecnhnology, Cambridge, Massachusetts.
63. **Larsson A**. (1999) Optical Studies in a DI Diesel Engine. *SAE Paper* 1999-01-3650.
64. **Lacoste, J., Crua, C., Heikal, M., Kennaird, D.,** and **Gold, M.** (2003) PDA Characterization of Dense Diesel Sprays Using A Common-Rail Injection System. *SAE Paper* 2003-01-3085.
65. **Launder, B. E.,** and **Spalding, D. B.** (1974) The Numerical Computation of Turbulent Flows. *Comp. Meth. Appl. Mech. Eng.* 3, 269-289.

66. **Lee, J.,** and **Nishida, K.** (2002) An Analysis of Ambient Air Entrainment into Split Injection D.I. Gasoline Spray by LIF-PIV Technique. *SAE Paper* 2002-01-2662.
67. **Lee, S. Y.,** and **Sung, U. R.** (2006) Recent Progress of Spray-wall Interaction Research. *Journal of Mechanical Science and Technology*, 20(8), 1101-1117.
68. **Liu, A.B.,** and **Reitz, R.D.** (1993) Modeling yhe Effects of Drop Drag and Break-Up on Fuel Sprays. *SAE Paper* 930072.
69. **Liu, F. S., Zhou, L., Sun, B. G., Li, Z. J.,** and **Harold, J. S.** (2008) Validation and Modification of WAVE Spray Model for Diesel Combustion Simulation. *J. Fuel,* 87, 3420–3427.
70. **Lyn, W. T.** (1957) Study of Burning Rate and Nature of Combustion in Diesel Engines. *J. Inst. Petrol.*, 43, 25.
71. **Matsui, Y., Kamimoto, K.,** and **Matsuoka, S.** (1979) A Study on The Time and Space Resolved Measurement of Flame Temperature and Soot Concentration in a D. I. Diesel Engine by The Two-Color Method. *SAE Paper* 790491.
72. **Melton, L. A.,** and **Verdieck, J. F.** (1985) Vapor/Liquid Visualization in Fuel Sprays. *Symposium (International) on Combustion*, 20, 1283-1290.
73. **Meyer, J., Haug, M., Schreiber, M.,** and **Unverzagt, S.** (1995) Controlling Combustion in a Spark Ignition Engine by Quantitative Fuel Distribution. *SAE Paper* 950107.
74. **Minato, A., Tanaka, T.,** and **Nishimura, T.** (2005) Investigation of Premixed Lean Diesel Combustion with Ultra-High- Pressure Injection. *SAE Paper* 2005-01-0914.
75. **Moon, S., Matsumoto, Y., Nishida, K.,** and **Gao, J.** (2010) Gas Entrainment Characteristics of Diesel Spray Injected by A Group-Hole Nozzle. *J. of Fuel*, 89, 3287-3299.
76. **Mundo, C., Sommerfeld, M.,** and **Tropea, M. C.** (1994) Experimental Studies of the Deposition and Splashing of Small Liquid Droplets Impinging on a Flat Surface. *ICLASS-94 Rouen.* France.
77. **Bobba, M., Genzale, C.,** and **Musculus, M.** (2009) Effect of Ignition Delay on In-Cylinder Soot Characteristics of a Heavy Duty Diesel Engine Operating at Low Temperature Conditions. *SAE Paper* 2009-01-0946.
78. **Naber, J. D.,** and **Siebers, D. L.** (1996) Effects of Gas Density and Vaporization on Penetration and Dispersion of Diesel Spray. *SAE Trans.*, 105, 3, 82-111.

79. **Naber, J. D.,** and **Siebers, D. L.** (1996) Effect of Gas Density and Vaporization on Penetration and Dispersion of Diesel Sprays. *SAE Paper* 960034.
80. **Nakagome, K., Shimazaki, N., Miimura, K.,** and **Kobayashi, S.** (1997) Combustion And Emissions Characteristics Of Premixed Lean Diesel Combustion Engine. *SAE Paper* 970898.
81. **Noguchi, M.,** and **Tanaka, Y.** (1979) A Study on Gasoline Engine Combustion by Observation of Intermediate Reactive Products during Combustion. *SAE Paper* 790804.
82. **Nurick, W. H.** (1976) Orifice Cavitation and Its Effects on Spray Mixing. *ASME J. Fluids Eng.,* 681–7.
83. **Odaka, M., Suzuki, H., Koike, N.,** and **Ishii, H.** (1999) Search for Optimizing Method of Homogeneous Charge Diesel Combustion. *SAE Paper* 1999-01-0184.
84. **Okude, K., Mori, K., Shiino, S., and Moriya, T.** (2004) Premixed Compression Ignition (PCI) Combustion for Simultaneous Reduction of Nox and Soot in Diesel Engine. *SAE Paper* 2004-01-1907.
85. **Onishi, S.,** and **Hong, S.** (1979) Active Thermal-Atmosphere Combustion (ATAC) - A New Combustion Process for Internal Combustion Engines. *SAE Paper* 790501.
86. **Oppenheim, A. K.** (1984) The Knock Syndrome-Its Cures and Its Victims. *SAE Paper* 841139.
87. **Payri, R., Tormos, B., Salvador, F.J.,** and **Araneo, L.** (2008) Spray Droplet and Velocity Characterization for Convergent Nozzles with Three Different Diameters. *J. Fuel*, 87, 3176-3182.
88. **Payri, F., Bermudez, V., Payri, R.,** and **Salvador, F. J.** (2004) The Influence of Cavitation on The Internal Flow And The Spray Characteristics in Diesel Injection Nozzles. *J. of Fuel*, 83, 419–431.
89. **Peng, Z. J., Zhao, H.,** and **Ladommatos, N.** (2003) Effects of Air/Fuel Ratios and EGR Rates on HCCI Combustion of n-heptane, a Diesel Type Fuel. *SAE Paper* 2003-01-0747.
90. **Pickett, L. M.,** and **Lopez, J. J.** (2005) Jet-Wall Interaction Effects on Diesel Combustion and Soot Formation. *SAE Paper* 2005-01-0921.
91. **Pogorevc, P., Kegl, B.,** and **Skerget, L.** (2008) Diesel and Biodiesel Fuel Spray Simulations. *Energy & Fuels*, 22, 1266–1274.
92. **Price, R. B., Hurle, I. R.,** and **Sugden, T. M.** (1968) *Symp. (Int.) Combust.,* 12 (1), 1093–1102.

93. **Raffel, M., Willert, C.,** and **Kompenhans, J.** (2000) *Particle Image Velocimetry*. Springer, Germany.
94. **Reitz, R. D.,** and **Bracco, F. V.** (1986) Mechanisms of Breakup of Round Liquid Jets. Enzyclopedia of Fluid Mechanics. In: Cheremisnoff, N., Editors. *Encyclopedia of Fluid Mechanics*. Gulf Publishing, Houston, Texas, 3, 233-249.
95. **Rhim, D. R.,** and **Farrell, P. V.** (2000) Characteristics of Air Flow Surrounding Non-Evaporating Transient Diesel Sprays. *SAE Paper* 2000-01-2789.
96. **Rhim, D. R.,** and **Farrell, P. V.** (2001) Effect of Gas Density and Number of Injector Holes on the Air Flow Surrounding Non-Evaporating Transient Diesel Sprays. *SAE Paper* 2001-01-0532.
97. **Rhim, D. R.,** and **Farrell, P. V.** (2002) Air Flow Characteristics Surrounding Evaporating Transient Diesel Sprays. *SAE Paper* 2002-01-0499.
98. **Ricou, F. P.,** and **Spalding, D. B.** (1961) Measurement of Entrainment by Axis-symmetrical Turbulent Jets. *J. Fluid Mech.*, 11, 21-32.
99. **Rottenkolber, G.,** and **Meier, R.** (2001) Combined ‘‘Fluorescence’’ LDV (FLDV) and PDA Technique for Non-ambiguous Two Phase Measurements inside the Spray of a SI-Engine. *Part. Part. Syst. Charact*, 18, 216–225.
100. **Sasaki, S., Akagawa, H.,** and **Tsujimura, K.** (1998) A Study on Surrounding Air Flow Induced by Diesel Sprays. *SAE Paper* 980805.
101. **Sasaki, S., Ito, T.,** and **Iguchi, S.** (2000) Smoke-Less Rich Combustion by Low Temperature Oxidation in Diesel Engines (in Japanese). *Proceedings. JSAE Annual Congress*, 2000, 17-20.
102. **Sepret, V., Bazile, R., Marchal, M.,** and **Couteau, G.** (2010) Effect of Ambient Density and Orifice Diameter on Gas Entrainment by A Single-Hole Diesel Spray. *Exp. Fluids,* 49, 1293–1305.
103. **Scolari, P.** (1997) Towards A Sustainable Mobility at the Turn of the Century: the Environmental Challenge. *ATA-Ingegneria Automotoristica*, 50,11-12.
104. **Settles, G. S.** (2001) *Schlieren and Shadowgraph Techniques: Visualizing Phenomena in Transparent Media.* Berlin, Springer.

105. **Siebers, D. L.,** and **Higgins, B. S.** (2000) Effect of Injector Conditions on the Flame Lift-off Length of DI Diesel Sprays. In: Whitelaw, J.H., Payri, F., and Desantes, J. M., Editors. *Thermo-and Fluid-dynamic Processes in Diesel Engines*. Berlin Heidelberg, Springer-Verlag.

106. **Siebers, D. L.** (2009) Recent Developments on Diesel Fuel Jets under Quiescent Conditions. In: Arcoumanis, C., and Kamimoto, T., Editors. *Flow and Combustion in Reciprocating Engines*. Berlin Heidelberg, Springer-Verlag.

107. **Siebers, D. L.,** and **Higgins, B.** (2001) Flame Lift-Off on Direct-Injection Diesel Sprays under Quiescent Conditions. *SAE Paper* 2001-01-0530.

108. **Siebers, D. L.** (1999) Scaling Liquid-Phase Fuel Penetration in Diesel Sprays Based on Mixing-Limited Vaporization. *SAE Paper* 1999-01-0528.

109. **Singh, S., Musculus, M.,** and **Reitz, D.** (2009) Mixing and Flame Structures Inferred from OH-PLIF for Conventional and Low-Temperature Diesel Engine Combustion. *Combustion and Flame,* 156, 1898–1908.

110. **Shen, J., Liburdy, J., Pence, D. V.,** and **Narayanan, V.** (2009) Droplet Impingement Dynamics: Effect of Surface Temperature during Boiling and Non-boiling Conditions. *J. Phys.: Condens. Matter*, 21,14.

111. **Shimazaki, N., Tsurushima, T.,** and **Nishimura, T.** (2003) Dual Mode Combustion Concept with Premixed Diesel Combustion by Direct Injection near Top Dead Center. *SAE Paper* 2003-01-0742.

112. **Shakal, J.,** and **Martin, J.** (1994) Imaging and Spatially Resolved Two-Color Temperature Measurements Through a Coherent Fiber-optic: Observation of Auxiliary Fuel Injection Effects on Combustion in a Two-Stroke DI Diesel. SAE Paper 940903.

113. **Soid, S. N.,** and **Zainal, Z.A.** (2011) Spray and Combustion Characterization for Internal Combustion Engines Using Optical Measuring Techniques-A Review. *Energy*, 36, 724-741.

114. **Soteriou, C., Andrews, R.,** and **Smith, M.** (1995) Direct Injection Diesel Sprays and the Effect of Cavitation and Hydraulic Flip on Atomization. *SAE Paper* 950080.

115. **Song, L. J.,** and **Abraham, J.** (2003) The Structure of Impinging Jet: Computed versus Theoretical and Measured Results. *Journal of Fluid Engineering*, 125, 997-1005.

116. **Stanton, D. W.,** and **Rutland, C. J.** (1998) Multi-dimensional Modeling of Thin Liquid Films and Spray-wall Interactions Resulting from Impinging Spray. *International Journal of Mass and Heat Transfer,* 41, 3037-3054.

117. **Stanglmaier, R. H.,** and **Roberts, C. E.** (1999) Homogeneous Charge Compression Ignition (HCCI): Benefits, Compromise, and Future Engine Applications. *SAE Paper* 1999-01-3682.

118. **Stella, A., Gu, G., Kompenhans, J., Richard, H.,** and **Raffel, M.** (2001) Three-Component Particle Image Velocimetry Measurements In Premixed Flames. *Aerosp. Sci. Technol.*, 5, 357-364.

119. **Styron, J.P., Kelly, Z. P., Lee, C. F., Peters, J.E.,** and **White, R. A.** (2000) Multicomponent Liquid and Vapor Fuel Distribution Measurements in the Cylinder of a Port-Injected, Spark-Ignition Engine. *SAE Paper* 2000-01-0243.

120. **Suh, H. K., Park, S.W.,** and **Lee, C. S.** (2007) Effect of Piezo-Driven Injection System on The Macroscopic And Microscopic Atomization Characteristics of Diesel Fuel Spray. *J. Fuel*, 86, 2833-2845.

121. **Suzuki, M., Nishida, K.,** and **Hiroyasu, H.** (1993) Simultaneous Concentration Measurement of Vapor and Liquid in an Evaporating Diesel Spray. *SAE Pape*r 930863.

122. **Tanabe, H., Sorihasi, T., Karita, S., Ha, J. Y., Fujimoto, H.,** and **Sato, G. T.** (1985) Experimental Study of Transient Jet (Distribution of Concentration, Velocity and Static Pressure in Jet) (in Japanese). *Trans JSME*, 51, 2235-2242.

123. **Takeda, Y., Keiichi, N.,** and **Keiichi, N.** (1996) Emission Characteristics of Premixed Lean Diesel Combustion with Extremely Early Staged Fuel Injection. *SAE Paper* 961163.

124. **Tao, F.,** and **Bergstand, P.** (2008) Effect of Ultra-High Injection Pressure on Diesel Ignition and Flame under High-Boost Conditions. *SAE Paper* 2008-01-1603.

125. **Tinaut, F. V., Melgar, A., Gimenez, B.,** and **Reyes, M.** (2010) Characterization of The Combustion of Biomass Producer Gas in A Constant Volume Combustion Bomb. *J. Fuel*, 89 (3), 724–731.

126. **Tinaut, F. V., Reyes, M., Gimenez, B.,** and **Pastor, J. V.** (2011) Measurements of OH* and CH* Chemiluminescence in Premixed Flames in a Constant Volume Combustion Bomb under Autoignition Conditions. *Energy Fuels*, 25, 119–129.

127. **Uyehara, O. A., Myers, P. S., Watson, K. M.,** and **Wilson, L. A.** (1946) Flame Temperature Measurements in Internal Combustion Engines. *Trans. ASME*, 17-30.

128. **Wakuri, Y., Fujii, M., Amitani, T.,** and **Rsuneya, R.** (1957) Studies on the Penetration of Fuel Spray of Diesel Engine (in Japanese). *Trans. JSME*, 25, 820-826.

129. **Wang, X. G., Huang, Z. H., Zhang, W., Kuti, O . A.,** and **Nishida, K.** (2011) Effects of Ultra-High Injection Pressure and Micro-Hole Nozzle on Flame Structure and Soot Formation of Impinging Diesel Spray. *Applied Energy*, 88, 1620–1628.

130. **Witze, P. O.** (1980) A Critical Comparison of Hot-Wire Anemometry and Laser Doppler Anemometry for IC Engine Applications. *SAE Paper* 800132.

131. **Wu, P.K.,** and **Faeth, G.M.** (1995) Onset and End of Drop Formation along the Surface of Turbulent Liquid Jets in Still Gases. *Phys. of Fluids*, 7, 11.

132. **Yao, M., Zheng, Z.,** and **Liu, H.** (2009) Progress and Recent Trends in Homogeneous Charge Compression Ignition Engines. *Prog. Energy Combust. Sci.*, 35, 398-437.

133. **Yanagihara, H.** (2001) Ignition Timing Control at Toyota "UNIBUS" Combustion System. *Proceedings of the IFP International Congress*, 2001, 35-42.

134. **Yeom, J.** (2008) Diagnosis of the Behavior Characteristics of the Evaporative Diesel Spray by Using Images Analysis. *J. Mech. Sci. Technol.*, 22, 1785-1792.

135. **Zhao, H.,** and **Ladommatos, N.** (1998) Optical Diagnostics for In-Cylinder Mixture Formation Measurements in IC Engines. *Prog. Energy Combust. Sci.*, 24, 297-336.

136. **Zhao, H.,** and **Ladommatos, N.** (1998) Optical diagnostics for soot and temperature measurement in diesel engines. *Prog. Energy Combust. Sci.*, 24(3), 221-255.

137. **Zhao, H.,** and **Ladammatos, N.** (2001) Engine Combustion Instrumentation and Diagnostics. *Warrendale, SAE*.

138. **Zhang, W., Nishida, K.,** and **Gao, J.** (2008) An Experimental Study on Mixture Formation Process of Flat Wall Impinging Spray Injected by Micro-Hole Nozzle under Ultra-High Injection Pressures. *SAE Paper* 2008-01-1601.

139. **Zhang, W., Nishida, K.,** and **Tian, J. P.** (2009) Spray-Spray and Spray-Wall Interactions in Diesel Sprays from Micro-Hole Nozzles under Ultra-High Injection Pressures. *ICLASS-2009*. Colorado, USA.

140. **Zhang, Y., Nishida, K.,** and **Yoshizaki, T.** (2001) Quantitative Measurement of Droplets and Vapor Concentration Distributions in Diesel Sprays by Processing UV and Visible Images. *SAE Paper* 2001-01-1294.

141. **Zhu, J. Y., Kuti, A. O.,** and **Nishida, K.** (2011) Effects of Injection Pressure and Ambient Gas Density on Fuel - Ambient Gas Mixing and Combustion Characteristics of D. I. Diesel Spray. *SAE Paper* 2011-01-1819.